

Fifth International Conference

MMM 2010

Multiscale Materials Modeling

October 04 - 08, 2010, Freiburg, Germany

CONFERENCE PROCEEDINGS

Editors:
Peter Gumbsch
Erik van der Giessen

FRAUNHOFER VERLAG

Organized by Fraunhofer Institute
for Mechanics of Materials IWM.
Hosted by University of Freiburg.



Supported by



Microstructure Modelling

Computing the phase diagram of the FeCr binary alloy by path-sampling simulation

G. Adjanor¹, M. Athènes²

¹EDF R&D Materials and Mechanics of Components Department, Moret-sur-Loing France, gilles.adjanor@edf.fr

²CEA-Saclay Service de Recherches de Métallurgie Physique, Gif-sur-Yvette France

Due to their potential application as structural materials for fusion and Generation IV reactors, chromium ferritic/martensitic steels have recently received considerable interest. Ab initio results have shown that due to magnetism the sign of the mixing enthalpy of the Fe-Cr system changes at low temperature. One of the most challenging tasks is now to establish how this effect influences the phase diagram of the system. In a recent study, Monte-Carlo simulations in the semi-grand canonical ensemble and the thermodynamic integration method were applied, with their respective limitations. The importance of proper estimations of the vibrational contribution to free energy was also outlined, although it could not be directly estimated by these usual methods.

We report on the application a transmutation path-sampling method on this system. The path sampling technique developed consists in estimating the chemical potential difference between two compositions by appropriate averaging of the work applied on the system during the gradual switch from one composition to another by atom “transmutation”, like usually done in Widom-type methods. Operating the transmutations progressively with the help of thermodynamic integration paths allows to alleviate ergodicity issues often found in complex alloys in which steric effects (atoms overlap) would normally cause massive rejections in the Metropolis test for usual Monte-Carlo simulations.

This transmutation path-sampling technique can be seen as a combination of the former usual methods in the limiting cases of fast and slow switching rates respectively, and it has the advantage of naturally including both vibrational and configurational contributions to the chemical potential, which can be possibly estimated separately. Moreover, the analysis of path histograms yields a built-in criterion for diagnosing the convergence of thermodynamic potential estimate, allowing to investigate the optimal switching rate.

Computational Modeling of the Sintering process in Thermal Barrier Coating Systems

Karim Ahmed¹, Jie Deng², Anter El-Azab^{1,3}

¹Materials Science Program, Florida State University, Tallahassee, FL, USA,
kaa08e@fsu.edu

²Currently with Sandia National Laboratories, Livermore, CA, USA

³Department of Scientific Computing, Florida State University, Tallahassee, FL, USA,
aelazab@fsu.edu

ABSTRACT

We apply a phase field model to understand the sintering behavior of columnar thermal barrier coating (TBC) structures. The model takes into account various sintering mechanisms, including surface and grain boundary diffusion, coupled with the elastic effects arising due to the thermal expansion mismatch in the TBC system. Numerical simulation of the initial sintering of model TBC microstructures has been performed using this phase field model. The preliminary results clearly illustrate the initial sintering behavior of the TBC system, the connection between diffusional processes and morphological change during the sintering, and the dependence of the sintering process on temperature and strain.

1. Introduction

A typical TBC system consists of several material layers that are applied to the surface of a superalloy to protect it from high temperature, rapid temperature transient, oxidation and corrosion in high temperature environments [1, 2]. The main layer of a TBC system is a low thermal conductivity ceramic, such as zirconia, with some porosity left into it to further reduce thermal conduction and provide elastic compliance to the substrate expansion or contraction upon heating or cooling. Prolonged operation of TBC materials at elevated temperatures, however, leads to sintering and densification and thus degrades its desirable characteristics; namely densification increases the elastic modulus and the thermal conductivity of the TBC layer. Understanding how sintering proceeds in TBC systems is thus important for improving the design of such systems. We have recently developed a phase field approach to model the sintering in TBC microstructures [3, 4]. This model is an extension of previous phase field models that were developed to study free sintering of particles [5, 6]. In this short communication, we present our sintering model and explain its features and capabilities in the context of sintering in TBC systems. In particular, we highlight the free energy formulation and the derivation of the kinetic equations governing the phase field variables, various sintering mechanisms (namely, the surface, grain boundary and bulk diffusion), as well as the formulation of the elastic problem due to thermal mismatch in the system. The theoretical formulation of the phase field model is presented in section 2, followed by a brief discussion of the numerical scheme and sample results in section 3.

2. Phase Field Modeling of Sintering

In phase field modeling, microstructure is described by a set of continuum phase field variables. Two types of phase field variables are used here to characterize the columnar structure in TBC system. The conserved mass density field $\rho(r,t)$ is used to describe the

distribution of solid material such that ρ is equal to 1 in solid phase and 0 in porosity. Different grains in the solid region are captured by the non-conserved field variables $\eta_\alpha(\mathbf{r}, t)$, which is equal to 1 in α -th grain and 0 otherwise. The interfaces are diffuse over which $\rho(\mathbf{r}, t)$ and $\eta_\alpha(\mathbf{r}, t)$ change continuously. Since these variables vary slowly in the bulk region and rapidly in the interfaces, their evolution gives the motion of interfaces as a function of time, which reveals the microstructural change in TBC system.

2.1 Free Energy of TBC system

The total free energy functional F of the TBC system can be written in the form:

$$F = \int_V \left[f(\rho, \eta_\alpha) + e(\eta_\alpha) + \frac{1}{2} \beta_\rho |\nabla \rho|^2 + \sum_\alpha \frac{1}{2} \beta_\alpha |\nabla \eta_\alpha|^2 \right] d^3\mathbf{r} \quad (1)$$

In this expression, $f(\rho, \eta_\alpha)$ is the bulk free energy density, which has minima representing the equilibrium between the void phase and the solid. $e(\eta_\alpha)$ is the elastic strain energy density arising from the thermal expansion mismatch between TBC and substrate. The last two terms are associated with the diffuse character of interface, where β_ρ and β_α are gradient coefficients proportional to the surface and grain boundary energies. The bulk free energy density $f(\rho, \eta_\alpha)$ can be approximated by a Landau-type polynomial expansion in the order parameters [7],

$$f = A\rho^2(1-\rho)^2 + B \left[\rho^2 + 6(1-\rho) \sum_\alpha \eta_\alpha^2 - 4(2-\rho) \sum_\alpha \eta_\alpha^3 + 3 \left(\sum_\alpha \eta_\alpha^2 \right)^2 \right] \quad (2)$$

with A and B being model parameters. It can be seen from the above expression that $f(\rho, \eta_\alpha)$ has minima in the void space ($\rho = 0, \{\eta_1, \eta_2, \dots, \eta_N\} = \{0, 0, \dots, 0\}$) and in each solid grain ($\rho = 1, \{\eta_1, \eta_2, \dots, \eta_N\} = \{1, 0, \dots, 0\} = \dots = \{0, 0, \dots, 1\}$), where N is the number of grains. These grains represent the solid sub-domains of the TBC system.

2.2 Elastic Strain Energy

Assuming that the solid region (TBC layer and substrate) in the TBC system is elastic and inhomogeneous, the elastic strain energy density in TBC system can be written in the form:

$$e(\eta_\alpha) = \frac{1}{2} C_{ijkl} \phi(\eta_\alpha) (\varepsilon_{kl} - \varepsilon_{kl}^\circ) (\varepsilon_{ij} - \varepsilon_{ij}^\circ) \quad (3)$$

In the above, C_{ijkl} is the elastic tensor of the solid phase, ε_{kl} and ε_{kl}° are the total strain and eigenstrain, respectively, and $\phi(\eta_\alpha) = 3\eta_\alpha^2 - 2\eta_\alpha^3$ is an interpolation function used to taper down the elastic modulus to zero in void space. In the TBC system, eigenstrain is induced by the thermal expansion mismatch between the TBC layer and substrate.

2.3 Kinetic Evolution Equations for Phase Field Variables

The evolution of the conserved mass density field ρ is governed by the Cahn-Hilliard type equation [8]:

$$\frac{\partial \rho}{\partial t} = \nabla \cdot \left(\mathbf{M} \nabla \frac{\delta F}{\delta \rho} \right) \quad (4)$$

The non-conserved phase field variables η_α are governed by Allen-Cahn structural relaxation equation [9]:

$$\frac{\partial \eta_\alpha}{\partial t} = -L \frac{\delta F}{\delta \eta_\alpha} \quad (5)$$

In above equations, M is the mobility tensor characterizing the contributions of surface diffusion, grain boundary diffusion and volume diffusion to the sintering process. L is the parameter characterizing the mobility of grain boundary migration.

3. Numerical Scheme and Results

3.1 Numerical Scheme

While the phase field model outlined above is applicable for general 3D case, only a 2D solution is presented here. In developing the 2D solution, the equations are discretized using finite difference scheme in space and explicit Euler method in time. Periodic boundary conditions are applied in solving the elastic problem.

3.2 Results

TBC systems are created by deposition methods that yield a variety of microstructural features. An idealized TBC microstructure of interest is the zigzag structure, which can be produced by rotating the substrate during the deposition [1]. Actual columnar structure of the TBC produced by electron beam physical vapor deposition (EBPVD) show some morphological variability, which we consider in [10]. Figure 1 displays the η_α field for a zigzag structure configuration. The substrate is not shown here as it does not contribute to the evolution of the structure. In general, sintering process starts at the top surface where the curvature is highest (at the corners). The initial sharp edges become rounded to decrease the local surface free energy, which drives materials transport from top to bottom by diffusion to fill in the gaps (pores) in TBC structure.

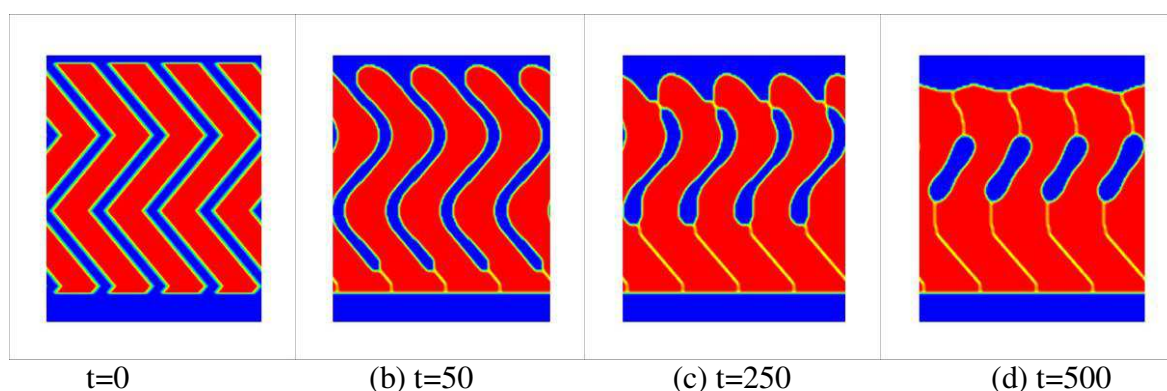


Figure 1. Time evolution of the TBC zigzag structure. The figure displays four snapshots of the non-conserved order parameter field η_α during evolution of an idealized zigzag configuration representative of EBPVD deposited TBC layers.

It is clear in Figure 1 that the current phase field model capture the neck formation at the top of the columns (see Figure 1(c)) as seen in experiment [11] and we also noticed that the structure was not fully densified during the simulation (see Figure 2) which is also in agreement with experiment [11].

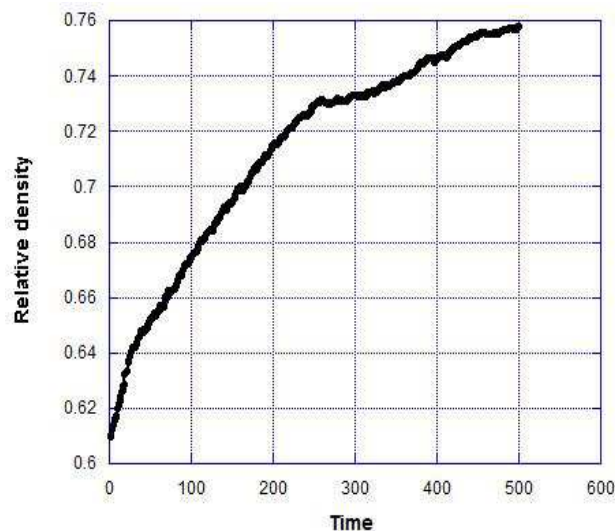


Figure 2. Evolution of the relative density with time during sintering for the zigzag structure shown in Figure 1.

The effect of temperature, and mismatch strain on the sintering behavior of a variety of TBC microstructure configurations will be discussed in details elsewhere [10].

Acknowledgements

This work was supported by the Florida Center for Advanced Aero-Propulsion (FCCAP).

References

1. N. Padture, M. Gell and E. Jordan, "Thermal Barrier Coatings for Gas-Turbine Engine Applications," *Science*, **296**, 280 (2002).
2. D. Clarke and C. Levi, "Materials Design for the Next Generation Thermal Barrier Coatings," *Annual Review Materials*, **33**, 383 (2003).
3. Jie Deng, Karim Ahmed and Anter El-Azab, "Phase Field Simulation of Sintering of Thermal Barrier Coatings," in FCAAP Annual Technical Symposium Proceedings--Advanced Materials Section (paper number 1, pp. 1-6). Orlando, FL, 2009.
4. Karim Ahmed, Jie Deng, and Anter El-Azab, "Computational Modeling of Microstructure Evolution in Thermal Barrier Coating Systems," in FCAAP Annual Technical Symposium Proceedings, Tallahassee, FL, 2010.
5. K. Asp and J. Agren, "Phase-Field Simulation of Sintering and Related Phenomena -- A Vacancy Diffusion Approach," *Acta Materialia*, **54**, 1241 (2006).
6. A. Kazaryan Y. Wang and B. Patton, "Generalized Phase Field Approach for Computer Simulation of Sintering: Incorporation of Rigid-Body Motion," *Scripta Materialia*, **41**, 487(1999).
7. L.D. Landau and E.M. Lifshitz, *Statistical Physics*, 3rd Edition, Pergamon Press, Oxford, 1980.
8. J. Cahn and J. Hilliard, "Free Energy of a Nonuniform System. I. Interfacial Energy," *Journal of Chemical Physics*, **28**, 258(1958).
9. S. Allen and J. Cahn, "A Microscopic Theory for Antiphase Boundary Motion and its Application to Antiphase Domain Coarsening," *Acta Metallurgica*, **27**, 1085(1979).
10. Jie Deng, Karim Ahmed and Anter El-Azab, to be published.
11. V. Lughetti et al., "Microstructural Aspects of the Sintering of Thermal Barrier Coatings," *Materials Science and Engineering A*, **368**, 212(2004).

Atomic Mechanisms of Structural and Superstructural Transformations in CuAuI Alloy

Starostenkov M.D.¹, Popova L.A.¹, Chaplygina A.A.¹ and Potekaev A.I.²

¹Altai State Technical University, 656038, Russia, Barnaul, Lenin Street, 46

²Tomsk State University, 634050, Russia, Tomsk, Lenin Street, 36

e-mail: genphys@mail.ru

ABSTRACT

The peculiarities of phase transformations order-disorder of CuAu alloy near equiatomic composition were studied by Monte-Carlo method in the dependence on temperature, vacancies concentration, deviation of its composition on stoichiometry and pressure. It was found that diffusion at low temperatures (400 K) took place at the expense of migration of Cu atoms over Cu sublattices without any order break. The mobility of Au atoms increased with the growth of temperature coming nearer to the stability of Cu atoms.

Cyclic transformation of crystal lattices FCT-FCC-FCT proceed in cycles heating-cooling. In this connection, the lattice parameters, tetragonality degree for CuAuI phase corresponding to L1₀ superstructure are close to experimental values. It was obtained that domains corresponding to L1₀ superstructure and divided by antiphase boundaries appeared in the disordering process. At the same time, nanoclusters corresponding to the germs of phases of L1₂ superstructure and areas of disordered solid solution were observed in the disordering process. The break of the stoichiometry of alloy composition decreased temperature of the beginning of phase order-disorder transitions, the level of alloy tetragonality.

1. Introduction

The ordered alloys and intermetallics are important objects of scientific researches i.e. they have the number of interesting for practical use physical and physics-mechanical properties. Superstructure L1₀ based on FCT of a crystal lattice is different from other types of superstructures typical for the alloys having the state of a full order because it has anisotropy of the packing of atoms components along the main crystallographic directions. Foliated packing of atoms components of the alloy in planes of type {100} is typical for the superstructure having equiatomic composition of alloys components in the state of full order. That is why the deviation from a cubic order is realized by the parameters of the lattice c/a . The transition FCT-FCC of a crystal packing takes place at a full disordering. It was experimentally stated that such transitions depended on the composition of the alloy, temperature, time during which the alloy was subjected to the given temperature, pressure, the presence of the defects of a crystal structure and other factors [1].

In the paper, the changes of structure-energetic characteristics at a thermal cycling were studied by the methods of computer experiment on the example of a model alloy CuAu in the dependence on its deviation from stoichiometry, concentration of vacancies, temperature and deformation.

2. The model of the computer experiment

The calculated crystal block in a start configuration consisted of $36 \times 36 \times 36$ elementary cells of FCC crystal and contained of about 2×10^5 atoms. Periodical boundary conditions were applied on the boundaries of the calculated block. The interactions between different pairs of atoms were given by the sets of Morse pair potential functions with the parameters taken from [2]. In this connection, temperature dependence of the coefficient of linear expansion of the alloy was taken into account. Start configuration of FCC lattice with the order corresponding to $L1_0$ superstructure was constructed. Then, the procedure of the search of the minimum of the configuration energy relatively the parameters a and c was carried out by the method of variation quazistatistics. As the result, FCC lattice was transformed into FCT with the degree of tetragonality $c/a=0.92$ and the values of the parameters $c=3.65\text{A}$ and $a=3.96\text{ A}$. The obtained values of the parameters are well agreed with reference data. The obtained structure was used as a start one for the making the following experiments. The structural reconstruction of CuAu alloy was studied using Monte-Carlo method. The choice of the method was stipulated by high velocity of calculations using big sizes of the calculated block. It was used only a vacancy mechanism of diffusion. The definite concentration of vacancies was introduced into the crystal randomly to activate diffusion process. The state of the alloy was changed in discrete moments of time; one act of self-diffusion corresponding to the jump of an atom into a vacant knot was taken by one iteration. Diffusion of atoms was conducted in correspondence with the tenets of a statistic theory of ordering. In every experiment, the conditional period of the duration of the calculation constituted 5×10^6 iterations. The temperature of the alloy was given to be constant and equal in the whole block.

The changes of the following parameters were studied during the experiment: configuration part of energy, entropy part, parameters of short-range order by Cowley, long-range order in Bragg-Williams approximation, degree of tetragonality c/a . The kinetics of the change of a domain structure in the processes of phase transitions order-disorder was analyzed. The deviation of the alloy composition from stoichiometry was given randomly by the throw of point substitution defects in the calculated block of crystal. Deformation of overall tension was given by the change of interatomic distances in the whole calculated block of the crystal.

Computer experiments showed the differences in the character of the change of short and long-range orders, configuration and free energies as in the volume of the crystal, so over the planes of the definite orientation in the dependence on temperature and the duration of thermoactivation. Diffusion in the ordered alloy CuAu1 of stoichiometric composition took place at relatively low temperatures (up to 200 K) at the expense of the displacements of Cu atoms over Cu sublattices with the presence of vacancies. The superstructural order was not broken. The relative mobility of Au atoms increased at the increase of temperature to 600 K and approached to the mobility of Cu atoms with the increase of temperature as over the planes so over the directions.

In the cycle heating-cooling, the alloy was subjected to step heating from 200 K to 1000K every 100 K and the following step cooling up to initial temperature. 5×10^6 iterations was made at every temperature. Tetragonal symmetry of the crystal changed into cubic one at the temperature of about 700 K in the process of the heating of the crystal. The reverse transition FCC - FCT took place at the cooling of the alloy. As the result, the parameters of the lattice c and a were close to the initial ones.

The graphs in Fig.1 (a, b) show the loops of hysteresis characterizing the velocity of proceeding of different phase transitions order-disorder and disorder-order. The formation of the loops of hysteresis was connected with the limitation of the simulated process in time. The calculated block had a monodomain structure at a start configuration. Several antiphase domains separated by antiphase boundaries were formed in CuAuI after thermocycling. Superstructure $L1_0$ can have six variants of APD: in twos in three interperpendicular directions. The distribution of atoms of the alloy components over APD was analyzed by the results of computer experiment.

The decrease of the amount of APB was observed with the decrease of temperature, up to two ones – at low temperatures. The boundaries of APD represented only APB of a shear type, C-domains were absent.

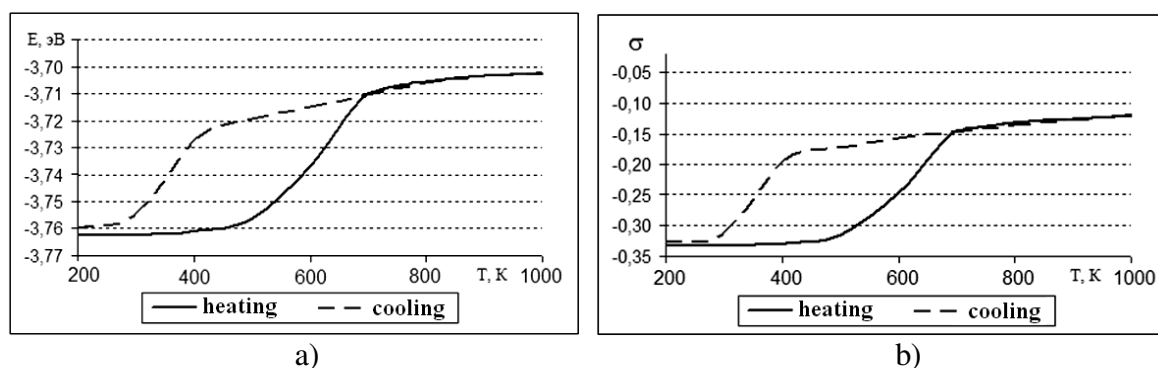


Figure 1. The loops of hysteresis in the change of configuration energy (a) and short-range order at the first coordination sphere (b) in the cycles heating-cooling.

The formation of the germs of phases of composition AB, A₃B, AB₃, phases of pure components A and B were found in the alloy structure during the ordering process. The germs of phases different from equivalent appeared to be short-living. Their number depended on temperature and duration of the experiment.

The processes of phase transitions FCT - FCC - FCT and consequently the processes of phase transitions order-disorder –order were more intensive and were displaced towards more low temperatures with the increase of the concentration of the vacancies introduced in the alloy.

The research of structural and superstructural reconstruction of CuAu alloy having the deviations from stoichiometric compositions $\pm 5\%$ was made during the cooling. The start block of crystal was given randomly by the distribution of Cu and Au atoms over the knots of FCC lattice. Then, the procedure of diffusion reconstruction of the calculated block was made using Monte-Carlo method by the search of configurations corresponding to the minimum of free energy at every given temperature.

The analysis of the change of the kinetics of a domain structure showed that the formation of six types of APD was observed at temperature 580 K (for alloy containing 45% of Cu) and higher than 640 (for alloy containing 55% Cu). The sizes of APB did not exceed 10% from the volume of crystal. Two types of APB of one orientation were preferable in the processes of the decrease of temperature and ordering as in the case of equiatomic composition. Small APD of other orientations were annihilated. The appearance of a small amount of germs of the phases of L1₂ superstructure of AB₃ or A₃B composition in phase composition of alloys having deviations from stoichiometry was found side by side with enlargement of APD of one orientation of L1₀ superstructure. The parameters of the lattice in three interperpendicular directions were equal at the initial configuration of the alloy in the disordering state. It was observed that the parameter of the lattice (c) in one of the crystallographic stresses was changing more quickly with the decrease of temperature. Fig.2 depicts the changes of the degree of the tetragonality of the alloys of CuAu system with temperature. As it is seen from Fig.2, the distortion of stoichiometric composition of the alloy leads to the decrease of the degree of tetragonality c/a .

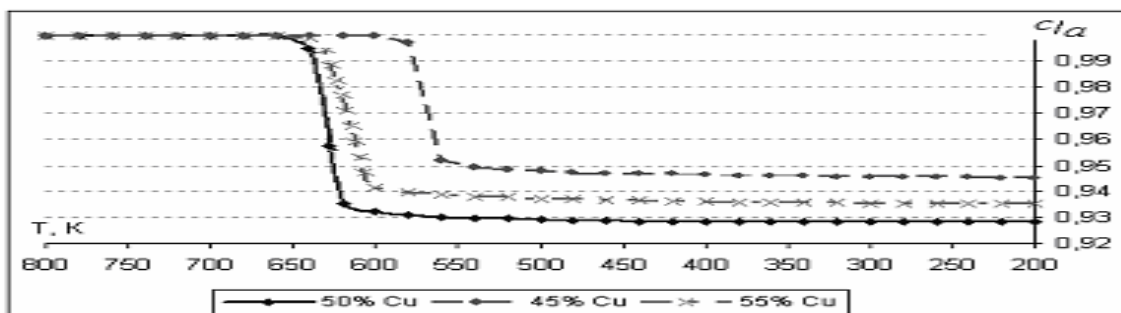


Figure 2. The dependence of the tetragonality of the alloy on temperature at different concentrations of the composition.

The dependencies of the long range order parameter and short range order parameter on temperature shows their changing for concentration from stoichiometry (Fig.3).

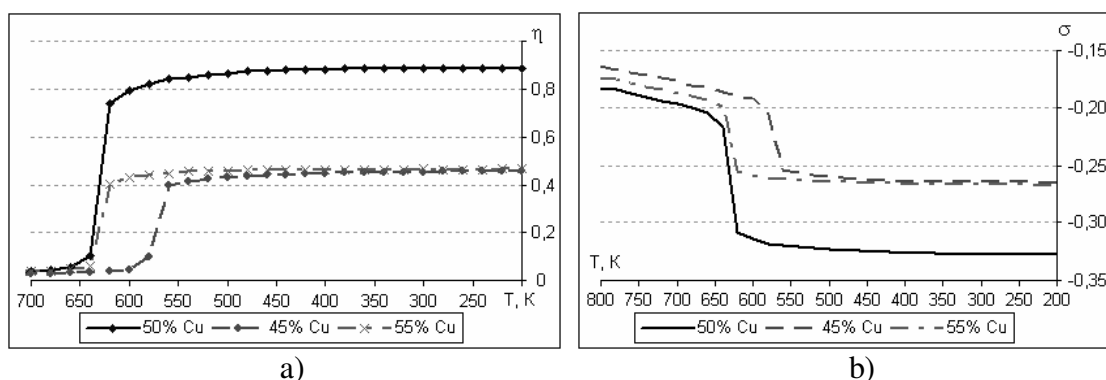


Figure 3. The dependence of the long range order parameter (a) and short range order parameter (b) on temperature at different concentrations of the composition.

Acknowledgements

The work was supported by the grant of RFBR № 090800695-a.

References

1. Hirth J.P., Lothe J. Theory of dislocations (2 ed., Wiley), 1982, 435 p.
2. Tsaregorodtsev A.I., Gorlov N.V., Dem'yanov B.F., Starostenkov M.D. Atomic structure of APB and its influence on the state of the lattice near dislocation in the ordered alloys with L12 superstructure. Physics of metals and metallography. 1984. V.58. №2. P. 336.

The Effects of Thermoactivated Atomic Reconstruction Near Planar Defects in the Ordered Superstructures $L1_2$ and $L1_0$

**Starostenkov M.D.¹, Kharina E.G.¹, Sinitsa N.V.¹, Rakitin R.Yu.¹
and Potekaev A.I.²**

¹Altai State Technical University, 656038, Russia, Barnaul, Lenin Street, 46

²Tomsk State University, 634050, Russia, Tomsk, Lenin Street, 36

e-mail: genphys@mail.ru

The superstructure of intermetallides and ordered solid solutions can have a variety of planar defects: fault defects, antiphase boundaries (APB). APB were deviated into conservative and non-conservative. In the first case, their presence did not cause any changes in the sequence of the planes packing by the atoms of the superstructure components, consequently the stoichiometry was not changed. Defects were formed as in the processes of growth of antiphase domains, so as the result of splitting of a superdislocation during deformations. The second group of APB was connected with the sequence of the planes packing by the atoms of components, and consequently with a local change of stoichiometry of the alloy composition. This type of a planar defect is observed only in the processes of thermoactivated growth or antiphase domains. One more group of planar defects is called the tubes of antiphase boundaries. Thus, planar complexes of structural defects and superstructural defects – fault defects and APB can also exist. Thermoactivated atomic reconstruction of superstructure $L1_2$ and $L1_0$ accompanied by local failure of structural and superstructural order took place near different types of planar defects. Superstructure $L1_2$ was studied on the example of alloys Cu_3Au , Ni_3Al and superstructure $L1_0$ on the example of $CuAu$ which were ordered on the basis of FCT lattice.

The Peculiarities of Structural Reconstruction of Nanofibers of L1₂ Superstructure Alloys Containing Long-Periodic APB in the Process of High-Velocity Tension Deformation

Starostenkov M.D.¹, Sinitza N.V.¹ and Potekaev A.I.²

¹Altai State Technical University, 656038, Russia, Barnaul, Lenin Street, 46

²Tomsk State University, 634050, Russia, Tomsk, Lenin Street, 36

e-mail: genphys@mail.ru

ABSTRACT

The peculiarities of structural reconstruction in nanofibers of ordered alloys of L1₂ superstructure containing periodical shear antiphase boundaries of type $\frac{1}{2} \langle 110 \rangle \{001\}$ were studied by the method of molecular dynamics. The nanofiber was presented in a form of rectangular parallelepiped with the basis in plane [001]. The nanofiber was subjected to high velocity tension deformation in direction $\langle 001 \rangle$ at the presence of rigid captures. Nanofibers of alloys Cu₃Au and Ni₃Al having a state of full superstructural order were chosen as the objects of the research. Four main stages of deformation – quazielastic, plastic, flow and facture were obtained in the computer experiment. Every stage was characterized by the appearance and accumulation of structural and superstructural defects: point dislocations, antiphase boundaries, fault defects. Temporal intervals of the stages existence in deformation process were changed in the dependence on the temperature and the number of APB introduced in the nanofiber. The presence of definite density of APB influenced on the value of extreme density of the nanofiber at low temperatures.

1. Introduction

The ordered alloys and intermetallides are important objects of scientific researches, since they have such unique for practical use property as positive temperature dependence of yield strength. Nowadays there are many models and theories trying to explain similar effect. It is considered that such planar defects typical for superstructures as antiphase boundaries (APB) can contribute in the effect of positive temperature dependence of yield strength. In case of nanostructures and nanoobjects, the above mentioned properties of materials can make substantial contribution in deformation behavior of materials.

In the paper, the research of structure-energetic transformations taking place in the process of high velocity tension deformation was made on the example of nanofibers of Ni₃Al intermetallide and Cu₃Au ordered alloy. The nanofibers of the materials under study contained the definite amount of antiphase boundaries oriented in the direction which was perpendicular to the axis of tension deformation.

2. The model and methods of computer experiment

The mechanisms of structural reconstruction in the process of high velocity deformation of uniaxial tension in metallic nanofibers were studied in the paper. Nanofibers of Ni₃Al intermetallide and Cu₃Au with L1₂ superstructure were used as the objects of the research.

The research of the dynamics of structural reconstruction was made by the method of molecular dynamics using Morse pair potential functions [1].

The calculated block of the nanofiber was presented in a form of a rectangular parallelepiped with a square basis in plane (001) and height (axis of the nanofiber) corresponding to direction $\langle 001 \rangle$. The size of the calculated block was equal to $12 \times 12 \times 18$ elementary cells ($4.07 \times 4.07 \times 6.20 \text{ nm}^3$). The total amount of atoms was equal to 10368. Mixed boundary conditions were applied to the boundaries of the block: free in directions $\langle 100 \rangle$, $\langle 010 \rangle$ and rigid or periodical in the direction $\langle 001 \rangle$ [2].

Dynamic uniaxial tension deformation was simulated by a forward displacement of all atoms composing rigid boundaries along the axis $\langle 001 \rangle$ for 0.002 nm after 0.1 ps that corresponded to the velocity of deformation $3.2 \cdot 10^9 \text{ s}^{-1}$. Computer experiment was made at the temperatures 10 K, 300 K and 1100 K (for Ni_3Al intermetallide) and 10 K, 300 K (for Cu_3Au ordered alloy).

The nanofiber of Ni_3Al intermetallide and Cu_3Au ordered alloy were investigated as in a start-ideal configurations (the absence of defects, besides free surface) so at the presence of even distributed antiphase boundaries (APB) $\frac{1}{2}\langle 110 \rangle\{001\}$ (from 1 to 7 boundaries simultaneously). The boundaries were introduced in the direction $\langle 001 \rangle$ along the length of the nanofiber so that their position corresponded to geometrical center from rigid boundaries (captures). The model corresponded to $\text{L1}_2(\text{M})$ superstructure.

3. The results and discussion

Four main stages of deformation of nanofibers of Ni and Al were determined earlier in paper [3].

Four main stages of deformation as in [3] were observed during the research in the result of a dynamic deformation of an ideal Ni_3Al nanofiber and Cu_3Au ordered alloy as at the presence of the definite concentration of APB of type $\frac{1}{2}\langle 110 \rangle\{001\}$. The stages were the following: quazielastic, plastic, flow and fracture. The typical mechanisms of structure-energetic transformations were realized at every stage of deformation. The examples of the change of stored energy of deformation and stress at the captures in the dependence on the duration of tension are shown in Fig.1 and Fig.2.

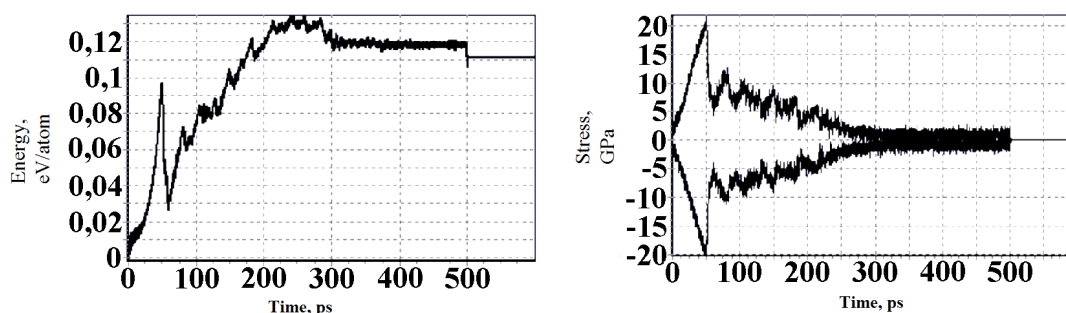


Figure 1. The dependence of stored energy of deformation and stress at the captures on time at temperature 300 K in Ni_3Al alloy.

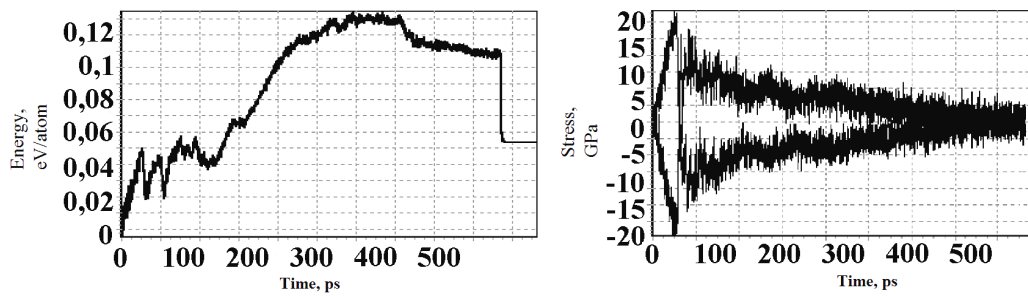


Figure 2. The dependence of stored energy of deformation and stress at the captures on time at temperatures 300 K in Cu_3Au .

The accumulation of vacancies, interstitial atoms and point substitution defects (PSD) took place at quazielastic stage of deformation. The amount of point defects increased with the increase of temperature of the experiment. The stored energy of deformation changed by the parabolic law, the stress at captures increased linear (Fig.1). The structure of the nanofiber was not changed that was proved by the absence of atoms with hexagonal closely-packed (HCP) and interstitial topologies of the nearest neighbors. The slipping of the parts of the nanofiber with the formation of antiphase domains (APD) took place at the end of the first stage. APD boundaries represented superstructural fault defects (FD) and APB. The slipping lines located at the angle $35-45^\circ$ to the axis of tension were seen on the side surface of the nanofiber at temperatures 10 K and 300 K at the end of the first stage of deformation.

Relative slipping of APB of type $\frac{1}{2}\langle 110 \rangle \{111\}$ was observed in the process of a plastic deformation. The mechanisms of structure-energetic transformations at the stage depended on the orientation of tension axis, the material of the nanofiber and the experimental temperature. New superstructural defects in a form of APB and APD were formed in Ni_3Al nanofibers.

The reconstruction of atomic structure took place during the stage of flow mainly in the area of neck formed at the end of the second stage. The values of the stored energy of deformation and stress at the captures were changed insignificantly at the stage.

After fracture, the nanofiber was divided into two parts, the reconstruction of atomic structure was not observed.

Besides general elements of distribution of deformation stages, some differences in the properties of nanofibers of Ni_3Al intermetallide and Cu_3Au ordered alloy are seen in Fig.1 and Fig.2 showing the dependences of the change of stored energy and stress at the captures on duration of deformation at temperature 300 K. The last one is characterized by lesser levels of energy and stresses in the areas of the existence of different stages of deformation. It can be noted that the beginning of the stage of plastic deformation of the nanofiber of Cu_3Au alloy is characterized by more considerable jumps of the change of energy and stress in comparison with Ni_3Al intermetallide. It is directly connected with lesser temperature of phase transition order-disorder and melting temperature typical for Cu_3Au alloy in comparison with Ni_3Al intermetallide. The jumps of the stored energy at the first stage of a plastic deformation of Cu_3Au nanofiber are connected with less energy of the formation of dislocation loops and slipping of superparticle dislocations leading to the formation of new antiphase domains. As the result, bifurcation of the stored energy of deformation is seen.

Four deformation stages were also observed after the introduction of the definite concentration of antiphase boundaries of shear type (SAPB) into the structure of a nanofiber.

It was found during the research of a long-periodic nanostructure that the presence of the defects of APB type considerably influenced on the change of temporal intervals of the beginning of a plastic deformation stage. Shortening of temporal intervals of quazielastic deformation stage took place after the introduction of APB in the nanofiber. At the same time, the change of the amount of introduced APB in the nanofiber did not influence essentially on the change of temporal intervals of the beginning of a plastic deformation stage. It was obtained that the duration of full rupture increased considerably at the increase of the amount

of introduced SAPB $\frac{1}{2}\langle 110 \rangle\{001\}$ at the temperature 10 K, 300 K. It was stated that the introduction of SAPB $\frac{1}{2}\langle 110 \rangle\{001\}$ into an ideal nanofiber with the definite period influenced on the value of maximum density. Thus, the decrease of stress at the captures was observed at T=10 K with the increase of the period of antiphase and as the result, the decrease of the value of the maximum strength decreased from 17.5 GPa to 16.5 GPa. On the contrary, the presence of internal defects of nanostructure did not influence on the value of maximum density at T=300 K and T=1100 K.

The effect of the influence of APB presence in the structure of the nanofiber decreased with the increase of temperature. The energetic interval of the accumulation of stored deformation energy leading to definite structure-energetic changes in the nanofiber at every stage of the process corresponding to tension of the deformed nanofiber decreased.

The internal reconstruction of the structure of nanofiber took place in the area of a neck at the stage of flow. The considerable changes of the values of stored energy and stress at the captures were not seen. The nanofiber was divided into two parts at the stage of fracture, structural reconstruction and changes of topology were not observed. The formation of new fault defects, twins was determined in some cases after superrapid cooling.

The role of long-period APB introduced in the nanofiber was essential only on the stages of quazielastic and plastic deformation. Their influence at the following two stages was not practically noticed, i.e. the multitude of defects competing with APB was accumulated at that stage.

The determined effects are clearly seen in the nanofiber of Ni₃Al intermetallide in comparison with Cu₃Au ordered alloy. It should be expected that the introduction of the nanofiber of more high-energetic defects such as APB of the same orientation but having local deviations in the composition from stoichiometric one can cause a considerable effect of strengthening of the nanofiber in comparison with APB of shear type.

Acknowledgements

The work was supported by the grant of RFBR № 090800695-a.

References

1. Tsaregorodtsev A.I., Gorlov N.V., Dem'yanov B.F., Starostenkov M.D. Atomic structure of APB and its influence on the state of the lattice near dislocation in the ordered alloys with L12 superstructure. *Physics of metals and metallography*. 1984. V.58. №2. P. 336.
2. Starostenkov M.D., Yashin A.V., Dudnik E.A., Sinitsa N.V., Khoroshilov D.E. Structure-energetic transformations in metallic nanofibers in conditions of high-velocity dynamic deformation of tension// *Perspective materials*. 2009. Special issue №7. P. 383-388.
3. Starostenkov M.D., Yashin A.V., Dudnik E.A., Sinitsa N.V. The research of structural transformations in Ni₃Al alloy under the influence of uniaxial tension deformation// *Deformation and fracture of materials*. 2009. №6. P. 28-31.

Influence of oxygen on the fracture of tungsten

Jürgen Almanstötter, Bernd Eberhard

OSRAM GmbH, I OSR R&D TM DM-E, Mittelstetter Weg 2, 86830 Schwabmünchen,
Germany, j.almanstoetter@osram.de, b.eberhard@osram.de

ABSTRACT

The thermal treatment of highly pure tungsten samples in oxygen atmosphere of 10^{-3} mbar (air) and three-point bending test lead to distinguished fracture behaviour. SEM observations reveal intergranular fracture by grain boundary decohesion for such treated samples. EBSD measurements were used to determine the grain boundary misorientations. One special type of grain boundary has been chosen for first-principles calculations of O segregation on a W grain boundary based on the FLAPW method as implemented in Wien2k. The Rice-Wang criterion indicates embrittlement of the grain boundary by oxygen in agreement with experimental results.

1. Experimental

Highly pure tungsten wire samples of 0.5 mm diameter were annealed at 1850 °C by direct current heating in a vacuum chamber at 10^{-3} mbar for 15 min. Wire lengths of 15 cm were used to guarantee a sufficient isothermal zone. During the annealing a constant temperature is applied by using a defined electrical current controlled by an optical pyrometer. The temperature is emissivity adjusted and influences of windows and lenses have been corrected. Samples of 1.5 cm length were cut from the isothermal zone of the wire and loaded in a three point bending test until fracture.

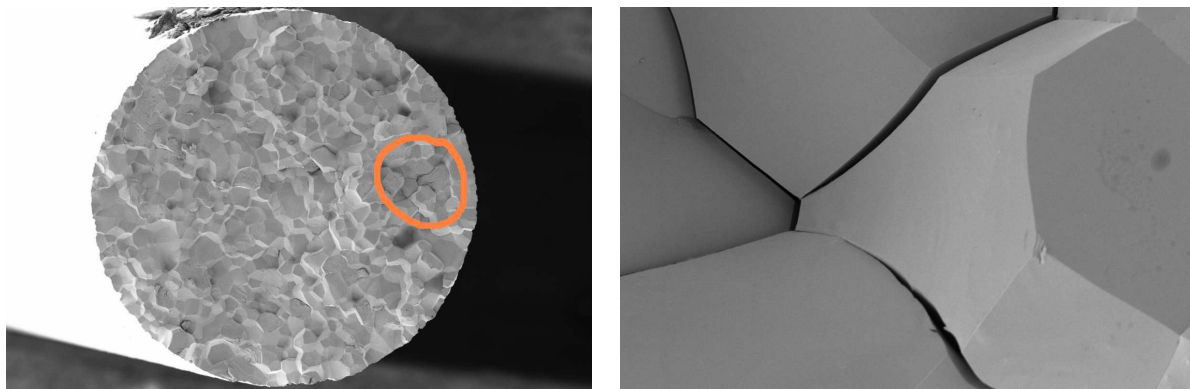


Figure 1: Fracture surface of annealed specimen at 1850°C for 15 min at contamination level of about 10^{-3} mbar air. Left: Surface showing complete intergranular fracture (magnification 150 x). Right: Zoom of the orange marked area with grain boundaries showing failure by decohesion (magnification 4000 x).

It is reported that for polycrystalline tungsten samples at temperatures between 1650 and 2600 Kelvin within an oxygen atmosphere at partial pressures of $< 1.3 \cdot 10^{-4}$ mbar a steady state between adsorption of O_2 from the surrounding gas phase and desorption of O atoms and oxide molecules is reached [1]. We estimated using data from [1] that an almost complete

monolayer is built up in our atmosphere with a dwell time of > 20 s. We expect that these conditions lead to oxygen diffusion into the material.

2. Electron backscatter diffraction (EBSD) measurements

As we identified the separation of grain boundaries as important mechanism in the fracture behaviour of the tungsten samples exposed to the oxygen partial pressure described, we concluded to consider the character of the grain boundaries. Figure 2 shows the result of an EBSD measurement of a heat treated sample. The colour coding of the grain boundaries indicate the angle ranges of misorientations. Small angle grain boundaries $< 15^\circ$ have been omitted in the visualization since the subgrain structure is not of interest for the fracture phenomena considered in the present study. Special emphasize should be given to the appearance of the red coloured grain boundaries within the angle range 35° – 39° (red colour) since in the following we investigate a grain boundary within this range in more detail.

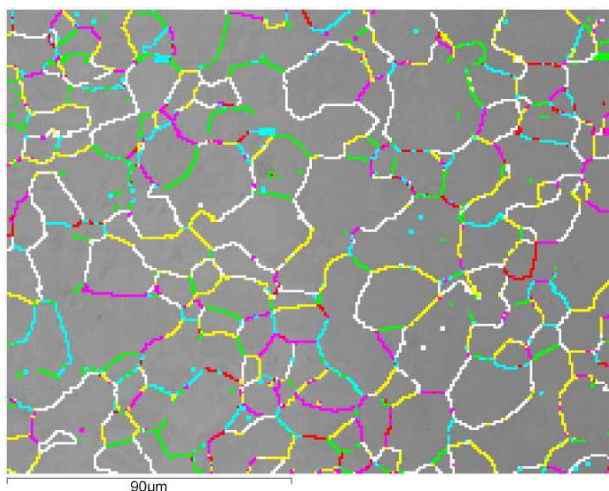


Figure 2: Grain boundary misorientation angles from EBSD mapping: green: 15° – 23° , light blue: 23° – 35° , red: 35° – 39° , magenta: 39° – 46.7° , yellow: 46.7° – 54.7° , white: 54.7° – 62.5° .

3. Geometry of the bcc $\Sigma 5(310)[001]$ grain boundary

Since it would be overwhelming to consider arbitrary grain boundary types by electronic structure calculations, we have chosen to concentrate on a given type with an angle appearing in our EBSD measurements. The grain boundary under consideration is the $\Sigma 5(310)[001]$ with an angle of 36.9° . The rotation axis of the grain boundary is the $[001]$ direction, whereas the grain boundary plane is the (310) plane of the bcc lattice. The representation of this grain boundary without an impurity could be done using a supercell within the orthorhombic space group No. 63 (Cmcm). Inserting an impurity breaks symmetry elements and leads to a supercell within the monoclinic space group No.12 ($C2/m$).

4. First-principles calculations

The first-principles electronic structure calculations in this study are based on the full potential linearized augmented plane wave (FLAPW) method [2] as implemented in the Wien2k code [3]. The cut-off parameters of the plane wave expansion are chosen to be $R_{MT} k_{max} = 8$ for the wavefunction, $G_{max} = 14$ for the charge density and the maximum l for the non-muffin tin (MT) potential expansion V_{NMT} to be 6. The MT radius is set to 2.3 a.u. for

tungsten and 1.9 a.u. for oxygen. The exchange-correlation functional is chosen to be GGA (PBE96). The energy of separation between core and semicore is -9 Ry. All calculations are carried out for the non-spin-polarized state. Local orbitals and the APW basis are used according to the default settings of Wien2k. For the integration of the Brillouin zone a $4 \times 4 \times 1$ k-point mesh is used. First the theoretical equilibrium lattice constant for tungsten has been calculated using these parameters taking the bulk in an orthorhombic cell of space group No. 63 with a result of $a_0 = 6.012057$ a.u. This value has been used for all further calculations.

The geometry optimization of atomic positions within the supercell is done by force minimization using a damped Newton scheme until the forces on every single atom in the cell are below 1 mRy/a.u. . To keep the lattice constant, the atoms were not allowed to relax along the [001] direction. The clean free surface (FS) and grain boundary (GB) surface energies are calculated by the energetics of the respective cells in reference to the bulk cell and the interface area A. The results are:

$$\gamma(\text{GB}) = (E(\text{GB}) - E(\text{bulk})) / 2A = 2.548 \text{ J/m}^2$$

$$\gamma(\text{FS}) = (E(\text{FS}) - (11/20) \cdot E(\text{bulk})) / 2A = 3.753 \text{ J/m}^2. \quad (1)$$

The factor 2 in the division means that two GB/FS interfaces are included in a supercell. The calculation of the bulk energy has been carried out under the same conditions as for the GB/FS system but with the W atoms arranged in periodically repeated bcc structure (20 atoms). An almost identical cell is important for the calculation of accurate energy differences between two structures. Experimental values in literature are only available for a (110) tungsten surface with a similar open structure as the (310) having $\gamma(\text{FS}) = 3.675 \text{ J/m}^2$ [4], giving confidence to our value.

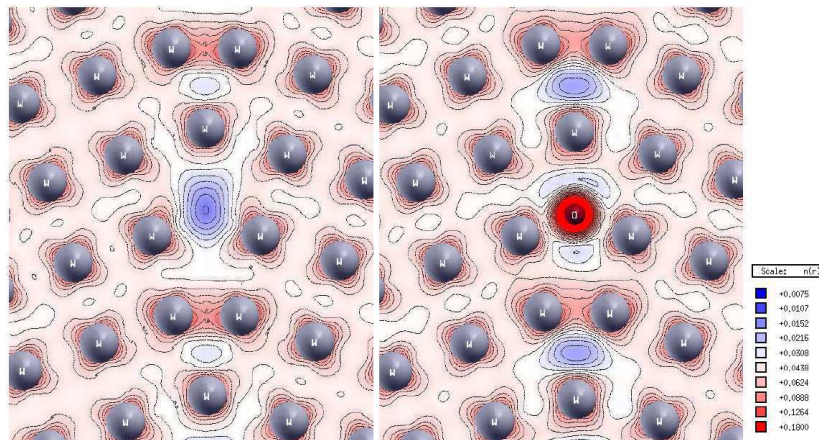


Figure 3: Valence electron density distribution perpendicular to a tungsten $\Sigma 5(310)[001]$ grain boundary (GB). Left: clean GB. Right: Oxygen segregated GB. Colours range from 0.0075 (blue) to 0.18 (red) electrons/a.u.³ on a logarithmic scale.

The results for the valence charge density of the clean and the oxygen segregated $\Sigma 5(310)[001]$ grain boundary are shown in figure 3. As to be expected, the clean grain boundary shows bonding with covalent character between the near sitting tungsten atoms. Depletion in valence charge is clearly observed in the open region of the boundary where impurities can be incorporated. Insertion of oxygen into this open area of the grain boundary leads not only to a change in valence charge in this area by the atom itself, but also to an additional depletion of electron density in vicinity of the tungsten atoms with shortest distance. This clearly influences the cohesion properties of the grain boundary.

The binding energy difference of an impurity in the free surface (FS) and grain boundary (GB) environments is very small with respect to the total energy. To obtain reliable binding energy differences, the FS and GB systems must be treated on equal footing and the atomic structures of the FS and GB should also be optimized with and without impurities.

The strength of interaction between an impurity and FS or GB is represented by its binding energy [5],

$$\begin{aligned}\Delta E_s &= E(\text{FS}) + E(\text{O}) - E(\text{O/FS}) \\ \Delta E_b &= E(\text{GB}) + E(\text{O}) - E(\text{O/GB}).\end{aligned}\quad (2)$$

The calculated binding energy for oxygen decreases from the free surface to the grain boundary. The thermodynamic theory of Rice and Wang [6] relates the change in the overall cohesive strength of a grain boundary to the binding energies of the GB and the free surfaces that would be formed by cleaving the GB, with and without impurity. The key quantity to be calculated is the Griffith work change or strengthening energy [5],

$$\Delta E_B = \Delta E_b - \Delta E_s = -1.6 \text{ eV}.\quad (3)$$

The negative value [5] indicates an embrittlement of the $\Sigma 5(310)[001]$ tungsten grain boundary by oxygen and confirms our experimental findings.

5. Conclusions

A critical oxygen partial pressure-temperature range exists, where the oxygen adsorption reaches an amount below one monolayer and a protective tungsten-oxide structure is no more build up. Oxygen atoms available during a given dwell time on the surface diffuse into the volume. The oxygen impurity can cause embrittlement of W grain boundaries leading to intergranular fracture.

References

- [1] U. Bänninger, E.B. Bas, Surf. Sci. 50 (1975) 279-295
- [2] D.J. Singh and L. Nordström, Plane waves, pseudopotentials and the LAPW method, Springer Verlag, New York, 2006
- [3] P. Blaha, K. Schwarz, G. Madsen, D. Kvasnicka and J. Luitz, WIEN2k, Technische Universität Wien, Austria, 2001 (ISBN 3-9501031-1-2)
- [4] M. Mrovec et al., Phys. Rev. B 75 (2007) 104119
- [5] W. T. Geng et al., Phys. Rev. B 60 (1999) 7149-7155
- [6] J.R. Rice, J.S. Wang, Mat. Sci. Eng. A 107 (1989) 23-40

Efficiency Study of Metal Foams for Heat Storage and Heat Exchange

A. August¹, B. Nestler², F. Wendler¹, M. Selzer¹, A. Kneer³, E. Martens¹

¹Institute of Materials and Processes, Karlsruhe University of Applied Sciences,
Moltkestrasse 30, 76133 Karlsruhe, Germany

²Institute of Reliability of Components and Systems, Karlsruhe Institute of Technology
(KIT), Haid-und-Neu-Str. 7, 76131 Karlsruhe, Germany

³TinniT Technologies GmbH, Erbprinzenstrasse 32, 76133 Karlsruhe, Germany

ABSTRACT

Metal foams promise to serve as better heat exchanger. They are of low weight which is one of the general characteristics of foams. But what does this mean? Metal foams with their channel systems of open pores can be used as a flow device or a fluid such as a PCM liquid can be inserted into the open areas of the foam. The advantage of metal foams is that the porosity builds a large surface which can be used to exchange heat. The total heat conductivity in the structure strongly depends on the conductivity of the metal. If there is a phase change material (PCM) inserted, heat is transferred by conduction from the thin metal structures to the PCM until the melting point of the PCM is reached. A part of the transferred heat transfer is used to melt the PCM. The result is that heat can be latently stored. For a wider usage of the advantages in heat transfer and heat storage, there is a need for simulation tools validated by experiments. Here we present a 3D simulation approach based on the phase-field method to analyse the thermal conductivity in air-filled aluminum foams with different pore structures. The results are compared with the thermal conductivity in massive aluminum and in pure air. The phase-field method is capable to model both the microstructure of the metal foam and the evolution of the heat.

1. Metal foams

Metal foams are materials with exceptional quantities: They evince extremely low density and at the same time outstanding mechanical, electrical, thermal and acoustic properties. For these reasons they are kindly regarded in machine tool building, machine construction, vehicle construction, architecture and another sectors: sports goods, heat exchangers, energy attics, catalytic converters, box radiators and so on.

However there are many difficulties in the use of aluminum foams, because of lacking sufficient regulations for construction, lacking production- and process parameters as well as lacking simulation data. There are increased requirements for appropriate knowledge of material properties, in particular of heat transfer and residual stresses for production and joining technologies, which are related to the intricate strut morphology of the material. As an example for the structures considered here, Figure 1 shows the photograph of a typical open pore aluminum foam.



Figure 1: Image of an aluminum open cell foam with 10 ppi and with an aluminium share of 8.23 %.

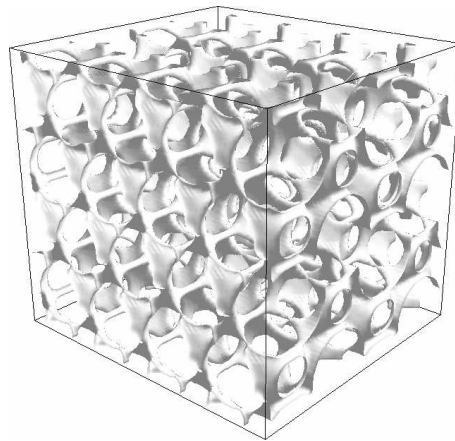


Figure 2: Regular test structure: Simulation domain filled by close packed spheres

2. Generation of foam structures with different porosities

To simulate the heat transfer in metal foams, the first step is to generate a 3D open pore structure in the interior of the computational domain. The strategy is to first consider regular and then random arrangements of spheres and polyhedrons. An example of a regular tailored structure is displayed in Fig. 2, which was created by close packing the space with slightly overlapping spheres. Built on this procedure, additional initial simulation data will be prepared in future work using experimental 2D micrographs to reconstruct real foam structures. For comparison, melting and solidification processes occurring in the pore space medium can be modelled.

3. Phase Field Modeling of Heat Diffusion

Phase-field models provide very powerful methods for simulation applications exploiting the complex mechanisms of microstructure formation and investigating the processing conditions influenced by the specific microstructure of the material. Characteristic quantities of the microstructure, phase transformation processes, heat and mass diffusion can be taken into account, [1]. Simulation studies enable the analysis of correlations of micro structure quantities, process boundary conditions and material and mechanical properties among themselves.

The basic concept of the phase-field method is a partitioning of the simulation domain in sub-domains - called phases- and a diffuse interface layer between the different distinct phases. A phase contains specific properties such as the aggregate state, an initial temperature, a specific

composition, a particular crystal orientation and possibly a residual stress. Two separate phases differ from each other in at least one of these properties. The complete set of all phases is described by the vector-valued order parameter

$$\vec{\phi}(\vec{x}, t) = (\phi_1(\vec{x}, t), \dots, \phi_N(\vec{x}, t)). \quad (1)$$

ϕ_α equals 1 in regions, where the phase α is present and $\phi_\alpha = 0$ where the phase α is absent. An exception is the diffuse layer which surrounds the phase α . Here ϕ_α changes continuously differentiably and monotone from 0 to 1. The simulation domain is allowed to contain furthermore K different components, e.g. chemical elements and compounds, also referred to as concentrations written as

$$\vec{c}(\vec{x}, t) = (c_1(\vec{x}, t), \dots, c_K(\vec{x}, t)). \quad (2)$$

Everywhere in the simulation domains, the following constraints have to be fulfilled

$$\sum_{\alpha=1}^N \phi_\alpha = 1 \quad \text{and} \quad \sum_{i=1}^K c_i = 1. \quad (3)$$

In a phase-field simulation, the entropy functional

$$S(e, \vec{c}, \vec{\phi}) = \int_{\Omega} \left[s(e, \vec{c}, \vec{\phi}) - \left(\epsilon a(\vec{\phi}, \nabla \vec{\phi}) + \frac{1}{\epsilon} w(\vec{\phi}) \right) \right] dx \quad (4)$$

is to be maximized on the basis of classical irreversible thermodynamics. Following conservation laws for the internal energy e , the energy equation can be derived by means of variational differentiation of the entropy functional. Applying the Gibbs relations, the evolution of the temperature follows everywhere in simulation domain by the equation

$$e = f(\vec{\phi}, \vec{c}, T) + Ts(e, \vec{c}, \vec{\phi}) = f(\vec{\phi}, \vec{c}, T) - Tf_{,T}(\vec{\phi}, \vec{c}, T), \quad (5)$$

where e is the internal energy and the notation $f_{,T}$ denotes the derivative of the bulk free energy density $f(\vec{\phi}, \vec{c}, T)$ with respect to the temperature. The evolution equation for internal energy is formulated as a balance law. The involved heat flux is derived from functional Eqn. (4) by a linear relation of the respective thermodynamic driving forces $\nabla \delta S / \delta e$ and $\nabla \delta S / \delta c_i$ using mobility (Onsager) coefficients L_{ij} :

$$\partial_t e = -\nabla \cdot \left(L_{00} \nabla \frac{1}{T} + \sum_{j=1}^K L_{0j} \nabla \left(\frac{-\mu_j}{T} \right) \right) \quad (6)$$

Heat transport by particle diffusion is neglected in here, hence the L_{0j} coefficients are set to 0. The transport term taking heat transport by conduction into account is defined as $L_{00} = k(\vec{\phi})T^2$, with a heat conductivity constructed as an interpolation of phase dependant values $k(\vec{\phi}) = \sum_{\alpha=1}^N k_\alpha \phi_\alpha$. In the present application, the phase field $\vec{\phi}$ is used just as a boundary condition in the problem of heat transport in a heterogeneous medium, hence it is not evolved in time. When studying heat transport under flow conditions, the partial derivative in Eqn. (6) will be replaced by the material time derivative, $\partial_t \rightarrow \partial_t + \vec{v} \nabla$.

4. Results - Heat Propagation in aluminum foams

In simulation studies we investigate the heat propagation in air filled aluminum foams depending on the fineness of the open pore structure and compare the results with those obtained for

the same total volume of pure aluminum or of pure air. Fig. 3 illustrate snapshots of the temperature field within the foam at an intermediate state of the simulation for two different heat inputs from the domain boundary, realized by Dirichlet boundary conditions for $T = 600K$ (bottom) and $T = 600K$ (top). In the first simulation the heat is imposed from the bottom boundary of the computational box, whereas in the second simulation the heat is symmetrically applied from the bottom and top boundary layer.

Table 1: Simulation parameters:

grid size	$100 \times 100 \times 100$ grid cells
phys. size of domain	$1cm^3$
initial temperature inside of the domain	$300K$
head conductivity of aluminum	$2.422 \cdot 10^6 J/(m^3K)$
head conductivity of air	$1.297 \cdot 10^3 J/(m^3K)$
boundary condition top	$600K$
boundary condition bottom	$600K$

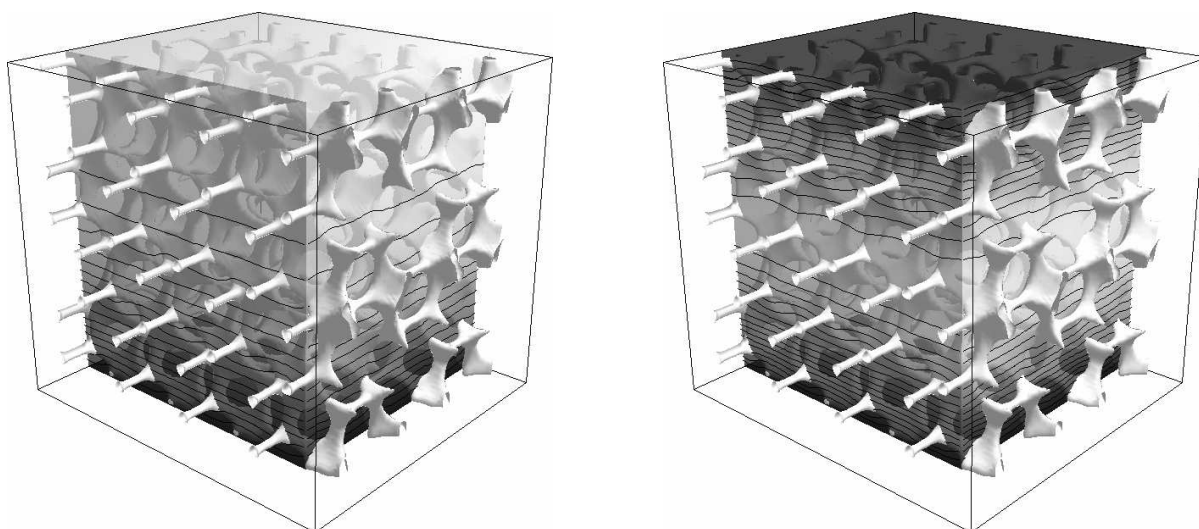


Figure 3: Simulated temperature field (isothermal surfaces indicated) in an air filled aluminum foam, heated at the bottom (left) and at the bottom and top (right).

References

- [1] B. Nestler, H. Garcke, and B. Stinner. Multicomponent alloy solidification: Phase-field modeling and simulations. *Physical Review E*, 71(4):41609, 2005.
- [2] Stöbener, Karsten. *Advanced pore morphology (APM) - Aluminiumschaum*. PhD thesis, Düsseldorf, 2007.
- [3] Stefan Ströhl. *Numerische und experimentelle Untersuchung des elastisch-plastischen Verhaltens von Metallschäumen*. PhD thesis, Düsseldorf, 2006.

Dynamics of Diffusion-controlled Dislocation Loop Coarsening in fcc Crystals

B. Bako¹, E. Clouet¹, and L.M. Dupuy²

¹CEA, DEN, Service de Recherches de Métallurgie Physique,
91191 Gif sur Yvette, France

²CEA, DEN, Service de Recherches Métallurgiques Appliquées,
91191 Gif sur Yvette, France

Dislocation climb mobilities obtained by vacancy bulk diffusion theory are employed to study the late-stage dynamics of prismatic dislocation loop coarsening with a nodal three-dimensional dislocation dynamics code in fcc metals. Results of our dislocation climb simulations are compared with the coarsening theory developed by Kirchner, Burton, and Speight. It is found that in the dilute phase, the dynamics of loop coarsening is well described by this theory. Dislocation dynamics simulations with both glide and climb are then presented. With dislocation glide, the resulting coarsening of the loops is always faster than with only climb, due to loop coalescence controlled by the dislocation glide. Depending on the initial size, density, and distribution of the dislocation loops, a cross-over from a coarsening by bulk diffusion enhanced by rare loop coagulation to a coarsening by bulk diffusion and coalescence due to dislocation glide is observed. The model of Kirchner, Burton, and Speight remains as a limiting case for systems where dislocations can not glide.

Multiscale analysis of deformation and fracture in coated material under dynamic loading. Numerical simulation

R.R. Balokhonov¹, V.A. Romanova¹ and S. Schmauder²

¹ Institute of Strength Physics and Materials Science (ISPMS), SB RAS, Russia,
rusy@ispms.tsc.ru

² Institut für Materialprüfung, Werkstoffkunde und Festigkeitslehre, University of
Stuttgart, Germany

ABSTRACT

Investigated in the paper is the deformation and fracture of the “steel substrate – boron coating” composite. A dynamic boundary-value problem in a plane strain formulation is solved numerically by the finite-difference method. To simulate the mechanical response of the steel substrate and boride coating use was made of a relaxation constitutive equation based on microscopic dislocation mechanisms and a fracture model taking into account types of local stress state. An introduction of a mesovolume with a boride hardened layer of a complicated geometry in an explicit form allows us to prescribe the length scales – scale hierarchy of inhomogeneities, whose characteristic sizes might differ by two orders of magnitude. A series of numerical experiments was conducted for varying strain rate of tension and compression. The local regions of bulk tension are shown to arise near the interfaces even under simple uniaxial compression of the composite that controls the mechanisms of fracture at the mesoscale. Computational analyses testify that: (i) the higher is the strain rate, the less intensive is the cracking of the coating, (ii) the macroscopic stress depends exponentially on the compression strain rate.

1. Introduction

Coating deposition technologies are widely used in civil engineering, gas-and-oil producing industry and agriculture for reconditioning machine parts and devices, and most of the constructional materials are the gradient and coated materials. Special attention is given for materials used in microelectronics, where an oxidation of surfaces results in multiple cracking, and different coatings can prolong lifetime of the elements.

The main goal of the paper is to simulate the mechanical behavior of a “steel substrate–boron coating” composite under dynamic loading of different types: tension and compression, and to investigate deformation and fracture of the composite under different strain rates.

2. Formulation of the problem

A dynamic boundary-value problem in a plane strain formulation is solved numerically by the finite-difference method.

Experimental evidence [1] shows that the diffusion borating deposition technique allows high-strength coatings to be produced with a needle-like, toothed shape of the “substrate–coating” interface. Figure 1b shows the structure of a mesovolume with a coating, which was used in the calculations and corresponds to that observed in a real experiment (see Fig. 1a). In the case in question, where the interface has a needle-like profile and complicated geometry,

we might single out the following types of inhomogeneities at different scale levels and their respective characteristic sizes. In particular, proper boride needles, whose size is $\sim 50\text{--}100\ \mu\text{m}$ (Fig. 1b), are independent stress concentrators. A quasiperiodic alternation of boride and steel needles results in formation of a peculiar stress-strained state at mesolevel II.

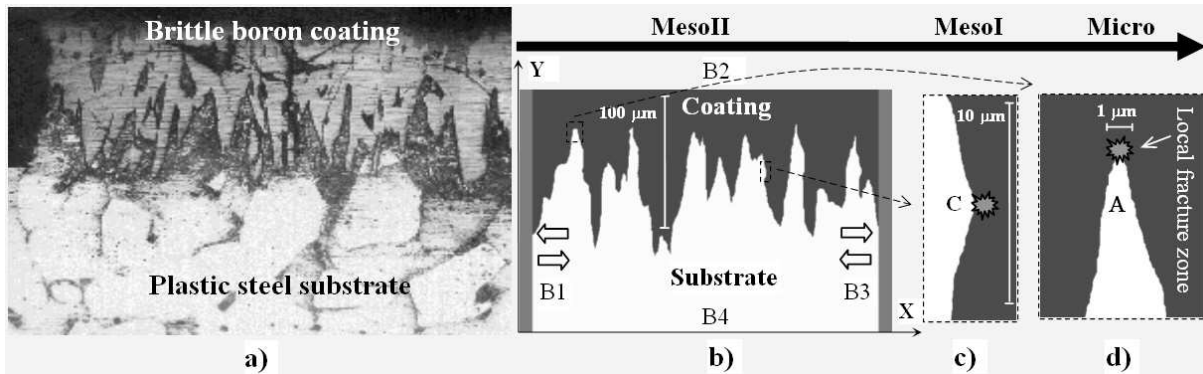


Fig. 1: Mesovolume of the composite under horizontal loading conditions and characteristic sizes of inhomogeneities at different scale levels: (a) experiment [1] and (b–d) simulation.

The shape of individual needles, in its turn, is not perfect and exhibits fine structure at a lower scale level. Throughout the interface profile, there are convexities and concavities. The characteristic size of these inhomogeneities is $5\text{--}10\ \mu\text{m}$ (Fig. 1c). The regions of "intrusion" of ductile steel into a more brittle and strong boride material are sources of geometrical stress concentration at mesolevel I.

The local fracture zone has a characteristic size of $\sim 1\ \mu\text{m}$ (Fig. 1d) and controls stress concentration processes at the microlevel. The boride coating fails near the interface in the vicinity of regions C or A, depending on the external loading condition (tension or compression). The formation of fracture zones results in both localization of plastic deformation in the steel substrate exhibited as shear microbands and crack propagation in the hardened layer.

Thus, an introduction of the structure of a mesovolume with a boride hardened layer of a complicated geometry in an explicit form allows one to prescribe the length scales – scale hierarchy of inhomogeneities, whose characteristic sizes might differ by two orders of magnitude: proper boride needles ($100\ \mu\text{m}$) – mesolevel II, curvature of the material – coating interface ($10\ \mu\text{m}$) – mesolevel I, and the local fracture zone ($1\ \mu\text{m}$) – microlevel.

To simulate the mechanical response of the steel substrate use was made of a relaxation constitutive equation based on microscopic dislocation mechanisms [2]:

$$\dot{\varepsilon}_{ij}^p = \frac{2\dot{\varepsilon}_r^p}{\sigma_{eq}} \exp\left\{-\frac{G_0}{kT} \left[1 - \left(\frac{\sigma_{eq} - \sigma_{eq}^A}{\tilde{\sigma}}\right)^w\right]^z\right\} S_{ij}, \quad T = T_0 + \int_0^{\varepsilon_{eq}} \frac{\beta}{\rho_0 C_v} \sigma_{eq} d\varepsilon_{eq}^p, \quad (1)$$

where $\dot{\varepsilon}_{ij}^p$ is the plastic strain rate tensor, S_{ij} – deviatoric stress tensor, σ_{eq} and ε_{eq}^p – equivalent stress and plastic strain, $\dot{\varepsilon}_r^p$ is the reference value of the plastic strain rate, G_0 is the energy that a dislocation must have to overcome its short-range barrier solely by its thermal activation, $\tilde{\sigma}$ is the stress above which the barrier is crossed by a dislocation without any assistance from thermal activation T_0 – initial test temperature, ρ_0 – material mass density, C_v – heat capacity.

Let us define the athermal equilibrium part of the current stress as for the STE250 steel [2]:

$$\sigma_{eq}^A(\varepsilon_{eq}^p) = \sigma_s - (\sigma_s - \sigma_0) \exp(-\varepsilon_{eq}^p / \varepsilon_r^p), \quad (2)$$

where σ_s and σ_0 are the saturation and yield stresses, ε_r^p is the reference value of plastic strain.

To describe fracture of the boride coating use was made of Huber's criterion modified to account for the difference in strength values of the tensile and compressive regions:

$$\sigma_{eq} = \begin{cases} C_{ten}, & \text{if } \varepsilon_{kk} > 0 \\ C_{com}, & \text{if } \varepsilon_{kk} < 0 \end{cases}, \quad (3)$$

where C_{com} and C_{ten} are the values of the tensile and compressive strengths.

4. Calculation results

Figure 2 shows the distribution of the stress tensor components under external compressive loading for the cases of needle-like and plane "coating-substrate" interfaces. It is clearly seen that under uniaxial compression of a coated material with the plane interface along the X-direction, only the values of σ_{xx} remain nonzero throughout the computational domain. In contrast, the serrated shape of the substrate-coating interface favors the development of a complex stressed state with nonzero values of the stress component σ_{yy} .

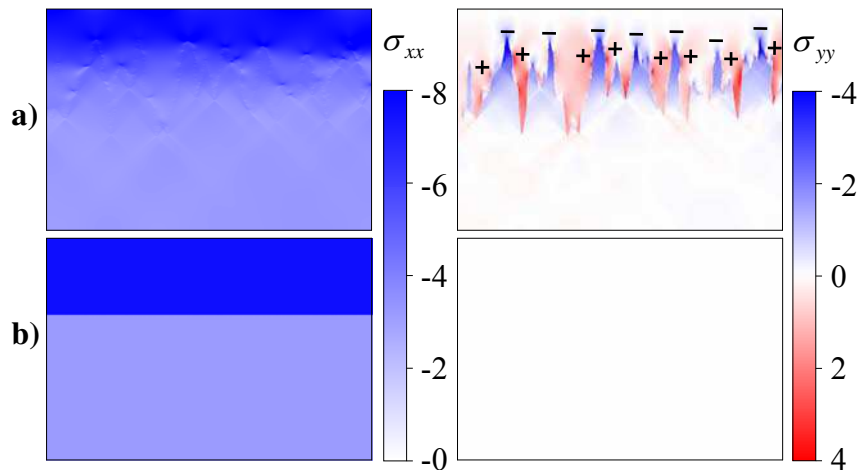


Figure 2. Distribution of stress tensor components ($\times 10^2$ MPa) for needle-like (a) and plane "coating-substrate" interfaces (b) under compression of the mesovolume.

Note that it is in the Y-direction that the material experiences both compressive and tensile stresses that in their absolute values are comparable to the values of external compressive loads. Thus, the regions of the steel substrate located between the boride teeth are subjected to compressive stresses while the teeth themselves experience tensile stresses.

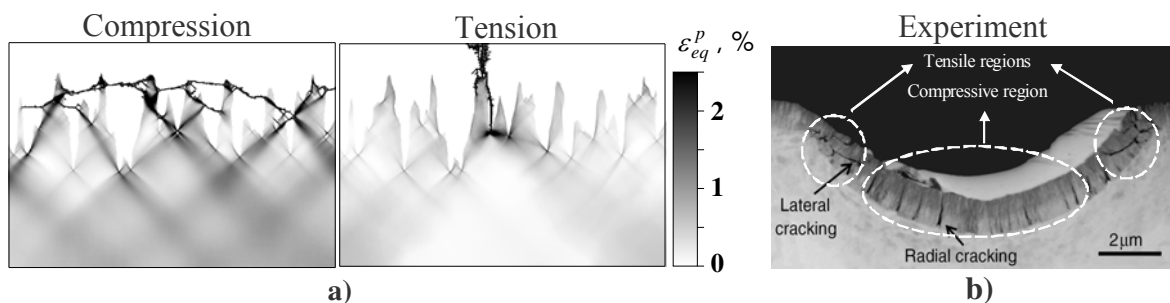


Figure 3. Distributions of the equivalent plastic strain (fractured regions in the coating are marked by black color) (a) and experimental mesoscopic section of a coating deposited on stainless steel after nanoindentation [3] (b).

Thus, local tensile stresses develop in different places under external tension and compression. This fact is responsible for the difference in fracture processes under tension and compression (Fig.3).

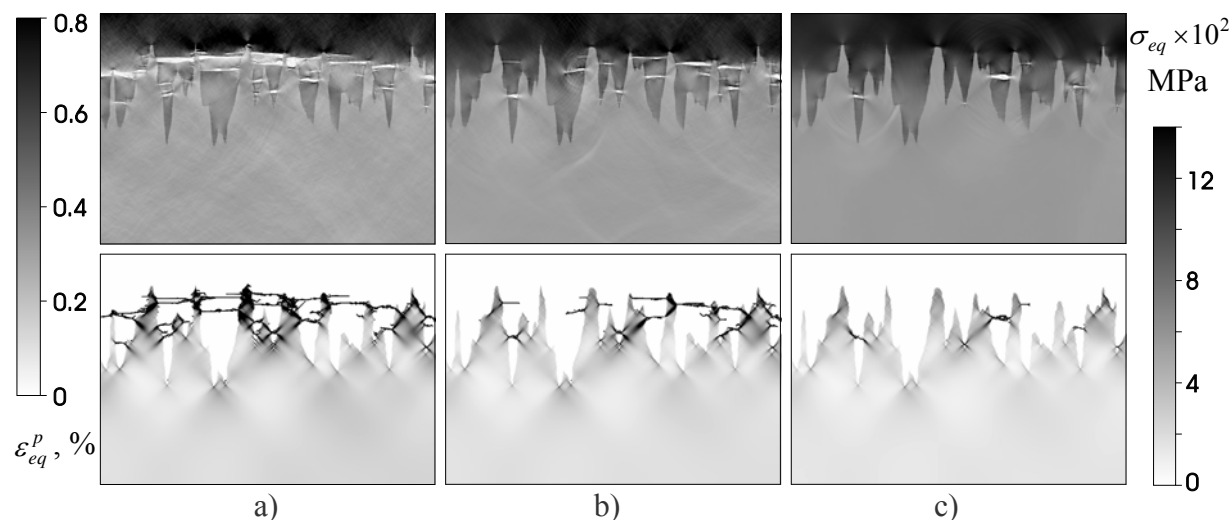


Figure 4. Distributions of equivalent stresses and equivalent plastic strains (fractured regions in the coating are marked by black color) for different strain rates of compression: (a) $3 \times 10^3 s^{-1}$, (b) $8 \times 10^3 s^{-1}$, (c) $24 \times 10^3 s^{-1}$. Total strain – 0.37 %.

The second conclusion is that the macroscopic strength under tension changes but only slightly with increasing strain rate, while both the total strain and homogenized stress of the fracture onset strongly depend on the value of the compression strain rate. The simulations testify that the higher the strain rate, the less intensive the cracking of the coating (Fig. 4) and, as a result, the higher the dynamic strength of the coated material. The explanation is the following. The value of stress concentration in C-type regions depends on the difference between mechanical properties of the steel and boron carbide ceramics. According to the model formulation the elastic stress of the boron material does not change but the current dynamic yield stress of the steel increases with increasing strain rate. Therefore, the stress difference at the “substrate-coating” interface and at a certain total strain decreases, and this decreasing arises only due a reduced plasticity of the steel substrate. In contrast to the external compression, the fracture of the coating under tension develops at the elastic stage of the steel substrate deformation. That is why the difference discussed does not change with increasing strain rate, and the macroscopic strength under tension changes but only slightly.

Acknowledgements

The work is supported by DFG (SCHM 746/84-1, SCHM 746/103-1) and by the President of Russian Federation through the grant MD-6370.2010.1.

References

- [1] Koval, A.V., Panin, S.V., Mesoscale deformation and cracking of surface-hardened low carbon steel. *Theoretical and Applied Fracture Mechanics*, 34 (2000) 117-121.
- [2] Balokhonov R.R., Romanova V.A., Schmauder S. Finite-element and finite-difference simulations of the mechanical behavior of austenitic steels at different strain rates and temperatures. *Mechanics of Materials*, 41 12 (2009) 1277-1287.
- [3] Tilbrook, M.T., Paton, D.J., Xie, Z., Hoffman, M., Microstructural effects on indentation failure mechanisms in TiN coatings: Finite element simulations. *Acta Materialia*, 55 (2007) 2489–2501.

Abnormal grain growth in electrical steels: a thorough simulation study

Luis A. Barrales-Mora¹, Manuel Krott² and Günter Gottstein³

^{1,2,3}Institut für Metallkunde und Metallphysik, RWTH-Aachen. Kopernikusst. 14, 52074 Aachen, Germany. E-Mail¹:barrales@imm.rwth-aachen.de.

The abnormal growth that the grains of the Goss orientation experience during the thermal treatment of electrical steels is still one of the unsolved problems in materials science. Several investigations have been carried out with the purpose of elucidating this problem. However, there has been so far only marginal success since the physical causes of the phenomenon remain unidentified. Several hypotheses for the problem have been proposed, they can be basically grouped into: a) energy advantage and b) mobility advantage. The first suggested mechanism works under the assumption that the Goss grain and/or their grain boundaries have a more favorable energetic state than the grains of the matrix. The second mechanism suggests that the grain boundaries of Goss-grains are highly mobile and thus can consume faster the matrix. In the present contribution, we make use of a 2D network model to study different conditions under which abnormal grain growth is achieved. The purpose of this investigation is not only to explore the conditions that lead to abnormal grain growth but also to study those which are detrimental to it. The response of the simulations to grain boundary-energy and mobility, heating rate, texture, etc., was studied. From the simulation results, the most important parameters for the processing of these alloys were identified. For example, it was found that a high heating rate is strongly detrimental for the formation of the Goss-texture. The results of the simulations are compared with experimental results and data available in the literature.

Numerical Determination of Effective Material Properties of Porous Media

Jürgen Becker¹, Andreas Wiegmann¹

¹Fraunhofer ITWM, Fraunhofer-Platz 1, 67663 Kaiserslautern, Germany
{becker,wiegmann}@itwm.fhg.de

ABSTRACT

The properties of porous media and composite materials depend strongly on the geometric distribution of the constituent materials. The GEODICT software permits to compute material properties based on three-dimensional computer-tomography (CT) images or virtually created structure models. In either case, the property is computed by solving a partial differential equation on the 3d mesh and postprocessing the solution. Thus, by varying the geometric parameters in the computer it is possible to design new porous media and composite materials with improved properties.

1. Introduction

Improving an existing material to achieve better performance or lower production costs is a challenge often encountered by material scientists. In case of porous materials, the “performance” of the material is usually related to certain effective properties of the medium, e.g. permeability, diffusivity or conductivity. Typical problems are e.g. to raise the conductivity of the material without lowering the permeability too much or to achieve the same conductivity with less material.

In order to achieve this goal, computer simulations can be useful. The basic idea behind them is to create a model of a new porous material first in the computer, predict its properties numerically and - by iterating this process - find a better material. The advantage of this process is that it allows to analyze porous materials before actually producing them.

However, to make this *virtual material design* possible, three steps are necessary:

In the first step, the ability of the numerical algorithms to predict the effective properties of the existing material has to be proved. To do so, a tomography image of the material is used. Then, using the segmented (and probably noise filtered) image as voxel mesh, the effective material properties like e.g. pore size distribution, diffusivity, permeability and conductivity are determined numerically. These results are then compared to measurements performed on the same material.

In the second step, the ability to produce realistic structure models virtually has to be shown. For this purpose a representative structure model is created virtually (often by a random process) using a small set of input parameters. For example, for fibrous structures these input parameters are fibre diameter and cross sectional shape, fibre length, directional distribution (anisotropy) and the porosity. It then has to be checked that the effective properties calculated for this model are the same as those calculated for the tomography image before.

Only if those first two steps are successful, we can in a third step study new materials. Starting point is the model created in step 2. Now, by changing the input parameters of the virtual model generator, the effect of for example different fibre diameters or porosities can be studied.

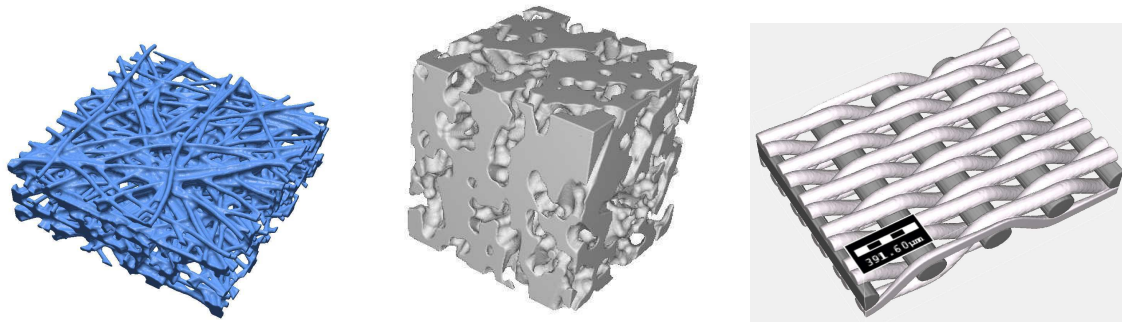


Figure 1: Examples of virtually created media, from left to right: fibrous gas diffusion layer, sintered ceramics filter, twill dutch weave metal wire mesh.

So a software tool enabling virtual material design necessarily has to have the abilities to a) import tomography images, b) create structure models virtually and c) determine the effective material properties numerically. These abilities are combined in GEODICT¹ and are explained in more detail in the following two chapters.

2. Virtually Created Structure Models

There are many different types of porous structures used in various fields of applications. Obviously, there are also many different approaches needed to create models of these structures. An often used porous medium is a fibrous nonwoven and the method used to create the structure model shows a very typical approach: the algorithm starts with an empty box into which fibres are then placed randomly until the desired porosity is reached. Random placement means that the actual fibre added is the result of a random process: the centre may be distributed uniformly in space, the direction distribution may follow a prescribed anisotropy², the fibre radius may be Gaussian distributed. In this way, the resulting 3D model is a random realisation of the underlying stochastic algorithm.

Similar approaches are used to model sintered materials. In this case spherical, rectangular or multiangular particles are used instead of fibres. A different approach is needed for woven structures³. Here, the structure is defined by the weave pattern and randomness may only enter if perturbances of the weave are to be modeled or in case of multi-filament fibres. Additional steps needed may be the addition of binder or adding different layers to form a composite material.

Independent on the method of creation, GEODICT uses a rectangular voxel mesh as discretisation. This allows to apply the same numerical algorithms on tomography images and on virtually created structures, which simplifies the comparison between imaged real and constructed virtual media.

3. Determination of Material Properties

Once the voxel mesh is created, the properties of the medium can be calculated numerically. For this it is important, that the structure model is representative of the porous medium. Only in this case, the properties are independent on the choice of cut-out imaged in the tomograph or the random realisation of the virtually created medium. This requires the structure model to be large enough to exhibit all characteristic features of the porous medium, which may demand

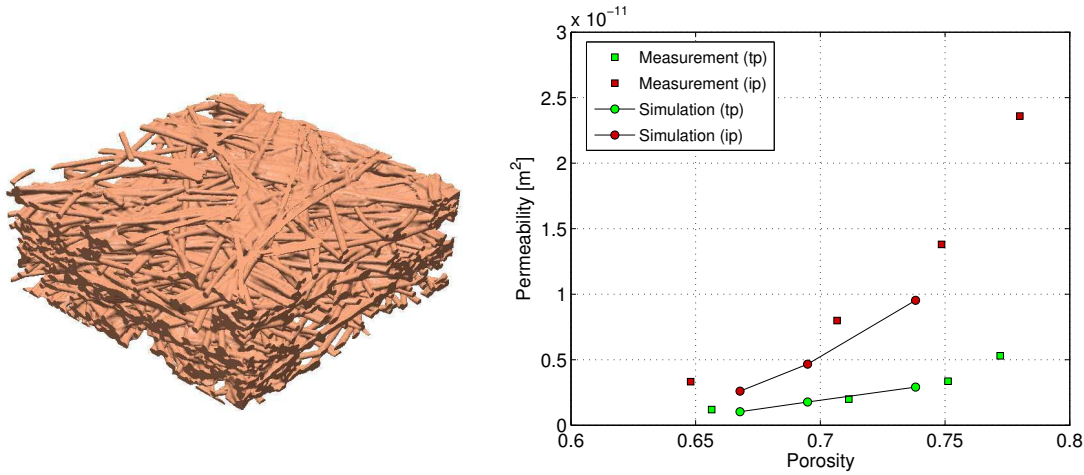


Figure 2: Left: tomography image of an uncompressed fuel cell gas diffusion layer. Right: calculated permeability compared to measurements performed on the same layer. Measurements were done under various levels of compression. The simulations were performed on three tomography images taken at different compression levels. The chart shows the anisotropy between in-plane (ip) and through-plane (tp) results and a good agreement between simulated and measured values. See Becker et al⁴ for more details

models to have 500^3 or even 1000^3 grid points.

Determinating the effective properties often requires to solve a partial differential equation. To determine the permeability, the flow of the fluid through the medium has to be simulated, i.e. Stokes' equation

$$-\mu\Delta u + \nabla p = 0, \quad \text{div } u = 0 \quad (1)$$

has to be solved in the pore space. The resulting velocity field u allows to determine the average velocity \bar{u} , which, together with Darcy's law

$$\bar{u} = -\frac{\kappa}{\mu} \nabla p \quad (2)$$

can be used to determine the permeability κ .

A similar approach can be used to determine the effective diffusivity. In this case the Laplace equation has to be solved in the pore space and Fick's first law is then used instead of Darcy's law to determine the diffusivity. Effective conductivity can be determined using the same ideas.

Solving (1) or other PDE's on the aforementioned huge voxel meshes is on the one hand demanding, but on the other hand the simplicity of the voxel mesh allows to reduce the amount of CPU time and memory extremely in comparison to more general finite element approaches. Therefore, GEODICT uses solvers developed specifically for large voxel meshes (e.g. the FFF-Stokes solver⁵ or the EJ-Heat solver⁶) and thus allows to find the solution in reasonable time.

4. Fields of Application

Porous materials appear as natural materials like soil, sand and rock, wood or cellulose fibres and membranes. They also include artificially created media like fibrous filters, sintered ceramics or woven meshes. Analysis of porous materials and virtual material design is therefore often needed.

GEODICT and the methods described in the previous chapters have successfully been applied to a variety of problems. Gas diffusion layers of PEM fuel cells have been analyzed^{4,7} and the results have been compared with measurements as shown in Fig 2. Furthermore, these tools were applied to predict the properties of metal wire meshes³, to simulate the thermal conductivity of wood fibre networks⁸ and of cast iron⁹.

References

- [1] A. Wiegmann. GEODICT virtual micro structure simulator and material property predictor. 2001–2010. <http://www.geodict.com>.
- [2] K. Schladitz, S. Peters, D. Reinel-Bitzer, A. Wiegmann, and J. Ohser. Design of acoustic trim based on geometric modeling and flow simulation for non-woven. *Comp. Mat. Science*, 38(1):56–66, 2006.
- [3] E. Glatt, S. Rief, A. Wiegmann, M. Knepfel, and E. Wegenke. Struktur und Druckverlust realer und virtueller Drahtgewebe. *Filtrieren und Separieren*, 23(2):61–65, 2009.
- [4] J. Becker, R. Flückiger, M. Reum, F.N. Büchi, F. Marone, and M. Stampanoni. Determination of material properties of gas diffusion layers - experiments and simulations using phase contrast tomographic microscopy. *J. Electrochem. Soc.*, 156:B1175–B1181, 2009.
- [5] A. Wiegmann. Computation of the permeability of porous materials from their microstructure by FFF-Stokes. Technical Report 129, Fraunhofer ITWM Kaiserslautern, 2007.
- [6] A. Wiegmann and A. Zemitis. EJ-HEAT: A fast explicit jump harmonic averaging solver for the effective heat conductivity of composite materials. Technical Report 94, Fraunhofer ITWM Kaiserslautern, 2006.
- [7] A. Pfrang, D. Veyret, F. Sieker, and G. Tsotridis. X-ray computed tomography of gas diffusion layers of pem fuel cells: Calculation of thermal conductivity. *International Journal of Hydrogen Energy*, 35(8):3751 – 3757, 2010.
- [8] H. Thoemen, T. Walther, and A. Wiegmann. 3d simulation of macroscopic heat and mass transfer properties from the microstructure of wood fibre networks. *Composites Science and Technology*, 68:608–616, 2007.
- [9] A. Velichko, A. Wiegmann, and F. Mücklich. Estimation of the effective conductivities of complex cast iron microstructures using FIB-tomographic analysis. *Acta Materialia*, 57: 5023–5035, 2009.

Strengthening and formation nano-composites in diamond-like amorphous carbon

A. YU. Belov¹

¹Institute of Crystallography RAS, Leninskii Prospect 59, Moscow, 119333 Russia
e-mail: belov@crys.ras.ru

Diamond-like amorphous Carbon (DLC) with high fraction of sp^3 -bonding, or tetrahedral amorphous carbon (ta-C), has immense potential for use in Micro-Electro-Mechanical-Systems (MEMS) because of its superior wear-resistant qualities and resistance to stiction. As DLC is biocompatible it also has the potential for use inside the human body for medical purposes. In this paper, the relaxation processes reducing the grown-in stress in tetrahedral amorphous carbon (ta-C) films during post-deposition annealing are studied at the atomic scale by molecular dynamics simulations with a modified Brenner's interatomic potential. The initial as-deposited state of ta-C is modeled using dense amorphous networks generated by ion-beam deposition simulation and possessing the grown-in stress of ~ 10 GPa [1-2]. During low-temperature annealing, energy and stress of the as-deposited ta-C are released with only minor changes in the short-range order. The corresponding rearrangements in the amorphous networks consist both in conversions from sp^3 to sp^2 and vice versa, however, without a reduction of the sp^3 content. The stress decreases gradually with annealing temperature. A nearly complete stress relief in ta-C with density of 3.2 g/cm³ was simulated at ~ 1000 K, which is in agreement with experimental data. It is also found that at higher annealing temperatures even tensile stresses can occur, while the sp^3 content exceeds 80%. The structural changes in ta-C indicate that as a result of the annealing the sp^3 bonded atoms have lower volumes than upon pure elastic expansion of ta-C to the stress-free state, with the volume difference accounting for the high grown-in intrinsic stress in ta-C films.

The annealing simulations show that at a lower density (2.9 g/cm³) of ta-C the structural relaxation can give rise to the formation of nano-composite structures (Figure 1), consisting of sp^2 -bonded clusters embedded into the highly tetrahedral matrix. The influence of the thermal annealing on the mechanical properties of ta-C was also investigated. It was found that the carbon nano-composite possesses a higher elastic modulus than the as-grown homogeneous ta-C.

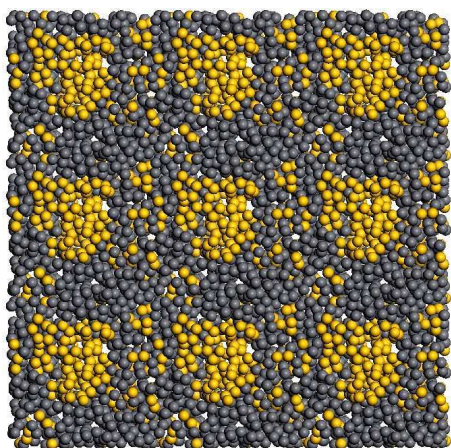


Figure 1. Simulated nano-composite of density 2.9 g/cm³, consisting of sp^2 -bonded clusters embedded into the highly tetrahedral matrix.

References

1. H.U. Jäger, A.Yu. Belov, Phys. Rev. B **68** (2003) AN 024201.
2. R. Gago et al., Phys. Rev. B **72**, (2005), AN 014120.

Level Set framework for the numerical modelling of microstructural evolutions in metals

M. Bernacki, R.E. Logé, P.O. Bouchard, T. Coupez

Mines ParisTech, CEMEF - Centre de Mise en Forme des Matériaux, CNRS UMR 7635, BP 207, 1 rue Claude Daunesse, 06904 Sophia Antipolis Cedex, France
Marc.Bernacki@mines-paristech.fr

Efforts aiming at improving the accuracy of the numerical predictions are now focusing on the modelling of microstructural phenomena that occur during the thermo-mechanical processing of metals and on the multi-scale coupling. The variety and complexity of these microstructural events render this modelling extremely challenging. Of course, the examples of such microstructural modelling could be multiply, but the essential steps of these microstructure scale approaches, in a FE context, are recurrent: the generation of a Representative Volume Element (RVE) of the considered microstructure, the generation of a finite element mesh adapted to this microstructure, the effect of the microstructure heterogeneities but also the topological evolution of this microstructure during the process and the improvement of macroscopic models resulting of this microscopic modelling.

The basic ingredients of the general micro model for metals developed at CEMEF are described in [1-5]. In this work, a new level set framework is proposed. It is shown that the proposed formulation, associated to adaptive anisotropic automatic remeshing, is an efficient and accurate tool to aboard the different steps described previously for several microstructural phenomena such as the recrystallization for polycrystal (see Fig. 1), the zener pinning for polycrystal with inclusions (see Fig. 2) or the modelling of ductile damage coming from the stages of nucleation, growth and coalescence of micro-voids.

- [1] Bernacki M., Chastel Y., Coupez T. and Logé R.E., 2008, *Level set method for the numerical modelling of primary recrystallization in the polycrystalline materials*, Scripta Mater. 58, 12, pp. 1129-1132.
- [2] Logé R.E., Bernacki M., Resk H., Delannay L., Digonnet H., Chastel Y., Coupez T., 2008, *Linking plastic deformation to recrystallization in metals, using digital microstructures*, Philosophical Magazine B, Vol. 88, Nos. 30–32, pp. 3691–3712.
- [3] Bernacki M., Resk H., Coupez T., Logé R.E., 2009, *Finite element model of primary recrystallization in polycrystalline aggregates using a level set framework*, Modelling Simul. Mater. Sci. Eng., 17, 064006.
- [4] Resk H., Delannay L., Bernacki M., Coupez T., Logé R.E., 2009, *Adaptive mesh refinement and automatic remeshing in crystal plasticity finite element simulations*. Modelling Simul. Mater. Sci. Eng. 17, 075012.
- [5] Bouchard P.O., Bernacki M., Khaoulani R.E., Milesi M., 2009, *On the role of particles distribution on damage and fatigue mechanisms*. Int. J. Mater. Form., Vol. 2, Supp. 1, pp. 935-938.

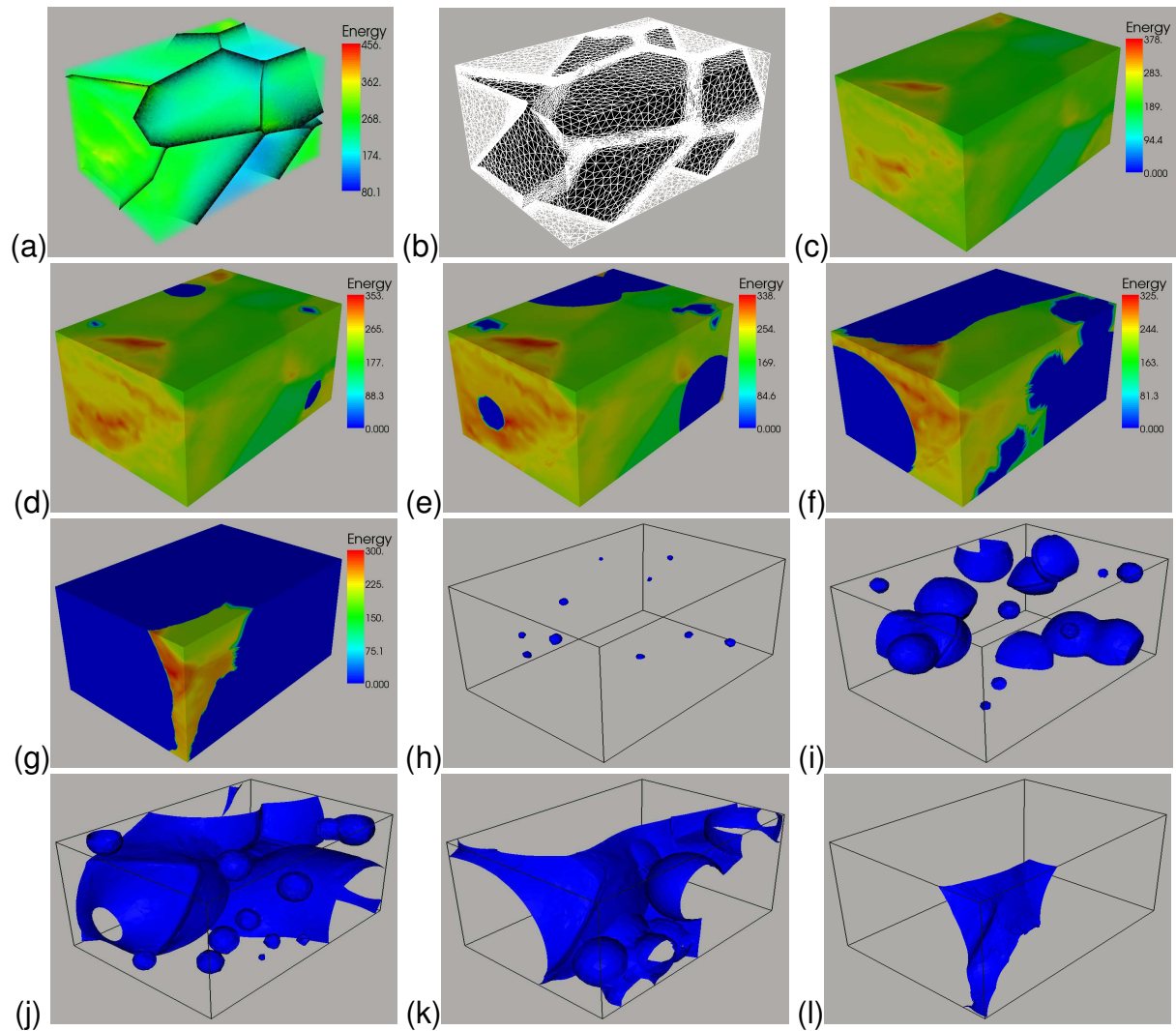


Figure 1: A 3D ten grains microstructure after plastic deformation: (a) external surface view of stored energy; (b) anisotropic meshing in white, grain boundaries in black; external surface view of the stored energy for recrystallized volume fractions of (c) 1%, (d) 15%, (e) 58%, (f) 80%, (g) 95% and corresponding recrystallized front (h-l).

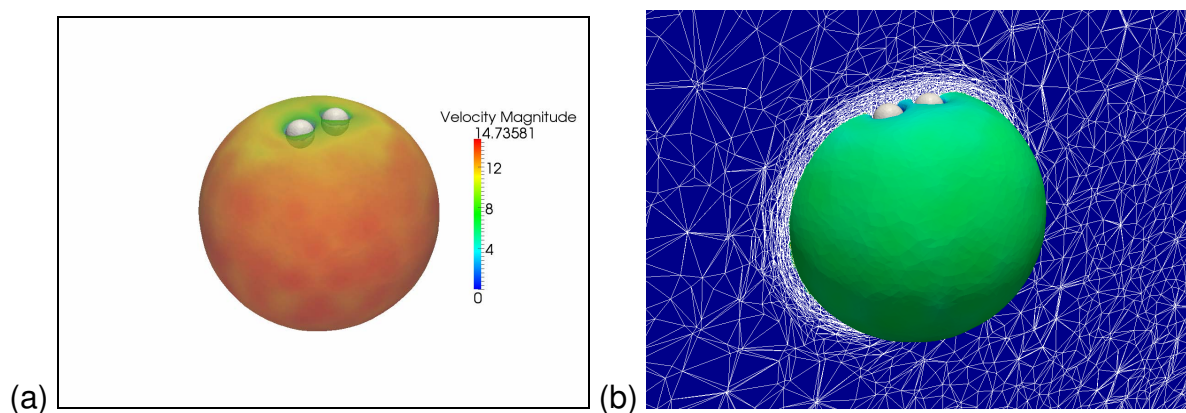


Figure 2: Breaking effect, due to the presence of two spherical inclusions, on the growth of one spherical grain: (a) velocity magnitude on the grain surface (b) mesh on a cutting plane.

Evaluation of Texture Models for Deformation and Recrystallization Applied to AA6016

Christian Bollmann, Günter Gottstein

**Institute of Physical Metallurgy and Metal Physics, RWTH Aachen University,
52056 Aachen, Germany**

ABSTRACT

The aim of this investigation was to evaluate the predictive power of texture models for deformation and recrystallization applied to the heat treatable 6016 aluminum alloy. The texture evolution during deformation was simulated with the GIA model, and the ReNuc / StaRT model was used to simulate the process of recrystallization. The models were evaluated by comparing experimental and simulated textures for a specific initial material condition and various processing conditions. The present study revealed that the texture evolution during deformation and recrystallization for this alloy can be well predicted for the chosen initial material condition.

1. Introduction

The heat-treatable Al-Mg-Si alloys are widely used for automotive applications, since 6xxx series alloys combine excellent formability, good surface appearance and high in-service strength. In order to optimize the formability, the crystallographic texture of the sheet plays an important role as it controls the plastic anisotropy. In particular, it is of importance to understand the formation of recrystallization textures in these alloys [1].

Since all processing steps may have an influence on the final recrystallization texture of the sheet, a Through Process Modeling (TPM) concept for modeling the texture evolution is needed to analyze distinctively different processing routes with respect to the main texture controlling processes, namely deformation and recrystallization. However, the models for deformation and recrystallization need to be evaluated for an exemplary processing route before the TPM concept can be applied to model complex processing chains for 6xxx series alloys. Such a virtual route may consist of only two consecutive processing steps: cold rolling and subsequent annealing. Thus, the development of recrystallization textures depending on the applied strain during deformation is of particular interest within this study and its accurate prediction would make a large step towards the application of the TPM concept for 6xxx series alloys in the future. Since the goal of this investigation is to evaluate the predictive power of the texture models for deformation and recrystallization, simulated textures are compared with experimental textures obtained for different amounts of cold rolling and subsequent annealing treatments.

The texture evolution during cold rolling was simulated with the advanced texture model GIA [2]. In order to simulate the texture evolution during recrystallization, the underlying physical processes nucleation and growth of nuclei need to be considered. Thus, two different models named ReNuc and StaRT were applied to simulate the subsiding processes during recrystallization [2, 3].

2. Modeling of Rolling Textures

The texture evolution during deformation was simulated with an advanced Taylor-type model by taking the interaction between next-neighbour grains into account. The Grain InterAction (GIA) model describes the deformation behaviour of an eight-grain aggregate embedded in a homogeneous surrounding. The deformation of the whole aggregate is fully prescribed to avoid deformation incompatibilities with respect to the surrounding matrix. However, the individual grains may develop shears and thus, each grain is allowed to deform differently. Strain compatibility is regained through the application of opposite shears. The remaining misfit is accommodated by the introduction of geometrically necessary dislocations (GND) which is associated with an additional energy term. The amount of relaxation, the active slip systems and the amount of slip on them is determined by minimization of the total plastic work due to slip of eight grains plus the energy introduced by the GNDs [2].

3. Modeling of Recrystallization Textures

The phenomenon of primary static recrystallization is based on two subsiding physical processes, the formation of nuclei and their growth into the deformed microstructure [4]. Thus, both processes are represented in a respective model to simulate the texture evolution during recrystallization on a physical basis. While the orientation distribution of nuclei is simulated with the Recrystallization Nucleation (ReNuc) model [2], the growth of nuclei is computed with the Statistical Recrystallization Texture (StaRT) model [3].

StaRT is a growth model which is discrete in time, but statistical in space. Hence, it has in principle the capability to produce real time kinetics for recrystallization and true recrystallized grain sizes. However, this investigation is concerned only with the texture evolution during recrystallization. In general, nucleation is assumed to be site saturated. After the nuclei orientations are determined with ReNuc, they are distributed in the deformation texture according to specific criteria. Then, the nuclei are allowed to grow into the deformed microstructure. Several growth modes are left free to change during growth in order to simulate a micro- and macro-growth selection. Finally, the impingement of growing grains will cease the growth of grains which is taken into account according to Avrami [5].

Nucleation is known to start at deformation inhomogeneities in the deformed microstructure. Since the GIA model reflects deformation inhomogeneities to a certain extent, it is a helpful tool to derive the orientation spectrum of potential nuclei from the deformation texture. ReNuc is the model that assembles the orientation distribution of nuclei from the priory simulated deformation texture. It evaluates physical quantities, i.e. the number of active glide systems per grain, to derive the orientation spectrum of potential nuclei. Therefore, ReNuc is linked with the deformation model GIA to answer the essential question which nucleation mechanism becomes active in each deformed grain. In the present model, three nucleation mechanisms are considered, namely nucleation at shear bands, transition band (TB) nucleation and grain boundary (GB) nucleation. It is to mention that the orientation spectrum of each nucleation mechanism is governed by at least one critical parameter. The critical parameters for the complete nuclei spectrum are usually obtained by fitting the simulated recrystallization texture to the experimental textures at one strain only. After the parameter set is determined, it is used to simulate recrystallization textures at all other strains. In this way, the existing models offer the possibility to model recrystallization textures (and nucleation textures) depending on the deformation history.

4. Simulation Results

In this study, the initial material was a modified hot band of AA6016 in fully recrystallized condition. The recrystallized grain size was about 50 μm . For comparison with experimental textures, the initial material was cold rolled on a laboratory rolling mill to a strain ϵ of 0.7, 1.5 and 2.0. Thereafter, the samples were annealed to fully recrystallize the material according to a specific temperature-time-curve in an air circulating furnace.

The texture evolution was simulated in strain steps of 0.025 up to the desired strain. The strict prescription of the plane strain state during rolling in the sheet center was slightly modified by allowing the individual components of the strain state to fluctuate randomly around the nominal plane strain state [6]. The dependency of the texture simulation on flow stress and work hardening was accounted for by using a generalized Voce law [7]. The corresponding Voce parameters were determined by compression tests.

Fig. 1 summarizes the predictions of the modified GIA model for cold rolling applied to AA6016 represented in the form of rolling texture β -fibers and volume fractions for the typical rolling texture components, i.e. Cu-, S/R- and B-orientation. In general, the model predicts very realistic volume fractions for the typical rolling texture components (Fig. 1b). In contrast to experimental textures, orientations close to B are more pronounced in the simulated rolling textures (Fig. 1a). However, the evolution of volume fractions for the typical rolling texture components upon strain follows the right trend. The predicted reduction of the cube orientation during deformation upon strain is slightly underestimated compared with experimental textures.

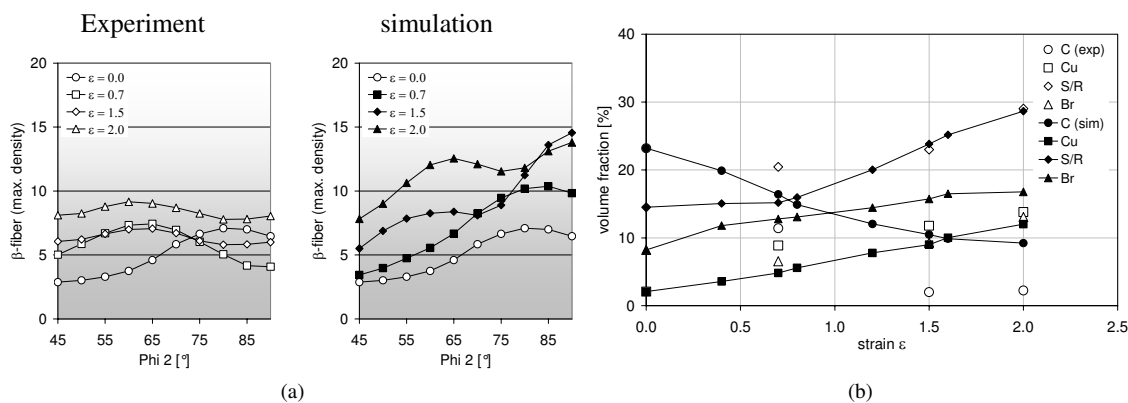


Figure 1. Simulation of rolling texture evolution as a function of strain ϵ : (a) maximum texture intensity along the β -fiber; (b) volume fractions of specific texture components depending on applied strain

Fig. 2 summarizes the predicted evolution of recrystallization textures as a function of strain. The calculated volume fractions for different texture components were classified into three typical texture component groups, namely cube components, β -fiber components and all other components (including random orientations). Obviously, the evolution of volume fractions for the three typical texture component groups upon strain is represented fairly well by the ReNuc / StaRT model (Fig. 2b). The important recrystallization texture components are predicted even with realistic intensity values (Fig. 2a). It is emphasized that the same set of ReNuc model parameters to determine the nuclei spectrum was used at all deformation degrees in this study. The StaRT model parameters were tuned to impose a strong growth selection on the nuclei spectrum, but they were, of course, not varied for different strains.

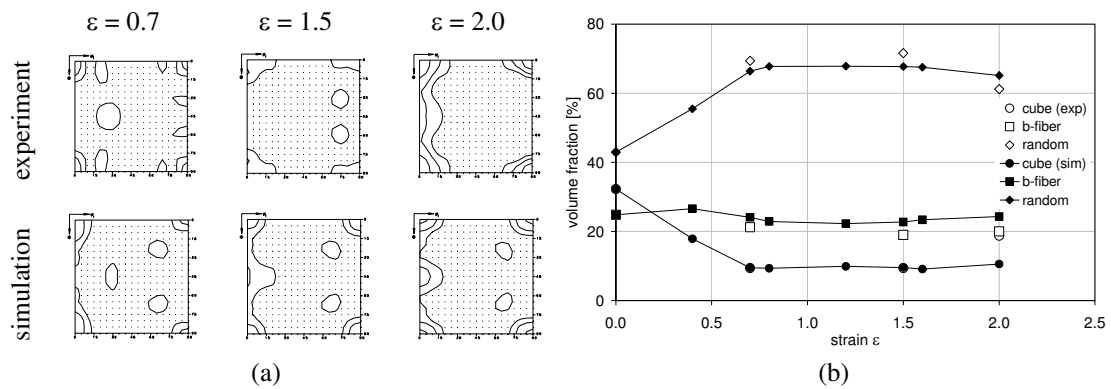


Figure 2. Simulation of recrystallization texture evolution as a function of strain ε :
 (a) $\varphi_2 = 0^\circ$ sections; (b) volume fractions of three typical texture component groups

5. Conclusion

The deformation model GIA and the recrystallization model ReNuc / StaRT were used to simulate the texture evolution during deformation and recrystallization for different processing conditions, i.e. different degrees of deformation. The present study revealed that the texture evolution of AA6016 during processing can be well predicted for the chosen initial material condition. The dependency of the recrystallization textures on strain was calculated very accurately. However, other specific initial material states, i.e. unrecrystallized hot band, need to be tested before the TPM concept can be applied to AA6016 since the initial material state has a significant impact on the prediction of cube orientations within the ReNuc / StaRT model.

Acknowledgements

The financial support of the M2i is gratefully acknowledged. This research was carried out under project number MC4.05210 in the framework of the Strategic Research Programme of M2i in the Netherlands (www.m2i.nl).

References

- [1] O. Engler, J. Hirsch: Mater. Sci. and Eng. A336, (2002) 249.
- [2] M. Crumbach, Thesis, RWTH Aachen (2005).
- [3] R. Sebal, G. Gottstein, Acta Mater. 50, (2002) 1587.
- [4] O. Engler, Mater. Sci. Technol. 12, (1996) 859.
- [5] M. J. Avrami, Chem. Phys. 7, (1939) 1103.
- [6] O. Engler, M. Crumbach, S. Li, Acta Mater. 53, (2005) 2241.
- [7] C. Tomè et. al., Acta Metall. 32, (1984) 1637.

The interaction of screw and edge dislocations with Cr precipitates in FeCr alloy: An atomistic study

G. Bonny¹ and D. Terentyev¹

¹Nuclear Materials Science Institute, SCK•CEN, Boeretang 200, B-2400 Mol, Belgium
gbonny@sckcen.be

Iron-chromium alloys are the base for ferritic and ferritic/martensitic steels, which have a wide range of applications as structural materials in aggressive high temperature environments, such as gas turbines in conventional power plants, or key components in future nuclear reactors. The appearance of Cr-rich precipitates (α' prime) after thermal ageing or irradiation is a typical feature of high-Cr ferritic/martensitic steels. α' particles, obstructing the motion of dislocations, are long known to be the cause of hardening and embrittlement, observed in steels and Fe-Cr binary alloys.

In this work, we consider the interaction of a screw dislocation and edge dislocation with Cr precipitates in a bcc Fe matrix using molecular dynamics techniques. We apply two different interatomic potentials: (i) one that has been widely used in the past five years in the literature to study primary damage and point defect properties and (ii) another one specifically accounting for the properties of the screw dislocation in the Fe-Cr system as obtained from the first principles calculations. The interaction mechanisms revealed using both potentials are described in detail and compared. The results obtained for the screw dislocation suggest that two principally different interaction mechanisms may operate depending on the interatomic model applied, while the results for the edge dislocation are very similar.

To conclude, the impact of the α - α' separation on the change of the yield stress due to the pinning of dislocations by the Cr precipitates is discussed.

STRESS INTENSITY FACTORS FOR CRACKS IN PORE CHANNELS STRUCTURES

Valery G. Borovik¹, **Aleksandra V. Borovik**²

¹ Frantsevich Institute for Problems of Materials Science,
Krzhizhanovsky str., 3, 03680, Ukraine, Kyiv-142,
e-mail: v_borovik@inbox.ru

² NTUU "Kyiv Polytechnic Institute",
Institute of Mechanical Engineering,
Prospect Peremogy, 37, b.1, Kyiv-56, Ukraine, 03056
e-mail: sandrochkaua@ya.ru

Microstructures first of all govern the strength properties of materials. Unidirectional fibers and channels structure provides high strength characteristics in a direction of fibers. Such materials are perspective for various areas of the industry and health.

At deriving of such materials by hot pressing of a bundle of parallel fibers to various values of the relative density are gained the pore channels which cross-sections with various shapes depending on the chosen technological regimes. At high homology temperature and minimum exterior pressure in the process of sintering of fibers the cross-sections of channels are roundish, in an extreme case, the circular shape are obtained. Pressing of a bundle of fibers at low homology temperatures leads to densification of the fibers cross-sections by plastic flow and formation the pore channels with cross-sections, similar to hypocycloids. At the minimum cohesion at the boundaries of fibers the process of pressing provides the pore channels with cross-sections of three- four-beam starlike flaws.

Change of stress intensity factors (SIF) along front of main crack which crosses pore channels with cracks is in-process observed. The forms of cross-sections pore channels were circles, an equilateral triangle, a triangle with the concave parties and starlike three-beam cracks. Peaked cross-sections of pore channels contained cracks for which the modification local SIF also is observed, at intersection of these channels by a main crack.

Problems of a linear fracture mechanics were solved by finite element method.

It is shown that pore channels with peaked cross-sections provides to smaller magnification local SIF at the front a main crack, than pore channels with circular cross-sections. Besides, the front of main crack which is close to pore channels with peaked cross-sections, leads to local magnification SIF on fronts of the cracks passing through apexes of these cross-sections. This magnification SIF mode I leads to the debonding between fibers and to a bending of a plane of main crack growth near to boundaries of fibers. There is a destruction of the crack front of main crack on fragments that promote to bending of its front in a growth plane.

The gained estimations of magnification local SIF on fronts of cracks pore channels at intersection by their main crack can be used for optimisation of crack resistance of boundaries between fibers. The observed mechanism of raise of resistance to fracture of materials with unidirectional fiber and channel structure brings the contribution to quasiviscous behaviour at failure. It shows one of ways of overcoming of friability of materials and is perspective for structural "viscous" ceramics, fatigue high-resistance metals etc.

Comparison of two Recrystallization Models within a TPM-Framework for Sheet Production

T. Brüggemann^{1,*}, Jhonson¹, V. Mohles¹, G. Gottstein¹, S. Heppner², G. Hirt², K.-F. Karhausen³

¹Institute of Physical Metallurgy and Metal Physics, RWTH-Aachen University, Germany

²Institute of Metal Forming, RWTH-Aachen University, Germany

³Hydro Aluminium Deutschland GmbH

*Brueggemann@imm.rwth-aachen.de, Institut für Metallkunde und Metallphysik, RWTH Aachen, D-52056 Aachen, GERMANY

The modeling of recrystallization textures is a crucial part of through-process simulation of aluminum sheet products. Various process and material parameters govern the kinetics of recrystallization (RX) in between rolling passes during exposure to elevated temperatures. Within a through-process modeling (TPM) scheme, proposed by the institutes IMM and IBF of RWTH Aachen University and Hydro Aluminium Deutschland, two different recrystallization texture models were compared: The *StaRT* model and the *CORe* model, both developed at IMM. The models differ in their approach to RX-texture modeling: *StaRT* uses a statistical method, whereas *CORe* is a cellular automaton. One outstanding *CORe*-feature is a detailed consideration of microchemistry evolution, mirrored in all effects controlling recrystallization kinetics, such as impurity drag, Zener drag, and recovery kinetics. So far, only the *StaRT* model had been used for TPM. Due to high calculation efforts and limited experimental foundation required for the validation of *CORe*, the latter model had not been implemented in TPM, yet. However, the possibility to include microchemistry and further improvements in RX modeling makes *CORe* attractive, especially for TPM. After extensive acceleration of *CORe* and experimental validation, *CORe* can now be utilized for TPM. In the present paper, results of the new TPM scheme with refined kinetics are compared to the previous approach for AA5182.

Coupled Crystal Plasticity-Phase Field Formulation to Describe the Microstructural Evolution in Polycrystalline Aggregates During Thermal Recrystallisation

E.P. Busso, G. Abrivard and S. Forest

Centre des Matériaux, Mines ParisTech, UMR CNRS 7633
B.P. 87, 91003 Evry Cedex, FRANCE

During thermo-mechanical processing, the strain energy stored in the microstructure of an FCC polycrystalline aggregate is generally reduced by physical mechanisms which rely, at least partially, on mechanisms such as dislocation cell or grain boundary motion which occur during recovery, recrystallisation or grain growth. The aim of this work is to develop a constitutive framework capable of describing the microstructural evolution driven by grain boundary curvature and/or stored energy during recrystallisation and grain growth. As recrystallisation processes depend primarily on the nature of the microstructural state, an accurate prediction of such phenomena requires that the microstructural heterogeneities which develop just before recrystallisation, such as dislocation cells and pile-ups, shear and twin bands, be properly described. The microstructural characteristics present in a polycrystal aggregate at the onset of thermal recrystallisation are first reproduced numerically. The constitutive behaviour of each grain in the aggregate is described using a non-local dislocation mechanics-based crystallographic formulation. Different measures of stored internal strain energy are determined based on the dislocation density distribution in the aggregate.

The minimisation of stored and grain boundary energies provides the driving force for grain boundary motion. To describe the interface motion, a phase field model taking into account the stored energy distribution is formulated and implemented within the continuum framework. A weak coupling between the grain boundary kinematics and the crystal plasticity model is made through the dislocation densities and the grain orientations. Furthermore, the parameters of the free energy are calibrated based on published Read-Shockley boundary energy data. To validate the proposed model, a polycrystalline aluminium aggregate is first cold deformed under plan strain conditions and then annealed. The predicted recrystallised material volume fraction evolution was found to have the same dependence on deformation levels and temperature as those reported in the literature.

Dislocation Junction formation and strength in hcp metals

L.Capolungo

Georgia Institute of Technology, GT-CNRS UMI2958
2 Rue Marconi, Metz, France
Laurent.capolungo@me.gatech.edu

Hexagonal closed packed (hcp) metals deform plastically via the simultaneous activation of several different deformation modes (i.e. twinning, slip). The relative contribution of each mode is directly related to the crystal's intrinsic properties -such as the c/a ratio, the stacking fault energy on all slip and twin systems, etc- and to the loading conditions. As in the case of cubic crystals, interactions between slip systems, which translate into latent hardening or softening at the macroscopic scale, are of particular interest. Indeed, these slip system interactions control microstructure development- and in particular the magnitude and strength of strain gradients.

Discrete dislocation dynamics simulations have been used with great success in cubic structures to predict junction formation and latent hardening parameters. A contrario HCP metals have been subject to much limited studies. The main limitations arise from (1) the elastic anisotropy of the crystal structure and, (2) from the multitude of junctions which can be formed. These critical issues are studied here.

An adaptative meshing finite element based discrete dislocation dynamics simulations code is developed to investigate the role of elastic anisotropy junction formation and hardening in different hcp metals with different degrees of anisotropy. The newly developed approach explicitly accounts for the transversely isotropic structure of hcp crystals. First, the study focuses on Mg, Zr, and Hf. The role of anisotropy is appreciated by comparing prismatic dislocation junction maps and stress strain response when solely pyramidal slip is active. Second, the model is used to predict all possible junction formation, and associated strength ("yield surface") in Mg. In particular, all interactions between basal, prismatic and pyramidal dislocations are considered.

Multiscale modelling of magnetisation structures and dynamics

Roy Chantrell¹, Oksana Chubykalo-Fesenko and Uli Nowak³

¹Physics Department, The University of York, YO10 5DD, UK; rc502@york.ac.uk

²ICMM Madrid, Spain

³Physics Department, University of Konstanz, Germany

Magnetic materials are currently routinely engineered on the nanoscale in increasingly complex structures in order to provide improved functionality. This poses a serious challenge to the physical modelling of the materials and in developing the required new approaches to device design. The current experimental studies of ultrafast laser driven dynamics provide an additional challenge since these can involve heating the material through the Curie temperature in sub-picosecond timescales. In order to meet these challenges, increasingly sophisticated theoretical approaches are required. Ideally this starts with calculations at the electronic level in order to determine the important physical parameters (spin, anisotropy and exchange) from first principles. In order to extend these calculations to non-zero temperatures and larger numbers of atoms, atomistic spin models are required. We will start by outlining the techniques involved in developing physically realistic spin Hamiltonians from ab-initio calculations and then describe the physical basis of the dynamic atomistic model used to study ultrafast phase transitions. The atomistic model will be applied to an understanding of the underlying physics of ultrafast laser driven processes and also of Heat Assisted Magnetic Recording. We will also use the model to develop an explanation of the optomagnetic reversal mechanism in which the magnetisation is reversed using circularly polarized laser pulses. Finally we will describe the Landau-Lifshitz-Bloch equation, which has the important property that it does not conserve the norm of the magnetisation, which makes it an ideal candidate for use in mesoscopic (micromagnetic) models for use at ultrafast speeds and elevated temperatures. The construction of such a model will be described and some recent calculations reviewed.

Formation and evolution of dislocation wall structures: Grain boundaries, cell walls, and self-similarity

Yong S. Chen¹, Woosong Choi¹, Stefanos Papanikolaou¹
and James P. Sethna^{1†}

¹LASSP, Cornell University, Ithaca, NY 14853, USA

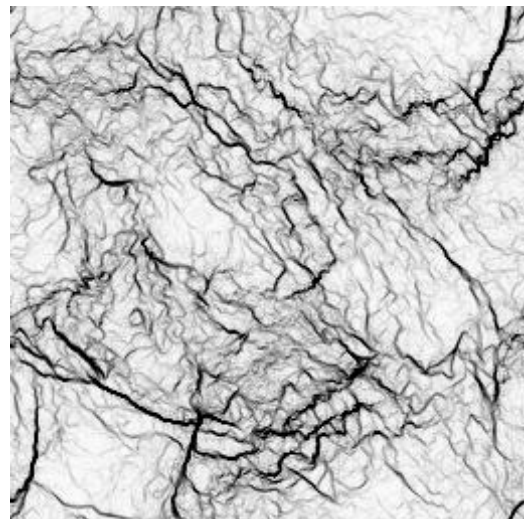
†Corresponding author: sethna@lassp.cornell.edu



Dislocation grain boundaries formed with climb

We explore the formation and evolution of wall structures in deformed crystals. We model the dynamics of the Nye dislocation density tensor starting from a smooth random initial deformation, by choosing a local velocity to be in the direction of net Peach-Koehler force on the dislocations. If dislocations are allowed to climb, polycrystalline structures form with sharp grain boundary-like walls. If dislocation climb is forbidden, cellular structures emerge with self-similar fractal morphology – closely resembling the cell wall patterns observed in experiments. We suggest that the fundamental distinction between cell walls and grain boundaries is that the former

are intrinsically branched in a characteristic fractal fashion. Our model exhibits realistic cell refinement under strain, with cell sizes decreasing and misorientations increasing as external strain is applied. We analyze our results in view of previous experimental studies of cell morphologies, both those which observed fractal structures and those that used scaling collapses suggesting a single scale for sizes and misorientations. Our simulations simultaneously show fractal structures and scaling collapses. We suggest that self-similar cellular structures are best studied using correlation functions, rather than artificially dividing them into distinct cells.



Dislocation cell structures formed without climb

See <http://arxiv.org/abs/1001.5053>

Morphologies during Nucleation in Al-Si binary alloys and Growth in Ternary Eutectic Systems

Abhik .N. Choudhury¹, Britta Nestler¹ Frank Wendler¹ and Mathis Plapp²

¹Institute of Materials and Processes, Moltkestrasse-30, 76131, Karlsruhe, Germany

²Laboratoire de Physique de la Matière Condensée, Ecole Polytechnique, 91128 Palaiseau, France

Solidification as a process is interesting both from an engineering perspective, because the morphologies at the microscale affect the functionality at the macroscale, and from the point of view of pattern formation, because of the enormous variety of structures that can form in 2D and 3D. In the present talk, we describe the treatment of the process of homogeneous and heterogeneous nucleation using the phase-field method and present a novel scheme to solve the Euler-Lagrange equations for the critical nucleus. Specifically, we choose the Al-Si system in this study, and treat the homogeneous nucleation of the Si-phase in the melt and heterogeneous nucleation at the eutectic growth front. We predict the shape of the nucleating Si-phase based on energetic arguments, by comparing the barrier to nucleation for different shapes. The barrier to nucleation is calculated as the grand chemical potential difference between the critical solid nucleus in equilibrium with the liquid, and the initial liquid, where the critical profiles are the solutions to the relevant Euler-Lagrange equations. We also treat growth morphologies of ternary eutectic structures in 2D and 3D and present comparison with theoretical predictions for the different growth arrangements in 2D. Finally, we show preliminary simulations of 3D growth forms during directional solidification at different eutectic and off-eutectic compositions.

Investigation and modeling of the material behavior due to evolving dislocation microstructures in fcc and bcc metals

T. Clausmeyer, B. Klusemann, S. Bargmann, B. Svendsen

Institute of Mechanics, Dortmund University of Technology, Germany,
till.clausmeyer@udo.edu

ABSTRACT

Many fcc and bcc metals subject to non-monotonic loading are known to exhibit different kinds of anisotropic hardening. This is due to evolution of, and interaction in, the dislocation microstructure depending on loading type. One purpose of the current work is the investigation of such evolution and interaction in single crystals as well as its effect on their hardening behavior. This is the basis for the development of a single-crystal model which accounts for the effects of a change in loading path on the critical shear stress for glide at the glide-system level. In work in progress, this single crystal model is being embedded in a Taylor-based texture model in order to examine the effects of such single crystal behavior on the behavior of the aggregate.

1. Microstructure development & stress-deformation behavior

The model development being pursued in this work is based on insight gained from experimental investigations involving material testing and microstructural characterization. Consider for example the results in Figure 1 for the interstitial-free steel DC06 (bcc). In this figure,

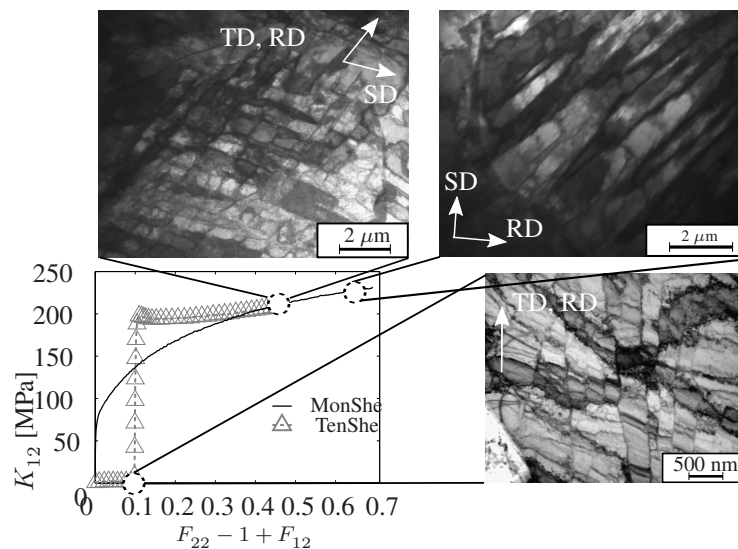


Figure 1: Comparison of dislocation microstructure and loading path in DC06. See text for details.

stress-deformation results are compared with TEM results (courtesy of the Institute of Material Science, University of Hannover) for the deformation microstructure. The former (Figure 1, lower left) are based on material test results for monotonic simple shear loading as well as orthogonal loading from plane-strain tension to shear [e.g., 1].

They are expressed in terms of the Cartesian shear component K_{12} of the Kirchhoff stress \mathbf{K} as a function of extension plus shear $F_{22} - 1 + F_{12}$ in terms of the corresponding Cartesian

components of the deformation gradient \mathbf{F} for monotonic simple shear loading (MonShe) and for orthogonal loading (plane-strain tension to shear: TenShe).

Consider first the case of monotonic simple shear. As shown by the TEM results at approximately 65% deformation (Figure 1, upper right), a typical cell-block / cell-block-boundary (CBB) dislocation microstructure develops in DC06 with dominant CBB orientation at about 45° to the rolling and shear directions. This is in agreement with previous work [2, 3]. In contrast, after about 10% monotonic tension in the rolling direction (Figure 1, lower right), dense dislocation walls approximately parallel to tension direction (TD) are observed. After orthogonal change from this path to simple shear and 35 % shear deformation, a checkerboard-like cell-wall dislocation microstructure (Figure 1, upper left) of almost square cell blocks bounded by walls oriented in the tension (TD) shear (SD) directions is created. This is also in agreement with previous work [2, 3].

As shown by the corresponding tension-shear stress-deformation curve, and as expected, cross hardening occurs in the transition from tension to shear. In particular, this is indicated by the increase in the yield stress above the monotonic shear level at 10 % extension. Such hardening behavior has been successfully accounted for in yield-surface and yield-stress models as based on the concept of evolving fourth-order structure tensors [1]. Physically, such hardening is thought to be due to the interaction of existing dislocation structures with new glide systems activated during an orthogonal loading-path change. These latter are in a sense latent during the tension phase [e.g., 2]. The observed softening after the stress overshoot can be understood as weakening of the planar persistent dislocations structures formed during pre-deformation [2].

2. Model formulation

As mentioned above, the modeling approach here is based in particular on the formulation of a single-crystal model for anisotropic, and in particular cross, hardening. The focus of this short work is the formulation and discussion of an initial simple single-crystal model for cross hardening as based on that of [4]. In work in progress, this and related models are being incorporated into Taylor-based texture modeling of the polycrystalline case.

The single-crystal model is formulated here in the context of continuum thermodynamics. As usual, it is based on the multiplicative decomposition $\mathbf{F} = \mathbf{F}_E \mathbf{F}_P$ of the deformation gradient \mathbf{F} as well as the assumption of small elastic strain. Assuming dislocation glide as the sole source of inelastic deformation, the usual form $\dot{\mathbf{F}}_P = \sum_a \dot{\gamma}_a \mathbf{s}_a \otimes \mathbf{F}_P^T \mathbf{n}_a$ of the flow rule is relevant here in terms of the glide direction \mathbf{s}_a and glide-plane normal \mathbf{n}_a . At the glide-system level, the flow rule is given by the implicit thermodynamic form

$$0 = \partial_{\dot{\gamma}_a} \zeta + \partial_{\dot{\gamma}_a} \chi \quad (1)$$

in terms of the stored energy rate density ζ and dissipation potential χ . Assuming dissipative hardening alone, ζ reduces to the simple form

$$\zeta = - \sum_a \tau_a \dot{\gamma}_a \quad (2)$$

in terms of the Schmid stress $\tau_a = \mathbf{s}_a \cdot \mathbf{M} \mathbf{n}_a$. Here, $\mathbf{M} \approx \mathcal{C}_E \mathbf{E}_E$ represents the Mandel stress, \mathcal{C}_E the elasticity tensor, and $\mathbf{E}_E = \frac{1}{2} (\mathbf{F}_E^T \mathbf{F}_E - \mathbf{I})$ the elastic Green strain tensor. For simplicity, we work with the simple power-law form

$$\chi = \frac{1}{1 + 1/m_0} \sum_a \tau_{c a} \dot{\gamma}_0 |\dot{\gamma}_a / \dot{\gamma}_0|^{1+1/m_0} \quad (3)$$

for the dissipation potential. In addition, τ_{c_a} represents the critical Schmid stress for glide, $\dot{\gamma}_0$ is a characteristic slip rate, and m_0 is the flow exponent.

The current model for τ_{c_a} is motivated by that of [4]. In essence, this model transfers the behavior of analogous phenomenological models with respect to loading direction and changes in this direction [e.g., 1] to the glide-system level. It takes the form

$$\tau_{c_a} = \tau_i + \tau_{d_a} + \tau_{l_a} . \quad (4)$$

Here, τ_i is a common background self-hardening coming from all active glide-systems, τ_{d_a} is a “dynamic” contribution on all currently active system, and τ_{l_a} is a “latent” contribution on currently non-active systems. Since we are interested only in the qualitative hardening behavior here, we follow [4] and work with the simple form

$$\tau_i(\alpha_P) = \tau_0 + \tau_{II} (1 - e^{-c_{II} \alpha_P}) + \tau_{III} (1 - e^{-c_{III} \alpha_P}) + \tau_{IV} \alpha_P \quad (5)$$

of $\tau_i(\alpha_P)$ as a function of α_P . Here, α_P is the total accumulated equivalent inelastic deformation with $\dot{\alpha}_P = \sum_a |\dot{\gamma}_a|$. Further, $\tau_0 = \tau_i(0)$ is the initial value of τ_i . In addition, c_{II} and c_{III} represent stage II and stage III saturation rates, respectively. Likewise, τ_{II} and τ_{III} represent the corresponding saturation values. Lastly, τ_{IV} is the contribution to τ_i from stage IV. Turning next to τ_{d_a} and τ_{l_a} , these are modeled via the Voce saturation forms

$$\dot{\tau}_{d_a} = c_d (\tau_{d_a}^{\text{sat}} - \tau_{d_a}) \dot{\alpha}_P \quad (6)$$

and

$$\dot{\tau}_{l_a} = c_l (\tau_{l_a}^{\text{sat}} - \tau_{l_a}) \dot{\alpha}_P , \quad (7)$$

respectively. As before, c_d and c_l represent the saturation rates. Further, $\tau_{d_a}^{\text{sat}}$ and $\tau_{l_a}^{\text{sat}}$ represent the saturation values which are glide-system and loading-path dependent. Indeed, we have $\tau_{d_a}^{\text{sat}} = q_d \tau_i$ if $\dot{\gamma}_a \neq 0$, and $\tau_{d_a}^{\text{sat}} = 0$ if $\dot{\gamma}_a = 0$). Likewise, $\tau_{l_a}^{\text{sat}} = 0$ if $\dot{\gamma}_a \neq 0$, and $\tau_{l_a}^{\text{sat}} = q_l \tau_i$ if $\dot{\gamma}_a = 0$. Here, q_d and q_l are additional material parameters.

3. First application: Single-crystal AA3103

As a first application, consider the behavior of fcc single-crystal AA3103 subject to monotonic simple shear and to orthogonal tension-shear loading. The goal here is to show that the above model does indeed exhibit cross hardening. To this end, we work with the following parameter values [4]. $C_{11} = 106.6$ GPa, $C_{12} = 54.66$ GPa, $C_{44} = 26$ GPa, $\dot{\gamma}_0 = 0.001$, $m_0 = 20.0$, $\tau_0 = 10$ MPa, $\tau_{II} = 10.45$ MPa, $c_{II} = 18.2$, $\tau_{III} = 14$ MPa, $c_{III} = 1$, $\tau_{IV} = 2.5$ MPa, $q_l = 0.6$, $q_d = 0.35$, $c_l = 4$, and $c_d = 100$. Using these, we obtain the results shown in Figure 2. The resulting stress-deformation curves are shown on the left for the cases of (i) monotonic simple shear loading, and (ii) orthogonal loading (uniaxial tension to simple shear) of a single crystal of AA3103. The [100] direction of the crystal is oriented in the tension direction, and [010] is the shear direction. On the right-hand side, results are shown for the evolution of τ_i as well as for τ_{d_a} and τ_{l_a} of a characteristic glide system in the orthogonal case.

As shown in Figure 2 (left), the model indeed predicts a stress overshoot upon change of loading path from tension to shear in comparison to the monotonic case. As the exact mechanisms of the formation of cells and cell-block-boundaries and the corresponding transient stress-strain behavior are, at least, not fully understood, phenomenological modeling of the microstructural evolution at different scales offers the means to capture the main characteristics of the material behavior. The results shown in Figure 2 (right) for τ_{d_a} and τ_{l_a} are those for a single representative glide system which activates during the transition from tension to shear. As expected,

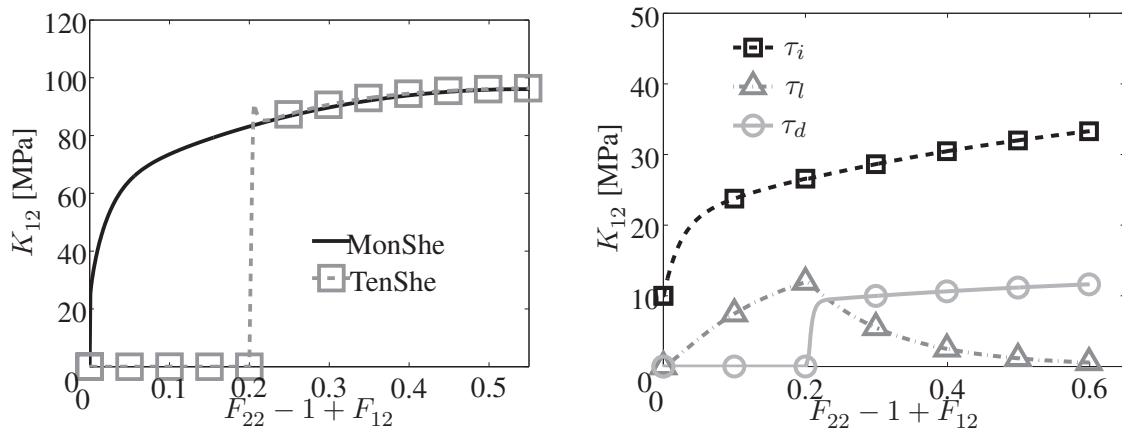


Figure 2: Monotonic and orthogonal loading of AA3103 single-crystal. See text for details.

note that τ_{da} is initially zero since the glide system in question is initial inactive and the corresponding dislocation structures have not yet developed. After transition from tension to shear, the glide system activates and τ_{da} grows toward its saturation value. In contrast, τ_{la} increases when the glide system is inactive (i.e., in a latent fashion), representing the build-up of planar dislocation structures in the tension phase which will lead to cross hardening upon orthogonal transition to shear loading. After this transition, τ_{la} reduces to zero during the active shear phase. This represents the effect on the hardening behavior of the breakdown and annihilation of planar dislocation structures (e.g., CBBs) which developed during the tension phase. As such, the correct qualitative behavior of the model is confirmed. Such a model for the bcc case of DC06 discussed in the last section as well as the polycrystal texture modeling represent work in progress and will be reported on at the meeting.

Acknowledgements

Financial support provided by the German Science Foundation (DFG) under contract PAK250 is gratefully acknowledged. The steel DC06 was provided by ThyssenKrupp Steel Europe AG. Thanks also go to A.H. van den Boogaard, University of Twente, for material testing, and to G. Gershteyn, University of Hannover, for the TEM analyses.

References

- [1] M. Noman, T. Clausmeyer, C. Barthel, B. Svendsen, J. Huétink, M. van Riel. Experimental characterization and modeling of the hardening behavior of the ferritic sheet steel LH800. *Mater. Sci. Eng. A* **527**, 2515–2526, 2010
- [2] S. Thuillier, E. F. Rauch. Development of microbands in mild steel during cross loading. *Acta Metall. et Mater.* **42**, 1973–1983, 1994.
- [3] Nesterova, E. V. and Bacroix, B. and Teodosiu, C.. Experimental observation of microstructure evolution under strain-path changes in low-carbon IF steel. *Mater. Sci. Eng. A* **309**, 495–499, 2001.
- [4] B. Holmedal, P. van Houtte, Y. An. A crystal plasticity model for strain-path changes in metals. *Int. J. Plast.* **24** (8), 1360–1379, 2008.

Atomistic kinetic Monte Carlo simulation of Iron Chromium phase decomposition parameterised on *ab initio* calculations

D. Costa^{1,2}, G. Adjanor¹, C.S. Becquart², C. Domain^{1,2} and P. Olsson¹

¹ EDF-R&D Département MMC, Les Renardières, F-77818 Moret sur Loing Cedex, France

² Laboratoire UMET, UMR 8207, Université de Lille 1, ENSCL, F-59655 Villeneuve d'Ascq Cedex, France

davide.costa@edf.fr

Thermal aging of iron chromium alloys is an important issue for the development of generation IV structural materials as well as for duplex stainless steel components in current generation nuclear power plants.

Chromium precipitation in the ferritic phase is observed in thermally aged materials and has an embrittling effect on the alloy. The aim of this study is to model the microstructure evolution of bcc iron chromium alloys under thermal aging using an atomistic kinetic Monte Carlo approach. Several studies related to this issue have already been performed, most of them being based on semi-empirical cohesive models. In this work, a kinetic Monte Carlo parameterisation based on *ab initio* predictions is proposed. In particular, the influence of the local ionic environment on the migration barriers has been taken into account. In particular, the properties of Fe/Cr interfaces have been studied. Results are compared to those obtained using a semi empirical potential based parameterisation and to available experimental data.

Temporal Coarse Graining in Dislocation Dynamics

Jie Deng and Anter El-Azab

Department of Scientific Computing, Florida State University, Tallahassee, FL 32306
(Email: aelazab@fsu.edu)

ABSTRACT

We use temporal statistics to model the source terms in the kinetic theory of dislocations by temporal coarse graining. Numerical results are obtained for the coarse graining time scale and cross-slip and junction rates.

1. Introduction

Statistical mechanics has been applied to model the collective behavior of dislocations [1-3]. A key question in this regard is how to account for the discrete dislocation events occurring over very short time scale in the continuum framework. To answer this question, we use temporal statistics to model the coarse graining time scale for the dislocation cross slip and short range reactions, from which the rate parameters of these discrete events are modelled. The latter is used to fix the source terms arising from cross slip and short range reactions in the kinetic theory of dislocations. Numerical results are obtained using temporal data generated using the method of dislocation dynamics simulations [4].

2. Theoretical and Numerical Analysis

In the kinetic theory of dislocations [2, 3], the evolution of dislocation system is described by the governing equations of continuum dislocation density fields:

$$\partial \bar{\rho}^\alpha / \partial t + \nabla \cdot (\bar{\rho}^\alpha \bar{\mathbf{v}}^\alpha) = \bar{S}^\alpha = \bar{S}_M^\alpha + \bar{S}_{CS}^\alpha (\bar{\rho}^\alpha, \bar{\rho}^\beta) + \bar{S}_{SR}^\alpha (\overline{\rho^\alpha \rho^\gamma}), \quad \alpha, \beta, \gamma = 1, 2, \dots, M \quad (1)$$

where M is the total number of slip systems, $\bar{\rho}^\alpha$ is the ensemble average of dislocation density $\rho^\alpha(\mathbf{x}, \theta, t)$, which is proportional to the probability of finding one dislocation at position \mathbf{x} with orientation θ on α -th slip system at time t , $\bar{\mathbf{v}}^\alpha$ is the average dislocation velocity and \bar{S}^α is the source term capturing the dislocation density change due to dislocation multiplication, cross-slip and various short-range reactions. While the multiplication source term is governed by the kinematics of dislocation configuration [3, 5], here we will focus on the modelling of source terms corresponding to cross slip and junction reaction. Consider a cross slip from slip system α to β . Since it induces dislocation density change in these two slip systems, it gives rise to two cross-slip source terms with the form

$$\bar{S}_{CS}^\alpha(\theta) = -\partial \bar{\rho}_{CS}^\alpha(\theta) / \partial t = -R_{CS}^\alpha 1_{\Theta_{CS}^\alpha}(\theta) \bar{\rho}^\alpha(\theta) \quad \text{and} \quad \bar{S}_{CS}^\beta(\theta) = \partial \bar{\rho}_{CS}^\beta(\theta) / \partial t = R_{CS}^\beta 1_{\Theta_{CS}^\beta}(\theta) \bar{\rho}^\alpha(\theta). \quad (2)$$

In Eqn. (2), $1_{\Theta_{CS}^\alpha}$ is the indicator function that equals to unity when $\theta \in \Theta_{CS}^\alpha$ and zero otherwise, where Θ_{CS}^α is a small angular range around screw dislocation direction θ_{CS}^α . The

derivative $\partial \bar{\rho}_{cs}^\alpha(\theta)/\partial t$ is the rate of dislocation density change due to the cross slip, which depends on the screw dislocation density as well as the rate parameter R_{cs}^α that characterizes the frequency of cross slip. In numerical simulation, $\partial \bar{\rho}_{cs}^\alpha(\theta)/\partial t$ can be approximated by $\Delta \bar{\rho}_{cs}^\alpha(\theta)/T$, where T is the coarse grain time scale and $\Delta \bar{\rho}_{cs}^\alpha(\theta)$ is the cumulative cross slip density over the time interval T . The junction source terms can be modelled in the same way except that they depend on the product of dislocation densities. Assume dislocations on slip system α to β react to form junctions on slip system γ , three source terms arise since these reactions induce dislocation density change in three slip systems:

$$\begin{aligned}\bar{S}_j^\alpha(\theta) &= -\partial \bar{\rho}_j^\alpha(\theta)/\partial t = -R_j^\alpha(\theta) \int_{\Theta_j^\beta} \overline{\rho^\alpha(\theta) \rho^\beta(\theta')} d\theta', \\ \bar{S}_j^\gamma(\theta) &= \partial \bar{\rho}_j^\gamma(\theta)/\partial t = R_j^\gamma(\theta) \int_{\Theta_j^\alpha} \int_{\Theta_j^\beta} \overline{\rho^\alpha(\theta') \rho^\beta(\theta'')} d\theta' d\theta''\end{aligned}\quad (3)$$

$\bar{S}_j^\beta(\theta)$ has a form similar to $\bar{S}_j^\alpha(\theta)$ by exchanging α and β . In Eqn. (3), Θ_j^β is the orientation range within which dislocation in slip system β is able to form junction with dislocation in slip system α with orientation θ . Θ_j^α has similar meaning. The time derivatives in Eqn. (3) represents the dislocation density change due to junction reaction, and they depend on the corresponding rate parameters and the product of dislocation densities that contribute to the junction. Same as in cross-slip case, these derivatives can be approximated in numerical simulation by utilizing the coarse grain time T . The above formulation shows that fixing the source terms requires the coarse graining time scale and the rate parameters. The former can be obtained by treating cross slip and junction reaction as the discrete events in stochastic point process [6] or time series [7] analysis, see detailed modeling in [5]. Here we will briefly show the formulation in time series analysis.

Consider a time series $\{X_t\}$ that represents the density of cross-slip or junction reaction at each discrete time. If $\{X_t\}$ is stationary, (i.e., its distribution is independent of time translation), its mean value μ is a constant and its covariance Γ and correlation c is dependent only on the time difference between two events:

$$\mu = E(X_t), \quad \Gamma(\tau) = E((X_t - \mu)(X_{t+\tau} - \mu)), \quad c(\tau) = \Gamma(\tau)/\Gamma(0) \quad (4)$$

where $E(\cdot)$ represents expectation value. From above correlation we may express the correlation time as the integral

$$T_c = \int_0^\infty c(\tau) d\tau \approx \int_0^{\tau_M} c(\tau) d\tau \quad (5)$$

where τ_M is a suitable upper integration limit. Since the correlation time is the time interval over which the statistical connection between events in a time series is maintained, it can be used to approximate the coarse grain time scale T . It is noted that Eqn. (4) and (5) are valid for stationary time series only, but the cross slip and junction density will increase as dislocation density increases, i.e., the original time series of cross slip and junction is not stationary. Thus, an appropriate stationarization method should be applied before using Eqn. (4) and (5) [5]. After that, the coarse graining time scale can be fixed by Eqn. (5) and then the rate parameters for cross-slip and junction reaction can be obtained from Eqn. (2) and (3).

The microMega dislocation dynamics code [4] has been used to generate the dislocation configurations required for temporal statistical analysis in copper crystal loaded in [100] direction at room temperature. The slip systems of copper are of $\langle 110 \rangle \{111\}$ type, and eight of them are activated for the loading direction specified here. Three simulation conditions are implemented: (1) strain rate $\dot{\epsilon} = 25s^{-1}$ and box size $L = 5\mu m$, (2) $\dot{\epsilon} = 10s^{-1}$ and $L = 5\mu m$, and (3) $\dot{\epsilon} = 25s^{-1}$ and $L = 7.5\mu m$. The initial dislocation density is $1.6 \times 10^{12} m^{-2}$ and $7 \times 10^{11} m^{-2}$, for the 5 and 7.5 micron boxes, respectively.

The output of simulation gives the densities of cross-slip and junction reaction at each slip system at each discrete time, which consists of multiple non-stationary time series. They are stationarized by subtracting the trend from them, and the resulting stationary time series are used to calculate the coarse graining time scale. It is found that the correlation time in cross-slip is larger than its counterpart for junction reaction, and they are in the range of 0.02-0.04 μs , with nearly no dependence on simulation conditions [5]. Because of that, the coarse grain time scale is set to be 0.04 μs for later calculation of the rate parameters. Note that this time scale is much longer than the characteristic time for individual dislocation events, while much shorter than the macroscopic evolution time of dislocation system.

Figure 1(a) shows the evolution of cross-slip rates in all the eight activated slip systems under the simulation condition (1). It is found that initially the cross-slip rates increase in an oscillatory fashion as time (or strain) increases. This indicates that although the thermal mechanism of cross-slip is independent of dislocation density, their collective behavior shows density dependence at the beginning. That is, as dislocation density increases, the internal stresses are developed to favor more cross-slip, making cross-slip occur more frequently. The oscillation of rate reflects the inhomogeneity of dislocation density and internal stress fields. Figure 1(a) also shows that at high strain level, cross-slip rates tends to approach an asymptotic window, which indicates the growth of cross-slip rate will be balanced by the constraining of cross-slip due to the increase of line tension of dislocations. The cross-slip rates under other simulation conditions show similar features. Figure 1b gives a typical rate evolution of a glissile junction reaction, which shows that strong fluctuation appears as junction rates develop. It seems that the junction rate can be decomposed into two parts: a slowly growing background component plus a strong fluctuation. The former can be associated to the work hardening rate of crystals and the latter is an apparent indication of the intermittent nature of plastic flow. It is interesting to compare the junction rate evolution with the previous investigation on dislocation avalanches [8, 9]. The former corresponds to the locking of moving dislocations, while the latter is associated to the dislocation unlocking, so they are coupled dislocation processes with opposite features. As the probability distribution of avalanches magnitude is given in [8, 9], here we plot the probability distribution of junction rates, see Figure 1c. It is found that, same as dislocation avalanches, junction rates also exhibit power law scaling in the form $p(R) \sim R^{-k}$, with the power coefficient k in the range 1.5-2.5. The fluctuation and power law scaling of junction rate is nearly independent of simulation conditions [5].

3. Concluding Remarks

A temporal statistics method has been applied to model the source terms arising from the cross-slip and short-range reactions of dislocations within the kinetic theory framework. The coarse graining time scale is approximated from the time series analysis, and the rate parameters of cross-slip and junction formation are determined by temporal coarse graining of these discrete events. The numerical results show that both cross-slip and junction rates

exhibit fluctuation during their evolution. Cross-slip rates tend to increase initially and approach a plateau at high strain level, and junction rates have power law scaling in their probability distribution. These features reflect important physics of collective dislocation motion and help to model the corresponding source terms. Work is underway to investigate the effects of temperature and loading conditions on the temporal statistics and incorporate it into the kinetic theory of 3D dislocation systems.

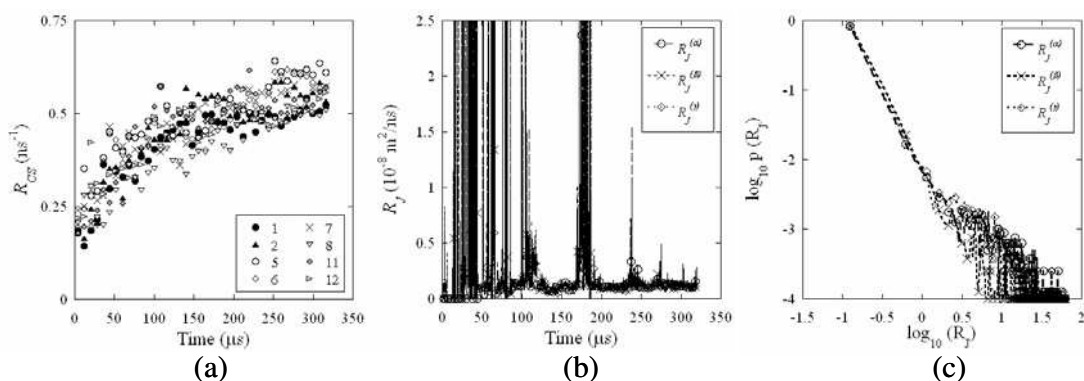


Figure 1. (a) Evolution of cross-slip rates for active slip systems. (b) Rates for junction reaction $[\bar{1}10](\bar{1}\bar{1}\bar{1}) + [101](11\bar{1}) \rightarrow [011](11\bar{1})$ and (c) their probability distribution.

Acknowledgements

This work was supported by the U.S. DOE Office of Basic Energy Sciences, Division of Materials Science and Engineering through contract number DE-FG02-08ER46494 at Florida State University.

References

- [1] I. Groma, "Link between the microscopic and mesoscopic length-scale description of the collective behavior of dislocations," *Physical Review B*, **56**, 5807 (1997).
- [2] A. El-Azab, "Statistical mechanics treatment of evolution of dislocation distribution in single crystals," *Physical Review B*, **61**, 11956 (2000).
- [3] J. Deng and A. El-Azab, "Mathematical and computational modelling of correlations in dislocation dynamics," *Model. Simul. Mater. Sci. Engng*, **17**, 075010 (2009).
- [4] B. Devincere and L. Kubin, "Mesoscopic simulation of dislocations and plasticity," *Materials Science and Engineering A*, **234**, 8 (1997).
- [5] J. Deng and A. El-Azab, "Temporal statistics and coarse graining of dislocation ensembles," *Philosophical Magazine*, in the press.
- [6] K. Sigman, *Stationary Marked Point Processes: An Intuitive Approach*, Chapman and Hall, New York, 1995.
- [7] P. Brockwell and R. Davis, *Introduction to Time Series and Forecasting*, Springer, New York, 2002.
- [8] D. Dimiduk, C. Woodward, R. LeSar and M. Uchic, "Scale-free intermittent flow in crystal plasticity," *Science* **312**, 1188 (2006).
- [9] F. Csikor, C. Motz, D. Weygand, M. Zaiser and S. Zapperi, "Dislocation avalanches, strain bursts and the problem of plastic forming at the micrometer scale," *Science*, **318**, 251 (2007).

POROUS MEDIA MICROSTRUCTURE RECONSTRUCTION USING PIXEL-BASED AND OBJECT-BASED SIMULATED ANNEALING – COMPARISON WITH OTHER RECONSTRUCTION METHODS

Diógenes, Alysson N¹, Fernandes, Celso P.², dos Santos, Luis O. E.³, Appoloni, Carlos R.⁴

¹ andiogenes@ufpr.br, Universidade Federal de Santa Catarina, Laboratório de Meios Porosos e Propriedades Termofísicas – LMPTCEP 88040-900 – C.P. 476 – Florianópolis, SC, Brasil

^{2,3} Universidade Federal de Santa Catarina, Laboratório de Meios Porosos e Propriedades Termofísicas – LMPTCEP 88040-900 – C.P. 476 – Florianópolis, SC, Brasil

⁴ Applied Nuclear Physics Laboratory (LFNA), Physics Department, State University of Londrina, P.O. Box 6001, 86051-990 Paraná, Brazil

The porous media characterization is indeed a very interesting problem for scientific and technological purposes, as its macroscopic properties determination have many applications in different areas, as soils, oil exploiting, buildings and mechanics.

Among the porous media been subjected to several studies, there are the reservoir rocks. Its porous microstructures geometries can present a high complexity organization and, consequently, several geometric and physical properties can be use to characterize these materials. We can mention the porosity, the pore size distribution and the permeability, usually obtained in laboratory experiments. For reservoir rocks these experiments are accomplished in testimonies extracted from the soil. They are often expensive, time consuming and sample destructive.

On the other hand, advanced techniques such as microtomography and serial sectioning provide a 3D description of the pore structures of rocks. Image analysis methods used over pictures of highly polished surfaces of porous materials taken with an electron scanning microscope or optical microscope have been used to describe porous structure. One of the most useful results of image analysis in the study of porous structure is the three-dimensional (3D) reconstruction of porous structure. The general objective of a three dimensional reconstruction is to mimic the geometry of real media, enabling the creation of numerical realizations of the sample with the desired geometric properties. This method has been applied to the prediction of important petrophysical and reservoir engineering properties such as permeability and formation factor with reasonable success.

The classical reconstruction method is the onset of the ones based in Gaussian Fields (TG) and its variations. It preserves a previously obtained autocorrelation function of the microstructure and generates a 3D image. The TG method presents problems in preserving connectivity. This happens because the two-order statistics reproduction is not sufficient to reproduce long-range geometry or patterns with characteristic shapes (e.g., pore spaces) for some cases, such as media with low porosity.

Another reconstruction methods preserving a different parameter, the pore size distribution, is the superposed spheres (SS). The method calculates the number of

spheres in order to reconstruct a given porous media, saving it's the porosity. Each sphere will superpose neighboring spheres according to a user-defined parameter. This method presents good results for connectivity, although it does not preserves the autocorrelation function.

The Simulated Annealing technique has been previously used to reconstruct porous media with relative success by several authors. These authors were able to reproduce sandstone rocks geometrical parameters and some connectivity for two-dimensional (2D) and 3D media, although, some authors remark that this last parameter wasn't well preserved in comparison with images obtained by X-ray microtomographic.

The Figure 1 shows an original reservoir rock microstructure image and its correspondent pore space binarized image.

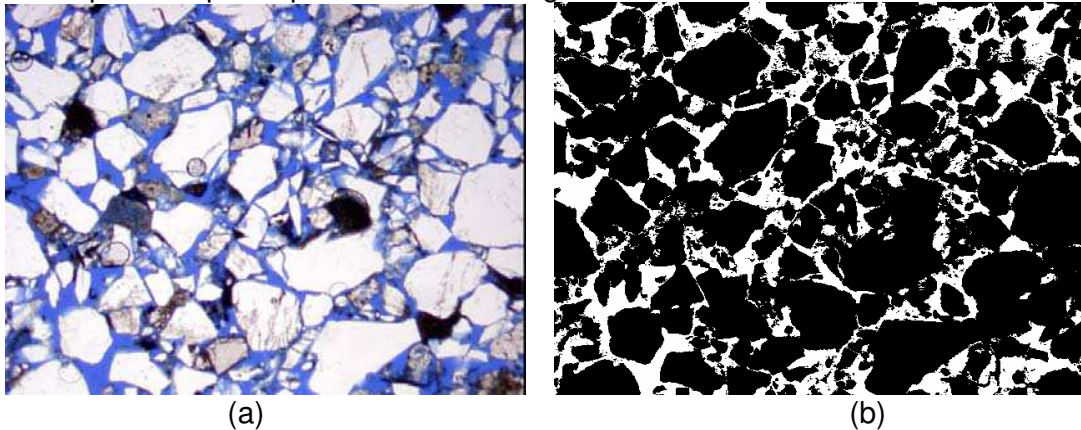


Figure1: Original reservoir rock microstructure image and its correspondent pore space binarized image.

The Figure 2 shows a pore space reconstruction using the Simulated Annealing technique presented at this research. This reconstruction reproduced the spatial correlation measured at the Figure 1(a).

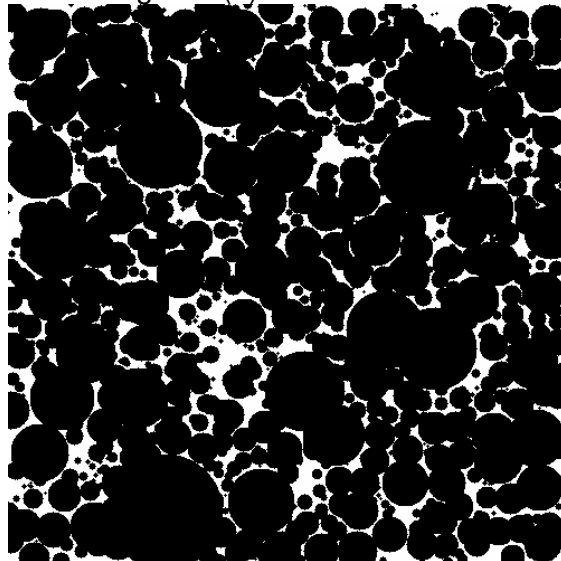


Figure 2: Sandstone microstructure image reconstructed using the Simulated Annealing technique proposed at this research.

The objective of this research is to present a technique for the porous media reconstruction in 3D using object-based and pixel-based simulated annealing methods. The main focus in the method is to preserve the connectivity and yet uphold desired geometrical parameters.

The results will be compared with the truncated Gaussian method, which is the most used for this purpose and with some samples' X-ray microtomographies obtained using a SKYSCAN 1172 X-Ray microtomograph equipment. The comparison method will be measuring the quadratic error to the autocorrelation function, pore-size distribution and fraction of percolating cells measured in previously acquired 3D microtomographic images.

Optimizing of mechanical properties of nanometals

**Romuald Dobosz, Marek Muzyk, Tomasz Wejrzanowski
and Krzysztof Jan Kurzydowski**

Warsaw University of Technology, Faculty of Materials Science and Engineering,
Woloska 141 str., 02-507 Warsaw, Poland
e-mails: rdobosz@inmat.pw.edu.pl, muzyk@inmat.pw.edu.pl,
twejrzanowski@inmat.pw.edu.pl, kjk@inmat.pw.edu.pl

The paper deals with the concept of optimizing of mechanical properties of nanometals, which are controlled by the properties of the grain boundaries (GBs). The model developed in this study takes into account stochastic nature of the population of the grain boundaries in metals and variability of their properties. The properties of grain boundaries, in particular Young modulus, were calculated by ab initio methods.

The results of atomic modeling were implemented into meso-scale Finite Element Method (FEM) model, in order to calculate the response of the polycrystalline aggregate to the applied load. Non-zero grain boundary thickness was assumed to account for nano-metric size of the grain interiors. Various aggregates were studied which differed, among others, in the grain size homogeneity described by the coefficient of variation of the grain equivalent diameter.

The results show that grain boundary properties and grain size homogeneity play an important role in shaping the properties of nanometals. These results are further used to indicate the rules for optimizing the structure/properties of nanometals.

Decohesion and buckling of thin films on substrates: a molecular dynamics approach

J. Durinck, A. Ruffini, J. Colin and C. Coupeau

Institut Pprime, CNRS-Université de Poitiers-ENSMA, SP2MI, F86962 Futuroscope
julien.durinck@univ-poitiers.fr

Coatings and thin films on substrates are widely used in industry in order to improve the mechanical properties of materials. It has been observed in many cases that the deposition processes may generate high residual stresses which may lead to morphological and structural modifications among which are the decohesion of the interface and the resulting buckling of the delaminated part of the film when the stresses are compressive.

Recently, the buckling of thin films on rigid substrates has been modeled at the mesoscale in the framework of the Föppl-Von Kármán's theory of thin plates and several buckle morphologies has been described such as circular blisters or telephone cord morphologies. But up to now this continuum approach does not take into consideration the plastic mechanisms of deformation nor the decohesion of the interface.

In this study we report on atomistic simulations using interatomic potentials of the buckling of a ultra-thin Al single crystal film on a infinitely rigid substrate. The buckling of the film has been characterized and compared with the results obtained in the continuum approach and the nucleation of dislocations in the high compressive areas of the buckle has been highlighted.

Likewise, the interfacial decohesion of a $\{111\}$ copper thin film on a $\{110\}$ tungsten substrate has been investigated when tangential and normal components of the separation between both crystals are applied. The stress-separation curves have been determined as a function of the mode mixity.

Atomistic study of grain size effect on elastic moduli in nanocrystalline tungsten

P. Valat-Villain¹, J. Durinck¹, P.-O. Renault¹, F. Badawi¹

Institut P', UPR 3346 CNRS - Université de Poitiers – ENSMA
Département de Physique et Mécanique des Matériaux
SP2MI - Téléport 2- BP 30179 - F86962 Futuroscope Chasseneuil CEDEX
Corresponding author : pascale.valat@univ-poitiers.fr

The influence of reduced size on various physical and mechanical properties of materials is a much debated subject. We are particularly interested in the elastic behaviour of metallic thin films. For a few years, we have been performing atomistic simulations using Finnis-Sinclair-type potentials and relaxation by means of molecular dynamics and molecular statics techniques in order to calculate elastic coefficients in nanosized systems. The first calculations concerning single-crystal tungsten wires and slabs have evidenced a strong surface effect on the equilibrium lattice parameter with appearance of anisotropy, and a significant softening of the Young's modulus when the crystal size is reduced [1].

The studies presented here deal with nanocrystalline tungsten. Bulk polycrystalline samples with grain sizes ranging from 3 to 8 nm and various microstructures were built by means of a Voronoi method and relaxed with molecular dynamics methods (XMD and LAMMPS codes). The bulk modulus, shear modulus, Young's modulus and Poisson's ratio were then determined thanks to suitable deformation tests. A moderate but significant decrease of the bulk modulus is observed as the grain size decreases (up to -25% compared to bulk single crystal for a 3 nm average grain size) while a very strong reduction of the shear and Young's moduli (up to 60%) is observed. This stiffness variation can be explained by the high grain boundary volume fraction in nanocrystallised samples, grain boundary regions having a lower stiffness than in-grain parts of the crystal.

[1] P. Villain., P. Beauchamp, F. Badawi, P. Goudeau, P.-O. Renault P., *Scripta Mater.* **50** (2004) 1247

Calculation of the *Peierls stress* from atomistic simulations for bcc tungsten: screw vs. edge dislocations

Authors: B. Eberhard, J. Almanstötter

OSRAM GmbH, I OSR R&D TM DM-E, Mittelstetter Weg 2, 86830 Schwabmünchen, Germany, b.eberhard@osram.de, j.almanstoetter@osram.de

ABSTRACT

For bcc metals, it is commonly assumed, that the mobility of screw dislocations is significantly lower than that of edge dislocations and, therefore, should control the low temperature plastic deformation behaviour. The mobility of dislocations depends on their Peierls energy barrier, defined as the activation energy required to move a dislocation in an otherwise perfect crystal. This connection between atomistic features and the overall mechanical behaviour makes a more detailed investigation of the atomistic system necessary. Also, the violation of Schmid's Law, stating that the critical resolved shear stress is constant and independent of the slip system and the external stress, is an important ingredient for the construction of macroscopic flow rules of the material, suitable e.g. for finite element calculations. In present work, these effects are studied for $1/2a \langle 111 \rangle$ screw and edge dislocations in tungsten. To this end, we constructed dislocations using elasticity theory in partially periodic simulation cells. After relaxation within a NPT-MD simulation, we applied an external shear stress to the system in order to force the dislocations to move at low simulation temperatures. The Peierls energy barriers and the corresponding Peierls stresses are derived.

1. Introduction

For artificial lighting, most often *temperature radiation* according to *Planck's law*¹ is used. The spectral emissivity of tungsten shows its maximum in the visible region, i.e. wavelengths between about 400nm and 800nm. This makes tungsten a candidate of choice for its use as electrodes in lighting industry as this means, that the theoretical efficacy of tungsten is even superior to a black body radiator. Of course, mechanical stability at these high temperatures where the radiated "light output" is not negligible has to be guaranteed, also. That's why for incandescent lamps the melting point of any material used must not be exceeded or only be reached in "real" lamps for daily use. Tungsten is *the* metal with the highest melting point and lowest evaporation rate and vapor pressure at a given temperature in the periodic table. In this work, we address the plastic properties of pure and Th-doped tungsten. For this, we employ *ab initio* derived *embedded atom potentials* (EAM) within a NPT-MD approach to edge and screw dislocations with and without Th in the core and derive the *Peierls stress* by suitably chosen driving forces.

2. Methodology and Simulation Cell

For the following, we performed Molecular Dynamics simulations, where atom trajectories are calculated by integrating *Newton's equation of motion*³. The force field was constructed using *embedded atom* (EAM) potentials which are derived from *ab initio* data of pure and artificial tungsten - thorium compounds². These data are used for fitting the following interaction scheme

(EAM):

$$E_{tot} := \frac{1}{2} \sum_{\substack{i,j \\ i \neq j}} \phi_{t_i t_j}(r_{ij}) + \sum_j F_{t_j}(\bar{\rho}_i) \quad \text{and} \quad \bar{\rho}_i := \sum_{\substack{j \\ i \neq j}} \rho_{t_j}(r_{ij}) \quad (1)$$

where $F_{t_j}(\bar{\rho}_i)$ denotes the embedding energy of atom type t_i , $\bar{\rho}_i$ the “electron density” from the environment at atom site i , $\phi_{t_i t_j}(r_{ij})$ the pair potential contribution and, finally, $\rho_{t_i}(r_{ij})$ the individual “electron density” contribution of atom type t_i .

3. Simulation for single Edge/Screw Dislocations

A single edge or screw dislocation ($b \propto \langle 111 \rangle$) in a simulation cell of approximately 50000 atoms was constructed. The cell orientation was:

- edge dislocation (s.⁴): x : $[111]$, y : $[1\bar{1}0]$, z : $[11\bar{2}]$
- screw dislocation: x : $[1\bar{1}0]$, y : $[11\bar{2}]$, z : $[111]$

The initial atomic configuration was calculated using linear elasticity and with following boundary conditions:

- edge dislocation:
periodic in $[11\bar{2}]$, free in $[111]$, constrained to the plane $(1\bar{1}0)$
- screw dislocation:
periodic in $[111]$, fixed for a cylindrical shell around the dislocation axis

Properly chosen atoms at the edge of the simulation cell were kept fixed, i.e. no equation of motion was solved for those atoms in order to ensure appropriate stress fields. The simulation cell was relaxed for about 5ps at intermediate temperatures (100K) and quenched afterwards, i.e. the kinetic energy of the assembly was removed. For relaxing the structures, a combined stochastic temperature and pressure algorithm was used. The resulting structures served as starting point for further simulations.

4. Peierls vs. pseudo-Peierls mechanism

For the motion of screw dislocations influenced by mechanical stress in bcc metals, two concepts are controversially discussed: the *pseudo-Peierls* and the *Peierls* mechanism. Their key attributes are:

- pseudo-Peierls mechanism:
 - Dissociation of screw dislocation forms stacking faults (Burgers vector $1/6 \langle 111 \rangle$) on threefold-symmetric $\{112\}$ planes
 - Constriction energy of partials necessary for dislocation glide
 - Violation of *Schmid's law* by symmetry considerations
- Peierls mechanism:

- Atoms in neighboring triangular $\langle 111 \rangle$ columns form spiral configurations with alternating winding direction
- Superposition of the strain field of a screw dislocation results in likewise strained atomic positions
- two competing positions for the screw dislocation are known. They differ about 6% in the interatomic distances, resulting in a high and low energy core

Therefore, the bcc lattice shows successive minimum energy positions for the screw dislocation and *Peierls barriers* between them. This should result in a conventional Peierls mechanism.

5. Stacking Fault Energy (SFE): The γ surface

A hint towards which mechanism (*pseudo-Peierls* or *Peierls*) is favored in tungsten, is given by the *stacking fault energy*. Here, the (relaxed) γ surface was calculated for the (112) plane according to the following procedure:

- The simulation cell was oriented as for the screw dislocation, periodic boundary conditions in x and z direction and a *Langevin* pressure algorithm in y direction were applied
- After relaxing the undisturbed cell, the cell was divided into two parts in y direction (normal to (112) plane), the two parts were shifted relative to each other
- The atoms were allowed to relax in y direction only

The results show very high energy densities (up to $0.30\text{eV}/\text{\AA}^2$), with a corresponding SFE of about $0.23\text{eV}/\text{\AA}^2$, so that a formation of a stacking fault on (112) is very unlikely. Therewith, no splitting of a screw into partials should be possible, i.e. there is no working *Sleeswyk* reaction in tungsten.

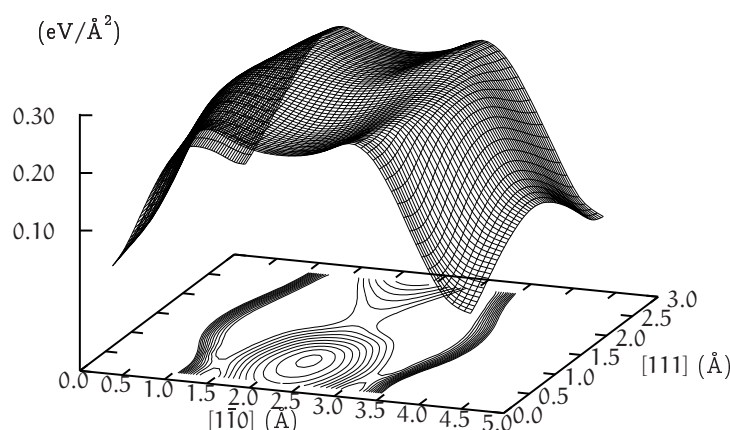


Figure 1: calculated gamma surface for the (112) plane

6. Peierls stress of the first kind: edge

To determine the *Peierls stress of the first kind* for the edge dislocation, we used the relaxed structure as described above and fixed the outer layers in $[1\bar{1}0]$ direction. In a subsequent step,

we applied the following pure shear strain:

$$\epsilon_{ij} \propto (\delta_{1i}\delta_{2j} + \delta_{2i}\delta_{1j}) \quad (2)$$

According to linear theory of elasticity, the elastic constant in the chosen coordinate system is given by $c_{1212} = \frac{e}{2\epsilon^2}$ with energy density e . For the thoriated tungsten, we substituted a W-atom with a Th-atom in-midst the dislocation core. Successively straining the lattice results in a energy vs. strain curve which, when fitted, gives $c_{1212} = 119\text{GPa}$ for the thoriated situation and a corresponding Peierls stress of $\sigma_P^t = 1.2\text{GPa}$. Assuming that the elastic constants remain unaffected for pure tungsten we use c_{1212} also for the calculation of the Peierls stress ($\sigma_P = 69\text{MPa}$). The huge difference in the critical shear stress between thoriated and pure tungsten shows once again the strong tendency of thorium to enhance the recrystallization temperature.

7. Peierls stress of the first kind: screw

To determine the *Peierls stress of the first kind* for the screw dislocation, we applied a procedure analog to the one used for the edge dislocation, i.e. fixing the outer layers and straining as already described. This time, the elastic constant used in the chosen coordinate system is c_{2323} . Fitting of the energy density vs. strain curve gives $c_{2323} = 153\text{GPa}$. The corresponding Peierls stress for pure and thoriated tungsten is calculated to $\sigma_P^p = 2.2\text{GPa}$ and $\sigma_P^t = 2.5\text{GPa}$, respectively, for deformation in *positive* $[1\bar{1}0]$ direction. The influence of Th atoms on the dislocation line is by far smaller for screw compared to edge dislocations. The deformation in *negative* $[1\bar{1}0]$ direction shows a slight asymmetry (s. Fig. 2) which is a consequence of the threefold symmetry of the stress field of a screw dislocation, and, therefore, shows a clear violation of *Schmid's law*. Furthermore, it could be shown, that the threefold symmetry of the the strain field is clearly destroyed before the dislocation relaxes in a new (stable) position.

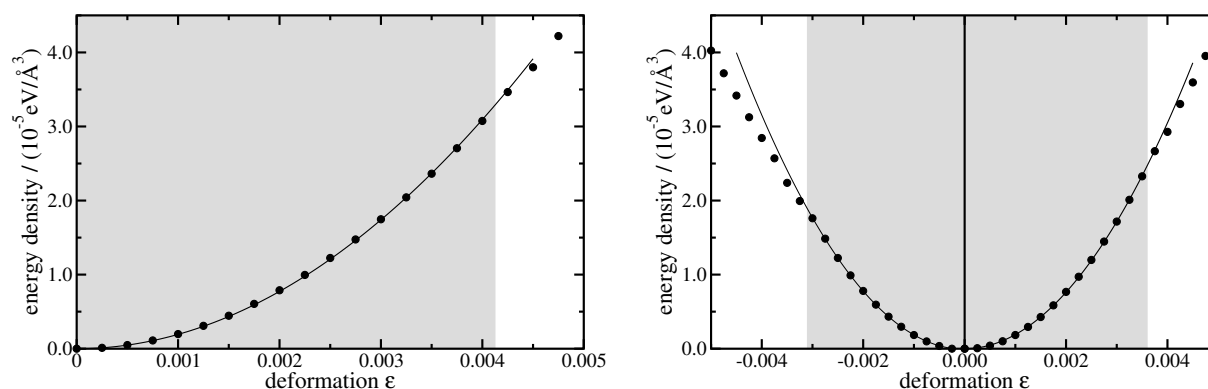


Figure 2: energy density vs.deformation for a screw dislocation in thoriated (left) and pure tungsten (right)

References

- [1] Planck M., *Ann. d. Physik* **4**, 553, 1901
- [2] Mishin Y., Farkas D., Mehl M. J., Papaconstantopoulos, D. A., *Phys. Rev. B*, **59**, 3393, 1999
- [3] <http://www.ims.uconn.edu/centers/simul>
- [4] Aslanides A., Pontikis V., *Phil. Mag. A*, **80**, 2337, 2000
- [5] Li J., *Modelling Simul. Mater. Sci. Eng.*, **11**, 173, 2003

Validation of phenomenological and dislocation-based constitutive laws for crystal plasticity of hexagonal Ti

A. Alankar¹, P. Eisenlohr¹, F. Roters¹, L. Wang², Y. Yang², T.R. Bieler², and M.A. Crimp²

¹Max-Planck-Institut für Eisenforschung, Max-Planck-Straße 1, 40237 Düsseldorf, Germany, p.eisenlohr@mpie.de

²Chemical Engineering and Materials Science, Michigan State University, 2527 Engineering Bldg, 48824 East Lansing, USA

Miniature bend samples of commercially pure alpha-Ti (hexagonal) were deformed to surface tensile strains between 0.02 and 0.15. Selected patches of the microstructure were followed through deformation. Surface and out-of-surface displacements, crystal orientation, and slip and twin system activity were determined by a combination of atomic force microscopy, electron backscatter diffraction, electron channeling contrast imaging and digital image correlation. Deformation of representations of the oligocrystalline patches, with an assumed columnar grain structure, was simulated under macroscopic boundary conditions using the crystal plasticity finite element method. Two types of constitutive laws, based on slip resistance and dislocation density, are validated against the experimental reference.

Response of a $\Sigma 11$ Asymmetric Tilt Grain Boundary in Copper to an Applied Shear Stress at Finite Temperatures

Saryu Fensin¹, Richard Hoagland², Steve Valone² and Mark Asta^{1,3}

- 1. One Shields Avenue, Department of Chemical Engineering and Materials Science, University of California, Davis, California, USA 95616*
- 2. Mailstop G755, Material Science and Technology Division, Los Alamos National Laboratory, Los Alamos, New Mexico, USA 87545*
- 3. 210 Hearst Mining Building, Department of Materials Science, University of California, Berkeley, California, USA 94720*

We present results of molecular dynamics simulations studying the temperature dependence of the structure and mechanical response to an applied shear stress for an asymmetric $\Sigma 11$ -tilt grain boundary in copper. At higher temperatures a disordered liquid-like layer forms at the grain boundary and becomes wider in width as the melting temperature is approached from below. Upon application of shear stress the boundary undergoes incremental normal displacement also known as coupled motion at low temperatures. This behavior is analyzed to determine the atomic mechanisms involved in the of the grain boundary. With increasing temperature, and associated disordering of the interface structure, the mechanical response switches to that of grain-boundary sliding at the highest temperatures, with more complex behavior being displayed at intermediate temperatures. The information about atomistic mechanisms and migration rates involved in grain boundary migration are important components for any multi scale model of microstructure evolution.

¹ sjindal@ucdavis.edu

Multiscale modeling of texture and plastic anisotropy in a cup drawing process

**Jerzy Gawad^{1,2}, Albert Van Bael^{3,4}, Paul Van Houtte³, Giovanni Samaey¹
and Dirk Roose¹**

¹ Department of Computer Science, Katholieke Universiteit Leuven, Celestijnenlaan 200A, 3001 Leuven, Belgium, jerzy.gawad@cs.kuleuven.be

² Faculty of Metals Engineering and Industrial Computer Science, University of Science and Technology AGH, Al. Mickiewicza 30, Krakow, Poland

³ Department of Metallurgy and Materials Engineering, Katholieke Universiteit Leuven, Kasteelpark Arenberg 44, 3001 Leuven, Belgium

⁴ Limburg Catholic University College (KHLim), Agoralaan 1, 3590 Diepenbeek, Belgium

The simulation of cold forming processes of metal sheets becomes fairly complex if the anisotropy of plastic properties is taken into account. The crystallographic texture of a sheet determines to a large extent the anisotropic behavior. At the same time, textures evolve due to plastic deformations. Since the history of straining in the neighboring regions of the deformed sheet is possibly diverse, one can also expect variations in the evolution of the texture. This entails heterogeneous distribution of the texture in the material, as well as inhomogeneity of the plastic anisotropy. To account for this evolution, the model has to span several length scales, from the rotations of individual grains in the polycrystalline material, up to the macroscopic deformation of the sheet.

In this work we present a multiscale model which takes into account aforementioned aspects of texture development during a cup drawing process. The macroscale part uses an elastic-plastic Finite Element model with an analytical constitutive law describing the yield locus. The local crystallographic texture is considered as a state variable in the FE integration points. A discrete form of the Orientation Distribution Function is used. The analytical approximation of the yield locus is constructed using multiple evaluations of a virtual experiment, conducted by means of the micromechanical polycrystalline plasticity ALAMEL model [1]. The same microscale model is utilized to predict the texture evolution in the FE integration points. The paper discusses various strategies that are applied to rebuild the approximation of the yield locus when the state variable describing the crystallographic texture has sufficiently changed. Variation of the plastic anisotropy due to different deformation path is analyzed. The influence of the deformation textures on the predictions of the planar anisotropy is evaluated.

References

[1] P. Van Houtte, S. Li, M. Seefeldt, L. Delannay, *Int. J. Plast.*, 21, 2005, 589-624

Strain gradient crystal plasticity for miniaturization and microstructures with interfaces

**M.G.D. Geers¹, I. Ertürk², P.R.M. van Beers¹, G.J. McShane²,
J.A.W. van Dommelen¹, V.G. Kouznetsova¹, V.S. Deshpande²**

¹Department of Mechanical Engineering, Eindhoven University of Technology,
P.O. Box 513, 5600 MB Eindhoven, The Netherlands

²University of Cambridge, Engineering Department, UK
e-mail: m.g.d.geers@tue.nl

The functionality of metal-based micro- and nanosystems strongly depends on the interplay between device dimensions and microstructural length scales. This critical interplay between dimensional and microstructural length scales triggers several distinct size effects, which tend to have a dominating contribution at particular component sizes. Using a simple classification of different size effects, related to different underlying physical mechanisms in the crystalline microstructure, this paper concentrates on the critical role of strain gradient enrichments in crystal plasticity.

This paper will focus on a number of important aspects of strain gradient crystal plasticity models, for which two apparently different models presented in the literature are taken as a reference:

- Thermo-dynamical aspects: Gurtin proposed a thermodynamically consistent theory of strain gradient crystal plasticity, which is well known in the literature. Interestingly, this framework is shown to be intrinsically dual to the physically based theory of Evers et al. This duality is briefly addressed, with a particular emphasis on the improved understanding gained on the role and structure of the free energy and the boundary conditions to be used.
- Physical aspects: discrete short-range interactions between dislocations have to be accounted for in the free energy. The convex and non-convex nature of the free energy is discussed for multi-slip dislocation interactions. Particular attention is given to the discrete-continuum transition, whereby the underlying discreteness of the dislocations is to be preserved properly in the continuum equivalent.
- Modelling aspects and required extensions to handle grain and phase boundaries: Standard boundary conditions and interface elements are not appropriate to handle grain boundaries. To remedy this, key aspects of an interface model are presented, which are intrinsically coupled to the underlying strain gradient plasticity framework.

Modelling the effect of the stress field of dislocations on carbon diffusion in BCC iron

Roberto Gomes de Aguiar Veiga¹, Michel Perez² and Charlotte Becquart³

¹Université de Lyon, INSA Lyon, Laboratoire MATEIS, UMR CNRS 5510, 25 Avenue Jean Capelle, F69621, Villeurbanne, France E-mail: roberto.veiga@insa-lyon.fr

²Université de Lyon, INSA Lyon, Laboratoire MATEIS, UMR CNRS 5510, 25 Avenue Jean Capelle, F69621, Villeurbanne, France

³Laboratoire de Métallurgie Physique et Génie des Matériaux (LMPGM), Ecole Nationale Supérieure de Chimie de Lille, UMR CNRS 8517, Bat. C6, F59655 Villeneuve d'Ascq Cedex, France

The effect of the stress field of dislocations on carbon diffusion in BCC iron has been investigated by means of a model that brings together continuum and atomistic scale approaches. Anisotropic elasticity theory, where the material is described as a continuum medium, has been used to introduce either an edge or a screw dislocation inside an otherwise perfect simulation box, and also to calculate interaction energies between the point defect (carbon) and the line defect far from the dislocation core. Going down to the atomic scale, in the vicinity of the dislocation core, local energy minima and saddle point energies have been obtained by molecular statics employing a recently developed embedded atom method (EAM) potential. Using information gathered from anisotropic elasticity theory and molecular statics, on-lattice AKMC simulations have been then performed for temperatures in the 300–600 K range, so as to study the behaviour of a diffusing carbon atom as it interacts with the dislocation stress field. The present model offers an atomistic view of the early stage of carbon segregation to dislocations during the static ageing process, opening a route for further investigation on the formation of carbon Cottrell atmospheres in iron.

Numerical Analysis of the Indentation Size Effect Using a Strain Gradient Crystal Plasticity Model

D. González, J. Alkorta, J.M. Martínez-Esnaola, J. Gil Sevillano

Department of Materials, CEIT and TECNUN (University of Navarra)
P. Manuel Lardizabal 15, 20018 San Sebastián, Spain
E-mail: dgonzalez@ceit.es. Phone: +34943212800. Fax: +34943213076

ABSTRACT

This work presents a finite element (FE) analysis of the indentation size effect (ISE) experimentally observed in tests performed at submicron scale. A 3D model of a conical rigid surface indenting on a Nb single crystal at different depths has been developed. The bcc Nb material has been characterized within a finite-strain framework through a crystal plasticity model incorporating strain-gradient hardening. The hardness evolution for different material orientations and different initial dislocation densities has been studied. The numerical results are compared with predictions of existing analytical models and with experimental results.

1. Introduction

From an experimental point of view, the indentation size effect (ISE) is a well-known phenomenon that becomes apparent at submicron scale with a decrease in the hardness measure as the indentation depth increases. Numerous works have reported the ISE experimentally, with different type of materials and arrangements [1-4]. The objective of this work is to study the ISE from a numerical point of view with the aid of a finite element (FE) model of an indentation experiment. A 3D model has been constructed, with a conical rigid surface with a round tip indenting on a single crystal of Nb. The bcc material has been simulated by means of a crystal plasticity model, implemented within a finite-strain framework. Of capital importance, the size effect phenomenon present in the experiments has been captured in the simulation work incorporating a strain-gradient formulation in the constitutive equations of the material model. The constitutive equations descend to the crystallographic slip nature of the plasticity event, and, under this crystallographic framework, a local density of geometrically necessary dislocations (GND) is obtained. The GND concept appears in this model closely linked with the strain gradient measure, as the works of Nye and Fleck et al. show [5,6]. The commercial FE program ABAQUS has been used in this analysis, complemented via FORTRAN user subroutines.

2. Model

The indentation process has been simulated by means of an FE model, with a rigid conical surface –with an angle of 19.7° – indenting on a semispherical volume of elasto-plastic material (see Fig. 1). The radius of the indenter tip is $0.01\ \mu\text{m}$ and its contact with the Nb material has been defined as frictionless. Three different crystallographic orientations have been studied for the Nb material, using forward the $\langle 001 \rangle$ as the reference one. For this case, a portion of 45° of the semispherical material volume has been modelled (as shown in Fig. 1). In order to study the hardness evolution with the indentation depth, eight different depth values have been considered, ranging from $0.01\ \mu\text{m}$ to $66\ \mu\text{m}$. Given the extent in the range

of study for the indentation depth magnitude, the same element size cannot be used for all these eight cases. For that reason, a unique mesh has been built, scaling its dimensions with the corresponding indentation depth of each case. The boundary conditions are illustrated in Fig. 1, with symmetry conditions in both lateral planes of the volume, and the nodes of the spherical bound with null displacements imposed. The mesh is constituted by 20000 first-order eight-noded isoparametric elements. The driven force of the simulations is the displacement of the indenter, imposed as a boundary condition. An exponential time dependence of this displacement, h , has been defined, so as to obtain an almost constant strain rate $-\dot{h}/h \cong \dot{\epsilon}_0 = 0.12 \text{ s}^{-1}$ for all the simulations of the analysis.

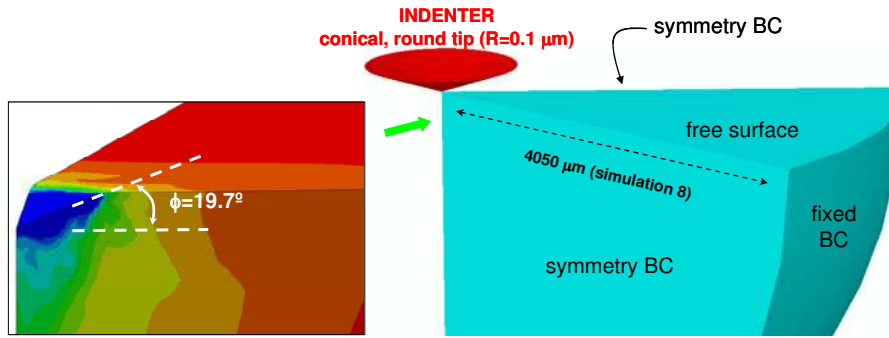


Figure 1. Boundary conditions of the indentation model.

The material constitutive model has been implemented at integration point level through a user subroutine (UEL in ABAQUS nomenclature), complemented with other home-made subroutines. A finite-strain analysis has been developed based on the Green-Lagrange strain tensor and the second Piola-Kirchhoff stress tensor. The plastic slip rates occurring in the 24 crystallographic systems considered in the modelled bcc material are assumed to depend on the resolved shear stress of each system, τ^α , by a power law [7], with a rate sensitivity of slip equal to 0.02. The reference critical resolved shear stress (CRSS), τ_0 , has been made to depend on the total dislocation density, ρ , through the uniform hardening law described in [4,8]. The resolution of the constitutive equations has been done through an implicit algorithm, resulting in a set of 6 non-linear equations, which is solved for the Piola-Kirchhoff tensor by means of a Newton-Raphson method [7]. The evolution of the SSD density (strain gradient independent) is based on a modified Kocks-Mecking kinetics, whereas the density of GND (gradient dependent) has been calculated from the gradients of slip as,

$$\rho_g = \sum_{\alpha} \rho_g^{\alpha} = \frac{1}{b} \sum_{\alpha} \left| \mathbf{n}^{\alpha} \times \nabla \gamma^{\alpha} \right| \quad (1)$$

where γ^{α} is the net amount of slip that has taken place in the α slip system, \mathbf{n}^{α} is the unit vector normal to the slip plane of this system and b is the modulus of the Burgers vector [9]. The parameters used in the constitutive equations of this material model approximately represent the room temperature behaviour of commercial purity Nb (99.8%). Elastic anisotropy has been considered in the simulations and an initial SSD dislocation density has been assumed with a value of 10^{12} m^{-2} .

3. Results

Fig. 2 collects the hardness results provided by the model for three different orientations of the indented monocrystal, namely, $\langle 001 \rangle$, $\langle 011 \rangle$ and $\langle 111 \rangle$. Two consecutive magnifications of the curves are also shown for large indentation depths –with each of the

zooms, the scale relation between axes is modified—. In all the three orientations, the same trend can be observed; the square of the hardness increases with the inverse of the depth, starting from a limiting value, obtained with large indentation depth values, when the *conventional* hardness measure is reached. This hardness growth attenuates, describing a descending trend for high values of the abscissa. In the case of the $\langle 001 \rangle$ orientation, higher hardness measures are obtained, though $\langle 011 \rangle$ orientation initially shows the same *conventional* hardness measure. Both $\langle 011 \rangle$ and $\langle 111 \rangle$ orientations present similar values.

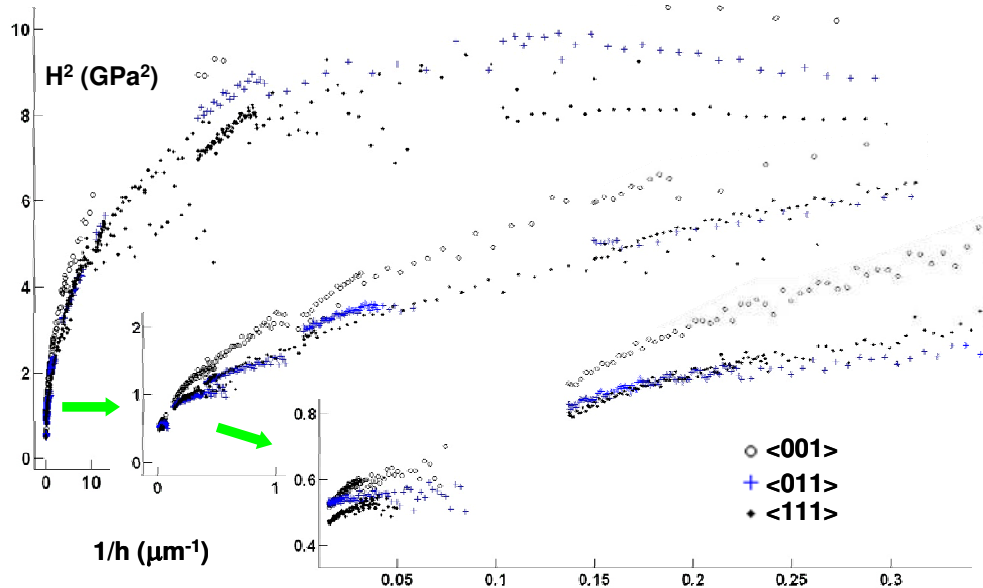


Figure 2. Square hardness vs. inverse of indentation depth for three different orientations.

Fig. 3 presents the previously shown hardness results for the $\langle 001 \rangle$ orientation, with an initial SSD density of 10^{12} m^{-2} , and those obtained with a higher initial dislocation density, equal to $5 \times 10^{14} \text{ m}^{-2}$. Obviously, hardness measure is higher in this last case for any indentation depth value. A zoom performed on this same figure shows the numerical results obtained for the reference case but without taking into account the strain-gradient effect—applied by means of Eqn. (1)—in the constitutive equations of the material model. As expected, the same hardness measure is provided by this modified model for any penetration value, which means that ISE has disappeared in this last case.

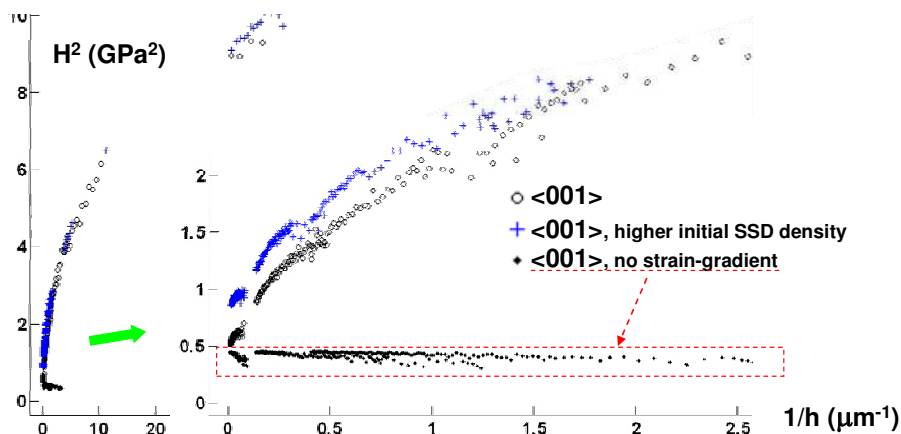


Figure 3. Square hardness vs. inverse of indentation depth for two different initial SSD densities; 10^{12} m^{-2} and $5 \times 10^{14} \text{ m}^{-2}$. The zoom also shows the results for a modification of the material constitutive model without incorporating the strain-gradient effect.

In the left part of Fig. 4 the numerical reference case is confronted with the analytical hardness equations defined by Nix and Gao [3] and Alkorta et al. [4]. The analytical model of

Alkorta et al. and the numerical results deviates from the classical Nix and Gao linear behaviour for shallow indentations –below 200 nm of penetration– due to the tip roundness of real indenters and the departure from the proportionality between the CRSS and the square root of the dislocation density, as explained in [8]. Alkorta et al.’s model describes the same curve trend that the numerical results, though a good fitting doesn’t exists between them –the analytical model is below the numerical points–. As explained by the authors in [4], their analytical model proposes an estimation of the GND density underneath the indenter tip that has to be considered as a lower bound of the real existing density, with an actual population of GND much higher than that proposed by the idealized patterned on which the analytical model is based.

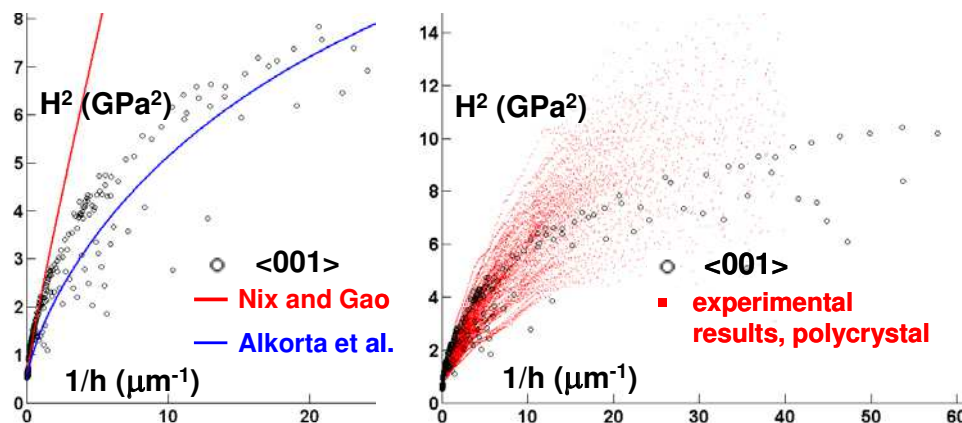


Figure 4. The numerical results are compared with two different analytical models, on the left, and with 100 experimental indentations obtained for polycrystalline Nb, on the right.

The right part of Fig. 4 compares the reference numerical results with those obtained experimentally and reported in [4] for a commercially pure polycrystalline Nb. As can be observed, the numerical curve is lying within the cloud of experimental points, where many different orientations are indented.

4. Conclusions

A finite element analysis of the ISE has been performed by means of a crystal plasticity model that incorporates strain-gradient dependent constitutive equations. The model simulates the indentation at different depths of a Nb monocrystal with a conical rounded tip. The hardness evolution for different material orientations and for different initial dislocation densities has been studied, comparing the numerical results with those predicted by the existing analytical models and with experiment measurements.

References

- [1] Stelmashenko NA, Walls MG, Brown LM, Milman YV. *Acta Metall Mater*, 1993; 41:2855.
- [2] Ma Q, Clarke DR. *J Mater Res*, 1995; 10:853.
- [3] Nix WD, Gao HJ. *J Mech and Phys Solids*, 1998; 46:411.
- [4] Alkorta J, Martínez-Esnaola JM, Gil Sevillano J. *Acta Mater*, 2006; 54:3452.
- [5] Nye JF. *Acta Met*, 1953; 1:153.
- [6] Fleck NA, Muller GM, Ashby MF, Hutchinson JW. *Acta Metall Mater*, 1994; 42:475.
- [7] Kalidindi SR, Bronkhorst CA, Anand L. *J Mech Phys Solids*, 1992; 40:537.
- [8] Foreman AJE. *Phil Mag*, 1967; 15:1011.
- [9] Acharya A, Bassani JL, Beaudoin A. *Scr Mater*, 2003; 48:167.

Simulation of diffusion processes in yttria tetragonal zirconia polycrystals

**R. L. González-Romero¹, D. Gómez-García^{1,*}, F. L. Cumbreira¹
and J. J. Meléndez²**

¹ Departamento de Física de la Materia Condensada, ICMSE, Universidad de Sevilla-CSIC, P.O. Box 1065, 41080 Sevilla (SPAIN)

* Corresponding author: dgomez@us.es

² Departamento de Física, Universidad de Extremadura, Avda. de Elvas, s/n, 06006 Badajoz (SPAIN)

Yttria tetragonal zirconia polycrystals (YTZP) are among the most prominent and potentially applicable ceramic materials. Their interest is related to the remarkable superplastic response at moderate temperatures. This superplastic response is a challenging phenomenon which still lacks from a widely-accepted explanation.

Matter diffusion along grain boundaries is a key ingredient of all models developed to account for this phenomenon. Despite its extreme importance, the mechanism for cation diffusion along grain boundaries as well the temperature and grain size dependences is far from being well-explained.

In this work, the analysis of the mechanism for cation diffusion along the grain boundaries of YTZP (including its dependence on temperature and grain size) has been studied by Molecular Dynamics (MD) simulations. It has been found that grain boundary diffusivity (especially the characteristic activation energy) depends greatly on the amount of aliovalent impurities. The implications for high-temperature plasticity are discussed in the context of recent models reported in literature [1].

References:

- [1] D. Gómez-García, E. Zapata-Solvas, A. Domínguez-Rodríguez and L. P. Kubin: "Diffusion-driven superplasticity in ceramics: Modelling and comparison with experimental data", *Physical Review B* **80** (2009), 214107.

Crystal growth and melting in NiZr alloy: bridging the gap between molecular dynamics simulations and phase-field modeling

Authors: M. Guerdane¹, F. Wendler¹, B. Nestler¹, H. Teichler²

Affiliations: ¹Institute of Materials and Processes, Karlsruhe University of Applied Sciences; ²Institute for Materials Physics, University of Göttingen, Germany

ABSTRACT

We undertake a quantitative study on the equivalence between phase-field modeling and molecular dynamics simulations with regard to describing the physics of crystallization kinetics in NiZr alloy melts out of chemical equilibrium. Such an equivalence test is important as it permits to verify whether it is legitimate to exchange physical parameters between these two fundamentally different modeling approaches when trying to bridge the gap between atomic and macroscopic scales.

Understanding the physics of solidification over lengths and times spanning from atomic scale -Å and ns- to microstructure scale - μm and seconds- represents one of the challenges of present materials sciences¹. One expects from credible multiscale models that descriptions at all scale levels be consistent with each other. The need for consistency requires a coupling between the microscopic and the macroscopic descriptions that can be achieved through transferring microscopic (atomic) key parameters into the macroscopic continuum models². Over the last decade, the phase-field (PF) method has emerged as a powerful phenomenological computational approach to model solidification processes and microstructure formation (i.e. dendritic evolution and cellular growth) on meso- and macroscopic scales³. The parameters which appear in the evolution equations cannot be derived within the framework of the PF model, therefore, they have to be imported from other considerations of those processes. Molecular dynamics (MD) simulations have advanced to an important alternative tool in providing necessary informations about these quantities. By transferring parameters from one phenomenological method (MD) to the other (PF), one assumes implicitly that both treatments are equivalent with regard to describing the same aspects of physics, regardless of their different assumptions and approximations and their different conventional length scales of optimal applicability. An explicit quantitative test of this equivalence, by comparing the predictions of both approaches for appropriate situations, has not been undertaken in the literature. In the present work, we carry out such a quantitative test by confronting results from MD simulations with predictions of PF modeling, in the case of solidification and melting of a two-phase NiZr system out of chemical equilibrium. With this equivalence test, we address at the same time two fundamental questions regarding the applicability of PF and MD approaches. The first question is whether a thermodynamic consistent PF model can be applied down to the range of atomic structure, without thermodynamic concepts losing their relevance at the atomic level. The second question is whether MD modeling is capable to treat properly relaxation dynamics driven by thermodynamics forces in a non-equilibrium state.

We perform MD simulations using an isothermal-isobaric (N, T, p) ensemble of N (up to 103693) particles. The atoms fill an orthorhombic basis cell with cyclic boundary conditions. We use pair potentials adapted to Hausleitner-Hafner potentials⁴. Further details about the method and the pair-potentials parameters are given elsewhere⁵. Preparation of the two-phase sample, $\text{Ni}_x\text{Zr}_{1-x}$ melt in contact with bcc Zr crystal (Fig. 1), is described in detail in our recent study⁶. Isothermal growth and melting dynamics are studied by considering a crystal-liquid

layered sample equilibrated at temperature T and brought into a non-equilibrium state by subjecting it to an abrupt temperature change ΔT below or above the liquidus line. This creates then an under- or supersaturated solution, respectively.

For the PF simulations, we use the thermodynamically consistent multi-phase field model given in⁷, for which many analytical and numerical methods have been developed in the past. Starting from an entropy functional, evolution equations are derived for the solute (Ni) concentration c :

$$\partial_t c = \frac{1}{T} \nabla \left(L_{11}(c, \phi) \nabla (\mu_{Ni}(c, \phi) - \mu_{Zr}(c, \phi)) \right),$$

$$\text{and for the phase field } \phi: \epsilon \tau \partial_t \phi = \frac{1}{T} \sigma \epsilon \nabla^2 \phi - \frac{1}{\epsilon} \frac{\partial w(\phi)}{\partial \phi} - \frac{1}{2T} \frac{\partial f(c, \phi)}{\partial \phi}.$$

The Onsager coefficient L_{11} is a function of the diffusion coefficients of Ni and Zr in both phases. μ_i is the chemical potential of component i , $f(c, \phi)$ is the free energy (FE) density, ϵ is related to the interface width, σ is the interface tension, $w(\phi) = \frac{9}{T} \sigma \phi^2 (1 - \phi)^2$ is an interface potential in the form of a multi-well and τ a coefficient that has to be determined for a reference system. All the PF simulations use the initial conditions as given by MD simulations. In the following we succinctly describe the PF key parameters calculated within our MD model.

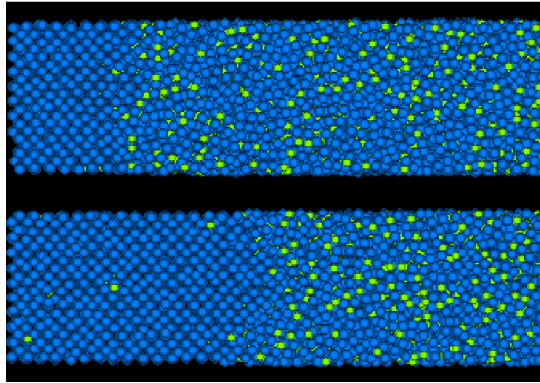


Figure 1: Top: Crystal-melt system equilibrated at $T = 1900$ K. Bottom: After cooling it down to $T = 1700$ K. Clearly visible is an expansion of the crystal, which implies an increase of the melt Ni-concentration after cooling.

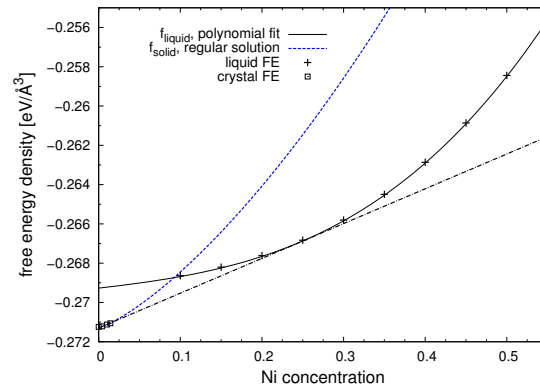


Figure 2: Interface position as a function of time during a solidification process at $T = 1700$ K, starting from a two-phase system equilibrated at $T = 1900$ K. Compared are results from MD, PF and sharp interface models.

Understanding of the crystallization process of alloy melts requires the knowledge of the chemical potentials of the involved phases, as they are the driving forces for a phase transition. This means that we need to determine the temperature and concentration dependent FE of the different phases. The crosses in Fig. 2 are FE values of Ni_xZr_{1-x} melts at $T = 1700$ K, as evaluated within the thermodynamic MD-based approach developed recently by Teichler and Küchemann⁸. The figure includes the FE of the bcc Zr crystal at very low Ni concentrations (squares).

The interface width 2ϵ is estimated by using the local order parameter Q_6 because of its high sensitivity in discriminating crystalline and liquid atomic environment. This analysis yields the interface thickness $2\epsilon \simeq 12 \text{ \AA}$. Further details can be found in our earlier work⁶. For calculating the coefficient $\tau = \frac{L_m}{\mu T_m^2}$, we use the melting temperature T_m , the latent heat L_m and the kinetic coefficient μ of the intermetallic compound $NiZr_2$. This is the binary crystalline structure with the nearest composition to the concentration range we are considering in this work and for which a steady-state kinetic coefficient can be defined. By using the free solidification and melting technique⁸, we get: $\mu = 0.082 \text{ m/sK}$, $T_m = 1610 \text{ K}$ and $L_m = 0.201 \text{ eV}$.

We determine the one-dimensional diffusion coefficients in liquid and solid by monitoring the

asymptotic limit of the mean-square displacement in x direction, as described in Ref.⁶. This calculations yield: $D_{Ni,liq} = 1.74$, $D_{Zr,liq} = 0.893$, $D_{Ni,sol} = 15.30$, $D_{Zr,sol} = 10^{-3}$ (units in 10^{-9} m²/s). Due to the fact that in the present case the growth kinetics is diffusion controlled, there is no need to accurately determine σ for $Zr_{crystal}$ - $[Ni_xZr_{1-x}]_{liquid}$ interfaces by using one of the available MD-based method. A value typical of a Zr-rich NiZr alloy would be largely sufficient. The only one known in the literature is that of pure Zr with $\sigma = 0.16$ J/m²⁹, that we use in our PF simulations. .

Fig. 3 displays the evolution in time of the front position at $T=1700$ K after undercooling the sample from $T = 1900$ K, for both modeling methods. Fig. 4 compares the corresponding Ni-concentration profiles after 20 ns of the solidification process. The agreement between MD and PF modeling (thick and thin solid line, respectively) is very satisfactory. A good matching concerns also the solute concentrations in liquid at the interfaces, $c_{l,I}^{MD} = 0.250$ and $c_{l,I}^{PF} = 0.246$, both correspond to the equilibrium concentration values of the respective modeling method at 1700 K. The slightly slower solidification rate in PF simulation may be partly explained by the small discrepancy between the equilibrium liquid concentration realized in MD simulations, $c_l^{MD}(1700\text{ K}) = 0.250$, and that following from the calculated FE, $c_l(1700\text{ K}) = 0.246$, by means of the double tangent construction. As a consequence, the concentration peak height at the interface (liquid side) during solidification -Fig. 4- is about 13% smaller in PF simulations than in MD ones. This means a smaller gradient of the chemical potential at the solidification front, and thus a slower solidification kinetics. The PF approach gives the possibility to verify this assumption, since we can 'by hand' shift the liquid FE curve vertically upwards so that the calculated equilibrium liquid concentration c_l matches with the MD one c_l^{MD} . Using the shifted liquid FE function in the PF simulation leads indeed to a better matching between PF and MD modeling, as illustrated by the dotted line in Fig. 3.

Dashed line on Fig. 3 represents the PF result of propagation dynamics of the front position for another formulation of the FE density, based on the standard ideal solution model which is often used in estimating the FE density of the liquid phase in PF modeling. This comparison is aimed at illustrating the advantage one has in using the MD-calculated FE over using FE formulations based on approximation models⁶.

We conclude that MD simulations and PF modeling give the same quantitative physical description of the solidification kinetics in a crystal-liquid structure of NiZr alloy out of chemical equilibrium. Such a comparison is rendered possible after the PF model key parameters, on which the growth kinetics depends sensitively, are calculated within the MD approach. This equivalence test is important as it provides a legitimacy to the exchange of physical parameters between both modeling approaches when trying to bridge the gap between atomistic, mesoscopic and macroscopic scales. Further studies show that this conclusion concerns the melting kinetics as well⁶. Our study provides evidence that the applicability range of the continuum PF model extends down to the atomic level, without thermodynamic concepts losing their relevance at this level. Moreover, thermodynamic and kinetic quantities -like the FE, the phase diagram, and the diffusivity- calculated for equilibrium conditions, seem to be a sufficient approximation for describing non-equilibrium situations.

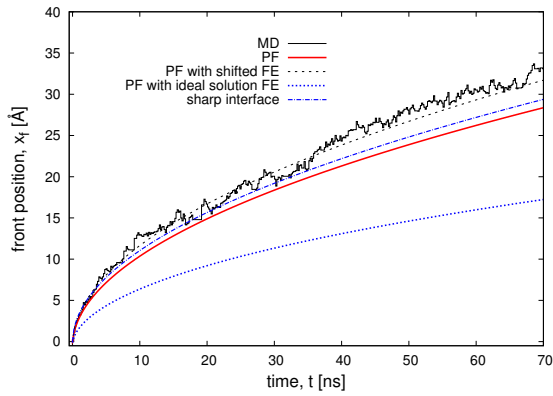


Figure 3: Interface position as a function of time during a solidification process at $T = 1700$ K, starting from a two-phase system equilibrated at $T = 1900$ K. Compared are results from MD, PF and sharp interface models.

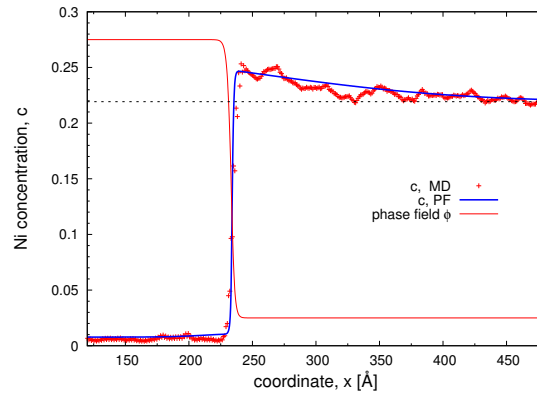


Figure 4: Ni-concentration profiles after 20 ns of a solidification process. The dashed line indicates the initial equilibrium concentration $c_i^{MD}(1900 \text{ K}) = 0.219$ from MD simulations, used as initial condition in PF simulations.

Acknowledgements

This work was supported by the German Research Foundation (DFG) under the research training group 1483.

References

- [1] J. J. de Pablo and W. A. Curtin, *MRS Bull.* **32**, 905 (2007).
- [2] A. Ramasubramaniam and E. A. Carter, *MRS Bull.* **32**, 913 (2007).
- [3] A. Karma, *Encyclopedia of Materials Science and Technology* (Elsevier, Oxford, 2001)
- [4] Ch. Hausleitner and J. Hafner, *Phys. Rev. B* **45**, 115 (1992).
- [5] M. Guerdane and H. Teichler, *Phys. Rev. B* **65**, 014203 (2001).
- [6] M. Guerdane, F. Wendler, D. Danilov, H. Teichler, and B. Nestler, *Phys. Rev. B* **81**, 224108 (2010).
- [7] H. Garcke, B. Nestler, and B. Stinner, *SIAM J. Appl. Math.* **64**, 775 (2004).
- [8] H. Teichler and M. Guerdane, in *Phase Transformations in multicomponent Melts*, edited by D. M. Herlach and R. Kirchheim (WILEY-VCH, Weinheim, 2008).
- [9] B. Vinet, L. Magnusson, H. Fredriksson, and P.J. Desre, *J. Colloid Interface Sci.* **255**, 363 (2002).

Predicting the Flow Stress Variation of 304 Stainless Steel during Hot Deformation Considering Grain Size Effect

M.H. Parsa¹, D. Ohadi²

¹Professor, School of Metallurgy and Materials engineering, University of Tehran, Iran.
PO Box 11155/4563, Tehran, Iran. E-mail: mhparsa@ut.ac.ir;

²Graduate student, School of Metallurgy and Materials engineering, University of Tehran, Iran

ABSTRACT

For the modeling of hot working operations in order to predict the resulted microstructure and mechanical properties, it is necessary to express the relationship between flow stress, temperature, strain and strain rate and microstructure evolution. In the present investigation a combined procedure has been applied for expressing hot deformation behavior. For this study AISI 304L austenitic stainless steel has been selected in which dynamic recrystallization occurs at critical deformation conditions.

1. Introduction

Many researches have been carried out to model the hot deformation of steel. Some of them are experimental [1-5] and some other are mathematical modeling [6-9]. Many different methods and theorems such as principle of irreversible thermodynamics [10], entropy principle [11], etc have been used.

Theory of invariants plays an important role in continuum mechanics. Rivlin and Ericksen (1955) [12] proposed that the stress tensor components can be expressed as polynomials in terms of components of certain kinematic tensors with invariance properties. Material symmetries impose limitations such as invariance on the constitutive relation. Complete information and details of this method can be found in references.

The aim of present research is to combine the experimental and mathematical methods to express an invariant constitutive relation between the deformation variables. Since 304L stainless steel remains single phase at high temperature ranges and there is no need to consider the second phase effect, it has been selected for the present research. Furthermore, its stacking fault energy is low, and therefore dynamic recrystallization can occur at critical conditions.

2. Procedure

In order to model hot deformation of steels, a constitutive equation based on invariant theory is proposed. This equation should include some of the most important variables affecting hot deformation of steel, such as stress, strain, strain rate, temperature and initial grain size. Considering an invariant structural form for flow equation, it has been tried to connect the flow stress to the other mentioned variables. The stress, strain and strain rate are supposed to be second order symmetric tensors, namely symmetric Cauchy stress tensor σ (nonpolar case), symmetric left stretch tensor V , and deformation rate tensor D (symmetric part of velocity gradient L). Initial grain size is introduced with as a vector which its three components λ_i -

(i=1,2,3) are the grain sizes in three perpendicular directions and it is associated with a skew symmetric matrix X by:

$$X_{ij} = \epsilon_{ijk} \lambda_k \quad (1)$$

According to principle of material objectivity or frame indifference, variables entered to the constitutive equations must be invariant under changes of reference frame. Cauchy stress σ , left stretch tensor V and deformation rate D are all objective quantities [13].

We consider form invariance under the proper orthogonal group which describes an isotropic material with no center of symmetry. Since skew symmetric tensors are associated only with axial vectors, no absolute vectors are involved and therefore there is no distinction between the proper and full orthogonal groups [12].

Flow stress is considered to be the form invariant symmetric tensor polynomial function of symmetric (left stretch tensor and rate of deformation tensor) and skew symmetric (initial grain size) tensors with flowing form:

$$P = \sum_{\alpha} I_{\alpha} (\Phi_{\alpha} + \Phi_{\alpha}^T) \quad (2)$$

where I_{α} s are polynomials in invariants belonging to an integrity basis for the tensors and vectors [12]. The invariants formed from matrices are the traces of the matrix products listed in Tab1. Φ_{α} s are the matrix products listed in Tab2 and Φ_{α}^T is the transpose of Φ_{α} .

Table 1 Matrix Products Whose Traces Form the Integrity Basis for the Proper Orthogonal Group [12]

Matrices	Matrix Products
a	a; a ² ; a ³
a, b	ab; ab ² ; ba ² ; a ² b ²
u	u ²
u, a	u ² a; u ² a ² ; u ² aua ²
u, a, b	uab; ua ² b; ub ² a; ua ² b ² ; ua ² ba; ub ² ab; ua ² b ² a; ub ² a ² b; u ² ab; u ² a ² b; u ² b ² a; u ² aub; u ² aub ² ; u ² bua ²

Table 2 Form Invariant Symmetric Tensor Polynomial Functions of Symmetric and Skew-Symmetric Tensors [12]

Matrices	Φ_{α}
	I
a	a; a ²
a, b	ab; a ² b; b ² a; a ² b ²
x	x ²
x, a	xa; xa ² ; axa ² ; x ² a; x ² a ² ; x ² ax; x ² a ² x
x, a, b	xab; bxa; xba; xa ² b; xb ² a; bxa ² ; axb ² ; xba ² ; xab ² ; axa ² b; bxb ² a; xa ² b ² ; xb ² a ² ; x ² ab; ax ² b; x ² a ² b; x ² b ² a; x ² axb u ² bua ²

Where a, b are symmetric matrices and u, x are skew symmetric matrices.

For simplification, the matrix products of degree four and more have been disregarded. So, the relevant invariant polynomial is in the form of:

$$\begin{aligned} \sigma = & I_1 I + I_2 V + I_3 V^2 + I_4 D + I_5 D^2 + I_6 (VD + DV) + I_7 (V^2 D + DV^2) + I_8 (D^2 V + VD^2) + I_9 X^2 + I_{10} (XV - VX) + \\ & I_{11} (XV^2 - V^2 X) + I_{12} (X^2 V + VX^2) + I_{13} (XD - DX) + I_{14} (XD^2 - D^2 X) + I_{15} (X^2 D + DX^2) + I_{16} (XVD - DVX) \\ & + I_{17} (DXV - VXD) + I_{18} (XDV - VDX) \end{aligned} \quad (3)$$

Considering applied stress in one dimension and spherical shape for grains (grain size is identical in every three perpendicular directions $\lambda_1 = \lambda_2 = \lambda_3 = \lambda$), equation (3) transformed into equation (4):

$$\sigma = I_2 \varepsilon + I_3 \varepsilon^2 + I_4 \varepsilon' + I_5 \varepsilon'^2 + 2I_6 \varepsilon \varepsilon' + 2I_7 \varepsilon^2 \varepsilon' + 2I_8 \varepsilon'^2 \varepsilon - 4I_{12} \lambda^2 \varepsilon - 4I_{15} \lambda^2 \varepsilon' - I_{18} \varepsilon \varepsilon' \quad (4)$$

where σ is the stress, ε is the strain, ε' is the strain rate and λ is the grain size.

3. Numerical Methods

In the first step, with the aid of reported stress-strain curves of 304L stainless steels [1-3] under different hot deformation conditions and using curve fitting methods up to peak stress, coefficients $I_2 \dots I_{18}$ have been approximated as shown in Tab3:

Table 3 Predicted Coefficients of Equation

I_2	I_3	I_4	I_5	I_6	I_7	I_8	I_{12}	I_{15}
$10^{18}/(T d \varepsilon' \varepsilon)$	$10^{19}*/(d \varepsilon'/(T \varepsilon))$	$10^{23}*/\varepsilon d \varepsilon'/T$	$10^{21}/(T d \varepsilon' \varepsilon)$	$10^{15}*/T d \varepsilon'/\varepsilon$	$10^{21}*/d \varepsilon'/(T \varepsilon)$	$10^{27}*/\varepsilon' \varepsilon/(T d)$	$10^{20}*/\varepsilon' \varepsilon/(T d)$	$10^{11}*/T d \varepsilon'/\varepsilon$

3. Results

In Fig 1 and Fig 2 the stress-strain curves derived using proposed equation have been compared with the experimental data for different deformation conditions.

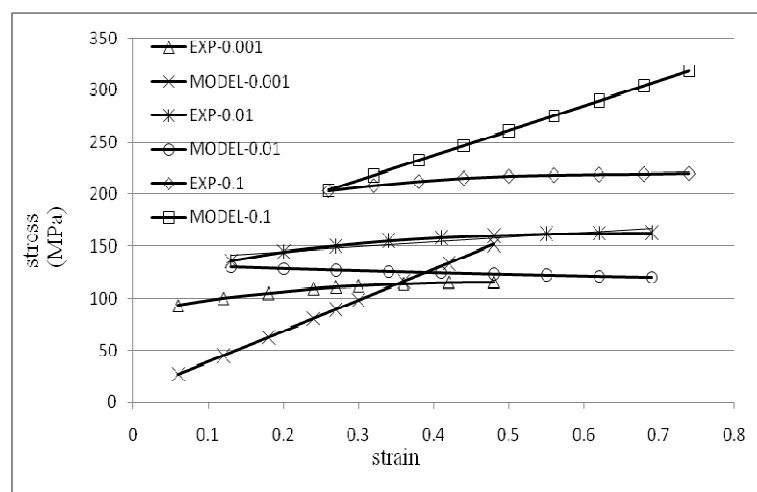


Figure 1. Stress-strain curves at 900°C and different strain rates (initial grain size=35 μ m).

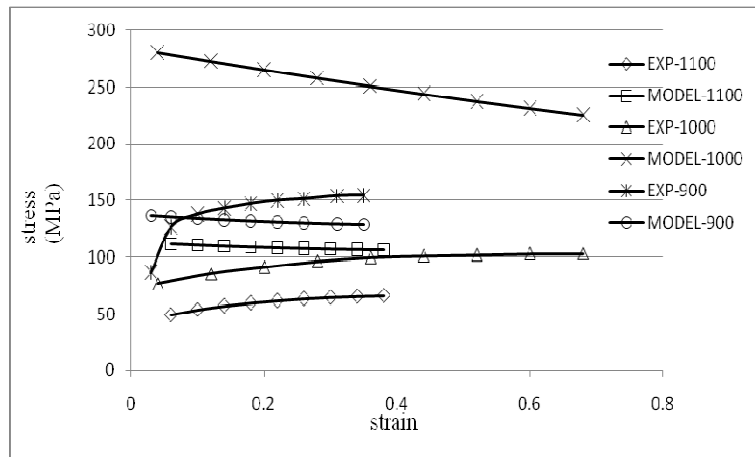


Figure 2. Stress-strain curves at $\dot{\epsilon}=0.01s^{-1}$ and different temperatures (initial grain size= $90\mu m$).

It can be concluded that there is reasonable agreement and logical relation between hot deformation variables and flow stress considering grain size effect using invariant theory. In the next step we're going to use the results for the flow stress prediction and predict the final grain size after hot deformation.

References

1. G. R. Stewart, J. J. Jonas and F. Montheillet, *ISIJ International*, 2004, Vol. 44, No. 9, 1581–1589.
2. A. Dehghan-Manshadi, M.R. Barnett, and P.D. Hodgson, *Metallurgical and Materials Transactions A*, 2008, Vol 39A, 1359.
3. A. Dehghan-Manshadi, M.R. Barnett, and P.D. Hodgson, *Materials Science and Engineering A*, 2008, Vol 485, 664–672.
4. H. Mirzadeh, A. Najafizadeh, *Materials Science and Engineering A*, 2010, Vol 527, 1160–1164.
5. H. Mirzadeh, A. Najafizadeh, *Materials Science and Engineering A*, 2010, Vol 527, 1856–1860.
6. P. Dadras, *Journal of Engineering Materials and Technology*, 1985, Vol 107, 97.
7. Abbas Najafizadeh and John J. Jonas, *ISIJ International*, 2006, Vol. 46, No. 11, 1679–1684.
8. John J. Jonas, Xavier Quelemenec, Lan Jiang, E' tienne Martin, *Acta Materialia*, 2009, Vol 57, 2748–2756.
9. H. Mirzadeh, A. Najafizadeh, *Materials and Design*, 2010, Vol 31, 1174–1179.
10. E. I. Poliak and J. J. JONAS, *Acta Mater*, 1996, Vol 44, No. 1, 127-136.
11. Heng Xiao, Otto T. Bruhns, Albert Meyers, *Journal of the Mechanics and Physics of Solids*, 2007, Vol 55, 338–365.
12. *Continuum Physics*, Edited by A. Cemal Eringen, 1971, New York, Academic Press.
13. *Continuum Theory of Plasticity*, Akhtar S. Khan and Sujian Huang, 1995, New York, Wiley.

Atomistic calculations of the elastic properties of Cu/Cu-oxide planar interfaces

Abdelmalek HALLIL¹, Jean-Marc RAULOT^{1,2}, Stéphane BERBENNI^{1,3} and Mohammed CHERKAOUI^{1,4}

¹Georgia Institute of Technology – CNRS (UMI 2958), 2 rue Marconi, 57070 Metz, France

²LETAM, CNRS FRE 3143, Université Paul Verlaine de Metz, 57045, France

³LPMM, ENSAM – CNRS FRE UMR 3236, 57078 Metz, France

⁴Georgia Institute of Technology, Atlanta Campus, GA 30332, USA

ABSTRACT

The objective of this work is to study the evolution of the interfacial excess energy as a function of tensile or/and shear stresses applied to planar interfaces in the aim of identify the interface elastic response that could be implemented into continuum interfacial fracture models. By using the semi-analytical approach, interface elastic properties, such as the intrinsic interfacial excess energy, intrinsic interfacial stress and interface elastic stiffness are given analytically in terms of the interatomic potentials of the material. These elastic tensors characterize the elastic response of a coherent interface under transverse and in-plane deformations and can be also computed by direct Molecular Dynamics (MD) simulations. To validate this methodology, an example of a coherent and homogeneous interface under normal deformation mode is considered. By using direct molecular statics simulations, the interfacial transverse strain and interfacial intrinsic free energy are computed for 2 Cu grain boundaries configurations. Then, preliminary results for a heterogeneous interface Cu/Cu₂O are also presented by mean of atomistic and *ab-initio* calculations. The computational results obtained from our simulations are in good agreement in comparison to the well-established theoretical framework in the literature.

1. Introduction

Solid interfaces play a major role in the study of physical and mechanical properties of nano-electronic devices. The mechanics of deformation at the nanoscale of such components differs substantially from the processes observed on meso-scopic level. At the atomic scale, the elastic response of an interface subjected to external mechanical loadings relies on the atomic behavior in terms of atomic structure and relaxations near the interface plane. Thus, the interfacial elastic properties such as interfacial stress, interfacial strain can be defined from the atomic displacements and the nature of interatomic forces acting between atoms.

In their recent work, Dingreville *et al* [1-3] have developed a semi-analytical method to compute the interfacial elastic properties of crystalline materials. The theoretical framework of this method consists on the derivation of the Shuttleworth equation [4] by introducing the concept of the transverse interfacial excess strain on the global formulation of the interfacial excess energy. This semi-analytical method is based on the idea of expanding the atomic energy and atomic stresses into power series as a function of the atomic displacements. A sequential coupling approach between atomistic and continuum mechanics is proposed for which the elastic properties of coherent planar interfaces are characterized by the Gibbs interfacial excess energy per unit undeformed interface area [1-3]:

$$\Gamma = \Gamma_0 + \Gamma_{\alpha\beta}^{(1)} \epsilon_{\alpha\beta}^s + \frac{1}{2} \Gamma_{\alpha\beta\kappa\lambda}^{(2)} \epsilon_{\alpha\beta}^s \epsilon_{\kappa\lambda}^s + \frac{1}{2} \Lambda_{ij}^{(2)} \sigma_i^t \sigma_j^t \quad (1)$$

where Γ_0 represents the interfacial intrinsic free energy, $\Gamma_{\alpha\beta}^{(1)}$ represents the intrinsic interfacial stress, $\Gamma_{\alpha\beta\kappa\lambda}^{(2)}$ and $\Lambda_{ij}^{(2)}$ characterize respectively the interfacial in-plane and transverse elastic behaviors. $\epsilon_{\alpha\beta}^s$ and σ_i^t are respectively the in-plane strain and the transverse stress.

In this paper, Molecular Dynamics (MD) calculations with tensile loadings are performed in order to evaluate Γ_0 and the transverse tensor $\Lambda_{ij}^{(2)}$ in the case of Cu/Cu and Cu/Cu-oxide interfaces. Once the concept is validated by comparing the predefined analytical results to the calculated values of these tensors, we will extend this method to heterogeneous systems such as Cu/Cu-oxide. This work is completed by preliminary *ab-initio* calculations in order to characterize the elastic response of such interfaces.

2. Description of the Cu/Cu grain boundaries and Cu(111)/Cu₂O(111) interface

MD simulations are designed explicitly to study the discrete atomic motions that occur within the interfaces region treated in this work. For Cu/Cu interfaces, two symmetric tilt interfaces with low-order coincident site lattice descriptions are considered: $\Sigma 5$ (310) and $\Sigma 13$ (510). The incoherent interface considered in this work is the most probable between Cu and its oxide Cu₂O [5]. These Cu grain boundaries and Cu/Cu₂O interface are represented in the fig. 1.

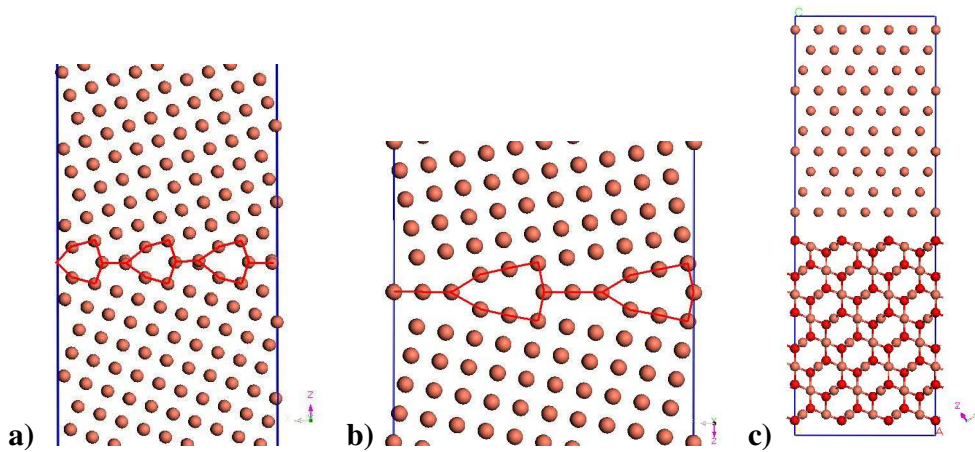


Figure 1: a) view of $\Sigma 5$ with its structural units; b) view of $\Sigma 13$ with its structural units; c) view of the Cu(111)/Cu₂O(111) interface.

Cell simulations are considered in 3 D and the periodic boundary conditions (PBC) are used in all directions (X, Y, Z). Therefore, all the cell simulations contain two similar interfaces. The calculation of the energy is based on energy minimization method. The interface configurations are constructed from relaxed bulk cell parameters. MD simulations for Cu systems are conducted by using the Cleri-Rosato EAM potential [6]. The interfacial excess energy is computed as a difference between the final simulated system ($E_{Fin}^{Cu_1+Cu_2}$) and the initial bulk configurations

$(E_{bulk}^{Cu_1} + E_{bulk}^{Cu_2})$ divided by two to account for the mirror image interface at the periodic boundary of the cell simulation. It is defined by the relation:

$$E_{int} \left[\frac{J}{m^2} \right] = \left(E_{Fin}^{Cu_1+Cu_2} - (E_{bulk}^{Cu_1} + E_{bulk}^{Cu_2}) \right) / 2A \quad (2)$$

3. Atomistic simulations results for Cu/Cu and Cu/Cu₂O interfaces

3.1 Direct Molecular Statics simulations with applied strains

In this section, MD simulations are performed to study atomistic behavior of the Cu interfaces under external loadings. The tensile stress is applied by subjecting the bi-material to uniaxial tensile deformation normal to the boundary plane. The magnitudes of the deformation to be applied on the system are defined so that each of the corresponding elastic stresses is less than the critical tensile stress required for dislocation nucleation of the <100> tilt interfaces considered in this work. In other terms, the deformation process occurs in the elastic regime. The system is held in thermodynamic equilibrium at the desired uniaxial stress.

By considering only the normal loading mode of deformation, the in-plane deformation $\epsilon_{\alpha\beta}^s = 0$ and the transverse stress can be expressed as $\sigma_j^t = \sigma_0 \delta_{3j}$. Thus, the interfacial excess energy from the equation (1) reduces to:

$$\Gamma = \Gamma_0 + \frac{1}{2} \Lambda_{ij}^{(2)} \sigma_0^2 \quad (3)$$

Molecular Statics (MS) calculations are then used to determine the minimum energy interface configurations as a function of the applied stress σ_0 for each deformation step.

3.2 Results

The calculated values of interfacial excess energy for each deformation step are plotted in the fig. 2-a. Since the deformation occurs in the elastic regime, the applied deformation ϵ_i in the X axis is expressed by its corresponding stress σ_i .

Because that we found a same behavior for both Cu grain boundaries ($\Sigma 5$ (310) and $\Sigma 13$ (510)), we reported only the results corresponding to the $\Sigma 5$ configuration. From the fig. 2-a, we observe that the interfacial excess energy exhibits a quadratic dependency with respect to the applied tensile stress. This is in good agreement with the equation (3) and the targeted tensors can be defined by fitting the different simulated points to the theoretical quadratic curve relating the interfacial excess energy to normal stresses. For the grain boundary $\Sigma 5$ (310), we obtained the *interfacial transverse strain* $\Lambda_{33}^{(2)} = 0.016 \text{ nm/GPa}$ and *interfacial intrinsic free energy* $\Gamma_0 = 0.9177 \text{ J/m}^2$ and for the $\Sigma 13$ configuration we obtained the values $\Lambda_{33}^{(2)} = 0.030 \text{ nm/GPa}$ and $\Gamma_0 = 1.023 \text{ J/m}^2$. Note that there is a discrepancy between the simulated values and those calculated analytically [2,3]. Actually this depends on the nature of the interatomic potential and its cut-off. The analytical values of these elastic tensors were determined by using the Mishin

EAM potential [7]. Also, the computation of the interfacial excess energy in this work includes the contribution of the bulk deformation energy [8]. As a result, the absolute interfacial excess energy must be computed only for atoms near the interface plane without considering the deformed bulk region. Spearot *et al* [8] showed that this correlation between the interface zone and the bulk region may cause a structural transition phenomenon in such grain boundaries systems. This concept can be explained by the presence of the constrained rigid bulk region and the releasing process related to the dissipation energy storage initially stocked at the interface region.

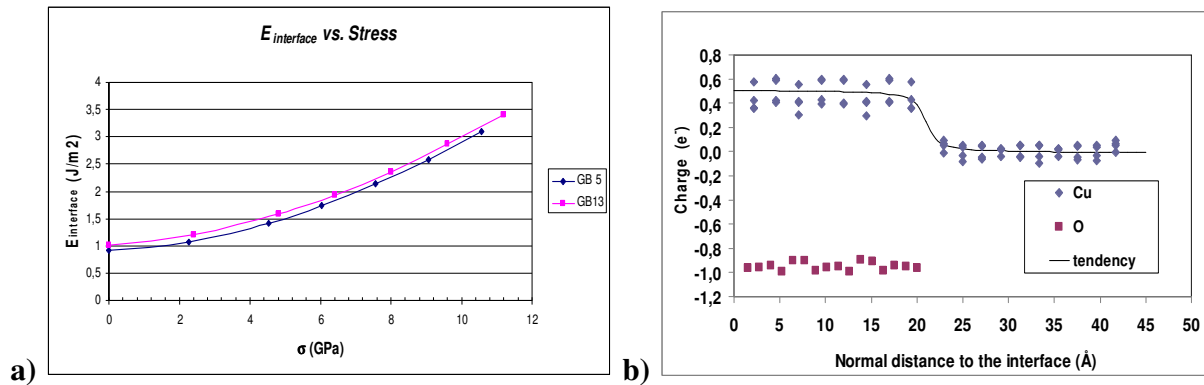


Figure 2: a) The interfacial excess energy vs. applied normal stress to the interface plane of Cu $\Sigma 5$ and $\Sigma 13$ grain boundaries; b) Charge profile on the heterogeneous Cu(111)/Cu₂O(111) interface.

The same methodology is used to study the Cu(111)/Cu₂O(111) interface by *ab-initio* calculations. Because that *ab-initio* calculations are time and CPU consuming, we present here only the preliminary results of heterogeneous Cu/Cu₂O interface. The fig. 2-b displays the charge distribution near the relaxed interface region showing that the Cu charge converge rapidly to its bulk value in the Cu₂O oxide environment $Q_{Bulk}^{Cu} = +0.546$.

4. Conclusion

Note that these results are obtained recently. This work needs more investigations in the side of atomic relaxations and the role that can play the geometry of the grain boundary structural units in coherent or incoherent interfaces.

5. References

- [1] R. Dingreville, J. Qu and M. Cherkaoui; *J. Mec. Phys. Solids*, **53** (2005) 1827
- [2] R. Dingreville and J. Qu; *J. Mec. Phys. Solids*, **56**, (2008) 1944
- [3] R. Dingreville and J. Qu; *Comp. Mat. Sci.*, **46** (2009) 83
- [4] R. Shuttleworth; *Proc. R. Soc. Lond. Ser. A* **63** (1950) 444
- [5] A. Soon, M. Todorova, B. Delley and C. Stampfl; *Phys. Rev. B* **73** (2006) 165424
- [6] F. Cleri and V. Rosato; *Phys. Rev. Lett.*, **48**, (1993) 22
- [7] Y. Mishin, M. J. Mehl, D. A. Papaconstantopoulos, A. F. Voter and J. D. Kress; *Phys. Rev. B* **63** (2001) 224106.
- [8] D. E. Spearot, L. Capolungo, J. Qu and M. Cherkaoui; *Comp. Mat. Sci.*, **42**, (2008) 57

Analytic Bond-Order Potentials for Modelling Topologically Close-Packed Phases in Transition Metals

**Thomas Hammerschmidt¹, Bernhard Seiser², Ralf Drautz¹,
and David G. Pettifor²**

¹Interdisciplinary Centre for Advanced Materials Simulation (ICAMS), Ruhr-Universität Bochum, Germany

²Department of Materials University of Oxford, United Kingdom

thomas.hammerschmidt@rub.de

ICAMS, Ruhr-Universität Bochum, Stiepler Strasse 129, 44801 Bochum

The formation of topologically close-packed (TCP) phases can significantly alter the mechanical properties of alloys and steels. Effects of TCP phase formation include precipitation hardening in steels but also degradation of creep behavior of Ni-based single-crystal superalloys. The precipitation of the TCP phases in Ni-based superalloys is attributed to refractory elements that are added in low concentration to improve creep resistance.

In this talk we present a microscopic understanding of the factors that control TCP phase stability by coarse-graining the electronic structure from density functional theory to tight-binding to bond-order potentials (BOPs). The analytic BOPs depend explicitly on the valence of the TM elements. By including up to sixth-moment terms the analytic BOP is able to reproduce the structural trend across the non-magnetic 4d and 5d TM series. We compare these results with our extensive density functional theory calculations of the TCP phases A15, C14, C15, C36, μ , σ , and χ .

Representation of Dislocation Dynamics Simulations

Craig S. Hartley¹, Jaafar A. El Awady² and Christopher Woodward³

¹ El Arroyo Enterprises, 231 Arroyo Sienna Drive, Sedona, AZ 86336-6341 USA
ElArroyo_Enterprises@msn.com

² Mechanical Eng. Dept., Johns Hopkins University, Baltimore, MD 21218 USA

³ Air Force Research Laboratory, 2230 10th Street, WPAFB, OH 45433

ABSTRACT

The dislocation content of each active slip system in a crystal is defined by its Dislocation Density Vector (DDV). Each DDV possesses signed screw and edge components having lengths equal to the length per unit volume of all dislocations of like sign lying in the slip plane, projected parallel and perpendicular, respectively, to the slip direction. The length of the DDV is proportional to the length/unit volume of dislocations of like sign and its orientation is a measure of the edge-screw character of the population. To demonstrate this representation, we analyze a simulation of a micropillar of single crystal Ni deformed in compression. Finally, we discuss possible extensions of the analysis to determine parameters characterizing the motion of the distribution.

1. Introduction

To provide input from DD simulations into crystal plasticity (CP) codes the discrete dislocation distributions produced by the former must be characterized by variables that capture the resultant length and character of the distributions on each operative slip system. Constitutive equations can then be constructed for CP codes that employ these variables in the description of deformation at larger length scales. In order to calculate the dislocation distortion and its rate associated with a DD simulation, an appropriate representation of the density of mobile dislocations on active slip systems is required. Quantities based on the edge-screw character of the population on a slip system [1] and on the rose of the direction of the dislocation structure [2] have been proposed. The dislocation density vector (DDV) description proposed by Hartley is directly related to the Nye tensor component [3] associated with dislocations on the relevant slip system. In addition, the DDV definition incorporates the concept of signed quantities [4] that represent the sense of the dislocation segments that contribute to the DDV representation. This work applies the DDV definition to the description of dislocation ensembles created by simulation of the deformation of a Ni single-crystal micro-pillar using the ParaDis DD code [5].

2. Dislocation Density Vector

The dislocation content of a volume element containing dislocations is described by the Nye tensor, $\boldsymbol{\alpha}$, giving the net Burgers vector flux, \mathbf{B} , of dislocations intersecting a section plane with \mathbf{n} as its unit outward normal: $\mathbf{B} = \boldsymbol{\alpha} \cdot \mathbf{n}$. It is convenient to define signed quantities for each slip system employing a dislocation coordinate system based on $\boldsymbol{\eta}$, a unit vector parallel to the Burgers vector, \mathbf{b} ; the normal to the slip plane, \mathbf{v} ; and the Taylor axis, $\boldsymbol{\xi}$. Define the senses of the vectors such that $\mathbf{v} = (\boldsymbol{\xi} \times \boldsymbol{\eta})$ points towards the extra half plane of a positive edge dislocation with unit tangent vector, $\mathbf{t} \parallel \boldsymbol{\xi}$. The sign associated with a pure screw dislocation is + or – according to whether \mathbf{t} is parallel or anti-parallel to $\boldsymbol{\eta}$. The unit tangent

vector of the i^{th} mixed dislocation is $\mathbf{t}^{(i)} = \boldsymbol{\eta}\cos\psi^{(i)} + \boldsymbol{\xi}\sin\psi^{(i)}$, where $\psi^{(i)}$ is the acute angle between $\mathbf{t}^{(i)}$ and $\boldsymbol{\eta}$. The contribution of this mixed dislocation to \mathbf{B} is

$$\mathbf{B}^{(i)} = (\mathbf{b} \otimes \mathbf{t}^{(i)}) \cdot \mathbf{n} = \mathbf{b} \left[(\boldsymbol{\eta} \cdot \mathbf{n}) \cos \psi^{(i)} + (\boldsymbol{\xi} \cdot \mathbf{n}) \sin \psi^{(i)} \right], \quad (1)$$

illustrating the influences of the orientation of slip system relative to the section plane and the character of the intersecting dislocation. The value of \mathbf{B} due to N dislocations crossing unit area normal to \mathbf{n} follows from summing the contribution of each:

$$\mathbf{B} = \left[\mathbf{b} \otimes \sum_{i=1}^N \mathbf{t}^{(i)} \right] \cdot \mathbf{n} = \mathbf{b} \left(\boldsymbol{\eta} \sum_{i=1}^N \cos \psi^{(i)} + \boldsymbol{\xi} \sum_{i=1}^N \sin \psi^{(i)} \right) \cdot \mathbf{n} \quad (2)$$

whence it is evident that the individual terms in the sums will have signs determined by the sense of the screw or edge components. Signed values of these sums are defined by summing separately those containing like signs. Writing $N_{S\pm}$ and $N_{E\pm}$ for the number of unit tangent vectors with positive and negative screw (S) and edge (E) segments and replacing each sum of terms with like signs by its average value gives the definition of the signed components of the dislocation density vector:

$$\boldsymbol{\rho}^{\pm S} = (N_{\pm S} \cos \bar{\psi}^{\pm S}) \boldsymbol{\eta} \quad \text{and} \quad \boldsymbol{\rho}^{\pm E} = (N_{\pm E} \sin \bar{\psi}^{\pm E}) \boldsymbol{\xi}. \quad (3)$$

The dislocation density vector components due to segments of like sign are the vector sums of the edge and screw components with like sign and their orientation is determined by the relative magnitudes:

$$|\boldsymbol{\rho}^{\pm}| = \sqrt{(|\boldsymbol{\rho}^{\pm E}|)^2 + (|\boldsymbol{\rho}^{\pm S}|)^2} \quad \text{and} \quad \bar{\Psi}^{\pm} = \tan^{-1} (|\boldsymbol{\rho}^{\pm E}| / |\boldsymbol{\rho}^{\pm S}|) \quad (4)$$

Clearly for a dislocation population with no net Burgers vector the magnitudes of the positive and negative components of the DD vector will be equal and their orientations will be anti-parallel.

To analyze the results of DD simulations to obtain the dislocation density vector associated with each active slip system, it is necessary first to identify all dislocations present with respect to their slip system and sense. The DDV in each slip system is then determined by performing counts for each slip system separately as follows. First two sets of equally spaced section planes are generated normal to $\boldsymbol{\eta}$ and $\boldsymbol{\xi}$. Since all dislocations in the slip system will lie in planes normal to \mathbf{v} , they will not intersect section planes in this orientation. The intercept densities of positive and negative dislocations with each section plane is then determined. The average positive and negative dislocation intercept density for planes normal $\boldsymbol{\eta}$ and $\boldsymbol{\xi}$, are $N_{S\pm}$ and $N_{E\pm}$, respectively. Finally, the length and orientation of the dislocation density vector for each signed set on the slip system is calculated from from equation (4).

3. Simulation Results

We now apply the DDV definition to the description of dislocation ensembles developed from the DD simulation of a Ni single-crystal tetragonal micro-pillar having dimensions $2.8 \times 2.8 \times 11.3 \mu\text{m}$ and an initial dislocation density of 10^{13}m^{-2} . The initial dislocation structure was composed of Frank-Read sources having random sizes, randomly distributed on the 12 slip systems in the simulation cell. The average dislocation segment length used in discretizing dislocation lines was $170b$. The micropillar simulations were performed under a compressive load with a constant uniaxial strain rate of 50s^{-1} along $[41\bar{3}]$. Complete description of the DD computations may be found in [6].

Calculations were performed on a snapshot of the dislocation microstructure after 16000 simulation time steps. Fig. 1 shows convergence of the computation for positive DDV

components as a function of Burgers vector magnitude, $|b|$, normalized by the spacing between the sectioning planes, h . Components of the negative DDV show similar behavior. It is clear that the positive DDV magnitudes and orientation converge quite fast as the number of sectioning planes increase. The maximum error is only about 5% when the spacing of section planes $h = 600b$, which is more than 3 times the average dislocation segment length used in the DD simulations.

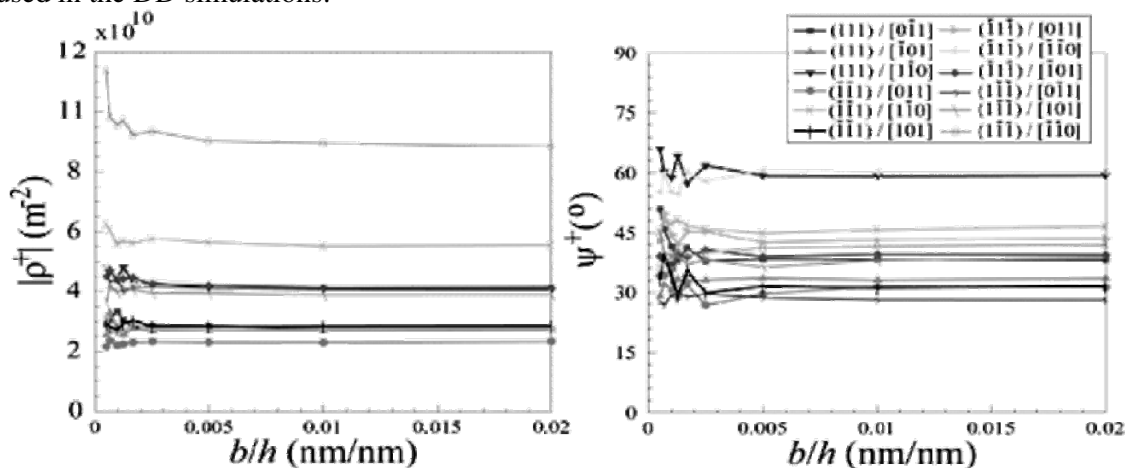


Figure 1. Convergence of the positive dislocation density vector components as a function of the Burgers vector magnitude normalized by the spacing between the sectioning planes.

Fig. 2 shows the evolution of the magnitude and orientation of the positive and negative dislocation density vectors as a function of simulation time step. These calculations employ a sectioning plane spacing of $h = 400b$, and were made on dislocation structure snapshots after 1, 100, 1000, 10000, 15000 and 16000 time steps, respectively.

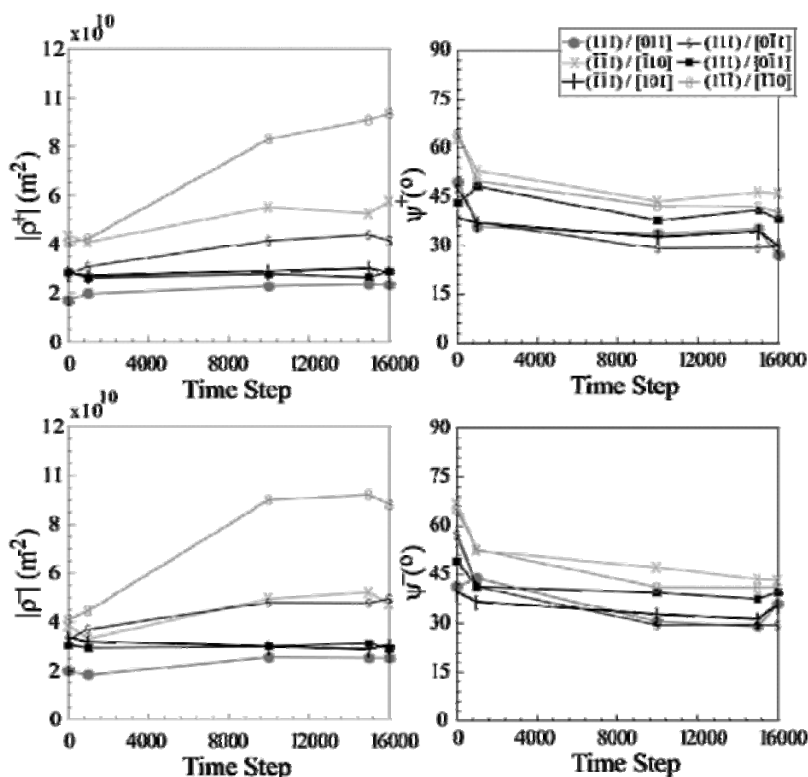


Figure 2. The evolution of the magnitude and orientation of positive and negative dislocation density vectors as a function of simulation time step.

4. Discussion and Conclusions

It should be noted that continuous fluctuations in the dislocation density are not captured in Fig. 2 since the current computations have been only computed at specific time steps. The fluctuations can be calculated if the current analysis were performed at each simulation time step. In addition, since the crystal is oriented for single slip most dislocation activities are observed on the slip plane with the highest Schmid factor, the $(\bar{1}\bar{1}1)/[\bar{1}\bar{1}0]$ slip system. This can be observed in Figure 2 from the continuous increase in the magnitude of the positive and negative dislocation densities. In addition, we can observe that the orientations of the DDVs do not change significantly with the extent of deformation in these calculations.

The DDVs calculated in this work apply to the entire dislocation content of the micro-pillar. The origin of the DDVs should be placed at the centroid of the sample. Subdividing the simulation volume into sub-regions affords the possibility of determining the variation in dislocation content throughout the specimen. In that case the DDVs calculated should be placed at the centroid of the volume from which they were obtained. Further resolution of the characteristics of the distribution can be obtained by calculating the centroid of the intersections of positive and negative dislocations with section planes and locating the associated DDVs for the volume sampled at the appropriate centroid.

The DDV provides a convenient and compact means of describing the evolution of dislocation structure in dislocation dynamics simulations. It provides information on the relative content of positive and negative segments and on the edge-screw character of the dislocation population. Experiments that follow the evolution of the DDV for various simulation conditions should be useful to provide quantitative information that can be used in constructing constitutive relations for crystal plasticity calculations based on these simulations. Experiments based on this premise are currently under way.

Acknowledgements

This work was supported by US AFOSR, and by a grant of computer time from the DOD High Performance Computing Modernization Program, at the Aeronautical Systems Center/Major Shared Resource Center. Authors CSH and JAE acknowledges support from a subcontract with Universal Technology Corporation.

References

1. Hartley, Craig S. (2003), *Phil. Mag.*, Vol. 83, pp. 3783–3808.
2. El Azab, Anter (2006), *Scripta Materialia*, Vol. 54, pp. 723–727.
3. Nye, J. F. (1953), *Acta Metallurgica*, Vol. 1, pp. 153–162.
4. Lardner, R. W. (1969), *International Journal of Engineering Science*, Vol. 7, pp. 417–425.
5. Cai, Wei and Hiratani, M. (2004) *ParaDis User Manual*. Livermore, CA : LLNL, 2004. UCRL-CODE-155933.
6. Rao, S. I., Dimiduk, D.M., Parthasarathy, T.A., Uchic, M.D., Tang, M., Woodward, C. (2008) *Acta Materialia*, Vol. 56, pp. 3245–3259.

Cr segregation at tilt grain boundaries in Fe-Cr alloys modeled at atomic scale level

Xinfu HE^{1,2}, Terentyev Dmitry² and Wen Yang¹

¹ China Institute of Atomic energy, P.O.Box:275-51, 102413, Beijing, China.
email: hexinfu@ciae.ac.cn

² SCK•CEN, Structural Materials Group, Nuclear Materials Science Institute,
B-2400, Mol, Belgium.

For a clear understanding of changes in metallurgical properties of ferritic steels due to irradiation and/or thermal annealing it is essential to know how radiation induced defects and impurities interact with grain boundaries (GBs). GBs are known to act as a sink and source of point defects, as a fast diffusion channel for interstitial impurities, as preferential sites for nucleation of secondary phase particles and as a trap for light gas atoms. Rearrangement of impurities and segregation of alloying elements, particularly P and He, is known to weaken the GB strength, thus inducing embrittlement. Radiation-induced Chromium segregation near grain boundaries is long known to cause a significant degradation in the physical, chemical and mechanical properties of austenitic stainless steels. In the case of ferritic/martensitic steels, the GB segregation of Cr is unclear and obviously depends on Cr content in the alloy, as was shown in a number of experimental studies.

In the present work, the interaction of point defects with $\langle 110 \rangle$ tilt GBs with different misorientation angles varied from 26 to 140° ($\Sigma 19(331)$, $\Sigma 9(221)$, $\Sigma 3(111)$, $\Sigma 3(112)$, $\Sigma 11(113)$, $\Sigma 9(114)$) in α -Fe have been studied using molecular static simulations. The GBs were constructed using the coincidence-site-lattice principle. The ground state structure of each GB was determined by minimizing the total energy of the simulation cell using the γ surface method, according to a set of interatomic potentials employed. The segregation energy for substitutional and interstitial Cr and He atoms at grain boundaries have been calculated in the present work. The segregation energy was found to have an oscillatory behavior away from the GB plane. Preferential sites for substitutional Cr atoms are located within a few layers of the GB region i.e. at distance of about 1.2nm away from the GB core. The most preferable site for a Cr atom at the GB is an interstitial position inside the core. Among studied GBs, interstitial Fe, Cr and He atoms are found to segregate to GBs, whose atomic structure exhibits open volumes, where the latter reside. The absolute value of the segregation energy was found to vary in the range 0.7-4 eV, 1.5-3.5 eV and 0.15-1.3 eV for Fe, Cr and He interstitial atoms, respectively, depending on the type of grain boundary considered. Therefore, a competition between these three elements during the segregation process can be expected.

Effects of Tilt Grain Boundary Property on Grain Growth using Multi-Phase-Field Model

Tomoyuki Hirouchi¹, Tomohito Tsuru² and Yoji Shibutani³,

¹JSPS Research Fellow, Graduate School of Mechanical Engineering, Osaka University, 2-1, Yamadaoka, Suita, Osaka 565-0871, Japan, hirouchi@comec.mech.eng.osaka-u.ac.jp;

²Nuclear Science and Engineering Directorate, Japan Atomic Energy Agency;

³Department of Mechanical Engineering, Osaka University.

ABSTRACT

The present paper is focused on the multi-phase-field model incorporating $\langle 110 \rangle$ tilt grain boundary (GB) properties depending on both energy by misorientation and asymmetry by inclination, which are key issues for the more practical grain growth behavior. The microstructure evolutions accompanying the grain growth in pure Al are simulated using the proposed method. The numerical results suggest that the inclination dependence lowers the effect of cusped GB energy and accelerates grain coarsening.

1. Introduction

Grain growth due to recrystallization deterministically leads the characterization of the microstructure of materials. This can be achieved by the elimination of grain boundary (GB) region and therefore it is strongly affected by GB properties [1]. To design the microstructure as required with high accuracy, the modeling based on the microstructure evolution driven by GB properties such as GB energy, mobility and asymmetry needs to be improved.

Currently, various numerical models have been developed to describe the microstructure evolution in which GB energy and mobility depend on the misorientation between neighboring grains and the inclination^[2–5], and the grain growth processes with $\langle 111 \rangle$ and $\langle 100 \rangle$ tilt GB properties obtained from molecular dynamics (MD) simulations have been performed^[4, 5]. However, for our knowledge, the microstructure evolutions accompanying the misorientation and inclination dependence of $\langle 110 \rangle$ tilt GB property which has the unique cusp in the energy map is not yet fully understood.

In this study, the multi-phase-field (MPF) model proposed by Steinbach et al. [6] is employed to represent the polycrystalline material, being combined with cusped GB energy map as a function of $\langle 110 \rangle$ tilt misorientation, which was obtained by MD simulations, and also inclination dependence^[7] for Al. Effect of inclination dependence to the grain growth behaviors is especially discussed.

2. Multi-phase-field modeling

Let us consider a polycrystalline system including N grains. The α -th grain is indicated by phase field ϕ_α , where ϕ_α takes a value of 1 (in the α -th grain), 0 (in the other grains) and $0 < \phi_\alpha < 1$ at GB region. The ϕ_α are not independent and must satisfy $\sum_{\alpha=1}^N \phi_\alpha = 1$. Here, general form of the free energy functional is described as follows:

$$F = \int_V \left[\sum_{\alpha, \beta (\alpha \neq \beta)}^N \left(-\frac{a_{\alpha\beta}^2}{2} \nabla \phi_\alpha \cdot \nabla \phi_\beta + W_{\alpha\beta} \phi_\alpha \phi_\beta \right) + \sum_{\alpha, \beta, \chi (\alpha \neq \beta \neq \chi)}^N W_{\alpha\beta\chi} \phi_\alpha \phi_\beta \phi_\chi + \sum_{\alpha, \beta, \chi, \epsilon (\alpha \neq \beta \neq \chi \neq \epsilon)}^N W_{\alpha\beta\chi\epsilon} \phi_\alpha \phi_\beta \phi_\chi \phi_\epsilon + \dots \right]. \quad (1)$$

The second term is regarded as the energy part of GB between grains α and β . The third term might be assumed as the triple junction (TJ) energies and so on [8]. In the present research, we assume that energies with more than fourth order are omitted although the third term is normally neglected. $a_{\alpha\beta}$ is the gradient coefficient and $W_{\alpha\beta}$, $W_{\alpha\beta\chi}$ are the heights of the energy barriers based on GB and TJ properties, respectively. The number of grains, N , in Eqn (1) can be replaced with $n = \sum_{\alpha=1}^N \sigma_{\alpha}$, where σ_{α} is a variable counting the local number of grains n with $\sigma_{\alpha} = 1$ for $0 < \phi_{\alpha} \leq 1$ and 0 for otherwise. The evolution equation of the phase field ϕ_i is derived as [6]

$$\frac{\partial \phi_i}{\partial t} = - \sum_{j=1}^n \frac{M_{ij}^{\phi}}{n} \left[\sum_{k=1}^n \left\{ \frac{1}{2} (a_{ik}^2 - a_{jk}^2) \nabla^2 \phi_k + (W_{ik} - W_{jk}) \phi_k + \sum_{l=1}^n (W_{ikl} - W_{jkl}) \phi_k \phi_l \right\} \right]. \quad (2)$$

Since the coefficients in Eqn (2) of a_{ij} , W_{ij} and M_{ij}^{ϕ} are related to the GB thickness δ , GB energy γ_{ij} and GB mobility M_{ij} , these can be written as follows, respectively.

$$a_{ij} = \frac{2}{\pi} \sqrt{2\delta\gamma_{ij}}, \quad W_{ij} = \frac{4\gamma_{ij}}{\delta}, \quad M_{ij}^{\phi} = \frac{\pi^2}{8\delta} M_{ij}, \quad (3)$$

where the diagonal components ($i=j$) are 0. Assuming that the TJ property is determined by the connected GBs as shown in Fig 1, the coefficient of the third term W_{ijk} is related to GB energies γ_{ij} by

$$W_{ijk} = W_{ik} \times w_0 \text{ (at } i \neq j \neq k), \quad w_0 = \left| \tanh \left(\frac{\gamma_{ik} - \bar{\gamma}}{\bar{\gamma}} \right) \right|, \quad \bar{\gamma} = \frac{2}{n(n-1)} \sum_{i,j=1(i \neq j)}^n \gamma_{ij}, \quad (4)$$

where w_0 is a weighting function proportional to the deviation from the averaged GB energy $\bar{\gamma}$. It must be set as 0 when $\gamma_{ij} + \gamma_{jk} < \gamma_{ki}$ at $n = 3$ because this inequality breaks the Young's relation of $\gamma_{ij} / \sin \theta_i = \gamma_{jk} / \sin \theta_j = \gamma_{ki} / \sin \theta_k$.

The misorientation dependences of $\langle 110 \rangle$ tilt GB energy γ_{ij} and mobility M_{ij} are shown in Fig 2(a). The energy is given by using GB energy map for Al obtained from MD simulations, and by fitting to normalized Read-Shockley (RS) relation of the first equation of Eqn (5) for low-angle range ($0^\circ < \Delta\theta < 15^\circ$, $165^\circ < \Delta\theta < 180^\circ$). The mobility is approximated as the second equation of Eqn (5) [9].

$$\gamma_{ij}(\Delta\theta_{ij}) = \gamma_m \frac{\Delta\theta_{low}}{\Delta\theta_m} \left(1 - \ln \frac{\Delta\theta_{low}}{\Delta\theta_m} \right), \quad M_{ij}(\Delta\theta_{ij}) = M_m \left[1 - \exp \left\{ -5 \left(\frac{\Delta\theta_{low}}{\Delta\theta_m} \right)^4 \right\} \right], \quad (5)$$

where $\Delta\theta_{low} = \Delta\theta_{ij}$ ($0^\circ < \Delta\theta < 15^\circ$), $180 - \Delta\theta_{ij}$ ($165^\circ < \Delta\theta < 180^\circ$), γ_m is the GB energy at $\Delta\theta = 15^\circ$, 165° , and M_m is the GB mobility at high-angle GB with misorientation greater (smaller) than $\Delta\theta_m = 15^\circ$ (165°). For computational convenience, $\gamma_{min} = 0.02 \text{ J/m}^2$ and $M_{min} = 0.05M_m$ are set. Additionally, assuming that the GB mobility is low at $\Sigma 3A$ ($\{111\}$) GB ($\Delta\theta_{\Sigma 3A} = 70.53^\circ$ i.e. coherent twin boundary) [1], the GB mobility is modeled by

$$M_{ij}(\Delta\theta_{ij}) = M_{min} + (M_m - M_{min}) \frac{\Delta\theta_w}{10} \left(1 - \ln \frac{\Delta\theta_w}{10} \right), \quad (6)$$

where $\Delta\theta_w = \Delta\theta_{\Sigma 3A} - \Delta\theta_{ij}$ ($\Delta\theta_{\Sigma 3A} - 10 < \Delta\theta < \Delta\theta_{\Sigma 3A}$), $\Delta\theta_{ij} - \Delta\theta_{\Sigma 3A}$ ($\Delta\theta_{\Sigma 3A} < \Delta\theta < \Delta\theta_{\Sigma 3A} + 10$). The above GB properties are limited in the case of symmetric tilt GBs. Thus, to extend the more general views on asymmetric tilt GBs into the MPF model, the inclination angle Φ is introduced using the local gradient of ϕ_i , ϕ_j and symmetric GB inclination angle Φ_{sym} as follows;

$$\Phi = |\Psi_{ij} - \Phi_{sym}|, \quad \Psi_{ij} = \left| \tan^{-1} \left(\frac{\partial \phi_i / \partial y - \partial \phi_j / \partial y}{\partial \phi_i / \partial x - \partial \phi_j / \partial x} \right) \right|, \quad \Phi_{sym} = \frac{\theta_i + \theta_j}{2}, \quad (7)$$

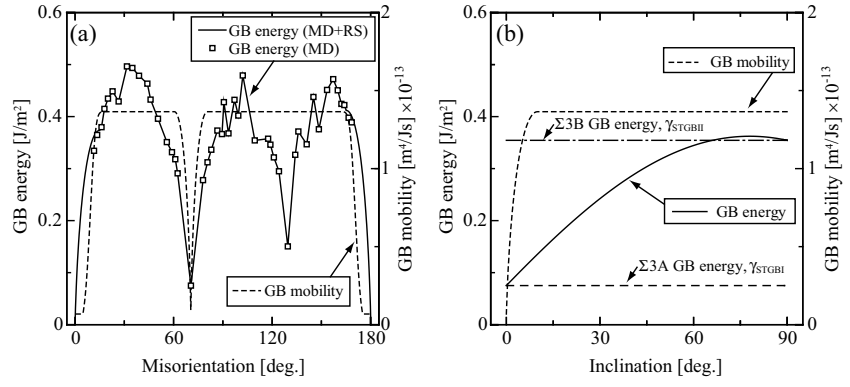
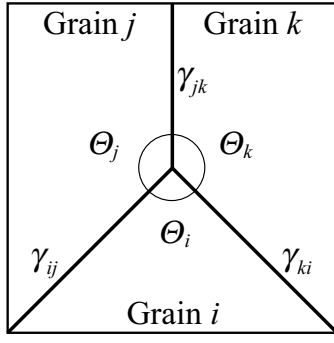


Figure 1. Relation between γ_{ij} and θ_i at TJ. Figure 2. $\langle 110 \rangle$ tilt GB energy and mobility depending on (a) misorientation and (b) inclination in the case of $\Sigma 3$ GB.

where θ_i and θ_j are the crystal orientation of grains i and j , respectively. The inclination dependences of GB energy and mobility are shown in Fig 2(b). This dependence of the energy can be written as the following Eqn (8).

$$\gamma_{ij}(\Phi) = \gamma_{STGBI} \cos(\Phi) + \gamma_{STGBII} \sin(\Phi), \quad (8)$$

where γ_{STGBI} and γ_{STGBII} are GB energies of $\Sigma 3A$ and $\Sigma 3B$ ($\{112\}$) ($\Delta\theta_{\Sigma 3B} = 109.47^\circ$, i.e. incoherent twin boundary), respectively. It is good correspondence to those of $\Sigma 3$ and $\Sigma 11$ GB energies from the MD simulation [7]. We apply this inclination dependence in the range of $\Delta\theta_{\Sigma 3A,B,\Sigma 11A,B} - 10 < \Delta\theta < \Delta\theta_{\Sigma 3A,B,\Sigma 11A,B} + 10$ ($\Sigma 11A(\{332\})$ ($\Delta\theta_{\Sigma 11A} = 50.47^\circ$), $\Sigma 11B(\{113\})$ ($\Delta\theta_{\Sigma 11B} = 129.53^\circ$)) and low-angle GB region, because low-angle GB energy is affected strongly by the inclination dependence [4]. The mobility is modeled in the range of $\Delta\theta_{\Sigma 3A,B} - 10 < \Delta\theta < \Delta\theta_{\Sigma 3A,B} + 10$ by

$$M_{ij}(\Phi) = M_{ij}(\Delta\theta_{ij}) + (M_m - M_{ij}(\Delta\theta_{ij})) \frac{\Phi_w}{10} \left(1 - \ln \frac{\Phi_w}{10} \right), \quad (9)$$

where $\Phi_w = \Phi$ ($\Delta\theta_{\Sigma 3A} - 10 < \Delta\theta < \Delta\theta_{\Sigma 3A} + 10$), $90 - \Phi$ ($\Delta\theta_{\Sigma 3B} - 10 < \Delta\theta < \Delta\theta_{\Sigma 3B} + 10$). The numerical scheme employed here is based on the algorithm proposed by Kim et al. [10] and further modified by Takaki et al. [11].

3. Numerical simulations

The grain growth simulations are performed using the randomly oriented initial microstructure in pure Al and the domain size is set as $1000\Delta x \times 1000\Delta y$. The computational and material parameters employed are finite difference grid size of $\Delta x = 0.1\mu\text{m}$, GB thickness of $\delta = 7\Delta x$, the maximum of GB mobility of $M_m = M_0 \exp(-Q_b/RT) \text{ m}^4/\text{Js}$, pre-exponential factor of $M_0 = 6.2 \times 10^{-6} \text{ m}^4/\text{Js}$, activation energy of $Q_b = 84 \text{ kJ/mol}$, temperature of $T = 573\text{K}$, R is the gas constant, and time increment adopted is $\Delta t = 0.005\text{s}$. A zero Neumann boundary condition is applied to all boundaries.

Figs 3(a) and 3(b) show the final microstructures without (Case A) and with (Case B) the inclination dependence of GB property, respectively. The microstructure in Fig 3(a) is finer and includes more GBs with large misorientation, which image is manifested by big difference of grading. Fig 4 shows the misorientation distribution at the final state. You can see the well-marked peaks at $\Delta\theta_{\Sigma 3A}$ and $\Delta\theta_{\Sigma 11B}$ in the case A, meanwhile the frequency of these GBs decreases in the case B because most of $\Sigma 3$ and $\Sigma 11$ GBs have higher energies than low-angle GBs and the energy for the whole system is decreased by an increase in the lower energy GBs during the grain growth. Alternatively, a peak at $\Delta\theta_{\Sigma 3B}$ is observed in the case B because

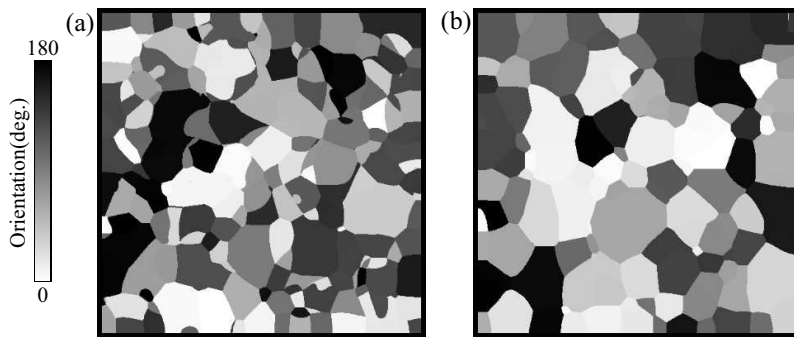


Figure 3. Microstructures after 360,000 steps (a) without and (b) with inclination dependence of GB property.

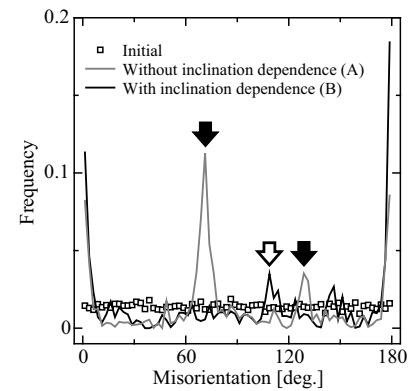


Figure 4. The effects of inclination dependence on the misorientation distribution.

$\Sigma 3B$ GB at $\bar{\phi} = 90^\circ$ completely corresponds to $\Sigma 3A$ GB at $\bar{\phi} = 0^\circ$. It can be said that these low energy Σ GBs disturb the grain growth and make the grains finer, and that the inclination dependence lowers the effect of cusps of GB energy map.

4. Conclusions

The $\langle 110 \rangle$ tilt GB energy obtained from MD simulations and GB mobility modeled, which depend on misorientation and inclination, were incorporated into the MPF model, and the grain growth processes with and without the inclination dependence were simulated. These results conclude that the inclination dependence lowers the effect of cusps of GB energy map and accelerates grain coarsening.

Acknowledgements

The author (TH) gratefully acknowledges the financial support by the Japan Society for the Promotion of Science for Young Scientists and the author (YS) does the financial support from MEXT, Japan, Grants-in-Aid for Scientific Research (S) (20226004).

References

- [1] Humphreys F.J. and Hatherly M., *Recrystallization and Related Annealing Phenomena* in 2nd edition, Elsevier, 2004.
- [2] Moelans N. et al., *Phys. Rev. B*, **78**(2), 024113(1–23), 2008.
- [3] Ivasishin O.M. et al., *Acta Mater.*, **57**(9), 2834–2844, 2009.
- [4] Kirch D.M. et al., *Acta Mater.*, **56**(18), 4998–5011, 2008.
- [5] Upmanyu M. et al., *Inter. Sci.*, **10**(2-3), 201–216, 2002.
- [6] Steinbach I. et al., *Physica D*, **134**(4), 385–393, 1999.
- [7] Tschopp M.A. et al., *Phil. Mag.*, **87**(25), 3871–3892, 2007.
- [8] Steinbach I. et al., *Physica D*, **94**(3), 135–147, 1996.
- [9] Humphreys F.J. et al., *Acta Mater.*, **45**(10), 4231–4240, 1997.
- [10] Kim S.G. et al., *Phys. Rev. E*, **74**(6), 061605(1–14), 2006.
- [11] Takaki T. et al., *Mater. Trans.*, **49**(11), 2259–2565, 2008.

Modeling of Micromechanical Deformation Systems of Magnesium based on Incremental Energy Minimization

Malek Homayonifar and Jörn Mosler

Materials Mechanics, Institute for Materials Research, GKSS Research Centre,
Max-Planck Str. 1, D-21502 Geesthacht, Germany
e-mail: malek.homayonifar@gkss.de

Magnesium and its alloys are promising materials for the transportation industries. Due to their high specific strength and their relatively low cost, they challenge aluminum alloys in automotive industries. However, they exhibit a relatively poor formability for traditional metal forming processes. This is directly related to the complex interplay between slip and twinning observed in magnesium single crystals.

In the present contribution, slip and twinning in magnesium are analyzed by means of a variational principle. The proposed method relies strongly on the variational structure of crystal plasticity theory, i.e., an incremental minimization principle can be derived in the case of a fully associative model which allows to obtain the unknown slip rates by computing the respective stationary conditions. Additionally, phase transition due to twinning is considered within the advocated model. In this approach, phase transformation occurs, if it is energetically favorable. The resulting algorithm invokes a Taylor-type phase transition which is enforced by considering a mixture energy. The model is calibrated at the scale of the magnesium single crystal and it is used to simulate a rolling process by employing the finite element method.

The results of the channel die test on magnesium single crystal are depicted in Fig. 1. The pronounced plastic anisotropy is evident. The texture evolution of a magnesium polycrystal is shown in Fig. 2. The higher density of basal poles around the center of the pole figure (Fig. 2b) is in good agreement with those observed in practice.

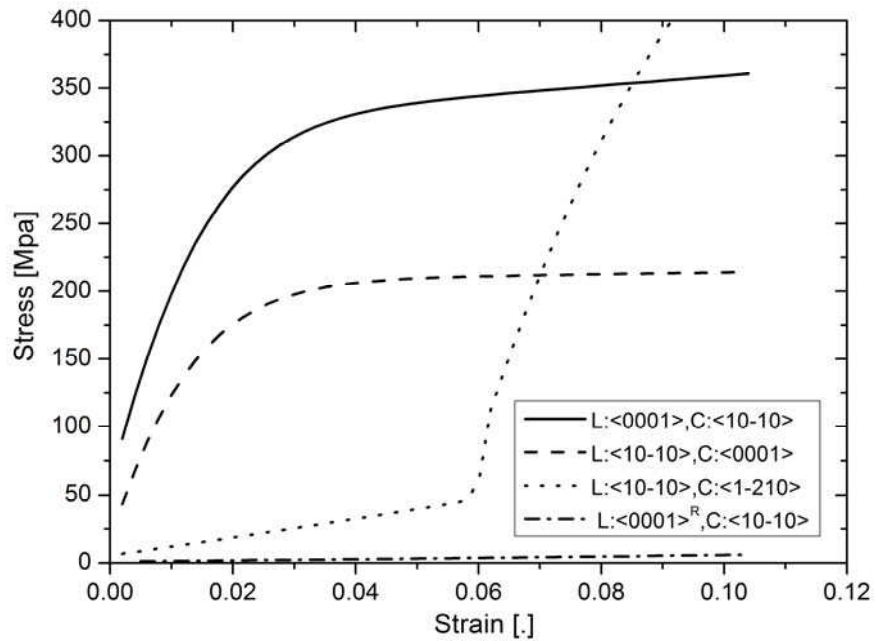


Figure 1: Numerical results of the channel die test for different orientations of magnesium single crystal, L and C indicate loading and constrained direction

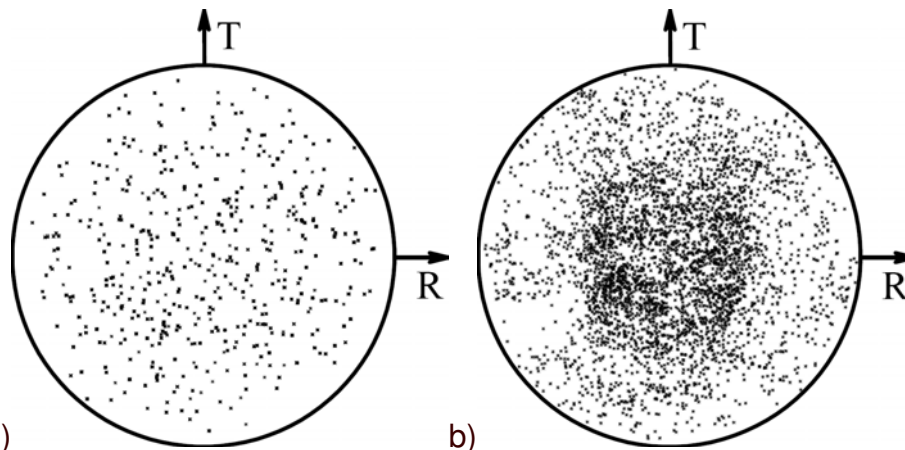


Figure 2: Simulated evolution of the basal texture in a rolling process. R and T indicate rolling and transverse direction, respectively. a) initial texture, b) texture after 0.68 compression strain (engineering)

Modeling mechanical behavior of geomaterials by the extended finite-element method

Wu Senjen¹, Naima Belayachi¹ Duc-Phi Do¹ and Dashnor Hoxha¹

¹Institut PRISME, Université d'Orléans,
Polytech'Orléans , 8 rue Léonard de Vinci, 45072 Orléans Cedex 2, FRANCE

This article aims at modeling the linear behaviour of geomaterials by a numerical homogenization method based on the extended finite element method (XFEM) (N. Moës et al. Int. J. Numer. Methodes Engrg.46 (1) 1999). Geomaterials are strongly heterogeneous materials whose behavior depends on structure, properties of constituents and geological history. We consider a particular class of geomaterials whose structures could be described as a matrix with various minerals inclusions and holes. Very often the modeling of geomaterials is performed either by an analytical approach, (sometimes through multistep homogenization procedures) or numerically, using a FEA and taking advantages of a supposed periodicity of the structure, even though this last hypothesis is rarely verified in practice. One of major obstacles in using direct numerical methods for estimation of effective properties resides in difficulties to construct a mesh able to fit to complexity of geomaterials structures which calls for considerable calculating resources. We propose to use XFEM that allows one to use meshes not necessarily matching the physical surface of the problem while retaining the accuracy of the classical finite element approach. The material interfaces in that case are represented by level set functions that are used in combination with XFEM. For validation purposes the MATLAB developed procedures are tested against results obtained by a direct Finite Element Analysis for some case-tests. As already mentioned in some previous works one has to use a sufficient fine mesh, albeit not fitting the geomaterials structure. In order to optimize the used mesh an original blending element has been used. Some comparisons of results obtained by using this method and results obtained by a direct FE analysis make on evidence the interactions between different phases and inclusions that are more or less pronounced following various patterns of constituent distributions.

The solubility of carbon in bcc iron under volumetric strain: comparison of DFT and semi-empirical methods

Dr. Elisaveta Hristova¹ (elisaveta.hristova@rub.de),

Dr. Rebecca Janisch¹, Prof. Dr. Alexander Hartmaier¹ and Prof. Dr. Ralf Drautz¹

¹ICAMS, Ruhr-Universität Bochum, Stiepelers Straße 129, 44801 Bochum, Germany

With the aim of investigating the interaction of C with dislocations in Fe by large scale molecular dynamics, we evaluate the transferability of different semi-empirical potentials. As a test case the carbon solubility in bcc Fe as a function of lattice strain is studied by ab-initio calculations based on density-functional theory (DFT) and by four different semi-empirical potentials: the embedded-atom method (EAM) potentials of Lau *et al.*^[1], Ruda *et al.*^[2] and Hepburn *et al.*^[3], and the modified embedded-atom method (MEAM) potential of Lee^[4]. DFT calculations are performed using the Vienna Ab Initio Simulation Package (VASP) and the semi-empirical static calculations using the ITAP Molecular Dynamics code (IMD). We found that in the presence of local volume expansion up to 5 % the solubility of carbon in bcc iron increases, except for the EAM potential of Hepburn. Furthermore, the excess enthalpy obtained by VASP is much more strain-sensitive than the one obtained by the semi-empirical potentials. A comparison of the applied methods reveals the trend that the semi-empirical potential results agree with the VASP results increasingly better in the sequence: EAM of Hepburn, EAM of Ruda, EAM of Lau, and MEAM. The different description of the carbon solubility in the presence of strain fields by the four semi-empirical potentials is due to different parametrization, construction and fitting of the EAM potentials, and in the case of the MEAM to the different formalism including angular dependent bonding.

[1] T.T. Lau, C.J. Först, X. Lin, J. D. Gale, S. Yip, and K.J. Van Vliet, Phys. Rev. Lett. 98, 215501 (2007).

[2] M. Ruda, D. Farkas, and G. Garcia, Comp. Mat. Sci. 45, 550 (2009).

[3] D.J. Hepburn and G.J. Ackland, Phys. Rev. B 78, 165115 (2008).

[4] B.-J. Lee, Acta Mater. 54, 701 (2006).

Modeling the evolution of subgrain structure during recovery and creep by discrete dislocation dynamics

Péter Dusán Ispánovity¹, István Groma², Maria Samaras¹ and Wolfgang Hoffelner¹

¹Paul Scherrer Institut, Villigen PSI, CH-5232, Switzerland

²Department of Materials Physics, Eötvös University Budapest, PO Box 32, H-1518 Budapest, Hungary

E-mail: peter.ispanovity@psi.ch

In a crystalline material, when it is exposed to high temperature, dislocations organize into low angle grain boundaries, that enclose cells (subgrains) with low dislocation content. It is well-known, that during recovery, i.e., when no external stress is applied, the subgrains gradually coarsen [1]. During creep such coarsening is also observed, but after a transient time a dynamic equilibrium is reached, where the subgrain size is constant – this state corresponds to the steady-state creep [2].

To study the above phenomena, we apply 2D discrete dislocation dynamics (DDD) simulations according to the following considerations:

1. In low angle grain boundaries the dislocation cores do not overlap, therefore a DDD approach is justified.
2. Since the time-scale and system size needed to study cell structure are still not available in 3D DDD simulations, one must remain in 2D.
3. Recently, with the help of a new 2D DDD method, the size of the possible dislocation ensembles has increased dramatically [3, 4].
4. Apart from the parameters determining the dynamics of the dislocation system there is no need to rely on any other input parameter such as grain boundary mobility.

In the talk we first summarize the main features of the DDD algorithm. Then we show, that the model is able to describe the main characteristics of recovery, namely, abnormal subgrain growth, power-law coarsening and the temperature dependence of the power-law exponent. In the case of creep, we find that the steady-state strain rate follows the traditional Norton's law, and the microstructure is characterized by a dynamic equilibrium. The average subgrain size (which is stress dependent) is constant. In sum, the 2D DDD model seems to be able to capture the main features of subgrain boundary motion and interaction.

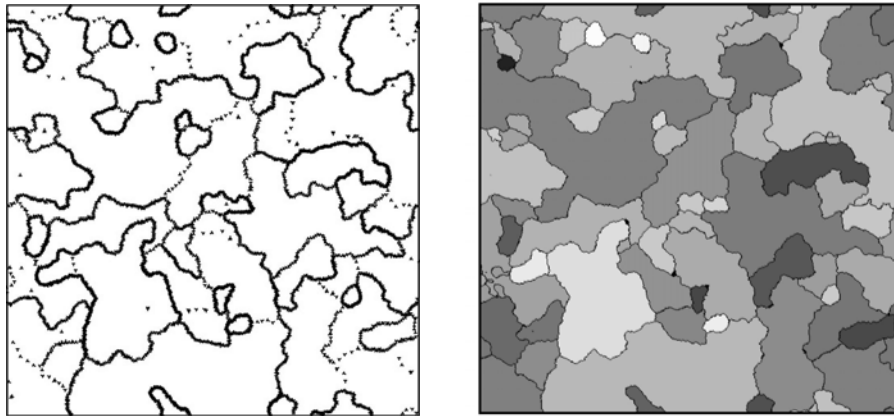


Figure 1. A dislocation configuration obtained by DDD simulations during recovery and the corresponding subgrain structure with gray level referring to the orientation.

- [1] F. J. Humphreys and M. Hatherly, *Recrystallization and Related Phenomena*. 2nd ed. Pergamon Press, Oxford, 2004.
- [2] M. E. Kassner, *Fundamentals of creep in metals and alloys*. 2nd ed. Elsevier, Amsterdam, 2009.
- [3] B. Bakó, I. Groma, G. Györgyi and G. Zimányi, Dislocation patterning: The role of climb in meso-scale simulations. *Comp. Mater. Sci.* 38, 22-28, 2006.
- [4] B. Bakó, I. Groma, G. Györgyi and G. T. Zimányi, Dislocation Glasses: Aging during Relaxation and Coarsening. *Phys. Rev. Lett.* 98, 075701, 2007.

Efficient calculation of long range magnetic interaction fields in a phase-field model for MSM alloys

Marcus Jainta^{1,2}, Frank Wendler¹, Christian Mennerich¹, and Britta Nestler¹

¹ Institute of Materials and Processes, Karlsruhe University of Applied Sciences, Germany,

² marcus.jainta@hs-karlsruhe.de

During the last years magnetic shape memory alloys (MSM) have attained interest as a new way to produce motion and force. The MSM effect takes place completely in the martensitic phase of a material and bases on the motion of low energetic twin boundaries induced by an externally applied magnetic field. The process exhibits fast response times and low energy costs in operation, and comes along with large strains (up to 10% were observed in Ni₂MnGa single crystals).

Our attempt is to model and simulate the microstructure evolution in a polycrystal composed of twin variants in an external magnetic field by using a multi-phase-field (PFM) approach combined with linear elasticity and micromagnetism. The approach adopts a PFM with order parameter of volume fractions $\phi = (\phi_\alpha(\vec{x}, t))_{\alpha=1}^N$ (N is the number of twin variants belonging to different grains with individual orientations), where every ϕ_α varies smoothly on the computation domain Ω . The constituting free energy integral formulation is of Ginzburg-Landau type, and depends also on the the displacement field \vec{u} and the spontaneous magnetisation \vec{m} :

$$\mathcal{F} = \int_{\Omega} \left[\left(\varepsilon a(\phi, \nabla \phi) + \frac{1}{\varepsilon} w(\phi) \right) + g(\phi, \vec{u}, \vec{m}) \right] dx.$$

The diffusionless phase transition of twin boundary motion is driven by the bulk free energy $g(\phi, \vec{u}, \vec{m})$, which contains, among other contributions, the demagnetisation energy (long range interaction among magnetic moments)

$$e_{\text{demag}} = -\frac{\mu_0}{2} M_S^2 (\nabla \psi \cdot \vec{m}),$$

where ψ is a scalar potential that solves $\nabla \cdot (-\nabla \psi + \vec{m}) = 0$ under certain boundary conditions on the topological boundary of Ω . The phase-field evolution for ϕ_α is derived from variational principles. For the displacement field, the complete dynamics is resolved by solving a wave equation, and for the micromagnetic evolution, the Landau-Lifshitz-Gilbert (LLG) equation is adopted.

The demagnetisation energy e_{demag} enters indirectly the evolution equations for \mathcal{F} and via the variational approach $\delta g(\phi, \vec{u}, \vec{m}) / \delta \vec{m}$ the effective field contribution in (LLG) as the demagnetisation field \vec{H}_{demag} . To cover the correct dynamics of the system, especially the evolution of twin boundaries and magnetic domain walls, it is crucial to resolve it properly. In the basic approach, the algorithm to calculate e_{demag} is computational expensive and not compatible to all optimisations used in our solver. Therefore, we present a hierarchical approach to enhance the computational efficiency in our software landscape and compare it to the intuitive solution. We also discuss the parallelised calculation using an implementation of the MPI standard.

Numerical study of convection-induced peritectic macro-segregation effect at the directional counter-gravity solidification of Ti-46Al-8Nb intermetallic alloy

A. Kartavykh¹, V. Ginkin², S. Ganina², S. Rex³, B. Schmitz⁴ and D. Voss⁵

¹Institute of Chemical Problems for Microelectronics (ICPM), B.Tolmachevsky per. 5, 119017 Moscow, Russia, karta@korolev-net.ru; ²Institute for Physics and Power Engineering (IPPE), Bondarenko sq.1, 249033 Obninsk, Russia, ginkin@ippe.ru; ³ACCESS e.V., Intzestrasse 5, 52072 Aachen, Germany, s.rex@access.rwth-aachen.de; ⁴Astrium GmbH Center Trauen (EADS Astrium), Eugen-Sänger-Str. 23, 29328 Fassberg, Germany, burkhard.schmitz@astrium.eads.net; ⁵European Space Agency (ESTEC), Keplerlaan 1, 2201 AZ Noordwijk, The Netherlands, daniela.voss@esa.int

ABSTRACT

The specific effect of centerline macro-segregation is firstly experimentally observed, analytically confirmed, numerically studied and modeled in the directionally solidified (DS) cylindrical Ti-46Al-8Nb (at%) samples. The segregation effect is explained from the positions of hydrodynamics, heat- and mass transfer of rejected Al solute in the solidifying vertical melt column. The convection-induced nature of primary segregation is demonstrated, followed by the fundamental peritectic transformation of local elongated channel-like Al-enriched area in the solid according to the phase diagram. It is shown that slightly pro-peritectic composition of the alloy is highly sensitive with this respect to the melt hydrodynamics and solidification regimes. The importance of special melt flow engineering is underlined at the industrial-scale solidification of Ti-46Al-8Nb for the manufacturing of structurally-uniform cast items.

1. Introduction

Ti-46Al-8Nb intermetallic alloy is both lightweight and creep resistant to high temperatures (~ 800°C), so being one of advanced materials for turbines of aircraft engines [1]. The conventional *Bridgman* process is predominantly applied for manufacturing of DS aero-engine blades [2], while near-net shape investment casting is one of the best processing routes for γ -TiAl based alloys. To optimize both these approaches in their conjunction, the laboratory refining of ingots growth technique was performed in multizone electro-furnace with *power-down* thermal profile operation. In this paper the problem is considered of specific macro-segregation appearance, firstly observed in some as-cast Ti-46Al-8Nb samples.

2. The Directional Solidification process arrangement

The TEM 01-3M laboratory high-temperature (up to 1700°C) gradient tube furnace is described in detail elsewhere [3] along with the technical drawing presented. Its heater consists of three in-line resistive coils; each is programmable operating. The rod-shaped sample has $\varnothing 8 \times 160$ mm dimensions where the remelting length amounts to about 50-60 mm. A heat sink plate is mounted to the cool end of the sample. The furnace was installed vertically, and DS proceeded upward. The temperature profile applied is shown in **Fig.1**. For research purposes the thermal profile had a slope continuously varying from steep to flat one along a sample that leads to joint wide-range variations of both axial thermal gradient (G_{ax}) at the growth interface, and solidification rate (V) during the DS process.

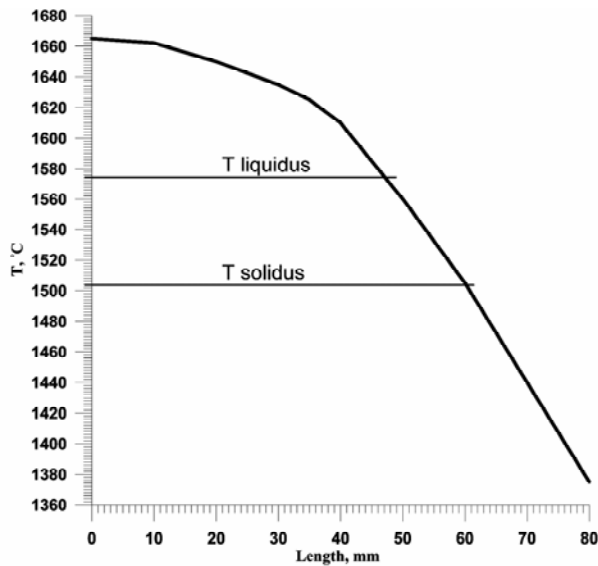


Figure 1. The steady-state thermal profile along a sample at the directional solidification beginning. Here and in the following the length axis is counted from the hottest top end side of vertically-installed sample.

Unidirectional solidification proceeded in the counter-gravity direction (upward) from the “cool” end to the “hot” one at the uniform lowering the thermal profile with the constant cooling rate (power-down rate).

3. The centreline macro-segregation pattern

The most pronounced segregation effect was revealed in the sample solidified with a cooling rate of 0.5 °C/s. The backscattered electrons (SEM-BSE) image of longitudinal section of this sample displays the channel-like area of changed microstructure being located in between 34 and 21 mm of sample’s length exactly along its geometrical axis. This area has the shape of spindle with the maximum diameter of 2 mm. The general view of segregation pattern in the transversal cross-section is shown in **Fig.2a**, where the central “spot” (2) and basic rim (1) structure differ noticeably. **Fig.2b** represents the local areas disposition of this section being subjected to EDX microanalyses whose results are given in the **Tab.1**. It is evident from the **Tab** that the sample’s core and periphery mostly show the difference in aluminium content. According to the phase diagram [4], represented in **Fig.3**, the nominal Ti-46Al-8Nb composition shows the solidification path proceeding in the close vicinity to the peritectic area, and its phase transformation sequence can be described as the complete β -solidification: $L \rightarrow L + [\beta] \rightarrow [\beta] \rightarrow [\beta + \alpha]$ (path 1). However, just ~1 at% increase of Al content (locally in the center of ingot according to EDX data) must shift the β -solidification path to the peritectic reaction $L \rightarrow L + [\beta] \rightarrow L + [\beta + \alpha]$ (path 2), once overcome the threshold composition of triple-junction point “J” in the phase diagram. Path 2 leads to the appearance of additional mechanism of α -phase formation in the solid. When directionally solidifying from the locally Al-saturated liquid, $\alpha(\text{Ti})$ is able to nucleate on the tips of β -dendrites [5], leading to the formation of primary polycrystalline grains with different symmetry and sizes compared to those formed in the neighboring ring-shaped area of β -solidification in the same cross-section. To explain the reasons and mechanism of local enrichment of the melt with Al solute ahead of the center of solidification interface (liquidus isotherm), the numerical modeling was applied.

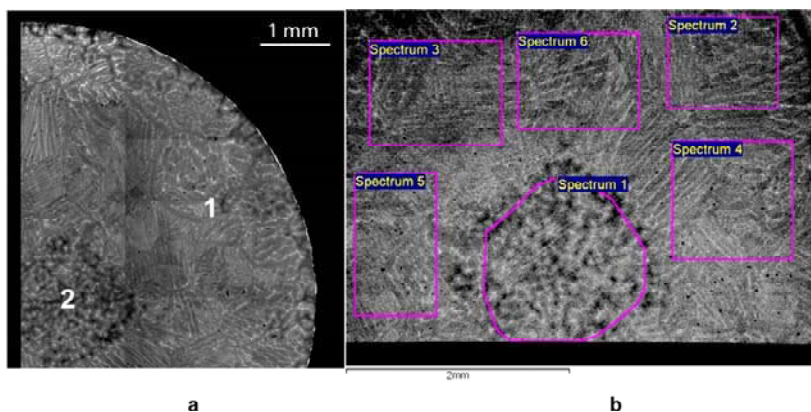


Figure 2. (a) General view of centerline macro-segregation pattern in the transversal cross-section of Ti-46Al-8Nb sample revealed by SEM-BSE mapping; (b) the local areas disposition subjected to EDX microanalyses whose results are given in the Tab.1.

Table 1. EDX microprobe analysis of chemical composition of different areas in the cross-section of a sample shown in Fig.2b.

Spectrum number	Microstructure	Chemical composition measured by EDX, at%		
		Al	Ti	Nb
1 (central spot)	$\alpha(\text{Ti})$ from peritectic reaction $L + [\beta] \rightarrow L + [\beta + \alpha]$	47.18	45.40	7.42
2	$\alpha(\text{Ti})$ from solid state $[\beta] \rightarrow [\alpha]$ transformation (<i>Widmanstätten</i> laths structure)	46.48	45.72	7.80
3		45.95	46.19	7.86
4		45.43	46.50	8.07
5		45.67	46.55	7.78
6		46.07	45.94	7.99

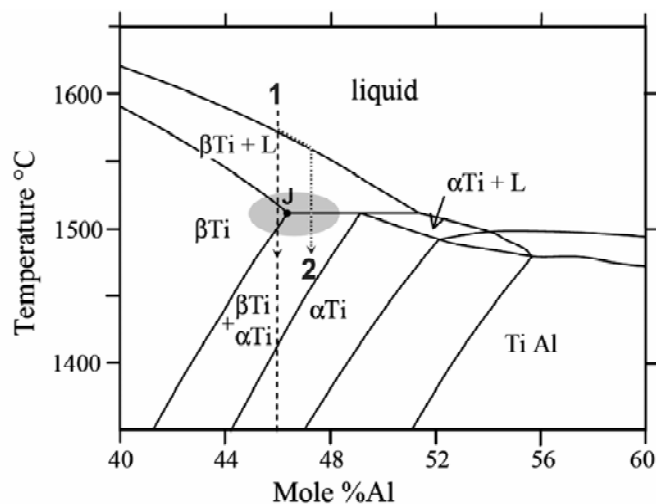


Figure 3. Isoleth Nb = 8 at% in the Ti-Al-Nb ternary system according to [4]. 1 – slightly pro-peritectic solidification path of the nominal composition Ti-46Al-8Nb (at%); 2 – peritectic solidification path of Al-enriched composition, proceeding locally in the axial part of a sample due to Al solute segregation.

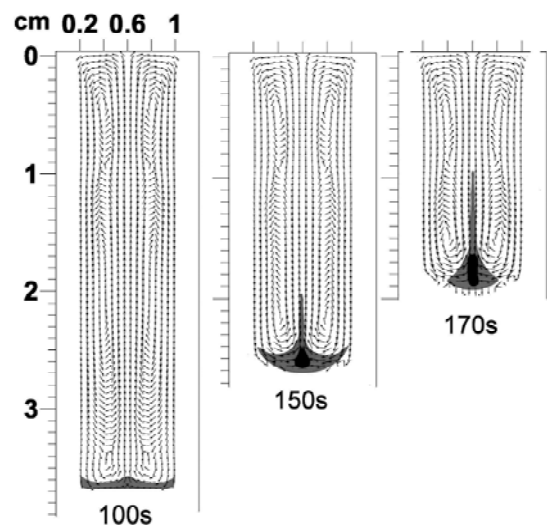


Figure 4. Distributions of hydrodynamic flow vector into the melt column for selected moments of the DS. Rejected and convectively-stratified Al-rich melt areas are superimposed where Al content amounts between 46÷47 at% (grey), and above 47 at% (black).

4. The numerical studies results and discussion

The GIGAN code developed by IPPE has been applied for a macro-scale 2D-description of the solidification process. This software package is based on numerical solution of *Navier-Stokes* hydrodynamics equations in *Boussinesq* form, and on specific algorithm of description of phase transition (*Stefan*) problem in mushy zone, taking in account the dual-phase nature of a substance, and the latent solidification heat release in this zone. The key thermo-physical properties of the alloy are known from [6]. The methods used for numerical solution of *Navier-Stokes* equations can be found in detail in [7-9]. The method applied for numerical description and solution of *Stefan* problem at the liquids interface is considered in [10].

The numerical analysis has shown that under applied “heating-from-the-top” conditions the thermo-gravitational convection (TGC) in melt is highly damped. The only driving force for TGC is the radial thermal gradient (G_R) depending in turn on the cooling rate. For the rate of 0.5 °C/s the kinetic effect of the stable negative G_R formation is characteristic when the

temperature of cooled peripheral area is lower compared to that at the axis of melt column. The distributions of hydrodynamic flow vector are given in **Fig.4** for selected moments of DS. The melt always flows downward along the crucible wall and rises upward along the centerline, forming by such the way the stable single convective cell. Meanwhile, the permanent rejection of Al solute (with segregation coefficient $k_S=0.923$) proceeds ahead of solidification interface towards the melt independently. This process becomes to be noticeable after the 100s since DS beginning, when the transient layer appears of ≈ 1 mm thickness with Al concentration ranging between 46 and 47 at%. This layer is shown superimposed in **Fig.4**. Due to the continuing DS, development of convection and concave bending of interface, the shape and structure of Al-enriched melt area transforms twofold: (i) pulls upward along the centerline by the melt flow; (ii) increases the Al concentration in the center of near-the-bottom part. This “supersaturated” bulb is shown in **Fig.4** with black, where Al content exceeds the “peritectic threshold” of 47 at%. TGC becomes most intensive in the close axial vicinity to the growth interface. The following values of the maximal flow velocity (V_F) have been calculated: $V_F = 4.0 \cdot 10^{-3}$, $6.1 \cdot 10^{-3}$ and $5.4 \cdot 10^{-3}$ cm/s at 100, 150 and 170s, respectively. The order of magnitude of *Reynolds* and *Rayleigh* numbers estimated from these flow rates suggests the weak laminar character of convection: $Re \sim 10^{-1}$ and $Ra \sim 10^2$.

For real development of the local Al-accumulating effect the coincidence of favorable conditions is necessary. These are as follows: (1) the stable negative G_R formation at the vicinity of liquidus isotherm; (2) $k_S < 1$; (3) the stable single convective cell formation; (4) the steady-state laminar character of flow into the melt column; (5) the comparable V and V_F values in their order of magnitude. The peritectically-transformed “spindle” was longitudinally formed between 130s and 170s of solidification, when V varied within the range of $(2.0 \div 4.5) \cdot 10^{-2}$ cm/s, G_{ax} dropped within the limits $17 \div 8$ °C/cm and G_R changed from (-5) to (-9) °C/cm, respectively. One can conclude that the revealed specific kind of peritectic macrosegregation is rather occasional consequence of both the alloy fundamentals, and the DS process parameters, i.e. is a furnace-sensitive event. Finally, the importance of hydrodynamic melt flow engineering is shown for the microstructurally-uniform solidification of near-the-peritectic alloy compositions. For example, the application of alternating magnetic fields could be advised at the industrial-scale casting of Ti-46Al-8Nb and related alloys [11].

Acknowledgements

The work is supported by the IMPRESS Integrated Project of FP6 (contract NMP3-CT-2004-500635); the RFBR grants 09-08-00844, 10-03-00338 and the contract 02.740.11.0505 of the Federal program “Research and scientific-pedagogical brainpower of innovated Russia”.

References

- [1] URL: http://ec.europa.eu/research/industrial_technologies/pdf/the-executive-summary-of-impres-project_en.pdf
- [2] D. Pan, Q.Y. Xu, J. Yu et al., Int. J. Cast Metals Res. 21 (2008) 308.
- [3] A. Kartavykh, S. Ganina, D. Grothe et al., Mater. Sci. Forum 649 (2010) 223.
- [4] V.T. Witusiewicz, A.A. Bondar, U. Hecht et al., J. Alloys Compd. 472 (2009) 133.
- [5] J. Eiken, M. Apel, V.T. Witusiewicz et al., J. Phys.: Condens. Matter 46 (2009) 464104.
- [6] I. Egry, R. Brooks, D. Holland-Moritz et al., Int. J. Thermophys. 28 (2007) 1026.
- [7] V. Ginkin, A. Kartavykh, M. Zabudko, J. Cryst. Growth 270 (2004) 329.
- [8] V. Ginkin, O. Naumenko, M. Zabudko et al., Numer. Heat Transfer B 47 (2005) 459.
- [9] V.P. Ginkin, J. Porous Media 8 (2005) 347.
- [10] V.P. Ginkin, S.M. Ganina, K.G. Chernov, Transport Theory Statist. Phys. 37 (2008) 412.
- [11] A. Kartavykh, V. Ginkin, S. Ganina et al., Mater. Chem. Phys. (2010) – submitted.

Microstructure formation and hysteresis in shape memory alloys

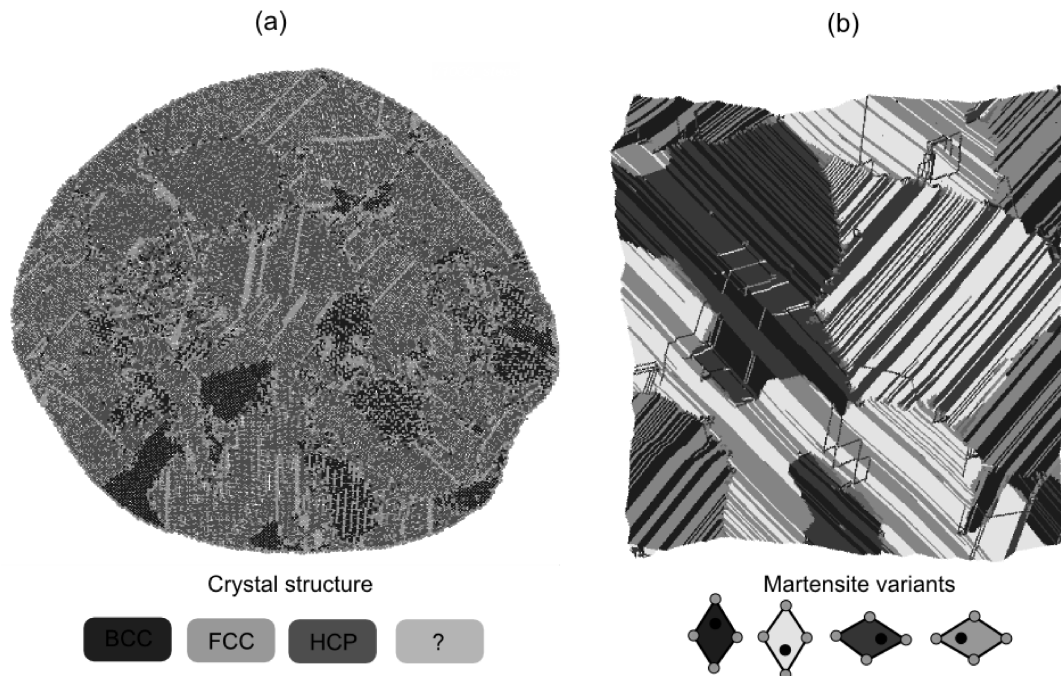
O. Kastner¹ and G.J. Ackland²

¹ Institute for Materials, Ruhr-University Bochum, Germany, oliver.kastner@rub.de

² School of Physics, University of Edinburgh, UK, g.j.ackland@ed.ac.uk

Shape memory alloys (SMA) exhibit a number of features which are not easily explained by equilibrium thermodynamics, including hysteresis in the phase transformation and "reverse" shape memory in the high symmetry phase. Processing can change these features: repeated cycling can "train" the reverse shape memory effect, while changing the amount of hysteresis and other functional properties. In the talk we present a molecular dynamics simulation study on this behaviour.

To simulate free evolutions of domain structures, atomic test assemblies must be sufficiently large and long computation times are required. Simulations of realistic 3D models therefore are limited by the computational resources available. Therefore we employ a 2D Lennard-Jones model proven to represent a reliable qualitative model system for martensite/austenite transformations. We investigate the formation of microstructure and the evolution of defect structures in simulations of cyclic transformation/reverse transformation processes with this model. The simulations show that the transformation proceeds by non-diffusive nucleation and growth processes and produces distinct microstructure, see figure. Upon transformation, lattice defects are generated, which affect subsequent transformations and vary the potential energy landscape of the sample. If the sample is cycled through a series of forward/reverse transformations, the amount of defects in each phase accumulate. Defects act as nucleation sources for the transition. Moreover, the location of the defects can be preserved through the cycling, providing a memory of previous structures.



Molecular dynamics simulations of martensitic domain structure. (a): Zirconium, 3D, 3.5 Million atoms. (b): Lennard-Jones crystal, 2D, 160,000 atoms.

Application of crystal plasticity to modeling the deformation behavior of sheet metal mesocrystals

Benjamin Klusemann¹, Bob Svendsen¹ and H. Vehoff²

¹Institute of Mechanics, TU Dortmund, Leonhard-Euler-Str. 5, 44227 Dortmund, Germany, benjamin.klusemann@tu-dortmund.de, bob.svendsen@tu-dortmund.de

²Chair of Material Science, University of Saarland, Saarbrücken, Germany, vehoff@matsci.uni-sb.de

ABSTRACT

In this work a material model formulation is presented, based on an algorithmic flow rule for small elastic strain, small time steps and plastic incompressibility based on finite kinematics. This leads to an explicit algorithm which is used for a crystal-plasticity-based model formulation for anisotropic elastic ideal viscoplastic materials. This model is applied to simulate thin sheet metal specimens with large grains subjected to tensile tests. The experimental results for a bcc Fe-3%Si sample loaded incrementally in tension are taken from [1]. The deformation of the individual grains have been measured as well as the local orientation after each loading step. These results are compared to the obtained simulation results of the deformation. Simulations are performed with crystallographic glide on either $\{110\}$ or $\{112\}$ systems or both systems simultaneously. First results showed, if no hardening is included the results are already in good agreement, which shows the importance of predicting initially active glide systems correctly.

1. Introduction

The direct dependency between microstructure and material properties and their mechanical response to a change in microstructure are basic principles in material science [2]. However, microstructures are often very complex ensembles of materials and crystallographic orientations which result in the fact that only few researchers have attempted to determine this correlation directly [3]. Therefore phenomenological models are well established and often used for simulating the plastic deformation of metals on the macroscale, meaning that the behavior is compared with, e.g., tensile test curves. To include local inhomogeneities local models are necessary for use in conjunction with homogenization techniques to describe the global behavior averaged over all inhomogeneities [4]. However, if the global results agree this will not automatically fulfill local agreement [5]. If the component size approaches microstructural length-scales such as grain size, size effects appear which influence the mechanical properties of the sample. These effects have been known for years and are still subject of active research [6, 7]. To understand and predict the behavior correctly simulation and experiment have to be compared locally. Therefore detailed experimental information of local details during plastic deformation is necessary [1]. To do a local comparison the simulation has to include the microstructural details, e.g., orientation details of a grain structure (e.g. [8]).

In this paper experimental results for a BCC Fe-3%Si sample loaded incrementally in tension are recalled from [1]. This sample is grown in such a way that throughout the sample there is only one grain over the thickness in which the grain boundaries are perpendicular to the sample surface. The deformation of the individual grains has been measured, as well as the local orientation after each loading step. In [9] a software package has been developed to automatically construct finite- element meshes directly from different measuring devices,

which is used to construct a FE mesh from the investigated sample. In the simulation a crystal plasticity model is used based on an algorithmic flow rule for small elastic strain, small time steps and plastic incompressibility formulated with finite kinematics.

2. Model formulation

In the current work, a material model is formulated in the context of continuum thermodynamics. In this context, the material behavior is related to energetic and dissipative processes, however, the formulation is isothermal. As usual, the energetic part is determined by the free energy density ψ . For the case of anisotropic metals with ideal viscoplastic behavior, the form $\psi(\mathbf{F}, \mathbf{F}_P) = \psi_E(\mathbf{F}, \mathbf{F}_P)$ holds for ψ . The inelastic deformation \mathbf{F}_P is assumed to be activated by the set (γ_1, \dots) of accumulated glide-system shears.

In this work, \mathbf{F}_P is modeled as a change of local reference configuration [10]. In this case, the (local) intermediate configuration represents the preferred constitutive reference configuration. In the context of "small" elastic strain relevant to metals, and isothermal conditions, ψ_E takes the form

$$\psi_E(\mathbf{F}, \mathbf{F}_P) \approx \frac{1}{2} \mathbf{E}_E \cdot C_{E0} \mathbf{E}_E \quad (1)$$

with $C_{E0} := C_E(\mathbf{0})$ the elastic stiffness, at constant deformation. Again in the context of small elastic strain, the approximation $\mathbf{M} \approx \mathbf{S}_E$, i.e., of the Mandel stress by the elastic second Piola-Kirchhoff stress is valid.

As usual, the glide system is represented by the corresponding glide direction, glide-plane normal \mathbf{n}_a , and direction transverse $\mathbf{t}_a := \mathbf{n}_a \times \mathbf{s}_a$ to \mathbf{s}_a in the glide plane. As usual, $(\mathbf{s}_a, \mathbf{t}_a, \mathbf{n}_a)$ represent an orthonormal system and are assumed constant with respect to the local intermediate configuration as determined by \mathbf{F}_P . In addition, they determine its evolution the constitutive form

$$\mathbf{L}_P = \sum_{a=1}^a \dot{\gamma}_a \mathbf{s}_a \otimes \mathbf{n}_a \quad (2)$$

for \mathbf{L}_P in terms of the active glide-system shears $\gamma_1, \gamma_2, \dots, \gamma_a$, with $a \leq g$ the number of active systems, and g the total number of systems. From this, we obtain in particular the form

$$-\partial_{\mathbf{F}_P} \psi \cdot \dot{\mathbf{F}}_P = \mathbf{M} \cdot \mathbf{L}_P = \sum_a \tau_a \dot{\gamma}_a \quad (3)$$

for the inelastic stress power in terms of the Schmid stress

$$\tau_a := \mathbf{s}_a \cdot \mathbf{M} \mathbf{n}_a. \quad (4)$$

The model formulation is then completed by the activation form

$$\chi = \sigma_A \sum_a \dot{\gamma}_a + \sigma_D \dot{\alpha}_r \sum_a \left\{ \left(1 + \frac{\dot{\gamma}_a}{\dot{\alpha}_r} \right) \ln \left(1 + \frac{\dot{\gamma}_a}{\dot{\alpha}_r} \right) - \frac{\dot{\gamma}_a}{\dot{\alpha}_r} \right\} \quad (5)$$

for the dissipation potential and corresponding flow potential

$$\phi(\varsigma) = \sigma_D \dot{\alpha}_r \sum_a \left\{ \exp \left(\frac{\varsigma_a - \sigma_A}{\sigma_D} \right) - \frac{\varsigma_a - \sigma_A}{\sigma_D} \right\} \quad (6)$$

In particular, this potential determines the flow rule $\dot{\gamma}_P = \partial_{\varsigma_P - \sigma_A} \phi_P$. Here, σ_A represents the activation stress for dislocation glide, σ_D the resistance stress to dislocation motion, and $\dot{\alpha}_r$ a characteristic strain-rate associated with dislocation motion.

Consider next the algorithmic formulation of the crystal plasticity material model for the time interval $[t_n, t_{n+1}]$ of duration $t_{n+1,n} := t_{n+1} - t_n$. In this case, the external variables \mathbf{F}_n and \mathbf{F}_{n+1} are known. Then the relative deformation gradient $\mathbf{F}_{n+1,n}$ is also known. Further, \mathbf{F}_{En} , $\dot{\alpha}_{rn}$, σ_{An} , and σ_{Dn} , as well as γ_n and τ_n , are known from the previous update. Consider first

the explicit formulation as based on forward-Euler integration of (6). In this case, the update of the inelastic state variables is based on that

$$\gamma_{an+1,n} = \begin{cases} 0 & \sigma_{an} \leq 0 \\ t_{n+1,n} \dot{\alpha}_{rn} \left\{ \exp\left(\frac{\sigma_{an}}{\sigma_{Dn}}\right) - 1 \right\} & \sigma_{an} > 0 \end{cases} \quad (7)$$

for the glide-system shears obtained from forward-Euler integration in terms of the activation stress $\sigma_a := |\tau_a| - \sigma_A$ for dislocation glide. Table 1 gives the corresponding material properties necessary for the model

Table 1 Used material properties for Fe-3%Si in the simulation

$C_{E,11}$ [GPa]	$C_{E,12}$ [GPa]	$C_{E,44}$ [GPa]	σ_A [MPa]	$\dot{\alpha}_r$ [s^{-1}]	σ_D [MPa]
222	135	120	220	0.001	20

3. Results

Figure 1 shows the observed experimental deformation compared with the deformation of the grains in the simulation. The presented experimental results also show the orientation gradient, however, the focus here is on the shape changes of the sample. For details concerning the orientation gradient see [1].

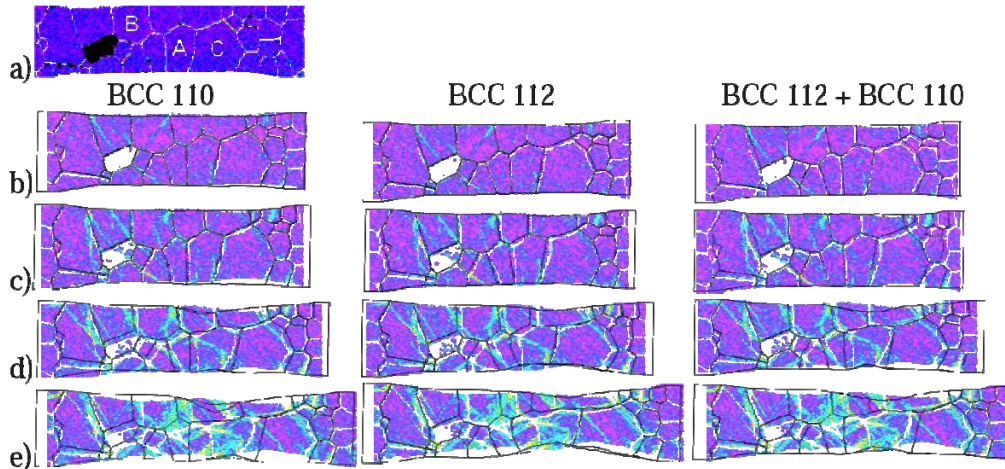


Figure 1. a) Initial experimental observed orientation gradient. b)-e) Comparison between observed experimental deformation (background) [10] for $\alpha_p \approx \{0\%, 1.5\%, 4\%, 10\%, 19.5\%\}$ to simulation results for different active glide system classes ($\{110\}$ (left), $\{112\}$ (middle), $\{110\} + \{112\}$ (right))

In the experiment strong necking is visible inside grain C and near grain A whereas these grains undergo also a strong extension. Until $\alpha_p \approx 20\%$ no clear shear band is visible which appeared during the further deformation and finally lead to the failure of the sample.

Simulations for the case of active $\{112\}$ glide system class shows a higher contraction than for simulations with active $\{110\}$ glide system class. In particular the deformation in grain C indicates that a deformation by active $\{112\}$ glide systems occurs in the mesocrystal. The simulation with active $\{110\}$ glide system class shows a very high elongation of grain A compared to experiment. The results for a simulation with $\{110\}$ and $\{112\}$ simultaneously active glide system classes show a slight dominance of the $\{110\}$ glide system class. However, the results for both systems active differ significantly from the results for one single glide system class, i.e., for the deformation behavior of the grain above grain A.

Concluding it can be obtained that the results with either glide system class show a slight deviation in the deformation structure, however the main deformation zones are depicted correctly. The simulation results with both glide system classes active simultaneously show that both classes are active at the same level of deformation with a slight dominating effect of the $\{110\}$ system. Therefore it is concluded that both classes are necessary to simulate the experimental tensile and to get sensible results.

First results including hardening on the different glide planes show a further improvement of reproducing the experimental behavior.

4. Conclusion

A crystal-plasticity-based model formulation for anisotropic elastic ideal viscoplastic materials on the basis of an algorithmic flow rule for small elastic strain, small time steps and plastic incompressibility based on finite kinematics is presented. This material model is used for the FE representation of the sample of a thin sheet metal specimen with large grains. The experimental results of the tensile test obtained in [1] are recalled and compared to the simulation results. The simulations were carried out for two sets of glide system classes separately, as well as simultaneously active, namely $\{110\}\langle 111 \rangle$ and $\{112\}\langle 111 \rangle$. The results show a slight deviation however, the main deformation zones were predicted correctly which shows the importance of determining the active glide systems at the beginning of the deformation correctly. In future work the model formulation introduced will be extended with hardening formulations to investigate the local hardening behavior of the different grains which will lead to more accuracy in the results

Acknowledgements

Partial financial support for this work, provided by the German Science Foundation (DFG) under contract Sv 8/8-1 is greatly acknowledged.

References

- [1] M. Henning and H. Vehoff. Local mechanical behavior and slip band formation within grains of thin sheets. *Acta Materialia*, 53(5):1285–1292, 2005
- [2] Groeber, M., Gosh, S., Uchic, M. D., Dimiduk, D. M., 2007. Developing a robust 3-D characterization-representation framework for modeling polycrystalline materials. *JOM Journal of the Minerals, Metals and Materials Society* 59 (9), 32–367
- [3] Langer, S. A., Fuller, E. R., Carter, W. C., 2001. OOF: an image-based Finite-Element analysis of material microstructures. *Computing in Science and Engineering* 3 (3), 1523.
- [4] Pierard, O., LLorca, J., Segurado, J., Doghri, I., Jun. 2007. Micromechanics of particle-reinforced elasto-viscoplastic composites: Finite element simulations versus affine homogenization. *International Journal of Plasticity* 23 (6), 1041–1060.
- [5] Kalidindi, S., Bhattacharyya, A., Doherty, R., 2003. How do polycrystalline materials deform plastically? *Advanced Materials* 15 (16), 1345–1348
- [6] Fu, H. H., Benson, D. J., Meyers, M. A., Aug. 2001. Analytical and computational description of effect of grain size on yield stress of metals. *Acta Materialia* 49 (13), 2567–2582
- [7] Fülöp, T., Brekelmans, W., Geers, M., May 2006. Size effects from grain statistics in ultra-thin metal sheets. *Journal of Materials Processing Technology* 174 (1-3), 233–2
- [8] Raabe, D., Sachtler, M., Zhao, Z., Roters, F., Zaefferer, S., Oct. 2001. Micromechanical and macromechanical effects in grain scale polycrystal plasticity experimentation and simulation. *Acta Materialia* 49 (17), 3433–3441
- [9] Henning, M., 2007. Größeneffekte auf die mechanischen eigenschaften -experiment und simulation. Ph.D. thesis, Saarland University
- [10] Svendsen, B., 2001. On the modelling of anisotropic elastic and inelastic material behaviour at large deformation. *International Journal of Solids and Structures* 38 (52), 9579–9599.

Signed dislocation densities and their spatial gradients as basis for a non-local crystal plasticity model

C. Kords, P. Eisenlohr, F. Roters

Max-Planck-Institut für Eisenforschung
Max-Planck-Straße 1, 40237 Düsseldorf, Germany
c.kords@mpie.de

A continuum dislocation density-based model for crystal plasticity is proposed, which accounts for both evolution in time and gradients in space. The dislocation structure is simplified as rectangular loops, i.e. signed dislocation densities of edge and screw character on each slip system. This allows to distinguish between the total amount of dislocations and the excess of one sign, i.e. the amount of geometrically necessary dislocations. The density evolution results from local dislocation reactions and the flux divergence. Dislocation reactions are described by rate equations and comprise the generation and annihilation of dislocation density as well as the transformation between dislocations in single and dipole configuration. The net flux of dislocations depends on the spatial gradient of the flux density and therefore renders the model nonlocal, i.e. size-dependent. Dislocation driving force results from a tensorial superposition of the applied stress and internal stresses arising from an inhomogeneous spatial distribution of the excess dislocation content. The model is solved at the integration point level of a finite element discretization and directly uses neighboring integration point data for the derivation of spatial gradients. It is evaluated for the cases of three-dimensional single and bi-crystalline Al.

A Multi-scale Model of Martensite Transformation Plasticity in Metastable Austenitic Steels

V.G. Kouznetsova, J. van Beeck and M.G.D. Geers

Eindhoven University of Technology, Department of Mechanical Engineering
P.O. Box 513, 5600 MB, Eindhoven, The Netherlands
V.G.Kouznetsova@tue.nl

Advanced high strength steels, such as metastable austenitic stainless steels, exhibit an excellent combination of strength and ductility. The remarkable mechanical properties of these materials at the macroscale level are related to their complex microstructural behaviour, resulting from the interaction between plastic deformation of the phases and the austenite to martensite phase transformation during thermomechanical loading. This microstructural behaviour is in turn a very complex function of alloying and thermomechanical processing, which is still not fully understood, thus limiting the optimal utilization of these materials.

The model incorporates several spatial levels bridged through appropriate homogenization techniques: (i) a macroscopic or engineering level; (ii) a mesoscale polycrystalline level; (iii) a microscale level of a single austenite grain; and (iv) a level of smaller domains within the austenite grain where the martensitic transformation takes place on particular crystallographic transformation systems. The model directly incorporates the coupling between elastic and plastic deformations of the phases and the transformation, as well as the dependence of the transformation on the previous thermomechanical history, allowing to account for various related phenomena, e.g. the mechanical stabilization of austenite.

Several examples are used to illustrate the ability of the model to predict the orientation and stress-state dependence of the transformation and the effect of the proper incorporation of the interaction between the plastic deformation of the austenite and the martensite transformation. The performance of the model is evaluated against experimental data, i.e. tensile tests and pure bending tests, including the non-trivial springback behaviour originating from the stress-state dependency of the transformation.

Modelling of texture formation in the cold-rolled ferritic-austenitic steel using self-consistent viscoplastic model and finite element method

Marcin Kowalski¹, Jerzy Jura^{1,2} and Thierry Baudin³

¹ **Institute of Technology, Pedagogical University, 30-084 Cracow, 2 Podchorazych Str., Poland, e-mail: markowal@ap.krakow.pl**

² **Institute of Metallurgy and Materials Science, Polish Academy of Sciences, 30-059 Cracow, 25 Reymonta Str., Poland**

³ **Laboratoire de Physico-Chimie de L'Etat Solide, UMR CNRS 8648, ICMMO, Universite de Paris Sud, 91405 Orsay Cedex, France**

ABSTRACT

The paper describes the application of the finite element method to predict crystallographic texture development in the cold rolled ferritic-austenitic steel. The modelling was carried out using the finite element code Abaqus and the subroutine VPSC5, including visco-plastic self-consistent model. The initial texture (set of single orientations) was generated based on the experimental texture of the annealed sample. The resulting textures obtained for finite element situated in inner area of the sample were in good agreement with the experimental data.

1. Introduction

In the last years a growing interest in application of the finite element method for crystallographic texture prediction has been observed [1-5]. This has been dictated by many advantages of this method, such as good projection of the stress and strain state, and securing of the material continuity (which is very important in multiphase materials modelling).

Among a number of multiphase materials the ferritic-austenitic stainless steels are currently one of the most important constructional materials. Due to their advantages, such as high corrosion resistance, good formability and weldability, the duplex steels are mainly used in chemical, power, paper, oil, food and shipbuilding industry.

Given this importance and versatility of duplex steels application, an attempt to prepare a computational system based on finite element method (commercial software Abaqus) combined with the VPSC5 code (visco-plastic self-consistent model [6]) has been made with the aim of texture prediction in the cold-deformed two-phase material. The system was verified using texture data for ferritic-austenitic steel.

The visco-plastic self-consistent model included in the VPSC5 subroutine suggests its application for multiphase materials due to the consideration of the problem of ellipsoidal inclusion embedded in homogenous matrix. In addition, inclusion during deformation became flat like a real grain in duplex steel.

2. Experimental data

The commercial ferritic-austenitic UR45N steel was used as a comparative material for verification of model results. The orientation distribution functions were determined using ADC method [7] based on pole figures measured by neutron diffraction method [8]. This method provides a very accurate estimation of global texture (in macro-scale).

3. Modelling procedure

The calculations were carried out in two steps. In the first step, local deformation gradient tensors for each finite element were calculated using Abaqus (and subroutine Vumat developed by the author). The isotropy of the material was assumed for the calculations in this step. In the second step, the deformation gradient tensors at each time increment for chosen

finite element were transmitted to the subroutine VPSC, which calculates orientation changes using the visco-plastic self-consistent model. The local deformation gradient tensor determined in the first step is considered now as global for VPSC5.

The orientations of crystallites in the initial state were generated from orientation distribution functions (ODF) calculated with pole figures measured using the neutron diffraction method for the annealed sample [8].

It was assumed that for 1200 initial orientations for BCC phase and 800 initial orientations for FCC phase, one finite element is assigned (according to the approximated volume fraction of phases in the experimental sample ~60% of BCC and ~40% of FCC). This approach allowed transferring global texture information to the micro-level (single orientation represents the single grain). The assumed number of orientations was sufficient to obtain a good representation of characteristic features of the initial texture for both phases and to simultaneously reduce the calculation time. The twelve slip systems $\langle 110 \rangle \{ 111 \}$ as well as the twelve twinning systems $\langle 110 \rangle \{ 112 \}$ for the FCC phase and forty-eight slip systems: $\langle 111 \rangle \{ 110 \}$, $\langle 111 \rangle \{ 112 \}$ and $\langle 111 \rangle \{ 123 \}$ for the BCC phase were assumed.

The advantage of the presented approach is that one can use average mechanical properties (in form of work-hardening curve of the investigated material) in single finite element. Because of this, the multi-phase character of the material (the interactions between FCC and BCC phases) is taken into consideration.

4. Results

Following the execution of the modelling procedure described above, the orientation distribution functions for 20%, 40%, 60% and 80% of r.r. were obtained. The model distributions and corresponding experimental ODF's for FCC and BCC phases cold-rolled up to 80% of rolling reduction are presented in (fig.1,2).

Additionally, the characteristic fibres for BCC phase: $\gamma - \langle 111 \rangle \parallel \text{ND}$, $\alpha - \langle 110 \rangle \parallel \text{RD}$, $\varepsilon - \langle 110 \rangle \parallel \text{TD}$ and for FCC phase: $\eta - \langle 001 \rangle \parallel \text{RD}$, $\alpha - \langle 110 \rangle \parallel \text{ND}$ and $(\tau - \langle 110 \rangle \parallel \text{TD})$ were performed in the form of skeleton lines for the annealed sample (0%) and for experimental and model samples after 80% of deformation. (Fig.3-8).

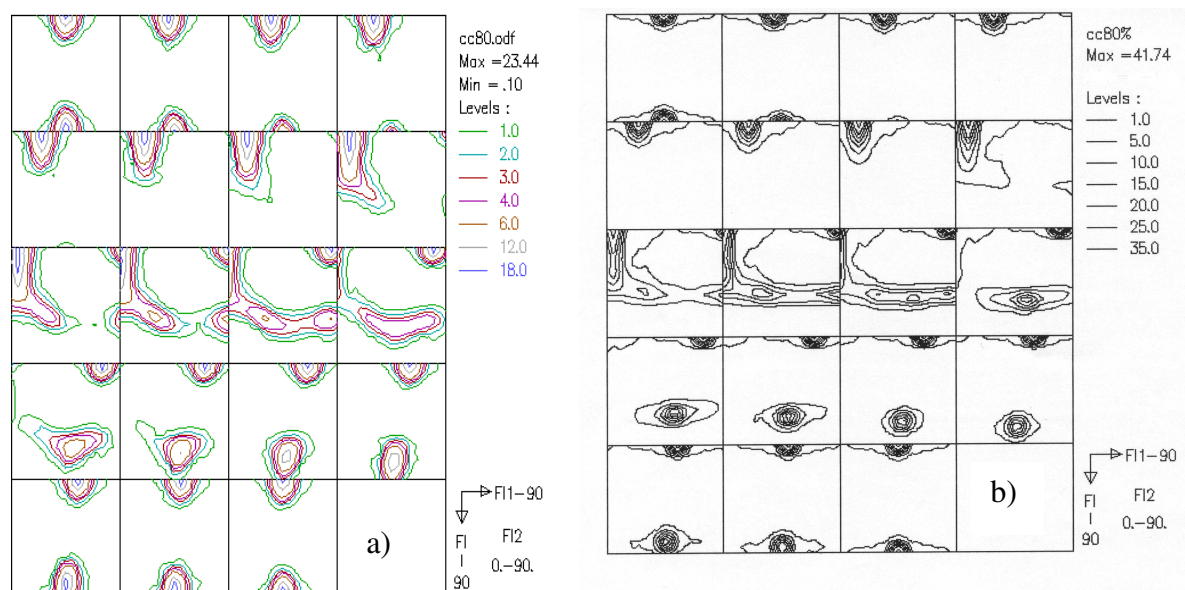


Figure.1. Orientation distribution function for BCC phase (80% r.r.): a) experiment, b) model

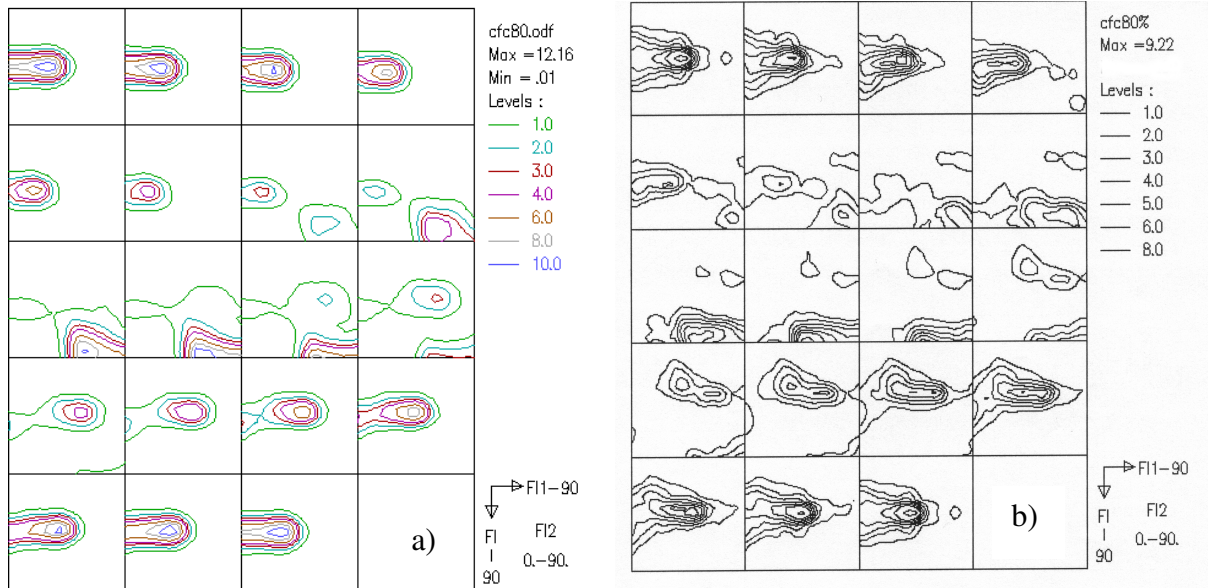


Figure.2. Orientation distribution function for FCC phase (80% r.r.): a) experiment, b) model

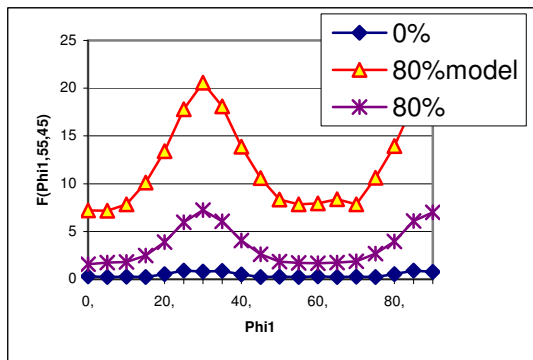


Fig. 3. Skeleton lines for BCC : (γ - $\langle 111 \rangle$ || ND)

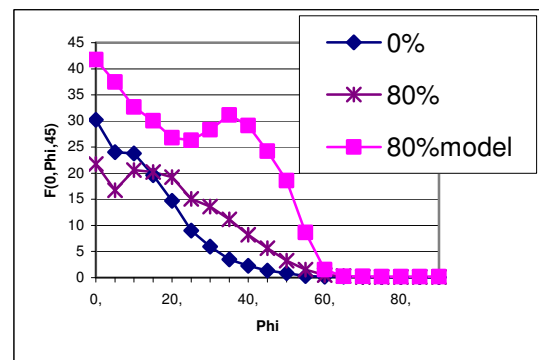


Fig. 4. Skeleton lines for BCC: (α - $\langle 110 \rangle$ || RD)

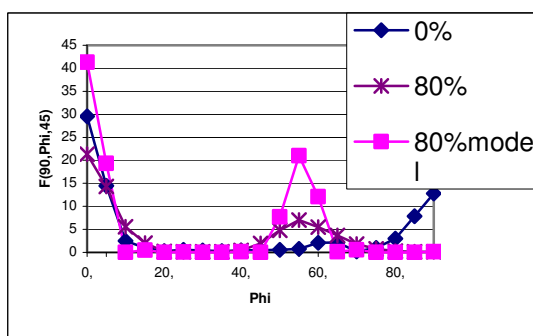


Fig. 5. Skeleton lines for BCC : (ϵ - $\langle 110 \rangle$ || TD)

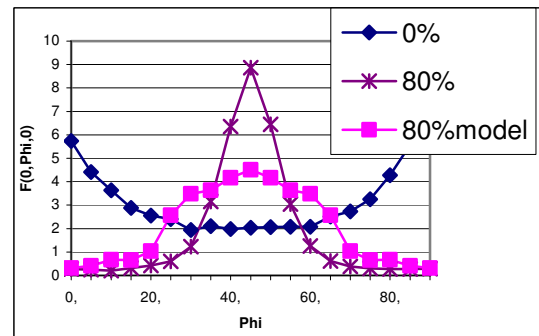


Fig. 6. Skeleton lines for FCC: (η - $\langle 001 \rangle$ || RD)

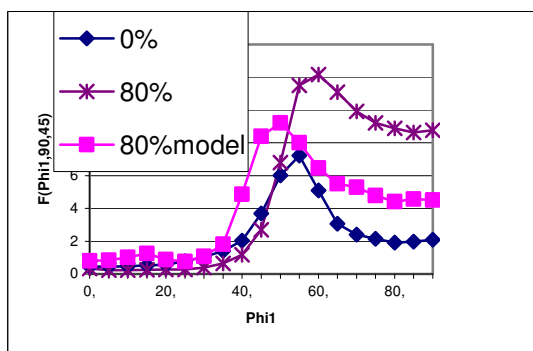


Fig. 7. Skeleton lines for FCC: (α - $\langle 110 \rangle$ || ND)

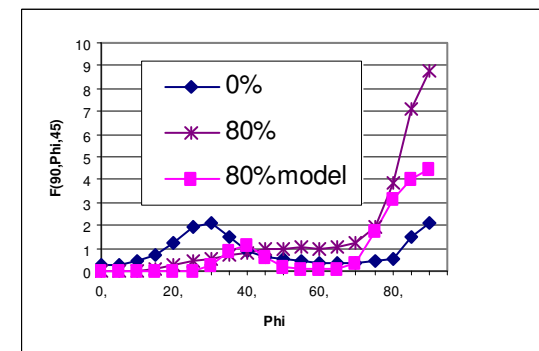


Fig. 8. Skeleton lines for FCC: (τ - $\langle 110 \rangle$ || RD)

5. Discussion

There are two significant advantages of the developed and tested modelling procedure for deformation texture prediction. Firstly, the mechanical properties are included in the procedure thanks to the introduction of the work-hardening curve, which represents the average properties of the investigated material. Secondly, the interaction between phases takes place in the volume of each single finite element, and not between finite elements.

The comparison of the model presented in the paper and the experimental ODF's for FCC and BCC phases has indicated that the developed approach allows to obtain very good reproducibility of the characteristic features of the experimental texture (fig.1,2).

By analyzing the orientation distributions along the characteristic skeleton lines (called fibres) one can find a very good representation of the γ -fibre for the ferrite model ODF (fig.3). The ε -fibre is also reproduced correctly (fig.5). The α -fibre (fig.4) was developed by increasing the deformation degree, however some deviations from the experimental distribution are apparent. Specifically, in the neighbourhood of $\{001\}\langle 110\rangle$ orientation, the local maximum of the orientation density in the model ODF is shifted towards $\{112\}\langle 110\rangle$ orientation.

For the austenite model ODF's with an increase of rolling reduction one can observe developing of the α -fibre with $\{110\}\langle 112\rangle$ brass and $\{110\}\langle 001\rangle$ Goss components. As it is observed in the experimental orientation distribution, the $\{112\}\langle 111\rangle$ copper orientation is not present in the model ODF's (fig.2) for 80% r.r (τ -fibre, fig.8). This results from the introduction of twinning as an additional deformation mechanism in the modelling procedure. The high orientation density near the $\{123\}\langle 634\rangle$ S-orientation characteristic for FCC deformation texture is also observed in the model distribution (fig. 2b).

6. Conclusions

The analysis of the obtained results provided the evidence that the developed modelling procedure based on FEM (Abaqus) and VPSC5 (visco-plastic self-consistent model of plastic deformation) may be successfully applied to predict formation of the crystallographic texture during cold forming of the multiphase material.

However, during analysis of modelling results one should take into account the fact, that in the ferritic-austenitic steels considerable differences in formed deformation textures can occur, e.g. induced by the chemical composition [9]. The additional deformation mechanism may also be activated, e.g. $\gamma \rightarrow \alpha$ phase transformation, which can effect the final texture. The parameters of heat treatment and plastic working can also have an influence on the resulting texture. Therefore, an individual treatment of each material in preparing the modelling procedure parameters is necessary.

7. References

- [1] D.Raabe, K.Helming, F.Roters, Z.Zhao, J.Hirsch, Materials Sc. Forum. 408-412, 257-262, (2002)
- [2] D.Raabe, Z.Zhao, S.-J.Park, F.Roters, D. Acta Mat. 50, 420-440, (2002)
- [3] S.R.Kalidindi, C.A.Bronkhorst, L.Anand, J. Mech. Phys. Solids, 40, 3, 537-569,(1992)
- [4] S.-J.Park, H.N.Han, K.H.Oh, D.Raabe, J.K.Kim, Mat. Sc. Forum, 408-412 371-376, (2002)
- [5] P.van Houtte, A. van Bael, J.Winters, Textures and Microstructures, 24, 255-272, (1995)
- [6] C.N. Tome, Modelling Simul. Mater. Sci. Eng. 7, pp. 723-738, (1999)
- [7] K.Pawlik, Phys. Stat.Solids B, 134, p.477 (1986)
- [8] J.Jura, Th.Baudin, M.H.Mathon, W.Świątnicki, R.Penelle, Materials Science Forum, 408- 412 , pp. 1359-1364, (2002)
- [9] N.Akdut, Kaltverformung von duplexwerkstoffen. Shaker Verlag (1996)

Microstructure Modeling on the Basis of the Phase-Field Method

Toshiyuki Koyama

Structural Metals Center, National Institute for Materials Science,
1-2-1 Sengen, Tsukuba, Ibaraki, 305-0047, Japan
KOYAMA.Toshiyuki@nims.go.jp

In the last two decades, the phase-field approach has become a useful and powerful tool for understanding and modeling phase transformations and microstructure evolutions across many fields in materials science [1,2]. The meaning of phase field is the spatial and temporal order-parameter field defined in a continuum diffused interface model. By using the phase-field order parameters, various types of complex microstructure changes observed in materials science can be efficiently described.

In this study, as typical examples of the phase-field modeling applied to complex microstructure changes in real alloy systems, our recent simulation results of the phase transformations and microstructure evolutions are demonstrated. In regard to the structural materials, the nano-scale precipitation in Fe-base alloys [3] and the microstructure evolutions in Ni-base superalloys [4,5] are explained. On the other hand, the phase-field modeling of the microstructure formations in magnetic materials [6-8] and ferroelectric materials [9] are mentioned as the applications to functional materials. Furthermore, the effective strategy for materials design, where the phase-field method is combined with the image-based property calculation, is also proposed.

- [1] T.Koyama, Science and Technology of Advanced Materials, 9(2008), 013006.
- [2] T.Koyama, Chapter 21 in "Springer Handbook of Materials Measurement Methods", H.Czichos, T.Saito and L.Smith (Eds.), (Springer-Verlag, 2006), pp.1031-1054.
- [3] T.Koyama and H.Onodera, Mater. Trans., 47(2006) 2765.
- [4] Y.Tsukada, Y.Murata, T.Koyama and M.Morinaga, Mater. Trans., 49(2008), 484.
- [5] T.Koyama and H.Onodera, Materials Science Forum, 561-565(2007), 2287.
- [6] T.Koyama and H.Onodera, Mater. Trans., 44(2003), 1523.
- [7] T.Koyama and H.Onodera, J. Phase Equilibria and Diffusion, 27(2006), 22.
- [8] T.Koyama and H.Onodera, ISIJ International, 46(2006), 1277.
- [9] T.Koyama and H.Onodera, Mater. Trans., 50(2009), 970.

Modelling the Microstructure Evolution of a Ferritic Hot-Work Tool Steel during Short-Term Creep

Friedrich Krumphals¹, Harald Wurmbauer², Volker Wieser³, Christof Sommitsch¹

¹Christian Doppler Laboratory for Materials Modelling and Simulation, Institute for Materials Science and Welding, Graz University of Technology, Kopernikusgasse 24, 8010 Graz, Austria, friedrich.krumphals@tugraz.at

²Department for Physical Metallurgy and Materials Testing, University of Leoben, Franz-Josef-Straße 18, 8700 Leoben, Austria

³Böhler Edelstahl GmbH & Co KG, Mariazeller Straße 25, 8605 Kapfenberg, Austria

ABSTRACT

Hot work tool steels have to sustain high thermal and mechanical loads. To establish an authentic lifetime prediction of hot work tool steels during service, an accurate investigation and characterization of microstructure evolution is obligate since the material properties depend on the microstructural configuration. Therefore the microstructure of a ferritic hot work tool steel was investigated at different heat-treatment stages. Short-term creep specimen were investigated after rupture and their microstructural state was characterized and compared with precipitation kinetics simulations. The investigated tool material, which has a bcc lattice structure, forms a distinct dislocation cell and subgrain structure, respectively, which is described by a dislocation density model for thermal creep using the rate theory, in which the precipitation state influences the subgrain boundary migration.

1. Introduction

In this work the microstructural evolution of a ferritic hot work tool steel during thermo-mechanical loads, i.e. creep load, is described by means of thermodynamic precipitation calculations performed with the software MatcalcTM [1,2] and simultaneously by dislocation density evolution calculations. The precipitation state of the specimen is characterized after the last annealing step, i.e. the final state before starting the experimental program as well as after rupture. The dislocation density calculations are performed with MathCadTM to describe the dislocation and subgrain structure evolution during the creep load range based on a model for thermal creep using the rate theory [3]. These results are compared with TEM dislocation density measurements.

2. Microstructure Modelling

1.1 Material definition

The chemical composition of the investigated hot work tool steel X38CrMoV5-1 is shown in Table 1. A standard heat treatment to achieve a martensitic structure with a hardness of 46 HRC was applied.

Table 1: Chemical composition of the BöhlerTM W300 hot work tool steel [wt. %]

W300	Fe	C	Si	Mn	Cr	Mo	V
	(Bal.)	0.38	1.10	0.40	5.0	1.30	0.40

1.2 Short term creep tests

The microstructure, i.e. precipitation state and dislocation density, of the creep specimen is characterized after the last annealing step. The short term creep tests are subsequently performed at temperatures between 500 and 590°C, i.e. below the last annealing temperature of 600°C and at stresses in the range between 350 and 900 MPa.

1.3 Modelling the precipitation kinetics and dislocation density evolution

The precipitation kinetics are simulated with the software MatCalcTM, the phase fractions f of the considered precipitates are MX (V(C,N)), M₃C (Fe₃C), M₆C (Cr₆C), M₇C₃ (Cr₇C₃), M₂₃C₆, (Cr₂₃C₆), M₂C (Mo₂C) and Laves phase, the particle number N per volume and the related mean radius of the particles, Rv_{mean} , are the main output parameters. N and Rv_{mean} are subsequently important input parameters for the dislocation density evolution model.

The precipitation state after the heat treatment, the thermal and mechanical loading conditions, the initial dislocation density as well as subgrain size are key parameters in the used physically based dislocation model according to Ghoniem et al. [3]. The basis of the model is to describe the dislocation structure evolution by:

- the generation and immobilization of dislocations at subgrain boundaries, i.e. multiplication as well as annihilation of dislocations due to interaction processes,
- the recovery of the static dislocations at the boundaries as well as the absorption of mobile dislocations in the cell wall,
- the generation of dislocations by emission from the cell wall,
- the dynamics of nucleation and growth of subgrains from dislocations within the cells as well as
- the subgrain growth due to coalescence driven by the subboundary energy.

Hence the total dislocation density ρ_{ges} , is separated into three categories of dislocations, namely mobile ρ_m , static ρ_s , and boundary dislocations ρ_b to consider all the specific dislocation dynamics mentioned above. As an example, the evolution of the boundary dislocation density is described in Eqn. 1,

$$\frac{d\rho_b}{dt} = \underbrace{8(1-2\zeta)\frac{\rho_s}{h_{\text{sg}}}v_c^s}_{\text{Absorption of dislocation and static recovery}} - \underbrace{\frac{\rho_b}{R_{\text{sub}}}M_{\text{sg}}\left[p_{\text{sg}} - 2\pi \cdot \left(\sum_{i=1}^7 Rv_{\text{mean},i}^2 \cdot N_i\right) \cdot \gamma_{\text{sg}}\right]}_{\text{Coalescence and growth of subgrains}} \quad (1),$$

where the parameter ζ depicts the annihilation at the subgrain boundary, v_c^s the creep velocity of static dislocations, h_{sg} the distance between two dislocations in the subgrain, M_{sg} the mobility of subgrains, p_{sg} the driving force of the subgrain boundary, $Rv_{\text{mean},i}$ the radius of precipitation class i , N_i the related number of particles per volume and γ_{sg} the surface energy of the subgrain boundary [3].

3. Results

The evolution of the phase fraction f of the precipitates and Rv_{mean} as a function of the thermal history were calculated with MatCalcTM and are depicted in Figure 1.

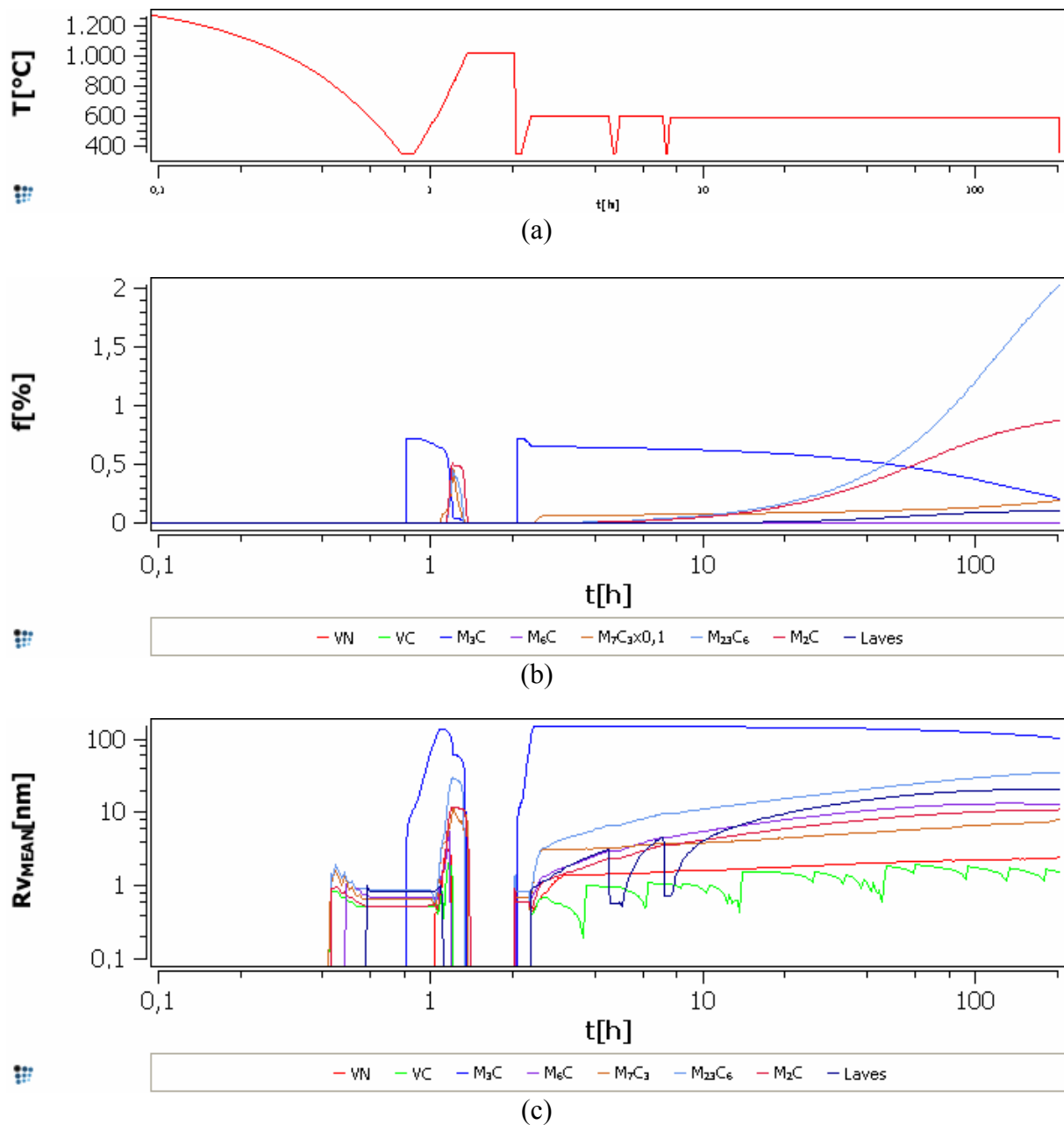


Figure 1. (a) Thermal history (heat treatment and subsequent thermal load of 195h at 550°C) of an investigated creep specimen as well as (b) the volume fractions of the precipitates (Note: The amount of M_7C_3 is divided by 10) and (c) the corresponding precipitation size evolution.

The MatCalc™ simulation was compared with the investigations on the creep specimen, which came to the same correlation that the Cr_7C_3 , $Cr_{23}C_6$ and Mo_2C precipitation volume fractions exhibit the highest amounts among the others (see Fig. 1b). The only discordance in the simulation is the decreasing volume fraction of Fe_3C compared to the TEM investigation.

The dislocation density calculations as compared with the TEM-investigations are depicted in Figure 2. The dislocation density after the last annealing step was found to be $6.4 \cdot 10^{14} \text{ m}^{-2}$ (Fig. 2b) and during creep load of 400MPa and 550°C for 195 hours, the material softens and the dislocation density decreases to a value of $9.3 \cdot 10^{13} \text{ m}^{-2}$ (Fig. 2c). The simulation started with the same initial conditions and predicted a final total dislocation density of about $1.4 \cdot 10^{14} \text{ m}^{-2}$ (Fig. 2a). Remarkable is the rapid decrease of the dislocation density at the beginning of creep test (see Fig. 2a), which is also close to reality, where a rapid change in the dislocation structure takes place at first, i.e. during the primary creep range.

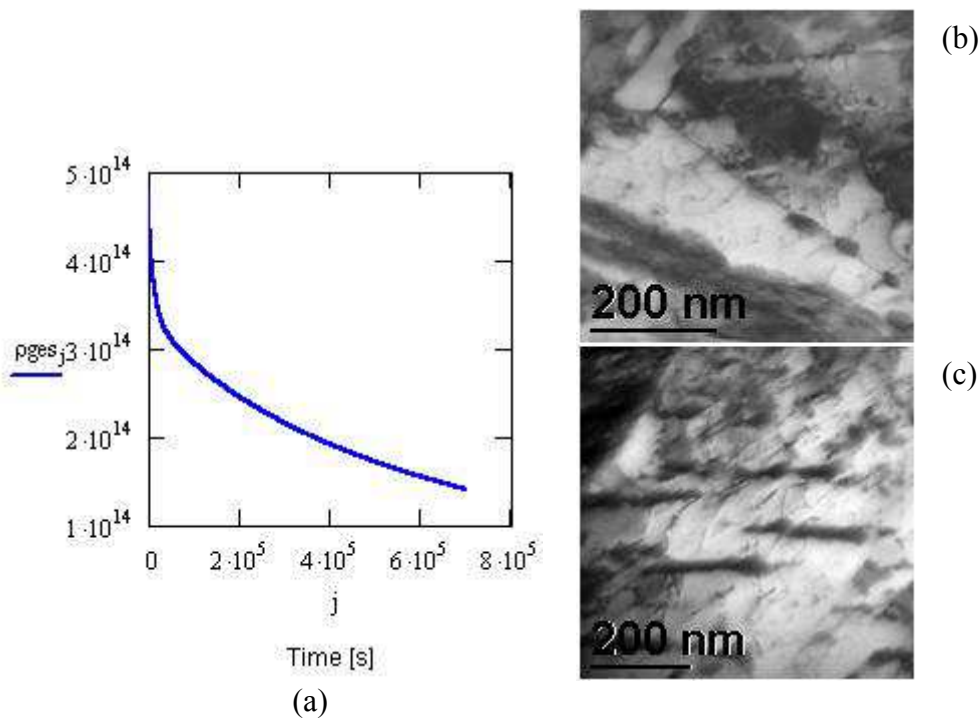


Figure 2. Simulation (a) and determination of the dislocation density by TEM investigations: (b) Initial state before creep testing and (c) investigated specimen after rupture.

4. Conclusion and Outlook

It is shown that by applying physical based models the microstructure evolution of a hot work tool steel during both heat treatment and creep loading can be described. The precipitation evolution during annealing as well as under thermal loading was modeled in order to consider the influence of the precipitation state on the mobility of dislocations. The initial measured dislocation density was also the starting parameter for the simulation to make a reasonable comparison. The initial precipitation state after heat treatment was considered and assumed to be stable. However, possible further precipitation reactions during creep, i.e. coarsening, were neglected. A coupling of the two models will be a main objective for future work.

References

- [1] Kozeschnik, E., Sonderegger, B., Holzer, I., Rajek, J., Cerjak, H., Computer simulation of the precipitate evolution during industrial heat treatment of complex alloys, Materials Science Forum, 539-543, 2007, 2431-2436.
- [2] Holzer, I., Rajek, J., Kozeschnik, E., Cerjak, H.-H., Simulation of the precipitation kinetics during heat treatment and service of creep resistant martensitic 9-12% Cr Steel, Proc. Materials for Advanced Power Engineering, Liege, 2006, 1191-1198.
- [3] Ghoniem, N., Matthews, J., Amodeo, R., A dislocation model for creep in engineering materials, Res Mechanica, 29, 1990, 197-219.

Dynamics and Kinetics of Dislocations in Metals under Dynamic Loading

Vasily S. Krasnikov¹, Alexey Yu. Kuksin^{2,3}, Alexander E. Mayer¹, Genri E. Norman^{2,3}
and Alexey V. Yanilkin^{2,3}

¹Chelyabinsk State University, Chelyabinsk 454021, Russia

²Joint Institute for High Temperatures of Russian Academy of Sciences,
Izhorskaya st. 13/2, Moscow 125412, Russia

³Moscow Institute of Physics and Technology, Dolgoprudny 141700, Russia

ABSTRACT

The work presented is devoted to the study of mechanisms and kinetics of plastic deformation of fcc metals under shock-wave loading (strain rates $> 10^5 \text{ s}^{-1}$). Under high strain rates the dependence of flow stress on strain rate becomes stronger [1,2] and its temperature dependence may change as well. It can be attributed to the change of the regime of dislocation motion. Indeed, dislocation velocity is high enough for over-barrier motion of dislocations (without thermal activation) and is limited by a phonon drag [2].

To study the behavior of metals under conditions described the two scale approach is developed [3]. It comprises molecular dynamics (MD) calculations of dislocation mobility and dislocations nucleation rate and 1D continuum mechanics model with equations for description of elastoplastic deformation, kinetics and dynamics of dislocations.

Dislocation velocities as functions of applied shear stress are calculated from MD in a wide temperature range up to the melting point. Velocity-dependent drag coefficient is introduced to approximate the data obtained, including relativistic region (where dislocation velocity approaches the sound speed asymptotically). The influence of vacancies, impurity atoms, precipitates and pores on dislocation motion is analyzed. The rate of homogeneous nucleation of dislocation loops is evaluated from direct MD simulations using statistical averaging approach and compared with the results of dislocations theory. Several models for the description of dislocations nucleation are discussed.

The results obtained are used to evaluate temperature dependence of dynamic flow stress and the evolution of dislocations subsystem under shock loading. Data on the attenuation of the elastic precursor and rare surface velocity profiles calculated for Al are in good agreement with the experiments [1].

References

- [1] G. Kanel, V. Fortov, S. Razorenov. Shock Waves in Condensed-State Physics. *Physics Uspechi*, **50**(8), 771, 2007.
- [2] V.I. Alshits and V.L. Indenbom. Dynamic Drag of Dislocations. *Soviet Physics Uspechi*, **18**(1), 1–35, 1975.
- [3] V.S. Krasnikov, A. Yu. Kuksin, A.E. Mayer, and A. V. Yanilkin. Plastic Deformation under High-Rate Loading: The Multiscale Approach. *Physics of the Solid State*, **52**(7), 1386–1396, 2010.

**Molecular Dynamics Simulation:
A Powerful Tool for Engineering Condensed Matter**
Thorsten Köddermann¹, Marco Hülsmann², Astrid Maaß³, Dirk Reith⁴

¹Computational Chemical Engineering Group, Fraunhofer Institute for Algorithms and Scientific Computing (SCAI), Sankt Augustin, Germany,
koeddermann@scai.fraunhofer.de

^{2,3,4}Computational Chemical Engineering Group, Fraunhofer Institute for Algorithms and Scientific Computing (SCAI), Sankt Augustin, Germany

Nowadays, molecular dynamics simulations are widely used to support the development process for new materials. The key to a quantitative property prediction is the accuracy of the simulation's foundation, the force field. A force field describes the intra- and intermolecular interactions by a semi-empirical equation and its associated parameters.

Manual adjustment and optimization of these parameters is, at best, extremely time-consuming. Hence, an automated parameterization scheme is essential in our pursuit to create tailor-made models for specific investigations in a timely fashion. This has been realized and implemented into a Gradient-based Optimization Workflow (GROW) [1-3] for the automated development of molecular models.

In this presentation, we will show how our developed simulation procedure technically works and we will present some example simulations of different chemical substances and their mixtures calculating condensed phase properties like densities, self-diffusion coefficients, viscosities, and enthalpies of vaporization.

Literature:

- [1] M. Hülsmann, T. Köddermann, J. Vrabec, D. Reith., GROW: A Gradient-based Optimization Workflow for the Automated Development of Molecular Models., *CompPhysCom*, 181: 499-513 **2010**.
- [2] M. Hülsmann, J. Vrabec, A. Maaß, D. Reith., Assessment of Numerical Optimization Algorithms for the Development of Molecular Models., *CompPhysCommun*, 181: 887-905 **2010**.
- [3] M. Hülsmann, T. J. Müller, T. Köddermann, D. Reith., Automated Force Field Optimisation of Small Molecules using the New Gradient-Based Software Package GROW, submitted.

Calculation of solid-liquid interfacial free energies from atomistic computer simulation

Brian B. Laird¹, Ruslan L. Davidchack², Yang Yang³ and Mark Asta⁴

¹Dept. of Chemistry, University of Kansas, Lawrence, KS 66046, USA, blaird@ku.edu

² Dept. of Mathematics, University of Leicester, LE1 7RH, UK

³ Dept. of Physics, East China Normal University, Shanghai 200062, China

⁴ Dept. of Materials Science, University of California, Berkeley, CA 94720, USA

ABSTRACT

The solid-melt interfacial free energy is a primary parameter governing the kinetics and morphology of crystal growth and nucleation, as well as in the wetting of a solid surface by a fluid. In this work we focus on the calculation of γ_{sl} from atomistic computer simulation. After briefly reviewing our work and that of others on the development of cleaving and capillary fluctuation methods (CFM) for systems ranging from idealized models (hard-spheres, Lennard-Jones) to more realistic models of metals and molecular materials, we discuss our recent efforts to determine γ_{sl} through the integration of a Gibbs-Cahn adsorption equation. As a test, we apply the Gibbs-Cahn method to two model systems: the Lennard-Jones crystal-melt interface and a hard-sphere fluid at a hard wall. The values for γ_{sl} so obtained are in good agreement with previous calculations by cleaving and CFM, but were obtained with significantly less computational effort.

1. Introduction

For solid-liquid interfaces, the interfacial free energy, γ_{sl} , plays a central role in understanding the morphology and kinetics of crystal growth and nucleation¹. Despite its importance, direct experimental measurements are difficult, few in number and generally not precise enough to resolve the often small orientation dependence (anisotropy). Because of the lack of experimental data, much of our current understanding of the material dependence of γ_{sl} comes via atomistic simulations².

The determination of γ_{sl} in a computer simulation is complicated by the solid elasticity, which precludes¹ the use of mechanical approaches commonly used for liquid-vapor or fluid-wall interfaces in which γ is equated to the integral of the excess interfacial stress. At present, there are two principal methods for the calculation of γ_{sl} via molecular simulation: In the *capillary fluctuation method* (CFM),³ the interfacial stiffness is obtained from the spectrum of interfacial fluctuations. By determining the anisotropy of the stiffness, accurate values of γ_{sl} can be obtained. In the *cleaving method*,^{4,5} γ_{sl} is obtained using thermodynamic integration - directly calculating the reversible work per unit area required to transform bulk crystal and melt systems into a system containing an interface. Both of these methods, which have been applied to a number of model and realistic potentials², are computationally intensive, so evaluations of γ_{sl} for a given system, with the exception of the Lennard-Jones system,^{6,7} are generally restricted to one point on the coexistence curve. More efficient simulation methods are needed facilitate the calculation of γ_{sl} over the full range of coexistence conditions.

Recently, Frolov and Mishin⁸ have demonstrated that γ_{sl} for the solid-liquid interfaces of mixtures can be determined by direct integration along the temperature-composition curve at fixed

pressure given a value of γ_{sl} for one of the pure components. They applied this formalism to the calculation of γ_{sl} for Cu/Ag mixtures of varying composition. Their approach, which we refer to as "Gibbs-Cahn integration", is based upon Cahn's extension⁹ of the interfacial thermodynamics of Gibbs¹⁰. Using the Gibbs-Cahn formalism, differential changes in γ_{sl} can be related to interfacial excesses that are readily calculated within an atomistic simulation, allowing for the determination of γ_{sl} along the coexistence curve by direct integration. As such, this technique is analogous to the use of the Clapeyron equation to determine phase boundaries by integration along the boundary.^{11,12} Frolov and Mishin have also employed this technique to determine the surface free energy of Cu(110) as a function of T at fixed pressure.¹³

In this work, we use the Gibbs-Cahn approach to demonstrate that γ_{sl} can be obtained at a variety of temperatures along a temperature-pressure coexistence curve by integration of the excess interfacial energy and stress along that curve, provided that the value of γ_{sl} has been previously determined for one temperature (for example, by CFM or cleaving). The result is a determination of γ_{sl} as a function of coexistence temperature with a computational effort that is not significantly more than the calculation of a *single* γ_{sl} value by CFM or cleaving. As an additional test, we also apply the formalism to the calculation of the interfacial free energy for a hard-sphere fluid at a structureless hard wall.

2. Gibbs-Cahn Integration

In a seminal paper⁹, Cahn generalized Gibb's interface thermodynamics by eliminating the need to define a dividing surface. For an r -component system containing a planar interface under hydrostatic stress, changes in γ are governed in Cahn's formalism by the following differential^{9,13,14}

$$d(\gamma A) = -[S/XY]dT + [V/XY]dP + \sum_{i,j=1,2} [(\sigma_{ij} + \delta_{ij}P)V/XY] d\epsilon_{ij} - \sum_{k=1}^r [N^k/XY]d\mu^k \quad (1)$$

where A is the interfacial area, S, V, T , and P are entropy, volume, temperature and pressure, respectively, and N_k and μ_k are the number and chemical potential of particles of type k . The quantities $\sigma_{i,j}$ and $e_{i,j}$ are the i, j components of the stress and strain tensors, respectively. In Eq. 1, X and Y are variables conjugate to displacements dx and dy (e.g., V is the variable conjugate to dP), and the notation $[A/XY]$ is defined as

$$[A/XY] = \begin{vmatrix} A & X & Y \\ A_l & X_l & Y_l \\ A_s & X_s & Y_s \end{vmatrix} / \begin{vmatrix} X_l & Y_l \\ X_s & Y_s \end{vmatrix} \quad (2)$$

where s and l denote bulk solid and bulk liquid and quantities without these designations refer to the interfacial system. The choice of X and Y allows one to eliminate two of the terms in the differential because a determinant vanishes if two columns are identical.

For a single component system ($r = 1$), a convenient choice is $X, Y = N, V$, equivalent to a Gibbs dividing surface with zero excess particle number. With this choice, the dP and $d\mu$ terms in Eq. 1 are zero (because a determinant is zero if two columns are identical), giving

$$d(\gamma A) = -[S/NV]dT + \sum_{i,j=1,2} [(\sigma_{ij} + \delta_{ij}P)V/NV]d\epsilon_{ij} \quad (3)$$

Simplifying, Eq. 3 is reduced to¹⁴

$$\frac{1}{A}d(\gamma A) = -\eta dT + \tau \frac{dA}{A} \quad (4)$$

where η and τ are the excess interfacial entropy and stress, respectively.¹

Eq. 4 requires knowledge of the excess interfacial entropy, η , which is not readily obtainable from simulation. To remedy this, Frolov and Mishin,¹³ transform Eq. 4 to

$$\frac{1}{A}d(\gamma A/T) = -\frac{e}{T^2}dT + \frac{\tau}{T} \frac{dA}{A} \quad (5)$$

which relates changes in γ to the more easily obtainable excess interfacial energy, e . The derivation of this equation is analogous to the derivation of the Gibbs-Helmholtz equation in thermodynamics.

3. Results

For our study, we use the truncated Lennard-Jones (LJ) potential of Broughton and Gilmer¹⁵. This potential has an advantage because its interfacial thermodynamics have been previously characterized^{4,6,16}. Starting from the values determined by Davidchack and Laird for γ_{sl} at the triple point ($T^* = kT/\epsilon = 0.618$), we can use Eq. 4 to determine the value of γ_{sl} at higher temperatures along the coexistence curve. To do this we have calculated the crystal density, ρ_c and the excess interfacial energy, e , and stress, τ at several temperatures ($T^* = 0.618, 0.809, 1.0, 1.25$ and 1.5) along the coexistence curve. See Reference 2 for simulation details.

The values of γ_{sl} above the triple point are obtained by numerically integrating Eq. 4 to obtain γ_g/T , from which γ_{sl} is easily determined. The results of these integrations are summarized in Fig. 1 along with the values determined by cleaving in Reference 6, for comparison. At $T^* = 1.0$, the values from Gibbs-Cahn integration agree within the error bars with those from cleaving, except for the values for (111), which are slightly higher in the current work. At $T^* = 1.5$, the values for (110) agree within the error bars for the two methods, but the current values for (100) and (111) are higher by 3-5% than those for cleaving, although the error bars on the latter are quite large. The origin of these discrepancies is not clear, although the current method, in addition to being less computationally intensive than cleaving, appears also to have significantly smaller statistical error. The current results were obtained with *significantly less computational effort* than required by either the cleaving method or the capillary fluctuation method (CFM).

In addition to the results for the LJ system, we have used the Gibbs-Cahn formalism to calculate γ_{sl} for a hard-sphere fluid at a hard structureless wall. Details of these results can be found in Reference 17.

Acknowledgements

This work was supported in part by NSF grant CHE-0957102. In addition, BBL gratefully acknowledges Mark Asta and the University of California, Davis for their hospitality during his Fall 2008 sabbatical where some of this work was performed.

References

- [1] W.A. Tiller, *The Science of Crystallization: Microscopic Interfacial Phenomena*, (Cambridge University Press, New York, 1991).
- [2] B.B. Laird and R.L. Davidchack, *J. Phys. Chem. B* **109**, 17802–17812 (2005).

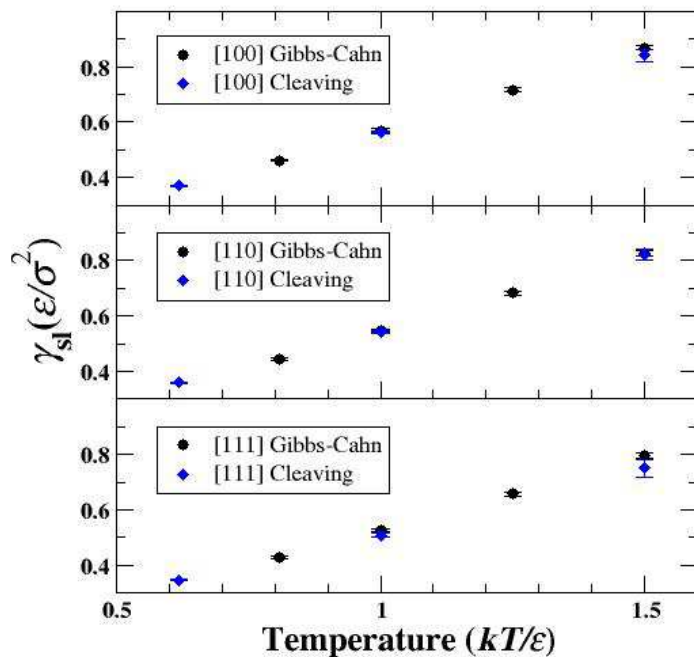


Figure 1: γ_{sl} for the LJ solid-liquid interface using Gibbs-Cahn integration (circles) and from cleaving (diamonds).

- [3] J.J. Hoyt, M. Asta, and A. Karma, *Phys. Rev. Lett* **86**, 5530–5533 (2001).
- [4] J.Q. Broughton and G.H. Gilmer, *J. Chem. Phys.* **84**, 5759–5768 (1986).
- [5] R.L. Davidchack and B.B. Laird, *Phys. Rev. Lett.* **85**, 4751–4754 (2000).
- [6] R.L. Davidchack and B.B. Laird, *J. Chem. Phys.* **118**, 7657 (2003).
- [7] C.A. Becker, D. Olmsted, M. Asta, J.J. Hoyt, and S.M. Foiles, *Phys. Rev. Lett* **98**, 125701 (4 pages) (2007).
- [8] T. Frolov and Y. Mishin, *J. Chem. Phys* **79**, in press (2009).
- [9] J.W. Cahn. Thermodynamics of solid and fluid surfaces. In W.C. Johnson and J.M. Blakely, editors, *Interfacial Segregation*, pages 3–23., ASM International, International Materials Park, OH, 1979.
- [10] J.W. Gibbs, *The Collected Works*, volume 1, (Yale University Press, New Haven, 1957).
- [11] D.A. Kofke, *Mol. Phys.* **78**, 1331–1336 (1993).
- [12] D.A. Kofke, *J. Chem. Phys.* **98**, 4149–4162 (1993).
- [13] T. Frolov and Y. Mishin, *Phys. Rev. B* **79**, 045430 (2009).
- [14] B.B. Laird, R.L. Davidchack, Y. Yang, and M. Asta, *J. Chem. Phys.* **131**, 114110 (8 pages) (2009).
- [15] J.Q. Broughton and G.H. Gilmer, *Acta metall.* **31**, 845 (1983).
- [16] J.R. Morris and X. Song, *J. Chem. Phys.* **119**, 3920–3925 (2003).
- [17] B.B. Laird and R.L. Davidchack, *J. Chem. Phys.* **132**, 204101 (6 pages) (2010).

Plumber's Wonderland Found on Graphene

Ju Li¹, Liang Qi¹, Ji Feng¹, Jian Yu Huang², Feng Ding³, Boris I. Yakobson³

¹Department of Materials Science and Engineering,
University of Pennsylvania, Philadelphia, Pennsylvania 19104, USA

²Center for Integrated Nanotechnologies,
Sandia National Laboratories, Albuquerque, New Mexico 87185, USA

³Department of Mechanical Engineering and Materials Science,
Rice University, Houston, Texas 77005, USA

Curvy nanostructures such as carbon nanotubes and fullerenes have extraordinary properties but are difficult to pick up and assemble into devices after synthesis. We have performed experimental and modeling research into how to construct curvy nanostructures directly integrated on graphene, taking advantage of the fact that graphene bends easily after open edges have been cut on it, which can then fuse with other open edges, like a plumber connecting metal fittings. By applying electrical current heating to few-layer graphene inside an electron microscope, we observed the in situ creation of many interconnected, curved carbon nanostructures, such as graphene bilayer edges (BLEs), aka “fractional nanotubes”; BLE polygons equivalent to “squashed fullerenes” and “anti quantum-dots”; and nanotube-BLE junctions connecting multiple layers of graphene. The BLEs, quite atypical of elemental carbon, have large permanent electric dipoles of 0.87 and 1.14 debye/Å for zigzag and armchair inclinations, respectively. An unusual, weak AA interlayer coupling leads to a twinned double-cone dispersion of the electronic states near the Dirac points. This entails a type of quantum Hall behavior markedly different from what has been observed in graphene-based materials, characterized by a magnetic field-dependent resonance in the Hall conductivity. Further simulations indicate that multiple-layer graphene offers unique opportunities for tailoring carbon-based structures and engineering novel nano-devices with complex topologies. (*PNAS* **106** (2009) 10103; *Phys. Rev. B* **80** (2009) 165407; *Nano Research* **3** (2010) 43)

A Molecular Dynamics Simulation of the Strength of Cementite Fe₃C

A. Luque, J. Aldazabal, J.M. Martínez-Esnaola, J. Gil Sevillano

CEIT and Tecnun (University of Navarra)

Manuel de Lardizábal 15. 20018 San Sebastián, Spain.

E-mail: jgil@ceit.es. Phone: +34943212800. Fax: +34943213076.

ABSTRACT

The metastable iron carbide Fe₃C (orthorhombic symmetry) is a constituent of many steels and, in particular, of the lamellar eutectoid α Fe/Fe₃C pearlite. Fully pearlitic steels of near-eutectoid composition with 12% to 14% cementite in volume transformed at low temperature possess a very fine microstructure of interlamellar spacing of the order of 100 nm, i.e. they are two-phase nanocomposites. By wire-drawing that spacing can be further reduced by a factor of ten, to about 10 nm, making of highly drawn fine pearlitic wires the strongest commercial material available in bulk quantities. Understanding the strength of such nanocomposite is paramount for its use as reinforcement of tyres. Knowledge of the strength of cementite is thus of utmost technical importance. Cementite is also of geological interest (*cohenite* in the geological literature) being present in iron meteorites and perhaps in the solid inner earth core. Surprisingly, the mechanical properties of cementite, even its elastic properties [1], are not fully elucidated. Using a recently proposed bond-order interatomic potential for the iron-carbon system [2], the room-temperature tensile strength of plain Fe₃C has been studied by performing molecular dynamics simulations.

1. Cementite strength

Surprisingly, to our knowledge no single crystalline direct mechanical data obtained by using micro/nanomechanical tests nowadays available exist for cementite. Some very scarce data from bending tests of small single crystalline cementite samples (1-3 μ m thick) were published long time ago [3] yielding fracture strengths from 4.6 GPa to 8 GPa; samples showed plastic deformation before fracture. By contrast, bulk compression tests of polycrystalline cementite at different temperatures have been published [4-6]; although at room temperature bulk cementite is brittle and breaks at about 2 GPa to 3 GPa, above 573 K bulk cementite is ductile. By extrapolation of the high temperature strength (ductile behaviour) to room temperature, a value from 5 GPa to 7 GPa is obtained. In conclusion, a value of about 6 ± 2 GPa is estimated from bending or compression tests (notice, however that grain boundary sliding is active in the high temperature compression tests). Measurements of bulk cementite strength at different temperatures are mainly available from indentation tests on relatively thick plates of single crystalline pro-eutectoid or eutectic cementite and less frequently on thin films or bulk polycrystalline specimens [4,7-17]. In all cases, the equivalent tensile strength at room temperature ranges from 3 GPa to 6 GPa, depending on crystallographic orientation, alloying or prior plastic deformation, 4 GPa being the most frequently quoted value for unalloyed cementite (1100 Kgf mm⁻² Vickers hardness). The reported values correspond to Vickers micro- or macro-hardness and should be considered as lower bound values, as some indentation cracking could have occurred in the tests. Measurement of the strength of pearlitic cementite is only accesible via diffraction measurements on account of its size (initial true thickness of about 10 nm after patenting). Cementite strength has been estimated about 5 GPa [18,19] from the partitioning of the

macroscopic stress and the measure of the lattice ferrite strain during in situ tension neutron diffraction test of heavily drawn wire or drawn and annealed wire pearlitic steel. Similar approximated values of about 5 GPa (a maximum cementite lattice strain in the range 0.014-0.019) have been obtained by direct measurement of the tensile lattice strain of cementite of patented or drawn-annealed pearlitic steel also by neutron diffraction in situ tests [20,21]. From the synchrotron measurements of the residual stresses in the cementite of a one-pass drawn pearlitic wire, a cementite tensile strength of about 4 GPa can be calculated too [22]. From the residual stresses of the cementite after drawing a fine pearlitic wire up to a true strain of 2 [23] plus the wire flow stress, a cementite strength of 4 GPa to 5 GPa is estimated. Summarizing, the range 6 ± 2 GPa covers nearly all published experimental measurements or estimations based on experimental results of the cementite tensile equivalent strength (the cementite tensile or compressive flow stress assuming ductile behaviour) at room temperature, for either bulk polycrystalline specimens or thin lamellar pearlitic cementite. The data covered by this range were obtained using very different experimental methods. We have not found in the literature any predictions of the cementite strength obtained from atomistic simulations.

2. Cementite elastic moduli

Ledbetter [1] has recently reviewed the state-of-the-art of our knowledge on the elastic properties of cementite, his conclusion being that despite much research done on this subject a precise value of the elastic moduli is rather uncertain. Few measurements based on reliable single crystalline samples exist and there are no experimental measurements of the whole set of 9 moduli of the orthorhombic cementite crystal. Most published values are estimations of the average polycrystalline moduli based on the elastic moduli of steel or cast iron. The values present a large dispersion and some conflicting discrepancies. For instance, the polycrystalline moduli obtained by Ledbetter by extrapolation to the cementite composition of the moduli of iron-carbon alloys with different cementite fractions are $E = 230 \pm 12$ GPa and $\nu = 0.275 \pm 0.03$ for respectively the Young and Poisson moduli. These results imply that cementite is stiffer than ferrite ($E = 212$ GPa, $\nu = 0.288$). However, an average of ten previously published values of the cementite Young modulus collected by Ledbetter yields $E = 180 \pm 21$ GPa, smaller than the isotropic ferrite Young modulus. Direct measurements of the elastic moduli of cementite single crystals suffer from difficulties of specimen preparation. Values obtained from measurements of the moduli of ferrite-cementite composites suffer from the hypothesis made for both eliminating the texture influence and for deconvoluting the moduli of the individual constituents of the composites. Also recently *ab initio* calculations of cementite structural, electronic and elastic properties have been made for the first time [24]. The predicted structural parameters agree within 1% with the experimental results and the interatomic bonding shows a complex mixture of metallic, covalent, and ionic characters. The authors have calculated the whole set of elastic moduli of the cementite crystal (Tab. 1). The Young and Poisson moduli obtained from averaging the moduli given in Tab. 1 are respectively $E = 194-203$ GPa and $\nu = 0.35-0.36$, i.e., cementite is theoretically predicted to be elastically stable and, on average, less stiff than ferrite, in agreement with most published experimentally-based results. The predicted bulk and shear modulus are respectively $B = 224-227$ GPa and $G = 72-75$ GPa. The bulk modulus is about 30% higher than experimental values measured under high pressures using diamond cells [25-27], but the discrepancy is attributed by Jiang and co-workers [24] to the non-linear effects associated to the very high pressures applied in the experiments. However, the most surprising result of the *ab initio* calculations of Jiang et al. is by far the extraordinary elastic anisotropy predicted for cementite, in particular the very small relative value of the c_{44} shear modulus. A comparison of c_{44} , that represents the stiffness of the lattice against (010)[001] shear, with the isotropic

average shear modulus G and with the c_{55} and c_{66} moduli gives a good idea of that unexpected behaviour.

Table 1. Elastic moduli of orthorhombic cementite Fe_3C from *ab initio* calculations allowing for internal atomic relaxations [24].

Stiffness elastic moduli (GPa)									
Derivation method	c_{11}	c_{22}	c_{33}	c_{12}	c_{23}	c_{13}	c_{44}	c_{55}	c_{66}
Energy-strain	388	345	322	156	162	164	15	134	134
Stress-strain	395	347	325	158	163	169	18	134	135
Phonon	384	325	283	-	-	-	26	134	125

3. Results of molecular dynamics simulations

We make use of a recently-proposed bond-order interatomic potential for the iron-carbon system [2] in order to obtain the tensile strength of plain Fe_3C . The numerical integration of motion equations employs a time increment, Δt , of 0.5 fs. The Nosé-Hoover thermostat was used for temperature control. The generated samples were cementite single crystals formed by 120 unitary cells. After generation, samples were relaxed at 300 K during 5.5 ps. After relaxation, the sample dimensions were $2.4 \times 2.7 \times 2.6 \text{ nm}^3$. Periodic boundary conditions were along the three axes. In each of the performed simulations, a different system dimension (lying along [100], [010] or [001]) was moved at constant speed equivalent to $d\epsilon/dt \approx 10^8 \text{ s}^{-1}$, while the other two remained the same. All the atoms of the system could freely move.

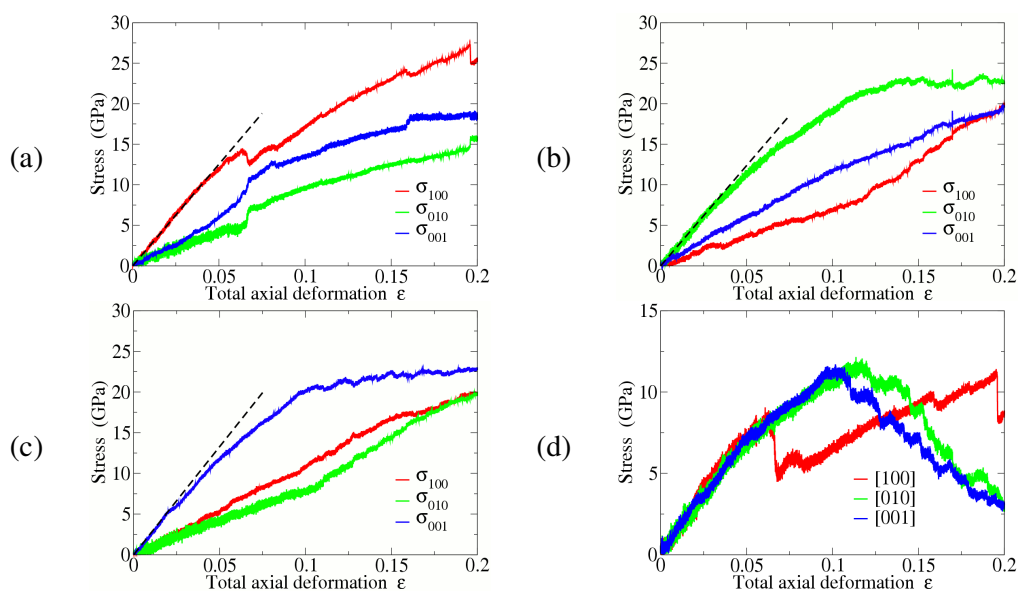


Figure 1. Stress-strain response of the cementite (a) stress-constrained along [100], (b) stress-constrained along [010] and (c) stress-constrained along [001]. (d) Von Mises equivalent stress vs. ϵ for the different constrained-stress directions.

Fig. 1.a-c shows the mechanical response of cementite to the applied strain along different directions. Not only the stress corresponding to the strained direction is shown, also the other two perpendicular stress terms are presented. Due to the boundary conditions applied to the system, the attained state of stresses with a very high hydrostatic component. To avoid this effect, we calculate the corresponding von Mises equivalent stress (Fig. 1.d). Simulations

yield a Young modulus along [100], [010] and [001] of 251 GPa, 247GPa and 266 GPa, respectively. Considering the von Mises equivalent stress, cementite strength is about 12 GPa.

Acknowledgements

This work was supported by the Basque Government (Eortek inanoGUNE IE08–225 and IE09–243) and the Spanish Ministry of Science and Innovation (Consolider nanoGUNE CSD2006 – 0053).

References

- [1] H. Ledbetter, *Mater. Sci. Eng. A* 527 (2010) 2657.
- [2] K.O.E. Henriksson, K. Nordlund, *Phys. Rev. B*, 79 (2009) 144107.
- [3] W. W. Webb, W. D. Forgeng, *Acta Metall.* 6 (1958) 462.
- [4] M. Umemoto, Y. Todaka, K. Tsuchiya, *Mater. Sci. Forum* 426-432 (2003) 859.
- [5] M. Umemoto, Y. Todaka, T. Takahashi, P. Li, R. Tokumiya, K. Tsuchiya, *Mater Sci. Eng. A* 375 (2004) 894.
- [6] T. Terashima, Y. Tomota, M. Isaka, T. Suzuki, M. Umemoto, Y. Todaka, *Scripta Mater.* 54 (2006) 1925.
- [7] M.C. Shaw, *Metal Cutting Principles*, 3rd. Ed., MIT Press, Cambridge, MA, USA (1960).
- [8] M.J. Collins, D.A. Woodford, *J. Iron Steel Inst.* 203 (1965) 184.
- [9] H. O'Neill, *Hardness Measurement of Metals and Alloys*, 2nd. Ed., Chapman & Hall, London (1967).
- [10] M. Yakushiji, K. Yoshiyuki, H. Matsumoto, T. Okamoto, *J. Japan Inst. Met.* 39 (1975) 606.
- [11] A. Inoue, T. Ogura, T. Masumoto, *Trans. Japan Inst. Met.* 17 (1976) 663.
- [12] A. Inoue, T. Masumoto, *Trans. ISIJ* 17 (1977) 143.
- [13] A. Kagawa, T. Okamoto, *J. Mater. Sci.* 18 (1983) 225.
- [14] H. Mizubayashi, S.J. Li., H. Yumoto, M. Shinotomai, *Scripta Mater.* 40 (1999) 773.
- [15] S. Li, H. Yumoto, M. Shinotomai, *J. Japan Inst Met.* 64 (2000) 134.
- [16] M. Umemoto, Z.G. Liu, H. Takaoka, M. Sawakami, K. Tsuchiya, K. Masuyama, *Metall. Mater. Trans A* 32A (2001) 2127.
- [17] M. Umemoto, Z.G. Liu, K. Masuyama, K. Tsuchiya, *Scripta Mater.* 45 (2001) 391.
- [18] Y. Tomota, P. Lukás, D. Neov, S. Harjo, Y.R. Abe, *Acta Mater.* 51 (2003) 805.
- [19] Y. Tomota, T. Suzuki, A. Kanie, Y. Shiota, M. Uno, A. Moriai, N. Minakawa, Y. Morii, *Acta Mater.* 53 (2005) 463.
- [20] A. Kanie, Y. Tomota, T. Suzuki, S. Torii, A. Moriai, N. Minakawa, *J. Soc. Mater. Jpn.* 53 (2004) 772.
- [21] A. Kanie, Y. Tomota, S. Torii, T. Kamiyama, *ISIJ Int.* 44 (2004) 1961.
- [22] M.L. Martinez-Perez, F.J. Mompean, J. Ruiz-Hervias, C.R. Borlado, J.M. Atienza, M. Garcia-Hernandez, M. Elices, J. Gil-Sevillano, Ru Lin Peng, T. Buslaps, *Acta Mater.* 52 (2004) 5303.
- [23] K. Van Acker, J. Root, P. Van Houtte, E. Aernoudt, *Acta Mater.* 44 (1996) 4039.
- [24] C. Jiang, S. Srinivasan, A. Caro, S. Maloy, *J. Appl. Physics* 103 (2008) 043502.
- [25] E. Duman, M. Acet, T. Hulser, E. F. Wassermann, B. Rellinghaus, J. P. Itie, and P. Munsch, *J. Appl. Phys.* 96 (2004) 5668.
- [26] J. Li, H. K. Mao, Y. Fei, E. Gregoryanz, M. Eremets, C. S. Zha, *Phys. Chem. Minerals* 29 (2002) 166.
- [27] H. P. Scott, Q. Williams, E. Knittle, *Geophys. Res. Letters*, 28 (2001) 1875.

Grain-Boundary Shear-Coupled Migration Affected By Intergranular Nanocracks

A. Luque, J. Aldazabal, J.M. Martínez-Esnaola, J. Gil Sevillano

CEIT and Tecnun (University of Navarra)

Manuel de Lardizábal 15. 20018 San Sebastián, Spain.

E-mail: jgil@ceit.es. Phone: +34943212800. Fax: +34943213076.

ABSTRACT

We have carried out simulations of molecular dynamics of bicrystalline samples presenting symmetrical tilt boundaries $\Sigma 17(530)$ perturbed by nanocracks lying on the grain boundary. The simulations were performed for copper at 300 K. We have studied how the crack size can affect the shear-coupled migration of the boundary. The embedded atom method was used and Nosé-Hoover thermostat was implemented. Periodic boundary conditions were set along the direction of application of the load and the tilt axis. Systems of constant width, X , and different crack sizes, $2a$, were generated. After relaxation, bicrystals were sheared at constant rate of 10^8 s^{-1} . The response of the cracked specimens follows the sequence: (i) shear-coupled migration of the grain boundary with increasing applied shear stress, (ii) intergranular crack propagation and (iii) dislocation emission and closing of the grain boundary dislocation loop.

1. Introduction

Shear-coupled migration (SCM) [1] of grain boundaries (GB) is a particular plastic strain mechanism that can either collaborate or compete with the other plastic mechanisms available to polycrystals: dislocation-mediated slip, GB sliding, twinning... SCM occurs diffusionless but it is thermally activated. It takes place at relatively low temperatures by collective atomic motion under high shear stress. This phenomenon implies that, as a shear stress τ is applied parallel to the GB, the GB migrates perpendicular to GB plane, inducing in the swept volume of the adjacent crystal a shear strain parallel to the boundary which magnitude is dictated by the bi-crystallography. The effectiveness of the applied shear stress is given in terms of the shear-coupling factor, β , the ratio of the shear displacement to the normal displacement of the GB, which is related to the dislocation content of the GB and to the GB misorientation [2]. This phenomenon is observed at both low and high misorientation angles, although there is a transition from “positive” to “negative” coupling at 35° - 40° : the sense of the GB migration changes (upwards vs. downwards, if τ is applied in the same sense) if that threshold is overcome. SCM has an active role in the mechanical behaviour of nanostructured materials. It is also important considering the changes (grain growth during nanoindentation and fatigue) in this type of materials, under the effect of high stress at low temperatures. Note that SCM requires high resolved shear stresses which are not available in polycrystals with conventional grain size. Hence, it is essential to understand and to master the SCM of GB in nanostructured materials to warrant their structural stability

2. Characteristics of the simulations

The MD technique used was the embedded atom method (EAM) and the potentials correspond to copper. Further details of both this MD technique and these potentials can be

found elsewhere [3]. The cut-off radius, r_{cut} , of the atomic interactions is 0.55 nm. The numerical integration of motion equations employs a time increment, Δt , of 2.5 fs. The Nosé-Hoover thermostat was used for temperature control. The generated samples were bicrystals presenting a symmetrical tilt boundary $\Sigma 17(530)/[001]$, where the first Miller indices indicate the GB plane and correspond to the y axis. The following Miller indices are the tilt axis and correspond to the $-z$ direction. The crack is contained in the same plane and the tip lies on the same direction. $\Sigma 17(530)$ is a symmetrical tilt boundary of high-angle misorientation (61.9°), yielding a shear-coupling factor of $\beta = -0.5$ (planar free GB).

Uncracked and cracked samples (three of each) were constructed at 0 K. For the uncracked samples, the X dimension is 4.2 nm, 10.6 nm or 14.9 nm. The Y dimension is 8.4 nm, 21.1 nm or 29.2 nm. The Z dimension is 2.2 nm. Cracked sample dimensions are $10.6 \times 21.1 \times 2.2 \text{ nm}^3$. Nanocracks were formed by removing the atoms of a 0.55 nm thickness band, centred in the GB, along 1/2, 1/3 and 1/4 of the specimen along the x axis, determining the crack size, $2a$ (Fig. 1.b). After generation, samples were relaxed: first at 0 K during 5 ps, then, along a linear temperature increase up to 300 K during 7.5 ps, and, finally, at 300 K for 12.5 ps. Some geometrical distortion of the initial shape, particularly, at the crack tip, could be observed. After relaxation, two rigid zones of 0.55 nm of thickness were set in the top and bottom layers of the samples. During the simulations, the bottom layer remained fixed, the top rigid zone was displaced along the x axis at constant speed equivalent to $d\gamma/dt \approx 10^8 \text{ s}^{-1}$, and the rest of atoms could move freely. Periodic boundary conditions were set along the x and z axes.

3. Results and discussion

The imposed shear displacement and the resulting force were stored during the simulations. Atomic positions were also periodically stored to analyse any structural changes [4]. We used the virial expression for calculating the applied stress tensor and, in particular, the term τ_{xy} . A modified virial expression [5] was used for representing the local stress. This modification accounts for the fraction of atomic bond length within a representative volume (in this case, a sphere of diameter equal to twice the lattice parameter) around a particular atom.

On one hand, the obtained τ - γ response for the three uncracked bicrystals coincides with what has already been reported [5,6]. It is important to note that $\beta \approx -0.5$, with (intermittent) elastic loading slopes very similar to the theoretical elastic shear modulus (27.3 GPa, for a single crystal, accounting for the sample orientation and the elastic anisotropy of copper). The SCM of a perfect flat GB is associated with a stick-slip phenomenon characterized by a critical value of τ of ~ 0.4 GPa. On the other hand, the observed τ - γ response for the three cracked bicrystals at 300 K (Fig. 1.a) indicates that the presence of cracks significantly affects the mechanical behaviour of the samples. The cracked samples are strengthened by the intergranular cracks. Initially ($\gamma < 0.05$ - 0.07), the cracked samples behave as the uncracked specimens, showing an elastic behaviour followed by the mentioned stick-slip behaviour associated with a SCM event when a critical value of τ is reached. However, in the cracked samples, τ needs to be increased to produce further deformation. The intergranular cracks pin the GB and, hence, the SCM can only take place away from the crack tips, making the GB to bow out (Fig. 1.c). As the misorientation between the GB and the crack tip increases, further GB migration becomes more difficult. When the angle formed by the GB and the crack plane is $\sim 31^\circ$, a different deformation mechanism activates: propagation of the crack can be observed (Fig. 1.d). That occurs at $\gamma = 0.055$ and 0.073 for the samples with $2a/X = 1/2$ and $1/3$, respectively, but it is absent from the one with $2a/X = 1/4$. Thus, there must also be a significant contribution of the crack length and, hence, the stress concentration to this

phenomenon. The crack opening close to the crack tip produces different events of dislocation-mediated intergranular fracture. Further crack propagation is hindered and the SCM mechanism is enabled again, which produces a further increase in the applied stress (up to 2 GPa). Then, dislocation emission takes place at $\gamma = 0.111$ and 0.119 for the samples with $2a/X = 1/3$ and $1/4$, respectively. However, it is not observed in the cracked sample of $2a/X = 1/2$ as τ is not high enough. The dislocations emitted are partial in the $\{111\}\langle 211\rangle$ system. They propagate in the bottom crystal until the GB dislocation loop closing (Fig. 1.e). This permits forming a new GB underneath the crack and makes the pinning effect disappear (in the sample of $2a/X = 1/3$, this is facilitated by the reduction of the crack size). Once the GB gets to detach from the crack, the sample deformation is accommodated by SCM (Fig. 1.f) at τ values of the same order of the critical τ value for uncracked samples. Finally, in the sample of $2a/X = 1/2$, where dislocation nucleation does not occur, a different mechanism activates: GB slip, which is also possible due to the reduced ligament dimension.

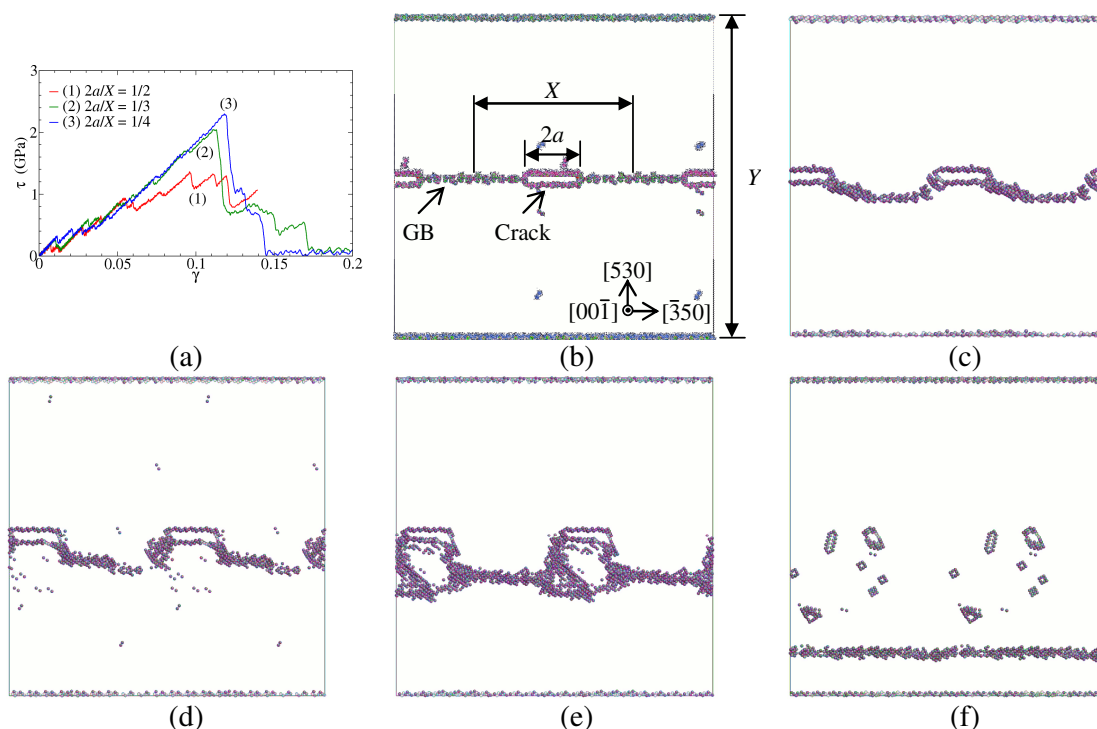


Fig. 1. (a) Shear stress - shear strain response of the cracked Cu bicrystals presenting a symmetrical tilt boundary $\Sigma 17(530)/[001]$ at 300 K. Detail of the sample of $2a/X = 1/3$: (b) $\gamma = 0$, (c) $\gamma = 0.07$, (d) $\gamma = 0.11$, (e) $\gamma = 0.12$ and (f) $\gamma = 0.2$.

The stress distribution ahead of the crack front during crack propagation will now be analysed. It should be reminded that, connaturally to the atomistic simulations, the position of the “crack tip” is not well defined, and concepts such as “sharp crack” have no sense here. However, the tip position can be bounded in the crack propagation plane. For this reason, the origin of the distances r to the crack tip has been considered as a fitting parameter. Thus, we calculate the (atomically) local stress, accounting for a local coordinate system in which crack propagation takes place along the 1 direction (Fig. 2.a). In this coordinate system, the stress components τ_{13} , τ_{23} and τ_{33} are nearly zero or small compared with the other stress terms (Fig. 2), and hence, they are not presented here. σ_2 can be fitted with a power-law function of r . For both samples, $\sigma_2 \propto r^{-1/2}$, which corresponds to the linear elastic solution proposed in the continuum for a sharp crack [5]. This is in line with other atomistic fracture results which permit expressing the opening displacement, Δu_2 , of the atoms in the crack faces ($\theta = \pm\pi$) in terms of $r^{1/2}$ [3]. The fits of this work yield a critical stress intensity factor, K_{Ic} , ranging

between $30 \text{ kPa}\sqrt{\text{m}}$ and $65 \text{ kPa}\sqrt{\text{m}}$. Although small, these values are of the same order of other K_{Ic} calculated on a stress basis, reported for heterogeneous dislocation nucleation in other crystal orientations, at the same temperature [3]. This indicates that crack propagation process is dislocation mediated and the generated dislocations are accommodated in the GB.

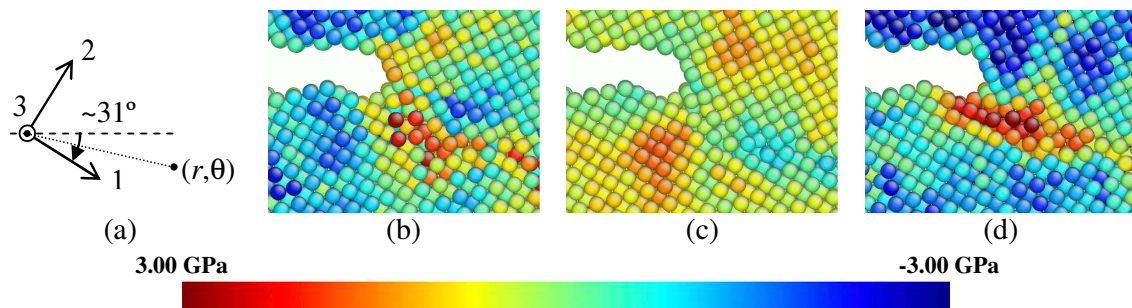


Fig 2. (a) Local coordinate system. (b) σ_1 , (c) τ_{12} and (d) σ_2 , for the cracked Cu bicrystal ($2a/X = 1/3$) presenting a symmetrical tilt boundary $\Sigma 17(530)$ with $\gamma = 0.074$ at 300 K.

4. Conclusions

The shear-coupled migration of the symmetrical tilt boundary $\Sigma 17(530)$ is hindered by the presence of intergranular cracks. The tilt boundary is pinned by crack tip and migration occurs with the bowing-out of the grain boundary. The applied shear stress needs to be increased above the critical value that makes a flat boundary migrate. Hence, nanocracks strengthen the material. Intergranular crack propagation is observed, which permits further advance of the grain boundary. The stress ahead of the crack behaves as $r^{-1/2}$, as proposed within the linear elastic solution for sharp cracks. The applied shear stress grows and activates new plastic deformation mechanisms, such as dislocation emission or grain boundary sliding. Dislocation emission and further shear-coupled migration occur. Finally, the boundary detaches from the crack tip and, in some cases, the smaller cracks disappear.

Acknowledgements

This work was supported by the Basque Government (Eortek inanoGUNE IE08–225 and IE09–243) and the Spanish Ministry of Science and Innovation (Consolider nanoGUNE CSD2006 – 0053).

References

- [1] A. Luque, J. Aldazabal, J.M. Martínez-Esnaola, J. Gil Sevillano, *Philos. Mag.* (2009), DOI 10.1080/14786430903097715.
- [2] J.W. Cahn, Y. Mishin, A. Suzuki, *Acta Mater.* 54 (2006) 4953.
- [3] A. Luque, J. Aldazabal, J.M. Martínez-Esnaola, J. Gil Sevillano, *Fatigue Fract. Engng. Mater. Struct.* 30 (2007) 1008.
- [4] J. Li, *Modell. Simul. Mater. Sci. Eng.* 11 (2003) 173.
- [5] A. Irastorza, A. Luque, J. Aldazabal, J.M. Martínez-Esnaola, J. Gil Sevillano, *Anales de Mecánica de la Fractura* 27 (2010) 491.
- [6] A. Luque, J. Aldazabal, J.M. Martínez-Esnaola, J. Gil Sevillano, *Phys. Status Solidi C* 6 (2009) 2107.

Simulation of the Deformation and Failure Behavior of Bronze Particle filled PTFE Compounds

Franz Hiptmair¹, Martin Reiter¹ and Zoltan Major¹,

**¹Institute of Polymer Product Engineering,
Johannes Kepler University Linz
Altenbergerstrasse 69, 4040 Linz, Austria**

ABSTRACT

Micromechanical simulations on bronze particle filled PTFE-Bz compounds were performed using a novel commercial software tool (Digimat, e-Xstream, Foetz, LX) in this study. These materials are frequently used in many tribological applications. While the homogenization method was used to characterize the temperature dependent deformation behavior as well as the heat conductivity performance of various model PTFE-Bz compounds, the finite element method was applied for modelling the local stress-strain state of the matrix during shear deformations. The inherent temperature dependence of the mechanical behaviour was considered up to 200 °C. Finally, shear stress-strain curves have been determined in finite element models.

1. Introduction

Particle filled PTFE compounds are frequently used for seals and gaskets in various engineering applications. The tribological properties of PTFE (low strength and wear resistance, insufficient heat conductivity) were improved by additional fillers. Particularly, microscopic size bronze particles are commonly used as fillers in PTFE compounds for various tribological applications. These PTFE compounds (PTFE-Bz) are microscopically inhomogeneous materials, revealing higher stiffness, strength and better heat conductivity than neat PTFE. Previous investigations [1] have shown that the distribution of the particle size plays an essential role in the quality of the tribological function for these materials. Materials having a bimodal particle structure on the contact surface revealed the optimum friction and wear performance.

To gain more insight into these dependences and to support further material development efforts micromechanical simulations were performed using a novel commercial software tool (DigiMat, eXstream, Foetz, LX). While the homogenization method was used to characterize the temperature dependent deformation behavior and the heat conductivity performance of various model PTFE-Bz compounds, the finite element method was applied for modeling the local stress-strain state of the matrix during shear deformations.

The properties of the PTFE model matrix were varied in the range of different existing materials considering the significant temperature dependence (from -15 °C to 200 °C) for these materials and two different bronze particle fillers (shape and size distribution) were applied. To characterize the effect of particle size and aspect ratio on the thermo-mechanical behaviour, both unimodal and bimodal particle size distributions and two different aspect ratios of these particles were used. The results of the simulations are described in terms of nominal stress-strain and shear stress strain curves and in terms of principal stresses and strains in the matrix between the particles.

2. Experimental Data

To determine proper material data for the simulation, monotonic compression tests were performed on both unfilled and bronze particle reinforced (PTFE-Bz) compounds over a wide test temperature range (-20 to 200 °C). Temperature dependent compressive modulus values are shown for both unreinforced PTFE matrix and for PTFE-Bz compounds in Fig 1. While the PTFE matrix data were used as input data for the simulation, the experimental results of PTFE-Bz compounds were compared with the simulation results.

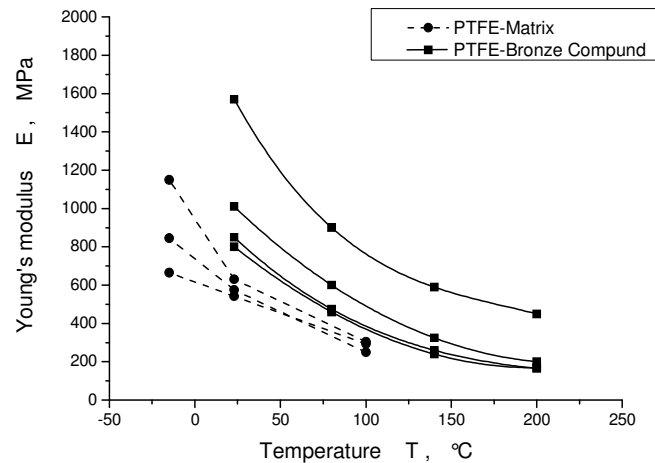


Fig.1: Comparison of experimental data for various PTFE-matrix materials and PTFE-Bronze compounds

The PTFE matrix was produced using various sintering parameters (SKF Economos Austria GmbH, Judenburg, A) and the dashed lines correspond to the specific values and reflect the range for the mechanical behaviour. Furthermore, different fillers and additional additives were applied in the compounds and the solid lines reflect the range for the compression behaviour over a wide test temperature range. The deviation between the various samples gives an indication of the contrast between compounds with good or bad mechanical properties.

3. Micromechanics Simulations by Homogenization

To estimate the mechanical properties of various PTFE-Bronze compounds at different temperatures for a specific volume fraction, a series of Digimat-MF simulations has been carried out using an elastic material model and the parameters necessary are listed in Table 1. The PTFE modulus values were determined in compression tests and the remaining input parameters were taken from the literature [2; 3; 4].

Table 1: Temperature dependent input parameters used for the mechanical analysis:

		-15 °C	23 °C	100 °C
Matrix	Young's modulus	1150	630	305
	PTFE-F300	Poisson's ratio	0.45	0.46
Inclusions	Young's modulus	108000	105000	103000
	Bronze(CuSn10Zn2)	Poisson's ratio	0.343	0.345

For both Matrix- and Inclusion-phase an Elastic-isotropic material behaviour was assumed and for the Mean-field homogenization the Double-Inclusion model was applied [5]. Initially the inclusions were taken to be spherical (solid lines in Fig 2). Since bronze particles often show slightly irregular shapes, randomly orientated inclusions with an aspect ratio of 2 have been modelled as well (dashed lines).

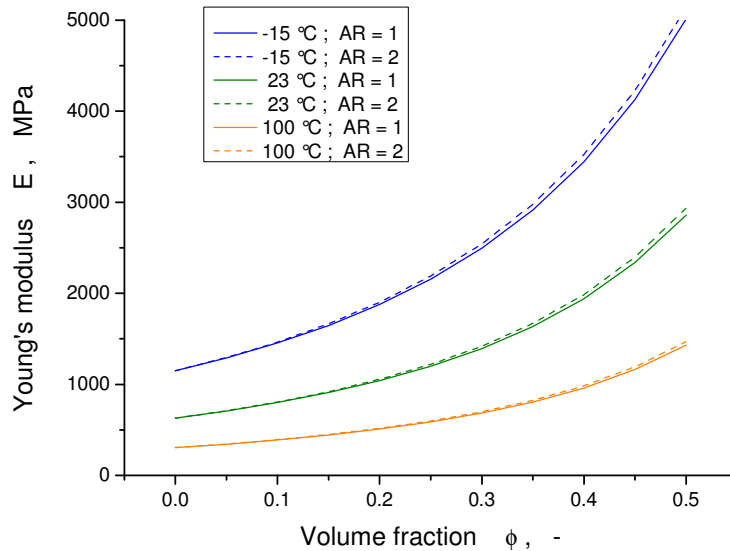


Fig. 2: Particle volume fraction dependence of Young's modulus at various temperatures and for AR 1 & 2

As one would expect, the modulus increases with increasing volume fraction of bronze fillers. The simulation also shows that compounds which have inclusions with an aspect ratio greater than unity feature a slightly higher elastic modulus than compounds with spherical inclusions.

4. Thermal conductivity simulation by Homogenization:

The heat conductivity performance of various model PTFE-Bz compounds has been simulated in Digimat-MF using Fourier's law. The input parameters (heat conductivities for matrix and inclusion materials) were taken from the literature [2; 3; 4]:

$$\lambda_{\text{PTFE}} = 0.25 \text{ W/(mK)} ; \lambda_{\text{Bronze}} = 74 \text{ W/(mK)}$$

Again the Double-inclusion model was used for the homogenization because preliminary trials have shown it gives the best predictions for this study and in addition it is not restricted to small volume fractions. To cover a wide range of material properties, the aspect ratio and orientation of the inclusion particles have been varied in the analysis: spherical inclusions (full lines, Fig 3); inclusions uniformly distributed around an AR of 2 and randomly orientated (dashed lines); same as before, but slightly orientated (tensor: $a_{11} = 0.5$; $a_{22} = 0.25$; $a_{33} = 0.25$) (dotted lines).

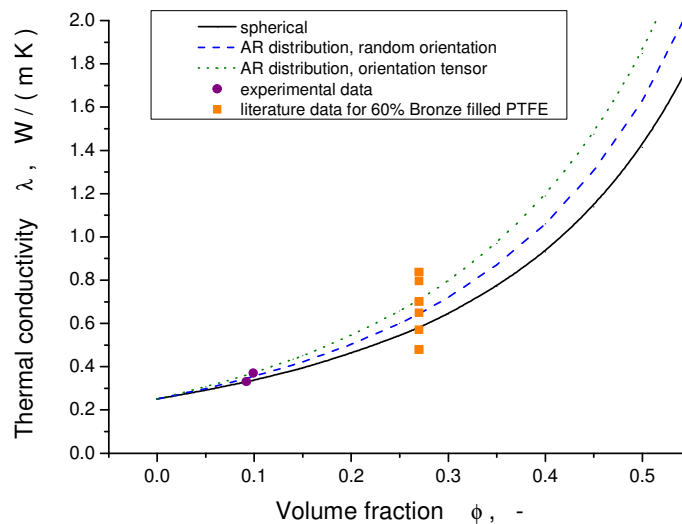


Fig. 3: Particle volume fraction dependence of the thermal conductivity

The calculated values were compared with experimental data [1] (round dots, Fig 3) as well as literature data (thermal conductivity data for a 60 m% bronze filled PTFE, obtained from data sheets of various suppliers; a compilation of such data can be found in [3]) (quadratic dots). The calculated heat conductivities were found to be in excellent agreement with available experimental and literature data.

5. Micromechanics Simulations by Finite Elements

Two μ -cells, one with an unimodal and one with a bimodal particle size distribution have been generated and the finite element method was applied for modelling the local stress-strain state of the matrix during shear deformations. While the unimodal distribution has a mean value of 10 μm , the bimodal distribution is divided evenly between two Gauss-curves with 2 and 10 μm as mean values. The RVE itself is $50 \times 50 \times 50 \mu\text{m}^3$ in size. For the Finite element analysis periodic boundary conditions were applied, the mechanical input parameters were taken from Tab 1 (23 °C).

The volumetric means for shear stress and shear strain were calculated by post-processing of both μ -cells. The resulting stress-strain curves for unimodal and bimodal particle distribution were found to be almost identical.

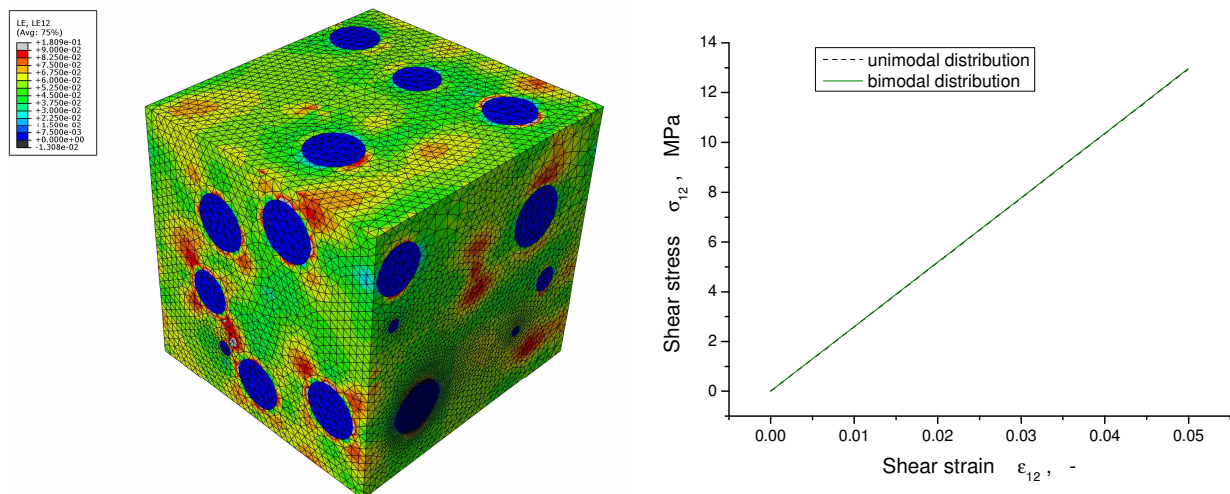


Fig. 5: Left: μ -cell with bimodal particle distribution under 5% shear-deformation
Right: Comparison of shear stresses for unimodal and bimodal particle distribution

References

- [1] Godor I., Major Z., Vezer Sz., Grün F.: Experimental definition of a failure model for the tribological behaviour of polytetrafluoroethylene bronze compounds; Proc. IMechE, **223**: 807 (2009)
- [2] DuPont-Fluoroproducts: *Teflon PTFE properties handbook*; Tech. Rep. H-37051-3; DuPont (1996)
- [3] Ebnesajjad S., Khaladkar P. R.: *Fluoropolymer Applications in the Chemical Processing Industries: The Definitive User's Guide and Databook Summary*, Plastics Design Library (2005)
- [4] Cardarelli F.: *Materials Handbook: A Concise Desktop Reference*; 2nd Edition; Springer; London (2008)
- [5] Digimat 4.0.2 Manual; e-Xstream engineering; (2010)

Laue diffraction spots obtained from 3D dislocation dynamic simulations

J. Martinez-Garcia¹, J. Senger², H. Van Swygenhoven¹ and D. Weygand²

¹ Paul Scherrer Institut (PSI), CH-5232 Villigen, Switzerland

² Institut für Zuverlässigkeit von Bauteilen und System (IZBS), Karlsruhe Institute of Technology (KIT), Kaiserstr. 12, 76131 Karlsruhe, Germany
Jorge.martinezgarcia@psi.ch

White beam Laue diffraction is nowadays a well-established technique for studying the microstructure of materials. Valuable information on the dislocation distributions appearing in the sample during plastic deformation, for instance, can be directly inferred from the shape and position of the diffraction spots. So far the experimentally observed features of the spots (i.e. streaking and splitting) has been explained on the basis of simple dislocations models, assuming random distributions of straight-line dislocations. In the present work, we attempt instead to describe the main features of Laue diffraction spots calculated from dislocation arrangements generated by 3D dislocation dynamics simulations as well as to discuss the main potentiality of this new computational approach.

Reconstruction of dislocations in interface layer Cu-Al₂O₃

Marcin Maździarz, Kinga Nalepka Paweł Dłużewski and Jan Cholewiński

Institute of Fundamental Technological Research Polish
Academy of Sciences, Pawińskiego 5B, 02-106 Warsaw, Poland
mmazdz@ippt.gov.pl Kinga.Nalepka@ippt.gov.pl pdluzew@ippt.gov.pl
jcholew@ippt.gov.pl

ABSTRACT

Using three different methods namely, CDT (Continuous Dislocation Theory), molecular TB-SMA (Tight Binding Second Moment Approximation) type many-body potential, and MEM (Molecular Effective Medium) theory, we are looking for the best possible reconstruction of dislocations in Cu-Al₂O₃ heterostructure.

1. Introduction

The issue of assessing the strength and functionality of heterostructures metal - ceramic is very important both from a cognitive, as well as from a practical point-of-view.

An important, often decisive factor is knowledge of the limit state in the transitional metal – ceramic layer (interface) .

The subject of our modeling is the mismatch dislocation structure - such as those formed in the case of crystal growth of copper on the surface of sapphire (Al₂O₃).

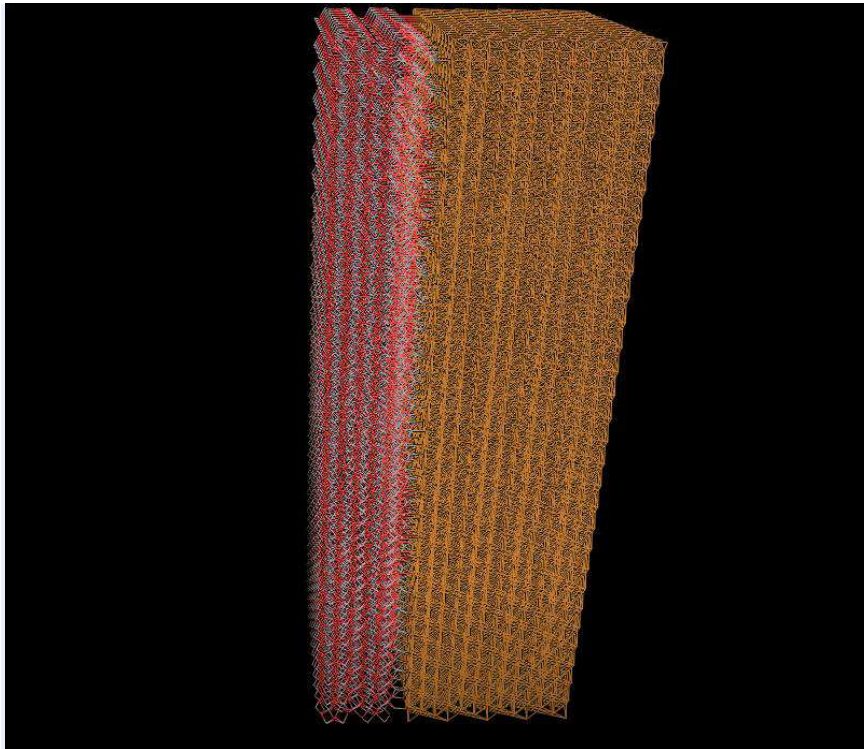


Fig.1. Copper on the surface of sapphire (Al₂O₃)

On the basis of existing experimental research conducted by high-resolution transmission electron microscopy (HRTEM) there is some knowledge available about the system of dislocations resulting from the mismatch between sapphire and copper [1].

We want to reconstruct the system of dislocations in the interface using various methods and compare the results. These methods are:

-Algorithm from Continuous Dislocation Theory based on newly derived analytical models for the insertion of dislocations to the continuum [2,3].

-Atomic method based on the model TB-SMA type many-body potential [1,4,5,6].

- Atomic method based on the original atomic model, in which the interaction occurring inside the layers of the Cu- Al₂O₃ interface will be formulated in accordance with the concept of the method of Effective Medium Theory [7,8].

2. The methods

2.1 Continuous Dislocation Theory - analytical equations for mixed straight dislocation

The displacement field around a mixed straight-line dislocation in an elastic material is defined by the classical formulas [2,3]

$$\begin{aligned}
 u_x &= \frac{b_x}{2\pi} \left(\arctan \frac{y}{x} + \frac{xy}{2(1-\nu)(x^2+y^2)} \right) - \frac{b_x}{2} \\
 u_y &= -\frac{b_x}{2\pi} \left(\frac{1-2\nu}{4(1-\nu)} \ln(x^2+y^2) + \frac{x^2-y^2}{4(1-\nu)(x^2+y^2)} \right) \\
 u_z &= \frac{b_z}{2\pi} \arctan \frac{y}{x} - \frac{b_z}{2}
 \end{aligned} \tag{1}$$

where the edge and screw components of the Burgers vector , b_x and b_z , are parallel to the x and z axes, respectively. Using the analytical equations of displacement field induced by discrete dislocations Eqn.1 we introduced dislocations into Cu- Al₂O₃ structure.

2.2. Tight-binding second moment approximation type many-body potential

In the TB-SMA approach [1,4,5,6] potential energy per atom is a sum of the repulsive energy E_{rep} , and the binding energy E_b :

$$E_{rep} = A \sum_i \exp \left(-p \left(\frac{r_i}{r_0} - 1 \right) \right) \tag{2}$$

$$E_b = -\xi \sqrt{\sum_i \exp\left(-2q\left(\frac{r_i}{r_0} - 1\right)\right)}$$

where r_0 is the distance between nearest neighbours at zero temperature and r_i is the distance of i atom from the considered one, A ; p , ξ and q are free parameters. Parameters are identified by elastic eigen-states approach [8] and differ from the values assumed by Dimitriev [1] but better reproduce energy density of the ideal crystal.

2.3 Potential based on Effective Medium Theory

Using Effective Medium Theory [7] we formulated original embedded-atom method (EAM) potential for Cu-Al₂O₃. The covalent and metallic interactions occurring in the ceramic layer and metal layer are described correspondingly:

$$E_n = \sum_{i=1}^N F_i(\rho_i) + \frac{1}{2} \sum_{i=1}^N \sum_{j=1}^N \Phi_{ij}(r_{ij}) \quad (3)$$

The function F_i is the energy of embedding of the i -th atom in the electron density ρ_i and Φ_{ij} is the energy of interaction of pair of atoms. EAM potential can be treated as a more flexible generalization of TB-SMA approach. To parameterize above potential elastic eigen-states approach was used with two kinds of tensile tests: so called relaxed tensile test, the sample cut off from the surroundings of the interface is being stretched in the direction normal to the interface and so called rigid tensile test.

3. Conclusions

We presented three methods of the reconstruction of dislocations in Cu-Al₂O₃ heterostructure. First, the analytical one, where equations of displacement field induced by discrete dislocations are used. Next two utilize molecular approach and respectively are based on tight-binding second moment approximation potential and embedded-atom potential.

Using these methods, a relaxed structure with minimal energy will be further chosen for nanoindentation simulation in which the behaviour of the dislocation structure if nonequilibrium configuration is investigated.

Acknowledgments

The research has been done in the framework of the Development Project N N501 156638 and R15 012 03 founded by Ministry for Science and Higher Education in Poland.

4. References

- [1] S.V. Dmitriev, N. Yoshikawa, M. Kohyama, S. Tanaka, R. Yang, Y. Tanaka, Y. Kagawa., *Modeling interatomic interactions across Cu/ α -Al₂O₃ interface*, *Comp. Mater. Sci.*, 36, 281-291, 2006
- [2] E. Kröner *Allgemeine Kontinuumstheorie der Versetzungen und Eigenspannungen*, *Arch. Rat. Mech. Anal.*, 4 (1960) 273–334.
- [3] P. Dłużewski, T.D. Young, G.P. Dimitrakopoulos, and P. Komninou. *Continuum and atomistic modelling of the mixed straight dislocation*. *International Journal for Multiscale Computational Engineering*, 8(3), 331–342, 2010.
- [4] V. Rosato, M. Guillope, B. Legrand, *Thermodynamical and structural properties of f.c.c transition metals using a simple tight-binding model*, *Phil. Mag.* 59, 321, 1989.
- [5] P. Dłużewski, M. Maździarz, G. Jurczak, P. Traczykowski *A hybrid atomistic-continuum finite element modelling of nanindentation and experimental verification for copper crystal*. *CAMES*, 15, 2008.
- [6] M. Maździarz, T.D. Young, P. Dłużewski, T. Wejrzanowski, and K.J. Kurzydłowski. *Computer modelling of nanoindentation in the limits of a coupled molecular–statics and elastic scheme*. *Journal of Computational and Theoretical Nanoscience* 7, 1-10, 2010.
- [7] K.W. Jacobsen, J.K. Norskov, M.J. Puska, *Interatomic interactions in the effective-medium theory*, *Phys. Rev. B* 35, 7423-7442, 1987
- [8] K. Nalepka, R.B. Pęcherski, *Modelling of the interatomic interactions in the copper crystal applied in the structure (111)Cu|| (0001)Al₂O₃*, *Archives of Metallurgy and Materials*, 54, 2, 481-492, 2009

Grain boundary energies for cubic-ZrO₂ bicrystals

**J. J. Meléndez¹, R. L. González-Romero², F. L. Cumbreira²
and D. Gómez-García²**

¹ Departamento de Física. Universidad de Extremadura. Avda. de Elvas, s/n
06006 Badajoz (SPAIN)

Email: melendez@unex.es

² Departamento de Física de la Materia Condensada, ICMSE, Universidad de Sevilla-
CSIC, P.O. Box 1065, 41080 Sevilla (SPAIN)

Zirconium dioxide-based ceramics have been extensively studied during the last years due to their use as structural and functional materials. Particularly, their mechanical (high strength at room temperatures, ability to exhibit superplastic behavior at high temperatures under some conditions) and electric (high ionic conductivity) properties have deserved much attention by the scientific and technologic communities. In polycrystals, these properties are intimately related to the nature and the physical properties of the grain boundaries. This is especially remarkable in ZrO₂ alloys, where the dopant species are well known to segregate to the grain boundaries, thus altering their behavior.

In this context, some works have paid attention to the concurrence of particular boundaries orientations (see, for instance, [1]); some others have focused on their behavior when aliovalent impurities are present (see, for instance, [2]). Despite this, the nature of the grain boundaries in ZrO₂ has not been put forth in a systematic way.

In this work, a systematic study of the grain boundary energies in a cubic-ZrO₂ bicrystal is presented. The study was carried out by Molecular Dynamics (MD) simulations of a single flat grain boundary for different orientations of the two grains and for different nature (*i.e.*, tilt or twist) of the boundary. The effect of impurities and the implications for high temperature creep are also discussed.

References:

- [1] P. Vonlanthen, B. Grobety: "CSL grain boundary distribution in alumina and zirconia ceramics", *Ceramics International*, **34** (2008), 1459-1472.
- [2] T. Oyama, M. Yoshida, H. Matsubara, K. Matsunaga: "Numerical analysis of solute segregation at $\Sigma 5$ (310)/[001] symmetric tilt grain boundaries in Y₂O₃-doped ZrO₂", *Physical Review B* **71** (2005), 224105.

Atomic- Discrete Simulation Of Crystal State Of Alloys Of A Complex Chemical Composition

Authors: Michail A. Baranov¹, Vladimir M. Shcherbakov², Evgenia V. Chernych³.

Affiliations: ¹656038, Chair of theor. mech., Altai St. Techn. Univ., Lenin str., 46, Barnaul, Russia, E-mail: Baranov183@mail.ru ; ²Altai St. Techn. Univ.;

³Altai St. Techn. Univ., E-mail: jane_5@mail.ru .

ABSTRACT

Proceeding from the assumption about spherical symmetry and undeformability of electronic shells of atoms the pair potentials describing interaction between atoms of an any sorts in a crystal of a multicomponent alloy are constructed. Chaotic disposition of atoms of different sorts on knots of crystal lattice forms its state. As the parameters of the state were considered S_m – the degree of lattice distortion and E_B – bond energy per atom. The atomic-discrete simulation of an equilibrium configuration of γ -phase crystal lattice is executed for ~30 industrially let out alloys. The calculated values of S_m and E_B correlate with experimentally observably indicators of mechanical properties of these alloys.

1. Interatomic interactions.

The electronic density ρ , accompanying each atom, was represented as sum of internal ρ_i and external ρ_e [1] subshells

$$\rho_i(R) = (n - q) \left(\frac{\beta}{\sqrt{\pi}} \right)^3 \exp(-\beta^2 R^2) \quad (1)$$

$$\rho_e(R) = \frac{q\alpha}{4\pi^3 R R_m} [\exp(-\alpha^2 (R - R_m)^2) - \exp(-\alpha^2 (R + R_m)^2)], \quad (2)$$

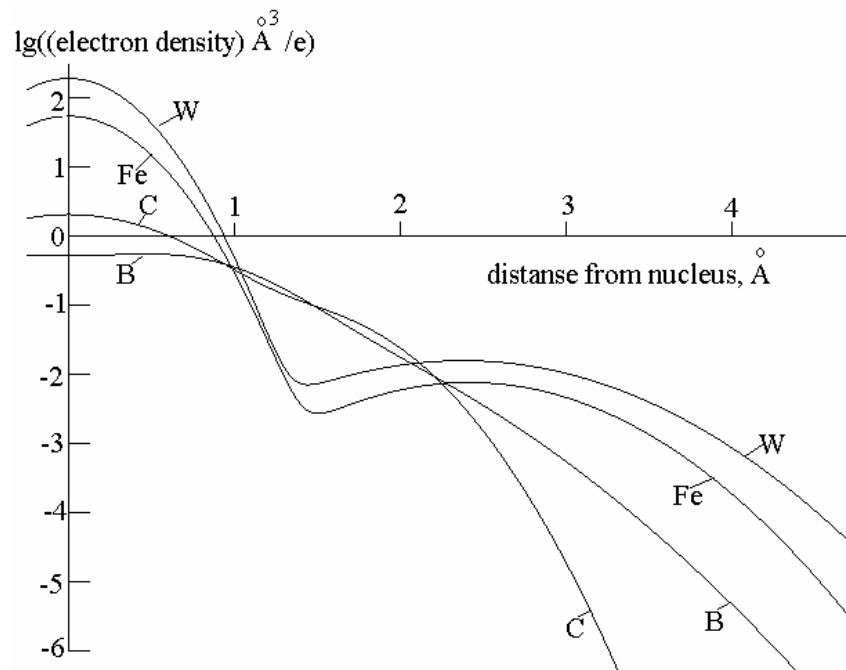


Figure 1. Dependence of the decimal logarithm of the electronic density multiplied on the \AA^3 on distance R from a nucleus for some atoms.

normalized on charges $n-q$ and q accordingly. Here n – is the charge of a nucleus expressed in elementary charges, α , β , q , R_m - parameters which have been determined from conditions of stability of unicomponent chemical aggregations. The interatomic potential was found as the sum of electrostatic energy of electronic shells and nucleus and energy of mutual repulsion of electronic shells caused by quantum effects and presented as corresponding overlapping integrals. In result the potential was expressed as complex analytical function on internuclear separation. Its parameters at the same time were parameters of electronic shells of interacting atoms. The offered approach allows to give the quantitative description of interaction between different atoms not only in crystals, but also in molecules. As an example on fig. 2 are shown the potentials of interaction between atoms of some elements.

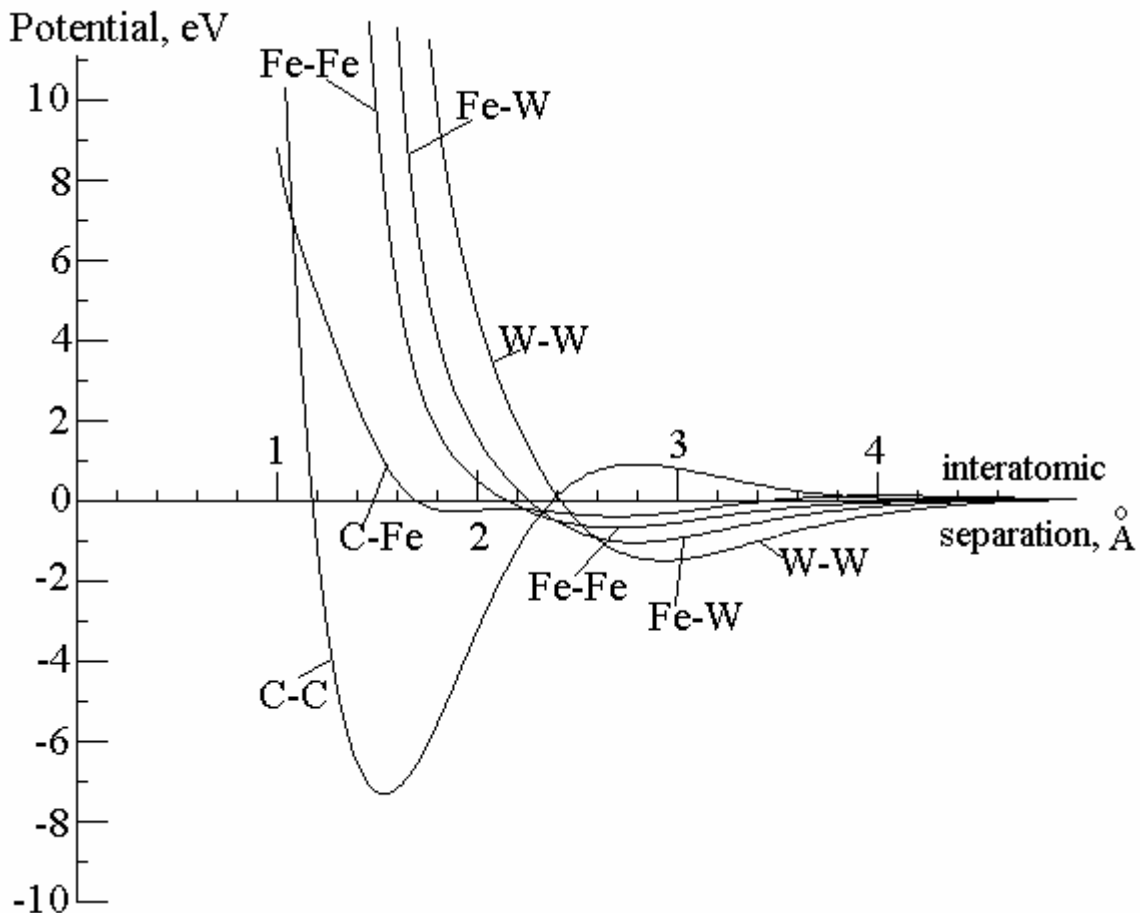


Figure 2. Interatomic potentials for some pairs of atoms.

2. Simulation of the crystal lattice state.

Overwhelming mass of modern metal materials are the steels and alloys presented by 10-15 chemical elements. The main phases (α , γ) of such alloys, as rule, are disordered crystals. Owing to chaotic distribution of atoms of various elements on knots of crystal lattices and local asymmetrical environment of each atom its equilibrium position appears displaced relatively geometrically correct position of knot. Therefore the lattice as whole appears distorted. These distortions are natural in the sense that they can not be created or eliminated by any artificial manners - heat treatment, mechanical deformation or at operation of details. For this reason the details of the machines exposed shock loadings and sharp differences of temperatures (valves, shovels of steam and gas turbines) are made of alloys of a complex chemical composition. The crystal of the basic phase of a multicomponent alloy is as though sated with a lot of chaotically distributed point defects of substitution and insertion. In this

connection it is meaningful to simulate and consider a state of a crystal as a whole instead of isolated point defect.

The modelling block was represented as a cube in the size 15x15x15 fcc cells. In a starting configuration the atoms of metals and silicon were chaotically disposed on knots of ideal fcc lattice so that the composition of the γ -phase correspond to given composition of alloy and all knots were occupied. Atoms of carbon were disposed in some of interknot positions. Then the borders of the block were fixed and atoms of inner region can to move in directions of forces acting at them to achievement of equilibrium state.

Table 1. The indicators of the mechanical properties and calculated values S_m and E_B .

N	approximate concentrations of main elements in alloy except Fe, weight %	mechanical properties				calculated parametrs	
		σ_B , MP	$\sigma_{0.2}$, MP	δ , %	HB	S_m , Å	E_B , eV
1	0.02C, 4Al, 0.2Si, 0.26Mn, 23Cr, 28Ni	490	216	30	-	0.039	4.295
2	0.03C, 0.4Si, 3Cu, 23Cr, 28Ni, 3Mo	540	216	33	200	0.044	4.388
3	0.06C, 1.4Ti, 1.5Mn, 15Cr, 36Ni, 3W	650	350	15	236	0.059	4.415
4	0.06C, 0.3Si, 1.3Ti, 15Cr, 36Ni, 4.5W	750	400	20	-	0.064	4.416
5	0.06C, 3.4Al, 0.5Si, 1.4Ti, 15Cr, 45Ni	590	215	15	-	0.050	4.378
6	0.03C, 0.3Si, 20Cr, 0.4Mn, 46Ni, 1Nb	535	205	28	159	0.041	4.381
7	0.05C, 21Cr, 46Ni, 1Nb, 4.5Mo, 3W	686	343	30	-	0.070	4.521
8	0.06C, 3Al, 0.4Si, 16Cr, 56Ni	720	360	50	-	0.049	4.389
9	0.06C, 0.4Si, 0.5Ti, 35Cr, 57Ni, 14W	750	-	30	-	0.083	4.542
10	0.03C, 6Al, 9.5Co, 1.5Nb, 3.5Mo, 9W	-	-	-	362	0.105	4.569
11	0.03C, 1Al, 14Cr, 63Ni, 5Nb, 5Mo, 5W	960	635	22	-	0.098	4.595
12	0.12C, 2Al, 1Ti, 15Cr, 6Co, 67Ni, 4Mo, 5W	-	-	-	285	0.093	4.469
13	0.03C, 5Al, 13Cr, 9Co, 59Ni, 2Nb, 5Mo, 5W	900	600	11	-	0.090	4.555
14	0.03C, 2Al, 15Cr, 6Co, 62Ni, 2Nb, 4Mo, 5W	1000	655	18	-	0.093	4.534
15	0.04C, 1Al, 2.5Ti, 18Cr, 66Ni, 5Mo, 4W	930	550	16	291	0.082	4.512
16	0.1C, 0.5Ti, 17Cr, 0.4Mn, 70Ni, 2.5Nb	680	280	22	-	0.062	4.393
17	0.13C, 2Al, 1Ti, 15Cr, 71Ni, 4Mo, 5W	980	588	20	-	0.092	4.518
18	0.07C, 2Al, 2Ti, 14Cr, 69Ni, 3Mo, 6W	670	-	3	320	0.090	4.532
19	0.07C, 3Al, 2Ti, 0.6V, 14Cr, 68Ni, 3Mo, 6W	616	-	6	320	0.091	4.520
20	0.07C, 4Al, 10Cr, 72Ni, 6Mo, 5W	588	-	6	288	0.085	4.554
21	0.07C, 20Cr, 78Ni	588	196	27	200	0.041	4.427
22	0.04C, 2Ti, 17Cr, 0.5Mn, 77Ni, 1Nb	833	441	20	-	0.059	4.443
23	0.03C, 1Si, 16Cr, 58Ni	645	264	20	-	0.048	4.555
24	0.03C, 1Si, 21Cr, 76Ni, 0.4Zr	656	-	33	-	0.044	4.550
25	0.02C, 5Al, 25Cr, 25Ni, 0.1Ce	770	-	-	-	0.040	4.292
26	0.01C, 4Al, 4Ti, 11Cr, 8Co, 59Ni, 1Nb, 6W	950	850	5	-	0.095	4.451
27	0.09C, 4Al, 4Ti, 14Cr, 8Co, 64Ni, 6W	833	735	3	-	0.098	4.403
28	0.08C, 2Al, 3Ti, 10Co, 60Ni, 1Nb, 1Mo, 2W	700	500	3	-	0.069	4.361
29	0.1C, 3Al, 4Ti, 12Cr, 5Co, 1Mo, 7W	800	700	3	-	0.110	4.458
30	0.03C, 1Al, 1Ti, 14Cr, 70Ni, 4Mo, 8W	581	279	14	-	0.072	4.547
31	0.15C, 5Al, 3Ti, 10Cr, 4Co, 68Ni, 4Mo, 5W	930	800	3	-	0.107	4.484
32	0.1C, 3Al, 2Ti, 15Cr, 5Co, 1Nb, 2Mo, 4W	784	-	3	-	0.095	4.451
33	0.13C, 4Al, 5Ti, 13Cr, 70Ni, 1Mo, 3W	883	686	3	-	0.107	4.397

As calculated parameters of the state were considered S_m – the average value of displacement of atom relatively the starting position and E_B – the bond energy per atom. In table 1 these parameters are shown for set of industrially let out alloys of different composition and confronted to their experimental indicators of mechanical properties. The subsequent analysis proves the presence of correlate dependence between calculated parameters of the γ -phase state and indicators of mechanical properties of the alloys.

As an example in fig. 3 the projection to a cubic plane of crystal lattice of a γ -phase is shown for alloy N 14. The vectors of atomic displacements for presentation are shown increased in 20 time. Thus the atomic-discrete simulation can be considered as the instrument of forecasting of mechanical properties of alloys.

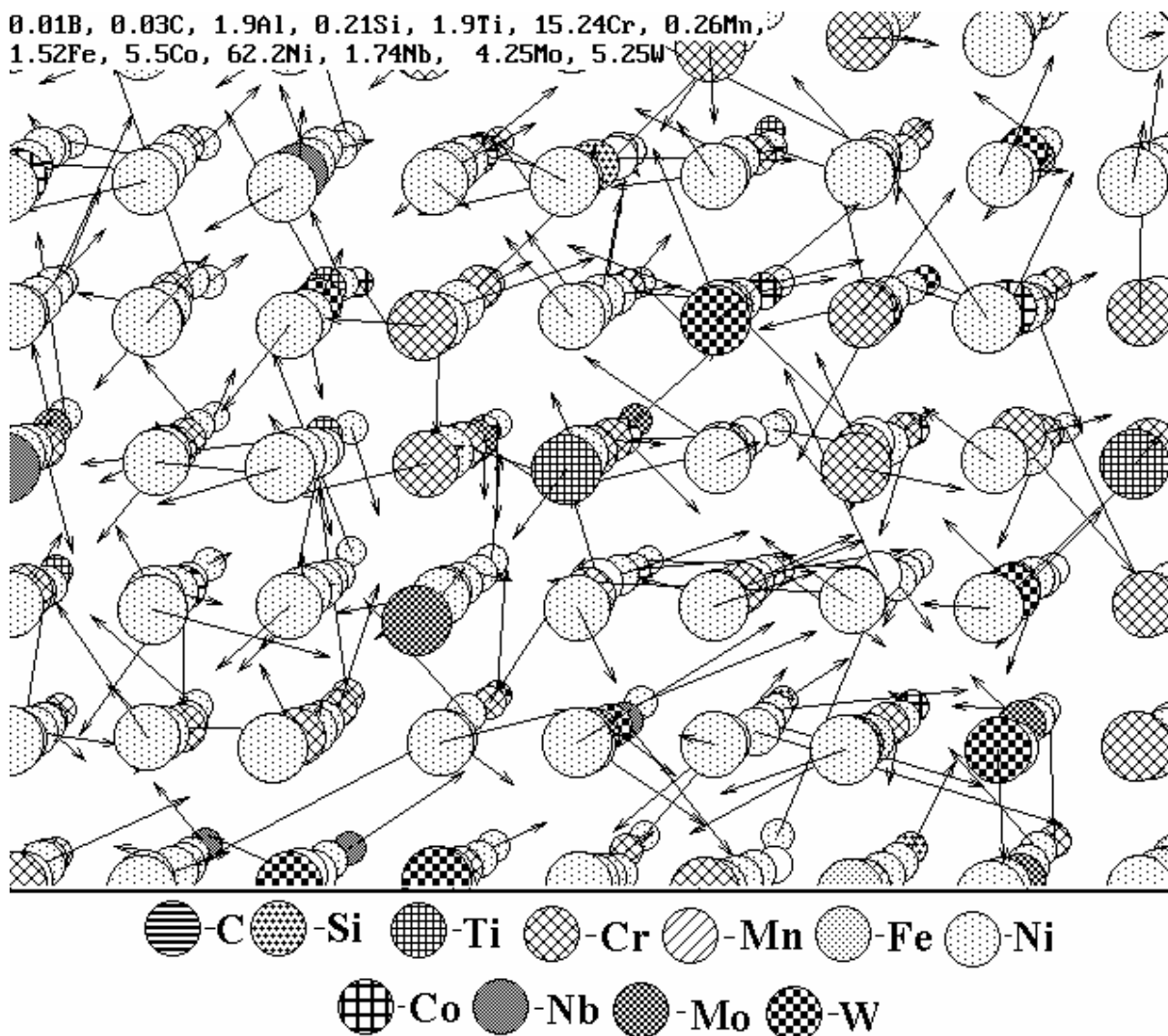


Figure 3. Configuration state of γ -phase of alloy 14.

References

1. Baranov M.A. Spherical symmetry of electronic shells of atoms and crystal stability.// electronic physical-technical journal V.1., iss. 1. 2006, p 49-62.
<http://eftj.secna.ru/0501/06013e.pdf>.

Comparative Study of Fatigue Crack Behavior in Experimental and Computational Methods

Shinya Miyazaki

Research Laboratory, IHI Corporation, 1, Shin-nakahara-cho, Isogo-ku, Yokohama
235-8501 Japan, e-mail:shinya_miyazaki@ihi.co.jp

ABSTRACT

High cycle fatigue tests and computational studies of coarse grained Ni alloy were carried out to investigate fatigue crack nucleation and propagation behavior. The alloy was directionally solidified to have prismatic grain structures. Fatigue tests of rectangular samples were performed by four-point bending under load control. Polycrystalline finite element analyses were conducted to investigate stress distributions of the specimen. The finite element analysis models were made based on grain distribution and orientation of tensile surface, it was characterized by electron-beam back scattering diffraction (EBSD) technique. Stresses were computed in global axis and local crystal orientation axis, resolved shear stresses, for whole grains. Longitudinal stress distribution is affected by inter-grain relationship, and is different from theoretically predicted one. Fatigue crack initiations tend to be occurred in areas indicating relatively high shear stresses in several slip systems. Fatigue crack propagation arrested in dissimilar slip system grain boundaries. Crack propagation resistance can be higher when a crack to proceed into grains which having geometrically different slip systems.

1. Introduction

Most of metallic materials are assumed to be isotropic and homogeneous, but real materials have some kinds of anisotropy or heterogeneity because of their imperfection of the microstructure. Especially precision casting generate significant anisotropic microstructures from its slow cooling rate, crystal grains are coarsened and form the texture like directionally solidification. These practical materials may exhibit different strength from ideal continuums, but such differences are not determined quantitatively. So structural integrity of machine components are usually guaranteed by setting sufficiently large safety factors, it leads to increasing thickness/weight. But it becomes needed to decrease the safety factors to lose weight for reducing energy consumptions and carbon dioxide emissions. In this situation, material's strength must be determined quantitatively to assess the structural integrity accurately. Fatigue strength is the most important factor for machine designing, so we concentrate on the fatigue behaviour, especially its nucleation and propagation of coarse grain material.

To understand fatigue crack nucleation and propagation behaviours, it is important to take notice to anisotropy and plane slip of metallic crystals. Many researchers have compared experimental fatigue tests and predictions of finite element analyses^{[1][2]}. In this work, the aim is to reveal fatigue crack nucleation and propagation behaviour by comparing finite element analyses.

2. Experimental procedure

Directionally solidified nickel-base superalloy having columnar grain structure was used in this study. Four rectangular samples were cut by electro discharge machine, and polished

mechanically and chemically. Their bottom plane normal was aligned parallel to the solidification direction. Size of the rectangular specimen was $W4\text{mm}\times H3\text{mm}\times L20\text{mm}$. Identification of crystal grain distributions and orientations of the bottom surface was obtained by the Electron-beam Backscattering Diffraction (EBSD) technique. The area for identification is 15mm length, including inner span gauge region (5mm) and extra 5 mm length areas on both sides as shown in Fig. 1 (a).

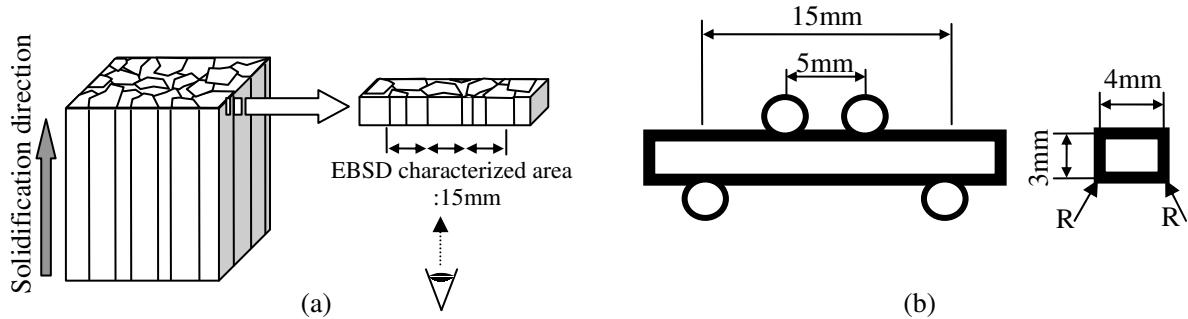


Figure 1. Schematics of sample and testing. (a) Geometrical relationship between solidification direction and rectangular sample (b) dimensions of four point bend test.

Crystallographic orientations were decided to have the longitudinal direction belong in a triangle $[100]-[110]-[111]$, so that all grains have the same relationship between the Schmid-Boas notation^[3] and the Miller indices of slip systems.

Fatigue tests were performed with four-point bending as shown in Fig. 1(b), its outer support span was 15mm and inner load span was 5mm. Cyclic loadings were operated under load control, stress amplitudes were 250MPa, 300MPa and 350MPa in stress ratio $R=0.1$. Every 5% increase in downward displacement, interruptions were made to observe generation of persistent slip bands (PSBs), crack nucleation and propagation in the inner span region.

After the fatigue tests, EBSD analyses were performed again to reveal geometrical relationships between PSBs/cracks and crystal grain boundaries. Because PSBs/cracks could not appear in EBSD map, some markings on the surface without damage to the specimen were employed to detect the location of PSBs/cracks.

Four specimens were used to bending test and EBSD analyses. These experimental results were compared with finite element analysis. In this paper, results of one specimen (stress amplitude=300MPa) is shown below.

3. Numerical analysis

The face centred cubic Ni alloy exhibits cubic anisotropy. Elastic constitutive relationship between stress (σ_{ij}) and strain (ϵ_{kl}) for the material is expressed by Hook's law, $\sigma_{ij}=C_{ijkl}\epsilon_{kl}$. Where C_{ijkl} is the tensor of elastic stiffness constants. There are three independent parameters, the values are $C_{11}=250.8\text{ GPa}$, $C_{12}=150.0\text{ GPa}$, and $C_{44}=123.5\text{ GPa}$ ^[4].

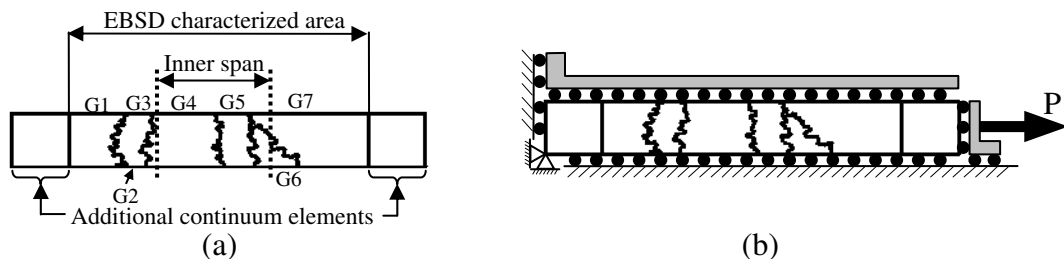


Figure 2. Illustrations of FEM meshes based on EBSD analysis. (a) Numbering of grains (b) Constraint and load conditions

Polycrystalline finite element mesh was created by tracing EBSD crystal grain map of the bottom surface as shown in Fig.2 (a). Additional elements of isotropic continuum are also created on the left and right ends to have enough distance between constraint/load points and the evaluation area. The anisotropic directions are defined by a local coordinate system for each grain, the x' - y' - z' axes are parallel to the direction [100], [010], and [001], respectively. Constraint and load conditions are shown in Fig.2 (b) schematically. The load is defined as a uniaxial along with the longitudinal direction, the magnitude is decided to generate the nominal stress equal to the maximum bending stress of experiment on the bottom surface.

4. Results and discussion

As shown in fig.2 (a), seven grains exist within the EBSD characterized area, and four are included in the inner span gauge area. Magnitude of the mean stress in each grain is thought to be predicted by the longitudinal elastic modulus. Elastic moduli in arbitral orientations can be calculated theoretically^[5]. An order of magnitudes of the theoretical elastic moduli about the four grains is $E_4 > E_7 > E_6 > E_5$.

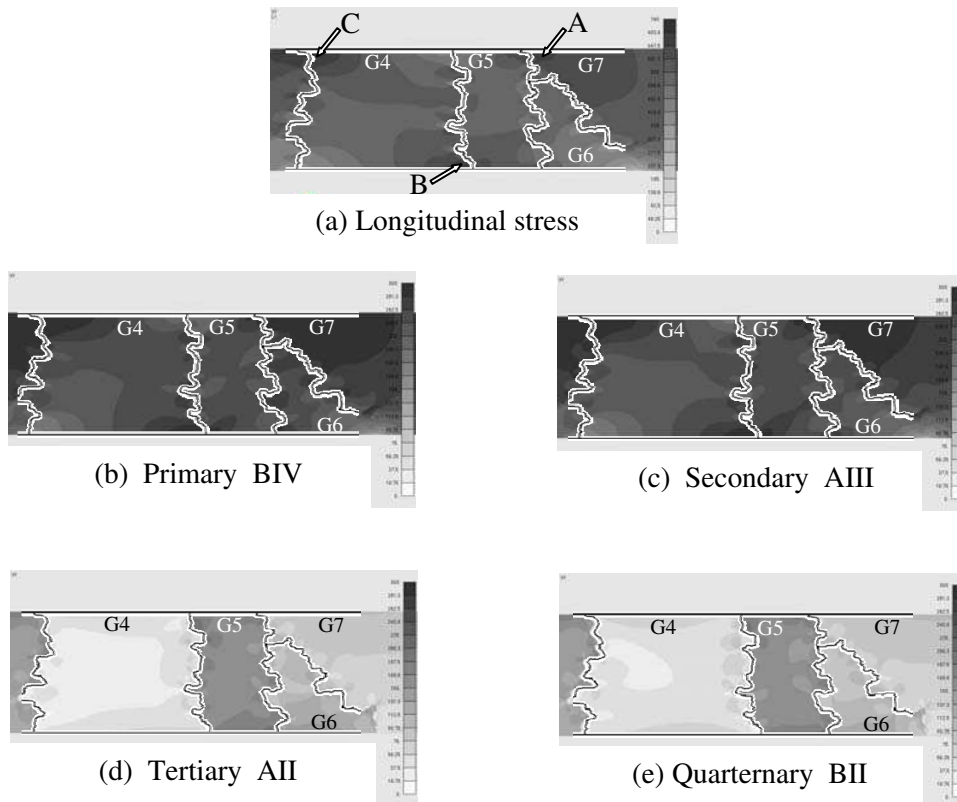


Figure 3. Distribution of the Longitudinal and Resolved Shear Stresses.

The distribution of the calculated longitudinal stress is shown in fig. 3 (a). While grain G5 has the lowest elastic modulus in theory, the grain exhibits high stress similar to the other grains. This grain bears whole load because it stretches across the whole width of the specimen. Some areas exhibit high stresses, for example A, B and C in the fig. 3(a). The stress concentration must be occurred by inter grain constraints.

Distribution of the resolved shear stresses, RSS, for slip systems of Primary :“BIV” in Schmid-Boas notation, Secondary: AIII, Tertiary: AII and Quarternary: BII are shown in Fig.3 (b)-(e). In primary and secondary slip RSS contours, all four grains represent similar stress. On the other hand, in tertiary and quarternary slip systems, only the grain G5 exhibits higher stress. In grain G5, these four slip systems have similar Schmid factors and activated equally.

As shown in later, the four slip systems are consisted of only two planes and three directions, this is advantageous to retain high dislocation mobility because it avoid complicated conjunctions of dislocations. So cumulative fatigue damages can be accumulated earlier in cyclic loading in this grain.

Fig.4 (a) shows a EBSD map with crack marks and (b) shows a micrograph of cracks on the bottom surface. Cracks are decorated by marks in (b). Stereographic projections of notable grains, G4 and G5, are also shown in Fig.4 (c). The crack denoted “A” in (a) and (b) was nucleated first in the G5 and progressed toward left upper and right down directions. This crack nucleation position corresponds to the fatigue damaging area predicted by FEM analysis. And the direction of the crack line corresponds to a trace of the activated slip planes. The crack propagation was prevented at grain boundary between G4 and G5 near “B” region. When the grains have dissimilar geometry for slip systems, grain boundary can be serious obstacles to crack propagation in early stage.

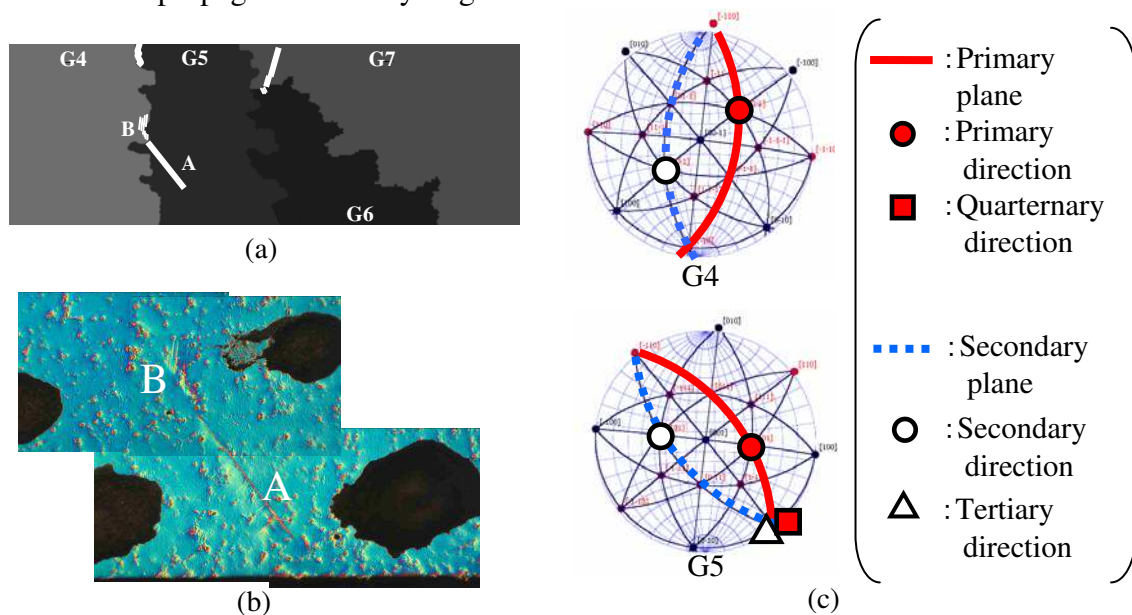


Figure 4. Information about cracks (a) EBSD map with marks (b) Micrograph of cracks (c) Stereographic projections with slip plane and slip direction notations

5. Conclusions

Comparison of fatigue tests and computational studies of Ni alloy lead to results below;

- Fatigue crack initiations tend to be occurred at areas representing higher shear stresses for three or more activated slip systems.
- Grain boundaries act as obstacles for fatigue crack propagation. The difficulty of propagation can be higher when crack to proceed into grains which having geometrically different slip systems.

References

- [1] Sackett, E. E., Germain L. and Bache M. R., “Crystal plasticity, fatigue crack initiation and fatigue performance of advanced titanium alloys”, *Int. J. Fatigue*, **29**, 2007, pp.2015-2021
- [2] Dunne F. P. E., Wilkinson A. J. and Allen R., “Experimental and computational studies of low cycle fatigue crack nucleation in a polycrystal”, *Int. J. Plasticity*, **23**, 2007, pp.273-295
- [3] Schmid E. and Boas W. I., “Plasticity of crystals”, F. A. Hughes & Co. Ltd, London, 1950, pp. 87-89
- [4] Charles K., “Introduction to Solid State Physics”, John Wiley & Sons, Inc, 2005, pp.84
- [5] Roger C. R., “The Superalloys”, Cambridge University Press, 2006, pp. 103-107

Modelling the kinetics of annealing - a case of freestyle racing

Volker Mohles¹

¹Institute of Physical Metallurgy and Metal Physics, RWTH Aachen University
Kopernikusstraße 14, D-52056 Aachen, Germany
mohles@imm.rwth-aachen.de

Historically, the main issue of multiscale materials modelling is to link various length scales and their corresponding time scales in one computer program. For instance, a large scale model may provide flexible boundary conditions for a small scale simulation, or, a small scale model provides in-situ input data for a large scale model. In such cases, the time scales are decoupled. However, there are also cases in which several different physical mechanisms of the same length scale, triggered by thermally activated events, can operate concurrently and on the same time scale. Examples for this occur during annealing treatments of alloys for homogenisation, hardening, or softening: particles may precipitate or dissolve, while the solute atoms diffuse through bulk, grain boundaries and dislocations. Moreover, recovery may take place, nuclei for recrystallisation may form and grow, and grain growth may set in. If plastic deformation is superimposed, e.g. by a testing machine, more thermally activated processes get involved, like dislocation slip. All these processes entail their own kinetics, and they can mutually interact in drastic ways, building road blocks for each other. Since the kinetics' depend on temperature differently, even rates of temperature transitions become important in industrially relevant annealing treatments. In the presentation, examples of simulations are shown in which a number of concurrent processes are taken into account. They demonstrate that the concurrency of consideration is essential to cover a whole range of experimental results consistently.

MODELLING OF THE MICROSTRUCTURE OF SINTERED CERAMICS FOR FINITE ELEMENT SIMULATIONS OF THEIR ELECTRICAL PROPERTIES

Müller T.¹, Raether F.², Meinhardt J.²

¹ Fraunhofer Institut für Silicatforschung (ISC), Würzburg, Germany
[thomas.mueller@isc.fraunhofer.de]

² Fraunhofer Institut für Silicatforschung (ISC), Würzburg, Germany

The microstructures of zirconia (3YSZ) toughened alumina (ZTA) ceramics are investigated by SEM and further characterised by quantitative image analysis. This leads to specific morphological parameters which are compared with the same parameters derived from model structures generated in voxel-based representative volume elements (RVE). Modified Voronoi clusters are employed to represent alumina and zirconia phases. Pores are added at the grain corners and edges respectively. After adjusting all the relevant morphological parameters of the model to the real ceramics' microstructure, the RVE has to be meshed for finite element simulations (FES). Hexahedral elements which simply use the voxel structure did not lead to sufficient accuracy of the FES simulation. As a first step, we therefore generate an adapted surface tessellation, using a general classed marching tetrahedra method. Special care is taken to preserve the topology as well as the individual volumes and interfaces of the model. In terms of processing time and accuracy of the FES it is very important to simplify the initially generated surface mesh in a manner that preserves detailed resolution at corners and along edges, while decimating the number of surface elements in flat regions, i.e. at the grain boundaries. From the surface mesh an adequate tetrahedral volume tessellation is created, which is used for the FES.

To simulate the macroscopic electrical behaviour of polycrystalline ZTA ceramics, the electrical properties of the individual constituting phases need to be measured. This is done by impedance spectroscopy. Equivalent circuits are employed and fitted to experimental data to obtain the individual properties. The sample composition was varied from pure zirconia to pure alumina. Previous work has shown that a good agreement between experimental and simulated data can be achieved in terms of thermal and mechanical properties. This approach is also applied to the electrical properties.

Simulation of Yielding Behavior in Polycrystalline Materials by the X-FEM

Yuji Nakasone¹ and Taiki Yoshizaki²

¹Dept. of Mech. Eng., Faculty of Eng., Tokyo University of Science; 1-14-6, Kudankita, Chiyodaku, Tokyo 102-0073, Japan; nakasone@rs.kagu.tus.ac.jp

²Former Graduate Student, Graduate School of Eng., Tokyo University of Science; 1-14-6, Kudankita, Chiyodaku, Tokyo 102-0073, Japan

Keywords: Yielding, Hall-Petch Relation, Shear Crack Model, Polycrystal, X-FEM

The shear crack model is often used to explain the Hall-Petch relation, or the grain size dependence of the macroscopic yield stress σ_Y expressed by the following formula: i.e.,

$$\sigma_Y = \sigma_0 + k d^{1/2} \quad (1)$$

where σ_0 and k are material constants and d the grain size.

The stress σ_Y is the stress at which plastic flow first takes place on a macroscopic scale. The stress σ_Y is generally considered as the stress required to make dislocations pile up against the boundary of a grain, in which a dislocation source exists, and propagate into adjacent grains. In other words, the yield stress σ_Y in the Hall-Petch relation is the critical value of the stress which breaks down the grain boundaries encountered first by the dislocation pile-ups.

The present paper, however, deals with yielding behavior throughout multiple grains to induce general yielding throughout the cross sections of polycrystalline specimens. The X-FEM is used to simulate the multiple-grain yielding behavior in 2D polycrystalline materials. The edge dislocation arrays on slip bands in rectilinearly anisotropic grains, whose principal elastic axes are randomly distributed, pile up against their boundaries. When the stress singularity parameter K_{II} in the vicinity of the tips of the slip bands exceeds a critical value, the propagation of the slip bands into adjacent grains should occur. When the K_{II} value is decreased after the penetration of the slip band into neighboring grains, the remote applied stress is increased so that the K_{II} value re-exceeds the critical value. The procedures above are repeated until the slip band propagates throughout the cross sections of specimens, or the general yielding occurs. The well-known Hall-Petch relation is also shown to be reproduced in the general yielding case. The slope of the relation, however, is greater in the general yielding case than in the local yielding case, implying higher constraints exerted by surrounding grains.

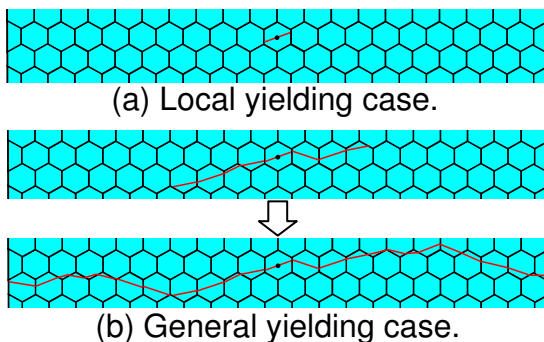


Fig. 1 Simulated yielding behavior in a polycrystalline material case.

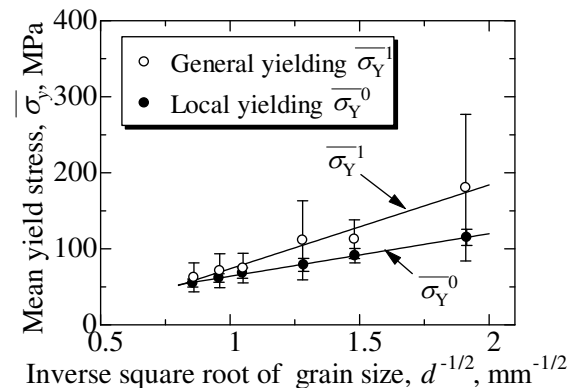


Fig. 2 Hall-Petch plots of the two cases.

Computationally Driven design of Innovative Cement-based materials - a multiscale approach on calcium leaching

Michael Griebel, Jan Hamaekers, Frederik Heber, Christian Neuen

Affiliations: Institute for Numerical Simulation, Wegelerstrasse 6,
53115 Bonn, Germany, griebel@ins.uni-bonn.de

Abstract

The CODICE project of the European Union aims at exploring the possibilities of forming stronger and more durable high-density calcium-silicate-hydrate varieties. C-S-H gel constitutes the main ingredient of cementitious skeleton and their life-service depends crucially on it. So far, the possibility of tuning the intrinsic nature and properties of the C-S-H gel has been out of reach. We overcome this by stronger simulation schemes in order to pass a wide range of length scales. The omnipresent use of cement-based materials belies the fact that they are a complex material with a truly multi-scale internal structure: from the atomic composition and reactions on the nanoscale, via the mesoscale with its colloidal model, up to the macro scale where hydration and hardening occurs in the initial phase and also cracks and fissures evolve under load.

Enhancing cementitious materials' life-service would be a tremendous benefit regarding their omnipresence on the planet. Hence, the study of the osteoporosis-like degradation processes is crucial. These processes mainly consist of the migration of ions which lead to the leaching of calcium and the deterioration of the cementitious structure as a whole. These processes are however inherently complex, as they take place on the nanoscale and occur very slowly. We accelerate them by placing the material in ammonium nitrate-rich solutions and employ state-of-the-art, fully parallel molecular dynamics simulations to calculate diffusion and convection coefficients. In a parameter-passing approach these values are fed into an adaptive, parallel finite element solver for the Poisson-Nernst-Planck equations that control the underlying phenomenon of ion migration.

The Excitation of Oscillation Modes Localized on an Interstitial Atom in 2-D Crystal

Starostenkov M.D.¹, Pozhidaeva O.V.¹, and Medvedev N.N.²

¹Altai State University, 656038, Russia, Barnaul, Lenin Street, 46

²Biysk Pedagogical State University, 659333, Russia, Korolenko Street, 52

ABSTRACT

The dependence of time of a point defect migration on the mode amplitude localized on it was studied in the paper. The frequencies and forms of fluctuations with small amplitudes of 2-D Ni crystal with periodically located interstitial atoms removed from each other were calculated in the experiment. Two positions of the interstitial atom were studied: in the middle of the equilateral triangle of the nearest neighbors and in the middle of the nearest neighbors' rhomb. The calculated block represented a crystal with periodically located interstitial atoms. Every calculated cell contained one interstitial atom and 16*16 primitive cells with applied periodical boundary conditions. The evolution of some modes at high amplitudes, when anharmonicity effects could not be neglected, was studied by the method of molecular dynamics. The oscillation modes with big amplitudes appeared to be unstable that led to their reconstruction and migration of interstitial atoms. The time of the beginning of interstitial atom migration for the modes with low frequency and sufficiently high localization parameter was found as the function of the amplitude of oscillation mode.

1. Introduction

The diffusion process taking place in metals and alloys plays one of the most important roles. Some investigators consider diffusion on mainly to occur on atomic level owing to coordinated atomic group motion resulting in materialization of either diffusion mechanism [1-3]. Most of investigators suppose vacancies migration or that of the interstitial atoms to be the leading mechanism in that case.

In the present work, the relation between the point defect migration outset time and mode amplitude localized on it was investigated. In the computer experiment, frequencies and forms of small-amplitude oscillations of 2D Ni crystal with atomic pack corresponding to {111} plane of FCC lattice were calculated. The investigated block represents a crystal with periodically situated interstitial atoms, one interstitial atom in each investigated cell containing 16×16 primitive cells with periodic limitative conditions applied. The Al-atom was used as an interstitial atom. Two positions of the interstitial atom were studied: in the middle of the equilateral triangle of the nearest neighbours and in the middle of the nearest neighbours' rhomb (Fig.1). The evolution of some not-small-amplitude modes was studied by means of the molecular dynamics method when the anharmonicity effects are not to be neglected. The oscillation modes with sufficiently big amplitudes prove to be unstable resulting in their reconstruction and migration of the interstitial atom. The interstitial atom migration outset time as function of oscillation mode amplitude was found for modes with a sufficiently low frequency and a sufficiently high parameter of localization.

To find the true own values of sufficiently great rated block where the interstitial atoms do not interact is the task of the present work.

2. Method of computer experiments and results

The computer experiment was performed in three phases:

1. Relaxation of atoms nearby the interstitial atom and record of findings in file.
2. Calculation of the crystal with the interstitial atom for point $q_x = q_y = 0$ and record of findings into file. The result is $2K$ of the true own frequencies and the same value of the own vectors corresponding to them. The own vectors are being normalized in such a way that their maximum absolute value component is equal to one which makes easier graphic representation of modes. The spectrum always contains a pair of zero frequencies in point $q_x = q_y = 0$, the motion modes of crystal as a hard whole correspond to them, therefore those modes were not considered.
3. The molecular dynamics of the oscillation mode chosen was implemented (the total number of modes was equal to 514 in that case). The oscillation mode has got one free parameter – the amplitude. If a small amplitude is given the mode found from the task of the own values is the exact solution and the molecular dynamics can not be started.

The oscillation modes were regulated in decreasing order of localization parameter (1):

$$L = \sum_{k=1}^{2K} |U_k|^2 / \left(\sum_{k=1}^{2K} |U_k| \right)^2 \quad (1)$$

The interatomic interactions were described with Morse's potential [4]:

$$\varphi(r_{ij}) = D\beta \exp(-ar_{ij}) (\beta \exp(-ar_{ij}) - 2), \quad (2)$$

where $a = 1.362768 \text{ \AA}^{-1}$, $\beta = 44.37877$, $D = 0.43205 \text{ eV}$.

By radius of cutting of 16 \AA potential, the lattice parameter was 2.6 \AA . The molar mass of Ni atom is 58.71 gm/mol , that of Al – 26.981 gm/mol .

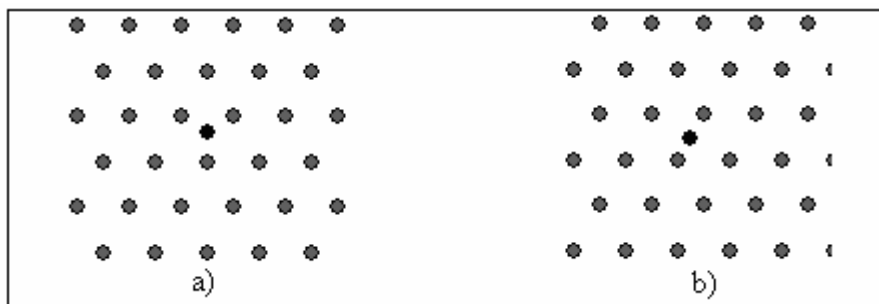


Figure 1. Locations of the interstitial atom.

We have got only one mode located on the defect in case when the interstitial atom was transferred into the middle of the equilateral triangle (Fig. 2a).

The second position with the interstitial atom transferred into the middle of the rhomb of the nearest atom neighbours is less symmetric (symmetry of the second order), resulting in larger quantities of modes located on the defect. We have found two localized modes (Fig. 2b, 2c)

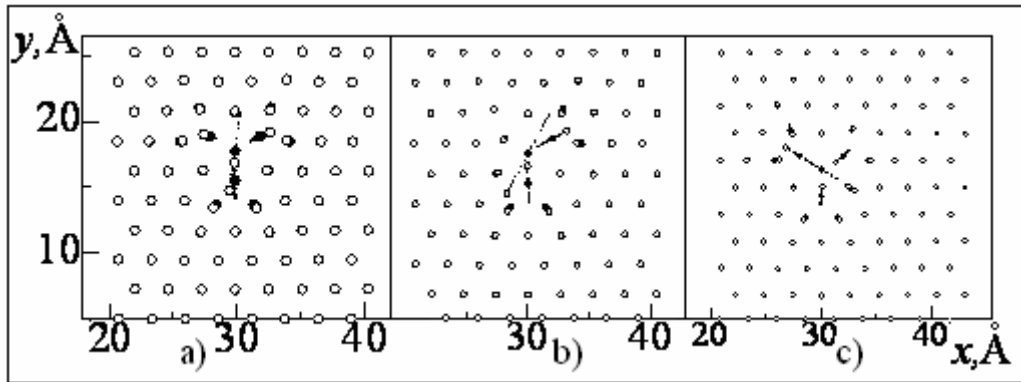


Figure 2. Modes; a) mode N2, $\omega = 76.47$ THz, $L = 0.197$, The interstitial atom is in the middle of the equilateral triangle of the nearest neighbours ; b) mode N1, $\omega = 76.47245$ THz, $L = 0.21925$, The interstitial atom is in the middle of the rhomb of the nearest neighbours; c) The same as in Fig. b for mode N2, $\omega = 76.47274$ THz, $L = 0.19332$, The interstitial atom is in the middle of the rhomb of the nearest neighbours. Designations: \bullet -balance positions of the atoms after relaxation; \circ -initial positions of atoms in the oscillation mode; thin lines are atom tracks.

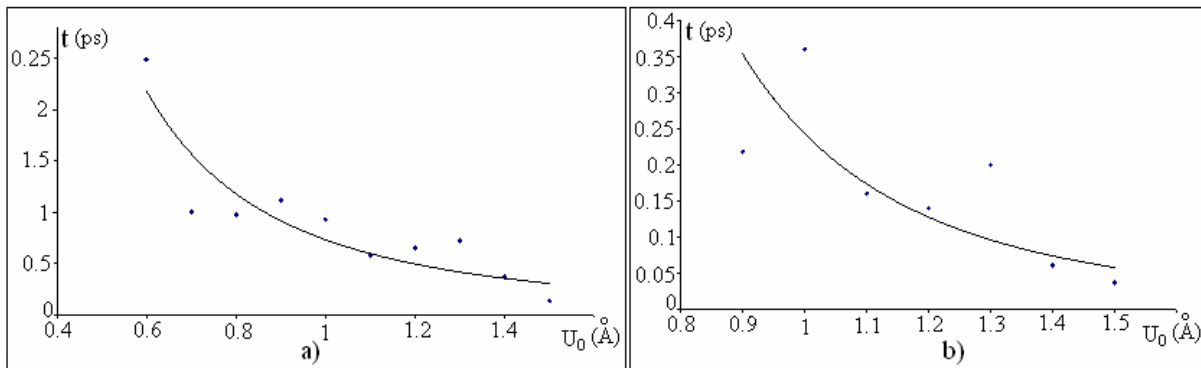


Figure 3. a). The curve giving the initial migration time of the interstitial atom against initial deviation. The results of the computer experiment for the oscillation mode with 76.47 THz frequency (2 mode) localized next to the interstitial atom in the Ni crystal. The interstitial atom is situated in the middle of the equilateral triangle of the nearest neighbors. b). The Curve giving migration outset time against initial deviation. The results of the computer experiment on oscillation mode with 76.4745 THz frequency (1 mode), localized nearby the interstitial atom of Al in the Ni-crystal. The interstitial atom is situated in the middle of the rhomb of the nearest neighbours.

By means of the computer experiment it was found that the position of the interstitial atom in the middle of the rhomb of the nearest neighbours gives crowdion solutions. By small amplitudes, localized quick – damping oscillators are observed in case when the interstitial atom is in middle of the nearest neighbours. The relations between interstitial atom migration outset time and initial deviation were found for all detected modes localized on the interstitial atom taking account of the two defect positions considered (Fig. 3, 4). The points mean simulating results and the curve is approximation of simulating results found by means of power function according to the least-squares method. The results shown in Fig. 3, 4 let us observe the fact that the mode proves to be unstable at sufficiently great U_0 values resulting in the lack of symmetry of the oscillation mode after definite delay time and migration of the interstitial atom; the delay time has tendency toward reduction as U_0 further increases.

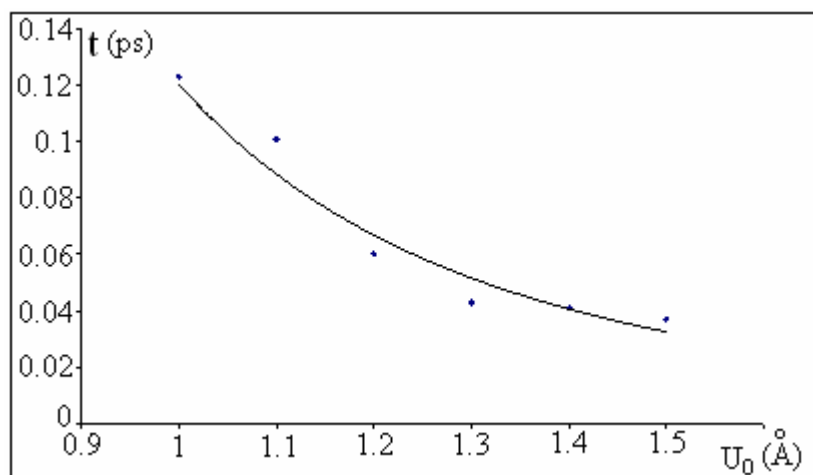


Figure 4. The same as in Fig.3b on oscillation mode with 76.47274 THz frequency (2 mode), localized nearby the interstitial atom of Al in the Ni crystal. The interstitial atom is situated in the middle of the rhomb of the nearest neighbours.

References

- [1] Poletaev G.M., Starostenkov M.D. Physics of the Solid State, **51**, 686 (2009).
- [2] Tchudinov V.G. Technical Physics Letters, **70**, 133 (2000).
- [3] Kassan-Ogly F.A., Naish V.E., Sagaradze I.V., Phase Trans. **49**, 89 (1994).
- [4] Tsaregorodtsev A.I., Gorlov N.V., Dem'yanov B.F., Starostenkov M.D., The Physics of Metals and Metallography, **58**, 336 (1984).

Atomic-Scale Study of Nanoindentation in Iron and Copper

Yuri Osetsky and Roger Stoller

¹*Materials Science and Technology Division, Oak Ridge National Laboratory, Oak Ridge, TN 37831, USA*

We present results of extensive molecular dynamics study of materials deformation during nanoindentation process in Fe and Cu. We have used different indentation surfaces namely $\frac{1}{2}\{110\}$ and $\{100\}$ in Fe and $\frac{1}{2}\{111\}$ and $\{100\}$ in Cu and spherical and cylindrical rigid indenters of diameter from 5 to 70 nm at indentation speeds 0.1-10 m/s in crystals of up to 1.1×10^8 atoms.

Plastic deformation at early stages or by small size indenter occurred mainly by emission of glissile dislocation loops. Large indenters may create complex three-dimensional structures that affect strongly the deformation process. Dislocation junctions of different structures and mobility were observed and classified from the point of view of their effects to nanoindentation process. A higher indentation loading rate was observed to promote the formation of shear loops on a nucleated circular dislocation in Fe.

Continuum theory of dislocations: finite element simulations of microstructure evolution during micro indentation

Giacomo Po and Nasr Ghoniem

University of California, Los Angeles
Los Angeles, CA. 90095-1597 U.S.A. (ghoniem@ucla.edu)

The collective behavior of dislocations is of fundamental importance in the microstructural evolution of plastically deformed crystals. In fact it represents the link between their macroscopic mechanical characteristics during plastic deformation and the underlying activity of single dislocations loops. Collective dislocation motion, governed by mutual interactions and applied stress field, determines the plastic component of strain during the deformation of crystals, which in turn affects the overall stress field. When the static framework of Continuum Theory of Dislocations is equipped with a constitutive law for the average dislocation velocity field, the dislocation density tensor field can be evolved together with deformation and stress fields in order to determine the elasto-plastic response of crystals under applied loads.

Here we present a finite element implementation of dynamic continuum theory of dislocations with applications to formation of dislocation patterns in plastically deformed copper. The study is inspired by recent developments in micro indentation experiments performed on copper single crystals oriented for plane strain, where dislocation densities are calculated from measured in-plane lattice rotation. Simulations are performed with different constitutive laws for the average velocity and comparison with experiments are presented.

Atomically-Constrained Network Dislocation Dynamics (ACNDD)

Giacomo Po, Nasr Ghoniem

Department of Mechanical and Aerospace Engineering, University of California, Los Angeles (UCLA), Los Angeles, California 91344, USA

ABSTRACT

A new formulation of Parametric Dislocation Dynamics is introduced based on concepts borrowed from graph theory. With this formulation, the topological reconfigurations of dislocation networks as a result of reactions (e.g. annihilation, junction formation and breakup, multiple dislocation tangles, etc.) can be easily simulated. The atomic constraints imposed on dislocation motion by junctions, obstacles, and boundaries are embedded in an extended finite element framework through the use of Lagrange multipliers.

1. Introduction

The evolution of the dislocation microstructure is known to be responsible of most of the macro-scale mechanical properties of crystals. Experimental observations¹ show that the dislocation microstructure develops in heterogenous patterns characterized by the simultaneous presence of low and high dislocation density regions during plastic deformation. These patterns, depending on the deformation mode, take the form of slip bands, shear bands, dislocation pile ups, dislocation cells and subgrains. Dislocation Dynamics has been shown to be an effective tool in capturing the effects of complex heterogenous dislocation distributions to investigation of plastic deformation. However, the effective representation of dislocation recombination in networks of entangled dislocations, due to processes such as annihilation and junction formation and breakup, remains critical in DD for the correct prediction of plastic flow. To meet this challenge, a new formulation of the Parametric Dislocation Dynamics Method² is developed where the topology of the network is described in terms of oriented graph theory³. In this framework, dislocation *nodes* interconnected by curved dislocation *edges* are introduced to discretize the continuum dislocation network configuration. The orientation of the edges is used to define a *flow* quantity, the Burgers vector, that must be conserved at the nodes. Some basic flow conserving graph operations such as *expansions* and *contractions* can be used to describe the topological changes during network reconfiguration due to junction formation and annihilation processes, therefore simplifying the complex evolution of dislocation networks.

The formation of junctions and boundaries (e.g. at the surface, at obstacles, at grain boundaries, or at second phase boundary) impose atomic constraints on the motion of dislocations. In particular, dislocation nodes must obey constraints imposed by their *incident* edges. Their motion must be such that the incident edges glide on their respective glide planes. This implies that junction nodes are constrained to move along specific crystallographic directions. Also, the presence of obstacles and impenetrable boundaries imposes constraints on dislocation network development. The weak form of the equations of motion in the presence of internal constraints is first derived in section 2, and its finite element version in 3. We end the paper with two applications of the method in section 4.

2. Irreversible Thermodynamics of Dislocation Motion with Internal Constraints

Let $r_i(l, t)$ describe the position of a dislocation line Γ in an elastic solid as a function of its arc length l and time t . Under the assumptions of negligible kinetic energy of dislocation core atoms and isothermal transformation, a variation $\delta \dot{r}_i(l, t)dt$ in the dislocation configuration leads to a non-positive change of Gibbs free energy of the solid that balances the virtual work of the force per unit length of dislocation line f_i ²:

$$\delta G = -\delta W = - \oint_{\Gamma} f_i \delta \dot{r}_i dt dl \leq 0 \quad \forall \delta \dot{r}_i \quad (1)$$

The force per unit length $f_i = \epsilon_{ijk} \sigma_{jm} b_m \frac{\partial r_k}{\partial l}$ exerted on a dislocation line is the Peach-Koehler force due to the elastic stress field σ_{jm} . The decrease in Gibbs free energy is due to energy dissipation caused by friction forces opposing dislocation motion. For dislocation velocities smaller than approximately half of the shear wave velocity friction forces are mainly due to viscous phonon and electron damping⁴ thus leading to the following expression for the loss of Gibbs free energy:

$$\delta G = - \oint B_{ij} \dot{r}_j \delta \dot{r}_i dt dl \leq 0 \quad \forall \delta \dot{r}_i \quad (2)$$

where the resistivity matrix B_{ij} is obtained as the inverse of the positive definite and symmetric mobility matrix. Combining Eqn. (1) and (2) the equation of motion of a dislocation line can be expressed in weak form as the stationary point of an energy functional having variation:

$$\delta \Pi = -(\delta W + \delta G) = \oint_{\Gamma} (B_{ij} \dot{r}_j - f_i) \delta \dot{r}_i dt dl = 0 \quad \forall \delta \dot{r}_i \quad (3)$$

The effects of atomic constraints on dislocation motion are taken into account introducing *internal* conditions in the form $L_{ij}(l, t) \dot{r}_j(l, t) = g_i(l, t)$ that are added to the original potential through the use of Lagrange multipliers $\lambda_i(l, t)$, therefore obtaining the following modified variational problem:

$$\delta \bar{\Pi} = \oint_{\Gamma} [(B_{ij} \dot{r}_j - f_i + L_{ji} \lambda_j) \delta \dot{r}_i + (L_{ij} \dot{r}_j - g_i) \delta \lambda_i] dt dl = 0 \quad (4)$$

3. Finite Element Implementation of the ACNDD

The first step towards the discretization of Eqn. 4 is obtained by dividing the dislocation network in separate *subnetworks*, each one composed of a number of dislocation loops interconnected by junctions. Each subnetwork is then further discretized into dislocation line elements Γ_e (*edges*) connecting dislocation *nodes*. Within each element, separation of variables is invoked to express both r_i and λ_i as the product of spatial-dependent element shape functions and time-dependent nodal degrees of freedom:

$$r_i(l, t) = N_{im}(l) q_m^e(t) \quad \lambda_i = M_{im}(l) p_m^e(t) \quad (5)$$

Upon substitution of Eqn. (5) in (4) the following discrete minimization problem is obtained for each subnetwork:

$$\delta \bar{\Pi} = \sum_e \left[\left(k_{mn}^e \dot{q}_n^e - f_m^e + \bar{k}_{nm}^e p_n^e \right) \delta q_m^e + \left(\bar{k}_{mn}^e q_n^e - \bar{f}_m^e \right) \delta p_m^e \right] = 0 \quad (6)$$

where the segment stiffness matrixes k_{mn}^e and \bar{k}_{nm}^e , and force vectors f_m^e and \bar{f}_m^e have been defined as:

$$k_{mn}^e = \int_{\Gamma_e} B_{ij} N_{im} N_{jn} dl \quad f_m^e = \int_{\Gamma_e} f_i N_{im} dl \quad (7)$$

$$\bar{k}_{nm}^e = \int_{\Gamma_e} L_{ji} N_{im} M_{jn} dl \quad \bar{f}_m^e = \int_{\Gamma_e} g_i M_{im} dl \quad (8)$$

Finally, standard assembly techniques are employed to express Eqn. 6 in global matrix form suited for numerical sparse symmetric solvers.

4. Selected Applications

As a first application of the ACNDD, we consider the simulation of dislocation pile-ups in micro-pillar compression. As shown in Fig. 1, the Frank-Read loop, initially the only subnet-

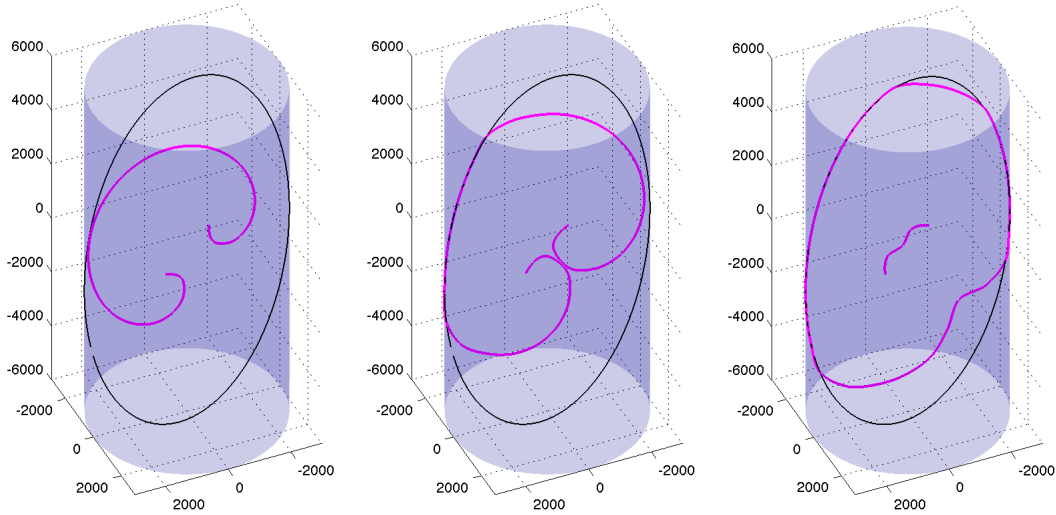


Figure 1: Consecutive stages of a Frank-Read loop expanding during micro-pillar compression in copper single crystals. Units are normalized by the magnitude b of the Burgers vector.

work in the system, bows out on its glide plane under the effect of the external and self stress field until it reaches the cylinder boundary, assumed impenetrable by dislocations. When a point r_i on the dislocation line reaches the boundary the constraint $\hat{n}_i \dot{r}_i = 0$ is introduced to allow only tangential motion with respect to the boundary (\hat{n}_i the in-plane normal to the cylinder boundary). While the outer part of the loop gradually conforms to the boundary the two inner arms of the loop get in contact and two dislocation edges merge in a junction edge with total Burgers vector equal to the sum of the colliding Burgers vectors. Since this results in a vanishing Burgers vector the junction segment is removed, thus originating two separate loops. The two loops, still interacting through their mutual stress fields, form now distinct subnetworks governed by independent systems of equations.

As a second application of the method we consider the simulation of a Hirth-lock junction formation. As illustrated in Fig. 2 two initially straight dislocations attract towards the common line between their glide planes under the effect of their mutual stress fields. Once two dislocation line elements collide, a common junction element is created having a Burgers vector equal to the sum of the original Burgers vectors, therefore making the junction element sessile.

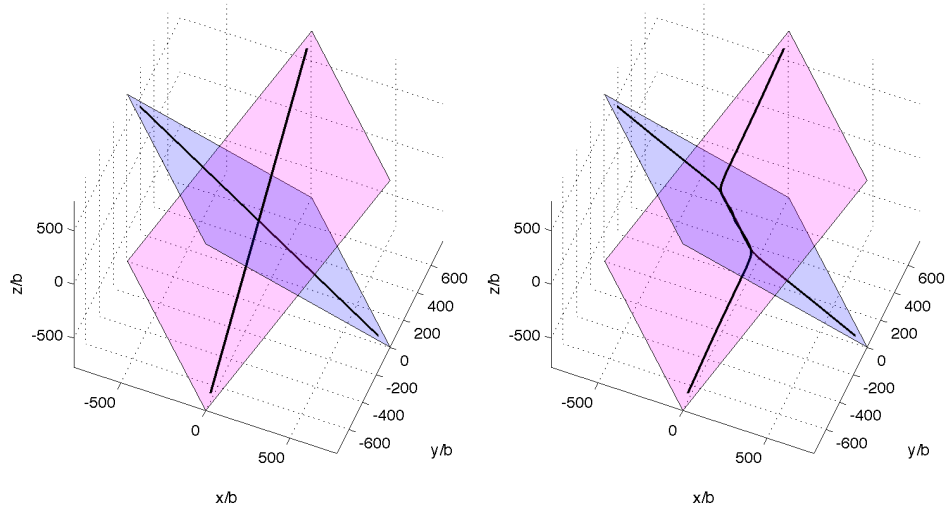


Figure 2: ACNDD simulation of the formation of a Hirth lock between a A $[0\ 1\ 1](1\ 1\ \bar{1})$ dislocation and a $[0\ 1\ \bar{1}](\bar{1}\ \bar{1}\ \bar{1})$ dislocation in copper single crystals.

The junction element can not bow on any glide plane, and is constrained to only zip or unzip along the intersection line. The constraint is imposed introducing additional equations governing the motion of the two dislocation nodes ending the junction element, namely $\hat{n}_i^1 \dot{r}_i = 0$ and $\hat{n}_i^2 \dot{r}_i = 0$, where \hat{n}_i^1 and \hat{n}_i^2 are the plane normals of the incident glide planes.

5. Conclusions

An overview of the ACNDD framework has been presented as a new formulation of the original PDD in the presence of internal constraints to dislocation motion. The method is mainly intended to simplify the treatment of dislocation reactions, such as junction formation and breakup, multiple dislocation tangles and nodes, and conformity to atomic constraints on dislocation motion. The method takes advantage of simple node and edge operations borrowed from graph theory to manage the network reconfiguration due to dislocation reactions. Simple applications of the method have been presented as examples of network reconfiguration and constrained motion.

References

- [1] H. Mughrabi. Dislocation wall and cell structures and long-range internal stresses in deformed metal crystals. *Acta Metall*, **31**(9), 1367–1379, 1983.
- [2] N.M. Ghoniem, S.- H. Tong, and L. Z. Sun, Parametric dislocation dynamics: A thermodynamics-based approach to investigations of mesoscopic plastic deformation. *Phys. Rev. B*, **61**(2), 913–927, 2000.
- [3] R. Diestel. Graph Theory. *Springer*, 3rd edition, 2006.
- [4] J. P. Hirth and J. Lothe. Theory of Dislocations. *Krieger Publishing Company*, 2nd edition, 1992.

Acknowledgements

Work is supported by the U.S. DOE, grant: DE-FG02-03ER54708.

Status of atomic-level simulations of solid phase epitaxial recrystallization of amorphous Si

M. Posselt

Forschungszentrum Dresden-Rossendorf, Institute of Ion Beam Physics and Materials
Research, P.O.Box 510119, D-01314 Dresden, Germany
E-Mail: m.posselt@fzd.de

In semiconductor technology amorphous Si layers are formed by ion implantation, and during subsequent annealing the solid phase epitaxial recrystallization (SPER) of the amorphous material takes place. In order to simulate the SPER process and to understand its atomic-level mechanisms, classical molecular dynamics calculations are employed since they allow the consideration of several thousand atoms and a time scale up to some hundreds of nanoseconds. In the last decade different authors investigated SPER in Si by this type of simulations, but the critical review shows that their results are not consistent with the experimental data. In most cases the SPER rate was strongly overestimated. Moreover, the results obtained by different groups under virtually equal conditions do not agree. This may be due to the different approaches used to prepare the initial state consisting of an atomic system with a nearly planar amorphous-crystalline interface. The main cause for the disagreement with experimental data is the inaccuracy of the interatomic potentials used in the different studies. The improvements considered in the present work are based on a better description of the amorphous phase using a modified potential without changing the established potential for the single-crystalline material. It is found that amorphous Si with realistic structural and thermodynamic properties can be obtained by certain modifications of known interatomic potentials, but these modifications do not yield the correct SPER rate. However, it is shown that the value of the SPER rate is strongly correlated with the melting temperature of amorphous silicon obtained by the corresponding modified potential. Obviously, this dependence can be explained by the fact that both melting and SPER are essentially determined by the flexibility of atomic bonds. The atomic mechanism of SPER consists in sequential local arrangements of atomic bonds and positions, preferentially along $\{111\}$ facets or terraces.

Multiphysics multiscale effects in two laterally coupled AlN/GaN quantum dots with wetting layer

Sanjay Prabhakar and Roderic V N Melnik

Wilfrid Laurier University, Waterloo, ON, Canada
M²NeT Laboratory, 75 University Avenue West, ON, Canada, N2 L3 C5
E-mail: rmelnik@wlu.ca

Coupled Quantum Dots (QDs) or QDs arrays provide an attractive potential building block for the next generation logic devices in the existing post CMOS technology for the purpose of quantum computing. These QDs arrays also find applications in optoelectronic devices such as Vertical Cavity Surface Emitting Lasers (VCSEL), photo voltaic cells and others where they may face challenges from thermal loadings. The study of electromechanical effects in such devices becomes very important as most of the materials in semiconductor nano structures are piezoelectric in nature. At the same time, this study requires taking into account multiple scales at which such devices should be analyzed. In this paper, we present the numerical simulations for the band structure calculations of two laterally coupled truncated GaN/AlN QDs under the influence of thermoelectroelasticity. By using Finite Element Method (FEM), we study the effect of thermoelasticity on the electronic properties of the two laterally coupled truncated GaN/AlN QDs in the presence of wetting layers based on the 8×8 Hamiltonian. The numerical values of several parameters such as electromechanical fields, eigenvalues and electron wave functions in the two laterally coupled truncated GaN/AlN QDs have been reported and they are compared to the previously reported results for single GaN/AlN truncated QDs (Nanotechnology 20, 125402, 2009). Simulations results show that several identical electron wave functions are present in the same QDs. Due to electron wave functions overlap in laterally coupled QDs, these parameters become more sensitive to thermal loadings compared to single truncated quantum dots. Figure 1 and 2 are the illustration of the wave functions and eigenvalues of the ground and first excited states in the coupled QDs structure without thermopiezoelectric effects. This project has been funded by NSERC and CRC.

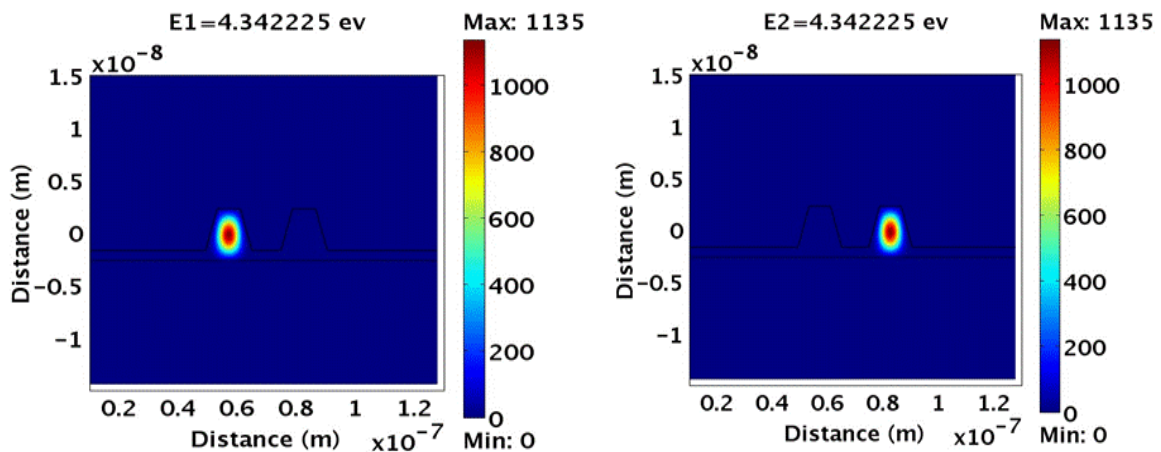


Figure: 1 Ground state wave functions in the left and right truncated QDs without thermopiezoelectric effects.

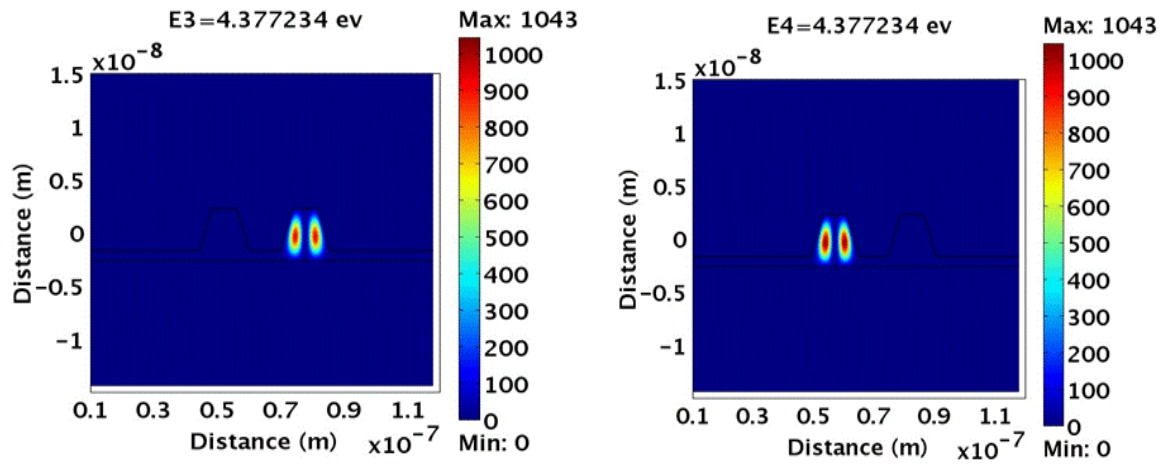


Figure: 2 First excited state wave functions in the right and left truncated QDs without thermopiezoelectric effects.

Modeling of Ti-6Al-4V Alloy by Artificial Neural Networks

N.S. Reddy^{1*}, C.H. Park², and C.S. Lee²

^{1*}School of Materials Science and Engineering, Gyeongsang National University, Jinju, Gyeongnam, 660-701, Korea.

²Department of Materials Science and Engineering, Pohang University of Science and Technology, Pohang, Kyungbuk, 790-784, Korea

Presently Ti-6Al-4V is the most widely used titanium alloy, accounting for more than 50% of all titanium tonnage in the world. The aerospace industry accounts more than 80% of this usage. The next largest application of Ti-6Al-4V alloy is medical devices or implants, which accounts 3% of the market. This alpha-beta alloy exhibits an excellent combination of corrosion resistance, strength and toughness. The properties of an alloy depend mainly on alloying elements, method of production, mechanical and thermal treatments. The relationships between the process variables and final properties of the alloy are very much complex, non-linear in nature, which is the biggest hurdle in developing proper correlations between them by conventional methods. An artificial neural network is an information processing and modeling system, which mimics the learning ability of biological systems in understanding an unknown process or its behavior. The knowledge about the unknown process, stored as neural network weights can be utilized to analyze and control the process.

In the present work, a model of artificial neural networks was developed for the analysis and prediction of the correlation between the process parameters, the alloying elements, microstructural features, beta transus temperature and mechanical properties in Ti-6Al-4V alloy. Sensitivity analysis of trained neural network models were studied which resulted a better understanding of relationships between inputs and outputs. The model predictions and the analysis are well in agreement with the experimental results.

Multiscale Modeling of Microstructure and Microstructural Evolution

Seth R. Wilson¹, Christopher G. Roberts², Anthony D. Rollett¹

¹Department of Materials Science and Engineering, Carnegie Mellon University,
5000 Forbes Avenue, Pittsburgh, PA 15213.

²Carpenter Technology, Corp. 101 Bern St., Reading, PA 19601

ABSTRACT

A level method for modeling polycrystalline grain growth in three dimensions has been described, along with basic tests to verify its correct operation. The key features of the model are the use of interface fields in place of fields associated with grains, together with velocity extension around multi-junctions in order to preserve their integrity during evolution. The use of the level set formalism permits explicit specification of interface properties such as energy and mobility. Velocity extension is used at boundaries and multi-junctions to ensure stability during evolution. As in all level set implementations, re-initialization is performed from time to time to maintain the shape of the level set functions around boundaries. To illustrate the need for multiscale modeling, results from moderately large-scale simulations of grain growth in the presence of pinning particles are described. By matching the fraction of particles on boundaries to examples of experiments in which higher than random fractions were detected, abnormal grain growth was observed in a few cases. In this instance the occurrence of abnormal grain growth was ascribed to a minor fraction of large grains with a low density of precipitates.

1. Introduction

An important outcome of multiscale modeling is to improve our understanding of physical phenomena. Microstructural evolution, whether via deformation or via annealing remains a challenging phenomenon to simulate. Even an apparently simple phenomenon such as grain growth in single-phase materials, where interface curvature is the driving force, is a challenge to model quantitatively. Grain boundary properties such as excess free energy and mobility are determined at the atomic scale. Solute drag operates at the nanometer scale. Particle drag operates at the sub-micron scale and so on and so forth. Particle drag is essential for grain size control in many engineered materials. Nevertheless, particles are also known to be strongly associated with abnormal grain growth. Recent experimental and simulation work has revealed that the spatial correlation of particles with grain boundaries departs significantly from random and that this can enable abnormal grain growth. The authors review recent progress towards developing a level set model for grain growth that can deal with both grain boundary anisotropy and particle interactions in detail. To illustrate the need for multiscale modeling of microstructural evolution, this article briefly describes the application of the Potts model to study the influence of pinning particles towards the initiation of abnormal grain growth.

The level set method can be used to accurately simulate the evolution of the sharp interface between two domains when a theoretical expression for the local velocity of this interface is known and computable. The level set method was first popularized by Osher *et al.* [1] and is used extensively in the fields of fluid dynamics and image analysis. Numerous books [2, 3] have been written about the level set method. For a brief introduction to the level set method, the reader is referred to [4].

Work with the level set method is not widespread within the materials science community, although application to second-phase particle dissolution has received some attention [5], as well as solidification [6]. The lack of interest is perhaps due to the fact that the level set method is a velocity-based formalism, and not an energy- based approach. However, if engineers are to develop computational models that simulate microstructure evolution on a truly mesoscopic scale, at lengths such that gradients in the free energy and diffuse boundary widths are not available at runtime, sharp-interface velocity-based models appear to be a useful next step. The level set approach described here permits explicit specification of boundary properties such as energy and mobility. It is also readily extended to include second-phase particles, solute diffusion, particle dissolution and other phenomena related to grain growth and coarsening. The level set could, for example, be coupled to a sub-voxel simulation (such as MD) to render it truly multi-scale, i.e. to compute velocities near the interface using a local molecular dynamics simulation and use velocity extension to advect the macroscopic boundary representation.

2. Interface Level Set Method

Given a theoretical expression for the local boundary velocity v , the level set method advects a scalar function $\varphi(x)$ in such a way so that the contour $\varphi(x) = 0$ (which represents the boundary) moves appropriately, via the simple PDE given by Eqn. 3. This may be implemented by a finite difference scheme on a regular grid. The mathematics community has provided a rigorous foundation for working with this equation even when $\varphi(x)$ develops discontinuities or undergoes topological transformations (see e.g. [3]).

One of the difficulties with the level set method is the need to extract explicit mesoscopic boundary velocity laws as functions of mesoscopic quantities from microscopic considerations. Because boundary normals n are obtained by simply taking gradients of the level set function $\varphi(x)$, i.e. $n = \text{grad}(\varphi)/|\text{grad}(\varphi)|$, the inclination-dependent boundary velocity may be explicitly computed as long as the misorientation is known. Therefore the level set method provides an ideal computational model to investigate grain growth problems in which energies and mobilities can be specified explicitly.

Clearly it is insufficient to model only single boundary motion but we must also model microstructural evolution in polycrystalline materials. The level set method was originally developed for modeling the motion of a single interface that decomposes space into only two separate domains namely, the region where $\varphi(x) > 0$; and the region where $\varphi(x) < 0$. Although a few authors [1, 7] have presented multi-level set methods for modeling the evolution of grain boundaries in polycrystalline materials, this paper is based upon a novel approach that we refer to as the interface level set method. A much more detailed exposition of the interface level set method will be presented in a later work. We provide here a brief description of the interface level set method.

To every grain associate the level set function $\varphi_i(x)$. The interior of grain i is defined as the set of all points x such that $\varphi_i(x) > \varphi_j(x)$, for all other grains j , Fig. 1. In contrast to the level set method, which defines boundaries as the set of points x such that $\varphi(x) = 0$, we will define the grain boundary between grains i and j as the set of points x such that $\varphi_i(x) = \varphi_j(x)$. To evolve the boundary i - j with a known local velocity $v_{ij}(x)$, we define the interface function

$$\varphi_{ij}(\mathbf{x}) = \varphi_i(\mathbf{x}) - \varphi_j(\mathbf{x}) \quad (2)$$

with $\varphi_i(x) > \varphi_j(x)$. We then advect the contour $\varphi_{ij}(x) = 0$ according to the traditional level set equation:

$$\frac{\partial \varphi_{ij}}{\partial t} = -\mathbf{v}_{ij} \cdot \nabla \varphi_{ij} \quad (3)$$

Note that Steinbach *et al.* [8] originally proposed such functions in the context of a multi-phase field model. As Steinbach points out, there are $N(N-1)$ such functions $\varphi_{ij}(x)$ at any point where there are N relevant level set functions. It is thus necessary to select a subset of the functions $\{\varphi_{ij}\}$ in order to obtain evolution equations for the $\{\varphi_i\}$. We therefore consider only the evolution equations for the interface functions $\varphi_{mj}(x)$, with m defined locally by $\varphi_m(x) > \varphi_j(x)$ for all j . There are $(N-1)$ such fields and so there are $(N-1)$ associated evolution equations, given by Eqn. (3) with $i = m$ and $1 \leq j \leq N$ and $j \neq m$. One more equation is needed to determine evolution equations for φ_i . We choose to impose the constraint

$$\sum \varphi_i = M \quad (4)$$

The constant M serves as an adjustable parameter in this model and does not have any physical significance.

We note that in regions corresponding to more than two grains, multi-junctions are very well-defined, and correspond to points at which all level set functions $\varphi_i(x)$ are equal. It follows that triple junctions and quad nodes are represented unambiguously in the interface level set method. We mention in passing that Eqns (3) must be modified near multi-junctions in order to couple boundaries together and enforce any relevant multi-junction force balance (such as Young's law).

All other issues relevant to level set models (such as initialization, re-initialization, and velocity extension) can be extended to the interface level set framework. These topics are discussed briefly below. Algorithms and data structures from the Mesoscale Microstructure Simulation Project were used extensively to implement the computer codes [9].

3. Initialization

Some very undesirable effects can occur if the interface level set equations are given initial data that deviates locally from a signed distance function. It is therefore necessary to estimate the boundary position and smooth the data accordingly before evolving. A procedure to estimate the distance to the nearest boundary at every point in the system was used [10] and we have built a method on top of this algorithm to generate the required boundary profile, even for points around multi-junctions. The procedure may be regarded as a type of data-constrained filtering, and has possible applications for the analysis of experimental data.

4. Reinitialization

In any level set model, it is necessary to ensure that the gradient near the zero level set does not stray too far from unity. There exist competing methods to do so, whose performance often reflects the effort required to implement them. To reinitialize the interface level set model, we have chosen to adapt a simple method proposed by Coupez [11]. To confine computation to relevant points near the boundary and prevent numerical oscillations, it is possible to penalize the gradient such that the target profile is sinusoidal (of specified width w). This is modifies the level set equation to read

$$\frac{\partial \phi}{\partial t} = -v_n |\nabla \phi| + \text{sign}(\phi) f(\phi) g(\nabla \phi) \left(\sqrt{1 - \left(\frac{\pi}{w}\right)^2 \phi^2 - |\nabla \phi|} \right) \quad (5)$$

The generalization of this equation to an interface level set model is immediate. However, multi-junctions require special consideration in order to maintain stability of the coupled fields around them. Detailed discussion of this feature of the model will be presented in a subsequent publication.

5. Velocity Extension

Coupling an ambient solute field or a particle dissolution model to an interface level set model requires a procedure known to the level set community as velocity extension (see [12]). Velocity extension involves interpolating to the boundary position to estimate the boundary velocity at every point near the interface, and then extending these values to all points in a larger neighborhood around the boundary. One of the ways in which extension occurs is via solving the following PDE to equilibrium in a thin tube around the boundary:

$$\begin{cases} v_n(\tau) = v_n(0), & \mathbf{x} \in I \\ \frac{\partial v_n}{\partial \tau} = -\text{sign}(\phi) \mathbf{n} \cdot \nabla v_n, & \text{otherwise} \end{cases} \quad (6)$$

This PDE penalizes the gradient of the velocity field with respect to the gradient of the level set fields, subject to the interface values as constraints. At equilibrium, all gradients in the local velocity field will point along tangents to the boundary, so that the velocity is constant along the boundary normals. The best computational results are obtained if spatial derivatives in this equation are winded toward the interface.

Around a multi-junction, it is necessary to conduct velocity extension for each interface individually. This involves updating a single scalar field for every interface, instead of one per grain, and so a data structure that associates a unique scalar field (the local velocity) with a distinct pair of integers is required.

6. Level Set Results

There are many tests that can be applied to a grain growth model to verify that it is operating correctly. A basic test is to simulate a single isolated grain, whose surface area should decrease at a constant rate, $16/3 \pi M\gamma$, where M is the boundary mobility and γ is the boundary energy. Fig. 2 shows the result of a simulation where such a grain is allowed to shrink (so that time evolution proceeds from right to left). The velocity is very close to the theoretical value until the grain is small compared to the width of the interface function used (typically 10 voxels).

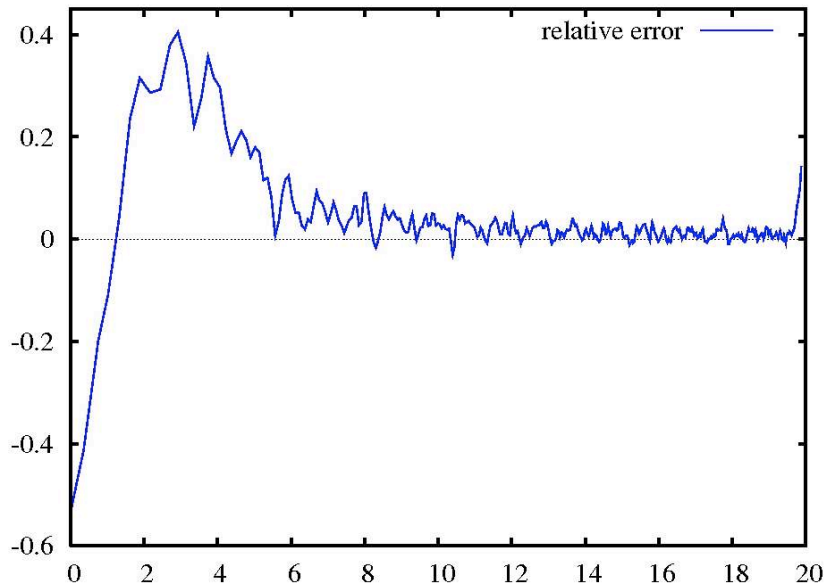


Fig. 2. Difference between the measured and theoretical shrinkage rates (rate of change of surface area) of an isolated (island) grain as a function of size (in pixels). The result shows that the rate is correct until small sizes are attained, where the rate diverges to larger and then finally smaller values.

Another test is to simulate polycrystal grain growth and measure the coarsening kinetics. Fig. 3 shows the results of simulating grain growth in a thin film (2D) configuration. After an initial transient, the graph becomes linear as expected, and as required for self-similar coarsening [13].

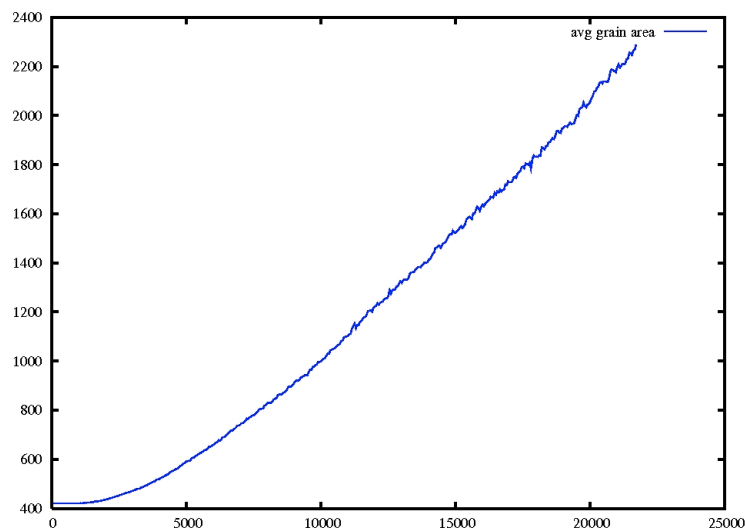


Fig. 3. Average area versus time, showing that the graph is linear after an initial transient, as required for self-similar coarsening.

A more severe test of the capability for modeling anisotropic grain boundary energies involves measuring dihedral angles at triple junctions. Fig. 4a shows the configuration of cylindrical caps used to perform such a test. The geometry is such that the cylindrical end caps are maintained in a self-similar fashion as they move down the domain (driven by the shortening vertical boundaries). The dihedral angles in the roots of the caps were measured and compared against the theoretical values, Fig. 4b. The results show that for not too large anisotropies, the model performs well. For anisotropies approaching wetting, however, the dihedral angles remain too large.

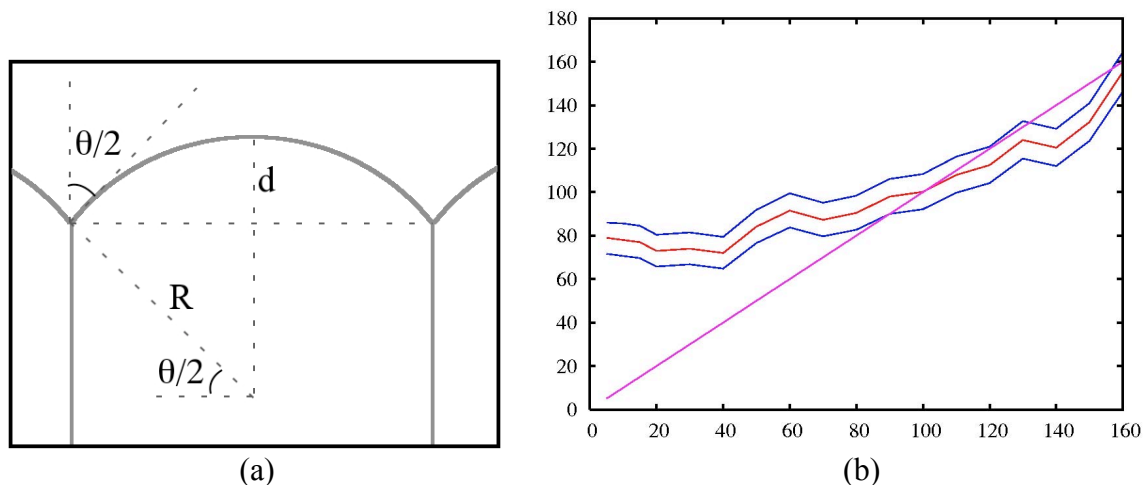


Fig. 4. (a) Diagram of a microstructure with cylindrical end caps; the vertical boundaries have a different energy than the boundaries in the caps, giving rise to a specific dihedral angle in the grooves of the caps. (b) comparison of the dihedral angle measured in the level set model (vertical axis) against the theoretical value (horizontal axis) determined from Young's Law. Wetting corresponds to a zero dihedral angle in the root of the cap.

7. Second Phase Precipitates and Grain Boundaries

A significant fraction of commercial alloys are not single-phase and develop properties that can be associated with the interaction between the primary and secondary phases. Certain processing techniques inherently lead to spatial distributions of second phases that are heterogeneous and/or which show an alignment with a specific workpiece direction, such as the direction of primary metal flow. The best-known examples involve rolled steel- and aluminum- plate materials in which inclusions/second-phase constituents/stringers are found as isolated bands along the rolling direction. In other situations, the spatial distribution of a second phase may exhibit a non-random correlation with internal points of reference such as grain boundaries. For example, the frequency of $60^\circ \langle 111 \rangle$ boundaries is often significantly higher than the random Mackenzie distribution, and the particle distribution on grain boundaries is frequently non-random in nickel-base superalloys [14].

Computational modeling enables the generation of digital microstructures that attempt to replicate experimentally-observed features as described above; likewise, modeling assesses the impact of these parameters on microstructural evolution. To address the effect of non-random distributions of particle on grain boundaries, a standard three dimensional Potts model was used, the details of which have been described in previous publications [15].

8. Application of Multi-Phase Modeling to Experimental Observations

The correlation of particles with the grain boundaries was varied in a series of simulations to quantify its impact on grain-growth stagnation and the variation in spatial distribution during annealing. Isotropic grain boundary properties were used and all particles were cubic with a volume of 27 voxels. The number fractions of particles on grain boundaries were varied between 0.3 and 0.7. The methods used to insert particles into 3D microstructures with a specified fraction located on grain boundaries were described by Roberts *et al.* [16]. For example, the case for which $V_v = 0.04$ and 30% of the particles are on boundaries in a 400^3 domain contained $\sim 94,800$ cubic particles with 28,400 particles placed explicitly on the grain boundaries and the remaining particles located within the grain interiors. Microstructures with various combinations of initial grain size, volume fraction, and number fractions of particles on grain boundaries were instantiated. The set of initial grain sizes was $\{7.6, 11.7,$

15.2, 18.4, 21.5 and 24.0} in units of voxels. The set of particle volume fractions was {0.04, 0.06 and 0.08}. The set of fractions of particles on boundaries was {0.3, 0.5 and 0.7}. The results of the simulations are presented in Fig. 5 as a plot of limiting grain size versus volume fraction.

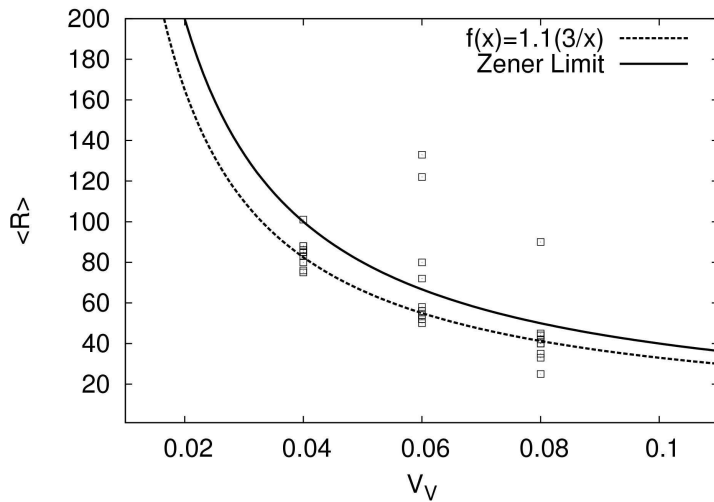


Fig. 5. Potts model predictions of the limiting grain size as a function of particle volume fraction for initial distributions in which 30%, 50%, and 70% of the particles were initially situated on grain boundaries. All points above the fitted line, $f(x)$, exhibited signs of abnormal grain growth.

A majority of the simulations resulted in a pinned microstructure at long times, as expected. The observed limiting grain size, D_L , was found to be slightly smaller than the original Smith-Zener prediction [17], as noted by various other researchers [18]. A few of the final grain sizes, however, lay well above or on the Smith-Zener limit [17], shown as a solid line. Analysis of the simulated microstructures at various times revealed abnormally large grains (i.e., a grain at least three times as large as the average grain size); an example is given in Fig. 6. The grain-size distributions provided additional confirmation that an initially uniform grain-size distribution had evolved into a bimodal distribution indicative of abnormal grain growth. A heterogeneous distribution of particles on grain boundaries was concluded to be the source of the AGG because it occurred reproducibly in simulations for which the initial grain-size distribution lay in a rather narrow range, i.e., $15.2 \leq \bar{R}_0 \leq 18.4$.

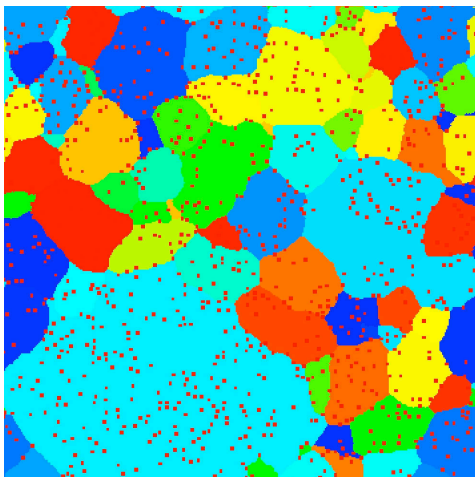


Fig. 6. Cross-section through a simulated microstructure (Potts model) showing an abnormally large grain consuming the matrix grains. Simulation conditions comprised isotropic grain-boundary properties, $T = 1.5$, $t = 100,000$ MCS, $V_v = 0.06$, and 70% of particles on grain boundaries.

Fig. 7 shows the evolution in average grain size for $V_v = 0.06$ and initial boundary fractions of 30% and 70%. In each graph, there are three distinct types of behavior: (1) No growth, as indicated by curves with zero slope, (2) normal grain growth followed by stagnation, and (3) normal grain growth followed by abnormal grain growth. The pinned microstructures were a result of the large initial grain size (small driving pressure) and the large ‘apparent’ volume fractions of particles on grain boundaries. With a low number fraction of particles on

boundaries (30%) and initial grain size of $\bar{R}_0=21.1$ or $\bar{R}_0=24.0$, there was sufficient drag pressure to be equal to or greater than the driving pressure. The third scenario with an initial grain size of $\bar{R}_0=18.4$, exhibited both normal grain growth and AGG; i.e., two regions of growth. The current findings suggest that the initiation of AGG is related to specific geometric features, i.e. non-random particle placement on grain boundaries and a specific range of initial grain size. The evidence appears to support the arguments presented by Rios [19] wherein local deviations in particle density coupled with neighboring large, candidate ("rogue") grains result in a transition from normal to abnormal grain growth.

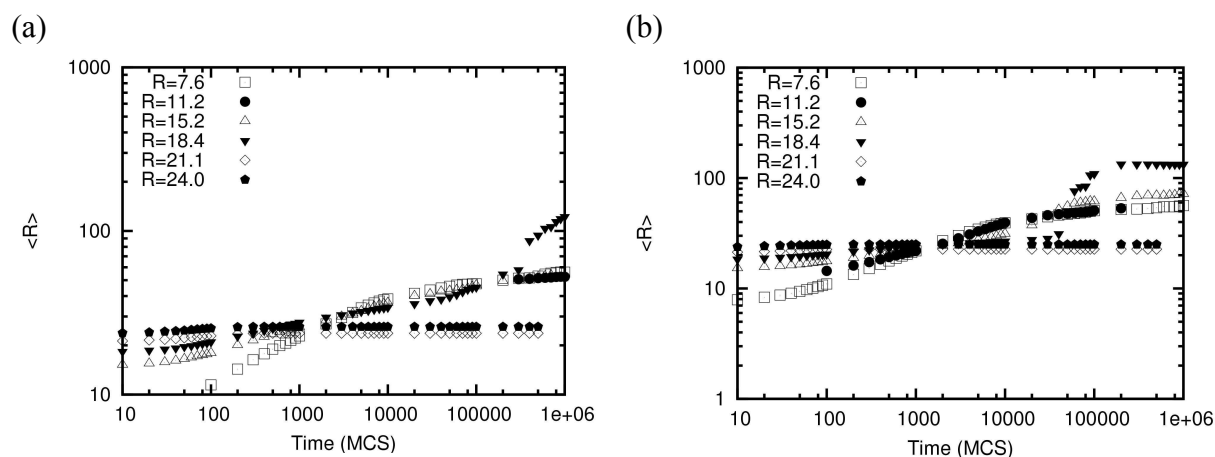


Fig. 7. Grain-growth kinetics as a function of initial grain size for $V_v = 0.06$: (a) 30% of particles on grain boundaries and (b) 70% of particles on grain boundaries. The "R" in the legend refers to the initial average grain size.

Summary

A level method for modeling polycrystalline grain growth in three dimensions has been described, along with basic tests to verify its correct operation. The key features of the model are the use of interface fields in place of fields associated with grains, together with velocity extension around multi-junctions in order to preserve their integrity during evolution. The use of the level set formalism permits explicit specification of interface properties such as energy and mobility. The approach also can thus accommodate information obtained at smaller length and time scales as, for example, in terms of grain boundary properties such as energy, mobility and diffusivity. Enhancements to the model are in progress to address particle-boundary interactions and particle dissolution. At a slightly larger length scale, results from a Potts model simulation of grain growth pinned by particles show that abnormal grain growth can occur even when microstructures are nominally pinned. The key circumstance appears to be when the grain size is smaller than the Smith-Zener limit but essentially all grain boundaries are pinned because the fraction of particles on boundaries is higher than the random correlation in position assumed for the Smith-Zener derivation.

Acknowledgements

The support of the Office of Naval Research under grant number N000140610183, program manager J. Christodoulou, is gratefully acknowledged. The authors gratefully acknowledge discussions with J-W Kim (Pittsburgh Supercomputing Center). The research was supported in part by the National Science Foundation through TeraGrid resources provided by the Pittsburgh Supercomputing Center and by the Air Force Initiative "Science and Technology Workforce for the 21st Century" (STW-21), Contract F33615-01-2-5225, which was managed jointly by the Air Force Office of Scientific Research, the Materials and Manufacturing Directorate of the Air Force Research Laboratory, and the Ohio State University. CGR

acknowledges support for a summer internship and computational resources from the DoD User Productivity Enhancement and Technology Transfer Program. Discussions with colleagues under the auspices of the Computational Materials Science Network (CMSN) under DOE/OBES support have been invaluable to this effort. Partial support of the MRSEC at CMU under NSF grant number DMR-0520425 is acknowledged. The Intel company is thanked for their support of computing equipment.

References

- [1] S. Osher & J. A. Sethian, *J. Computational Physics* vol. 79 (1988) pp. 12–49.
- [2] S. Osher & R. Fedkiw, *Level set methods and dynamic implicit surfaces* (Springer, New York) (2003).
- [3] Y. Giga, *Surface Evolution Equations: A Level Set Approach* (Birkhauser Verlag, Basel) (2006).
- [4] S. Osher & R. P. Fedkiw, *J. Computational Physics* vol. 169 (2001) pp. 463–502.
- [5] F. J. Vermolen, E. Javierre, C. Vuik, L. Zhao & S. van der Zwaag, *Computational Materials Science* vol. 39 (2007) pp. 767–774, Vermolen, F. J. Javierre, E. Vuik, C. Zhao, L. van der Zwaag, S.
- [6] J. A. Sethian & J. Strain, *J. Computational Physics* vol. 98 (1992) pp. 231-253.
- [7] X. Zhang, J.-S. Chen & S. Osher, A multiple level set method for modeling grain boundary evolution in polycrystalline materials, Tech. Rep. CAM report 06-69, UCLA (2006).
- [8] I. Steinbach & F. Pezzolla, *Physica D* vol. 134 (1999) pp. 385–393.
- [9] Mesoscale Microstructure Simulation Project, <http://www.matforge.org/cmu>, accessed July 2010.
- [10] S.D. Sintay and A.D. Rollett. “Microstructure modeling using dual grid center of mass iso-contouring”. LA-UR 09-04435
- [11] T. Coupez, “Convection of local level set function for moving surfaces and interfaces in forming flow”. NUMIFORM 2007, *Materials Processing and Design: Modeling, Simulation and Applications*, J.M.A. Cesar de Sa and A.D. Santos, eds. (2007) pp. 61-66.
- [12] D. Adalsteinsson and J.A. Sethian. “The fast construction of extension velocities in level set methods.” *J. Comp. Phys.* vol. 148 (1999), pp. 2-22.
- [13] Mullins, W. W., *Acta metall. mater.* vol. 39 (1991), pp. 2081-2090.
- [14] C.G. Roberts, S.L. Semiatin, A.D. Rollett, *Scripta mater.*, vol. 56 (2007), pp. 899-902.
- [15] A. D. Rollett and P. Manohar, “The Monte Carlo Method”, in *Continuum Scale Simulation of Engineering Materials*, D. Raabe and F. Roters, eds. (Wiley-VCH) (2004) pp. 77-114.
- [16] “Two-phase microstructure generation in 3d based on 2d sections of a nickel alloy” C.G. Roberts, S.L. Semiatin, and A.D. Rollett, *Proc. ICOTOM-15, Ceramic Trans.* vol. 201 (2008) pp 771-778.
- [17] C. S. Smith, *Trans. AIME* vol. 175 (1948), pp. 47.
- [18] M. A. Miowdownik et al., *Scripta. Mater.* vol. 42 (2000) pp. 1173.
- [19] P R. Rios, *Acta Mater.* vol. 45 (1997) 1785-1789.

Multiscale Simulation of Deformation Processes in Welded Steel Specimens

Varvara Romanova¹, Ruslan Balokhonov¹, Siegfried Schmauder²

¹Institute of Strength Physics and Materials Science, Russian Academy of Sciences,
pr. Academicheskii 2/4, 634021 Tomsk, Russia, varvara@ispms.tsc.ru

²Institut für Materialprüfung, Werkstoffkunde und Festigkeitslehre,
Stuttgart University, Pfaffenwaldring 32, D-70569, Stuttgart, Germany,
Siegfried.Schmauder@imwf.uni-stuttgart.de

ABSTRACT

A three-dimensional numerical analysis of the meso- and macroscale deformation behavior of welded low-carbon steel specimens is performed. A mathematical model based on a double-limit yield criterion was constructed to describe propagation of Lüders bands at the macroscale. To take into account mesoscale deformation, a weld-affected microstructure was explicitly introduced in the calculations. The role of the free surface, grain boundaries and interfaces between the seam and the heat-affected zone (HAZ), and between the HAZ and the base metal in processes of stress concentration and plastic strain localisation is studied.

1. Introduction

Engineering predictions of the deformation and fracture behavior of welded structures are generally based on the estimations of macroscopic characteristics (e.g. static, dynamic and fatigue strength, yield stress, etc.) Actually, due to the presence of interfaces of different sorts and scales stresses concentrate at different scales, resulting in multiscale processes of deformation and fracture. Thorough study of the multiscale processes takes on a special significance since gradual accumulation of irreversible deformation and damage on lower scales can give rise to the macroscopic failure of the welded structure.

This paper is devoted to the 3D numerical analysis of the deformation processes in welded steels at the meso- and macro-scales with an explicit account for a dog-bone shape of the macroscopic specimens and microstructure features of the weld-affected material (Fig. 1).

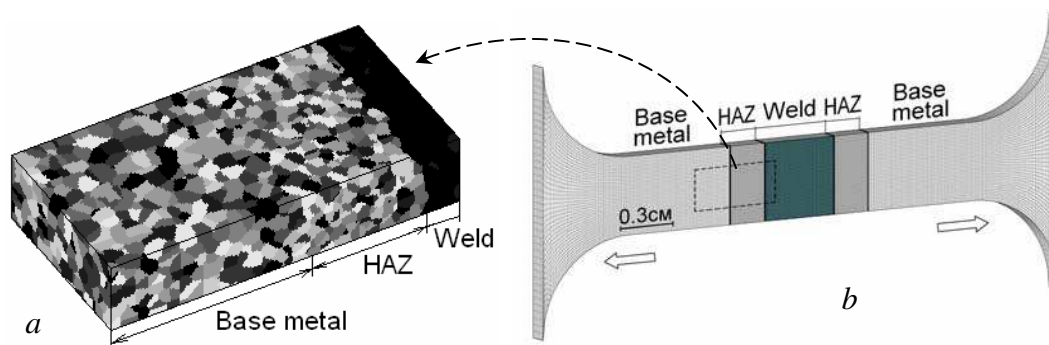


Fig. 1. Micro (a) and macro models (b) of welded joints.

2. Double-limit yield criterion

We assume that the material retains its meso and macroscale continuity under elastic-plastic deformation and, thus, mathematical tools and numerical methods of continuum mechanics

can be applied. The general system of equations for an elastic-plastic material incorporating the laws of conservation of mass, momentum and energy and the constitutive relations in the form of Hook's relation has been presented in extensive literature (see, e.g., [1]). In the examples discussed below, the system of equations supplemented by boundary conditions was solved numerically by the finite-difference method [1].

Let us formulate a criterion of elastic-to-plastic transition with account for Lüders band evolution. Experiments (e.g., [2]) showed that dislocations originally presenting in the material are immobilized. The detachment of the dislocations and the nucleation of new defects capable of plastic flow initiation require a higher stress level than the one at which subsequent propagation of dislocations takes place. This kind of model underlies the local double-limit yield criterion used here to simulate the evolution of localised plastic deformation in welded specimens at meso- and macroscales.

We proceed from a von Mises yield criterion according to which the transition from an elastic to a plastic state takes place if the equivalent stress reaches a critical value. Two critical values are used in the examined model: a higher limit σ_t (triggering stress) is necessary to initiate plastic flow in an elastically strained material, whereas a lower limit σ_y (yield stress) is assumed for a material undergoing plastic deformation:

$$\sigma_{eq} = \begin{cases} \sigma_t & \text{if } \varepsilon_{eq}^p = 0 \\ \sigma_y(\varepsilon_{eq}^p) & \text{if } \varepsilon_{eq}^p > 0 \end{cases} \quad (1)$$

Here $\sigma_y(\varepsilon_{eq}^p)$ is the strain-hardening function chosen for low-carbon steels in the form of

$$\sigma_y = \sigma_t - 96.3 \exp\left(\frac{0.025 - \varepsilon_{eq}^p}{0.0753}\right) [\text{MPa}]. \quad (2)$$

3. Evolution of localized plastic deformation at the macroscale

A three-dimensional welded steel specimen was approximated by the finite-difference mesh of $300 \times 40 \times 10$ elements (Fig. 1(b)). Tensile load was applied to the opposite ends of the specimen. Average mechanical characteristics of the seam and the base metal are given in Tab. 1. The mechanical properties in the HAZ varied linearly between maximum values corresponding to the seam and minimum values at the interface with the base metal. Let us examine the main stages in the development of macroscopic plastic flow in the welded low-carbon steel specimen including formation of Lüders fronts, their propagation through the specimen and stage of the quasi-uniform deformation.

Table 1. Macroscopic (average) mechanical properties.

	Shear modulus, GPa	Bulk modulus, GPa	σ_t , MPa	σ_{y_0} , MPa
Base metal	80	133	426	329.7
Seam	112	186	329	590

The stress level in the HAZ near the interface with the seam is comparable to the magnitude of stresses developing in the near-grip regions (fig. 2(a)), and simultaneous incipient plastic deformation is observed in these zones. On further loading, however, Lüders fronts are formed at the HAZ-base metal interface, whereas the plastic flow near the grips virtually

terminates (fig. 2(b)). Formation of the Lüders fronts corresponds to the drop portion in the stress-strain curve between the upper and the lower yield points (Fig. 3).

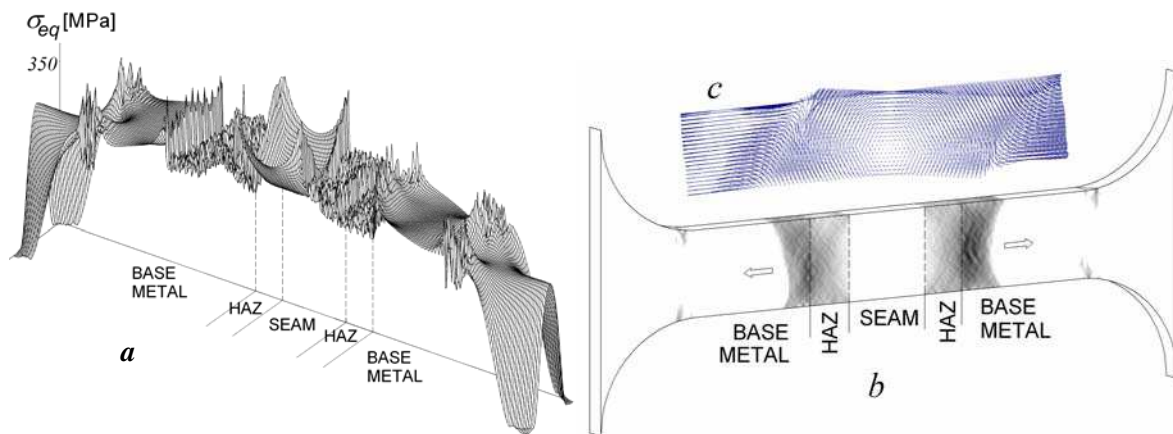


Fig. 2. Equivalent stress (a) and equivalent plastic strain patterns (b) at 0.23% of tension and velocity vectors in the region of welded joint (c).

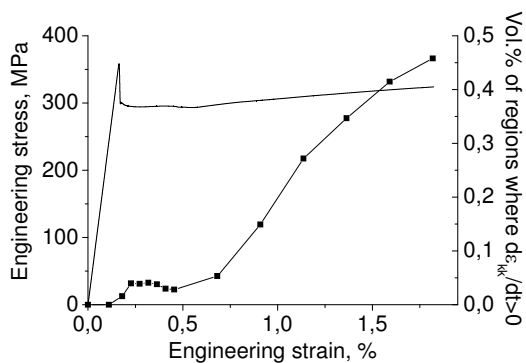


Fig. 3. The stress-strain curve (solid line) and vol.% of regions where mesoscale bulk deformation is positive (dotted line).

Thereafter Lüders fronts begin to propagate across the specimen along the tensile axis at an approximately constant velocity. This is represented by a horizontal portion of the stress-strain curve. The plastic strain rate is at a maximum in the fronts and is nearly zero behind them. The propagation of the Lüders bands is controlled by a competing plastic strain nucleation process in the elastic material ahead of the Lüders fronts and that of strain hardening behind them. The fronts originally shaped like an hour-glass may be further transformed into straight lines directed at an angle to the tensile axis. In this case, the deformation in the counter-propagating fronts

is accomplished by transversal shifting. The specimen undergoes periodic displacements perpendicular to the axis of tension. Powerful vortex motion is observed in the region of the welded joint (Fig. 2(c)). Once the entire material capable of plastic deformation is involved in plastic flow, the stress-strain curve reaches the strain-hardening stage.

4. Microstructure-based simulation of deformation processes in welded steel specimens

A microstructure model of the weld-affected material reproduces change of the grain size throughout the seam, HAZ and base metal regions, Fig. 1(a). The grains differently colored are varied by their elastic and plastic properties. The strain-hardening and Hall-Petch relations were taken into account in constitutive models of individual grains so that the smaller grains in the HAZ possess a higher yield stress than those in the base metal. The yield criterion, Eqn. (1), was used to describe elastic-to-plastic transition at the mesoscale.

Grain boundaries give rise to the stress concentration from the beginning of loading, with the maximum stresses observed near triple joints of grains markedly different by their elastic modules. The highest values of stresses appear at the interfaces between the HAZ and the base metal and between the HAZ and the seam (Fig. 4). The specimen free surface, in turn, serves as an interface between the metal and air. That is why a scatter of local stresses relative

to the average level is essentially more pronounced on the free surface than in the bulk of the material (Fig. 4). This is the mechanical reason for plastic deformation to originate on the surface in the base metal regions adjacent to HAZ. Incipient shear bands consequently propagate into the bulk as a front of localized plastic deformation. The stress-strain curve demonstrates the yield tooth, a horizontal part and the strain-hardening stage (Fig. 3).

According to experimental data [3], microcracks mainly originate in the regions of hydrostatic tension. From this viewpoint it is interesting to analyse evolution of hydrostatic strains ε_{kk} in the weld-affected material. Under external tension the material undergoes positive mesoscale ε_{kk} at the initial stage of loading. In compression, however, the regions where $\varepsilon_{kk} > 0$ are not observed under elastic deformation but appear in the vicinity of incipient shear bands. Volume content of these regions increases in a non-linear manner as plastic deformation develops. As far as local stress here achieves a critical value, microcracks are expected to occur.

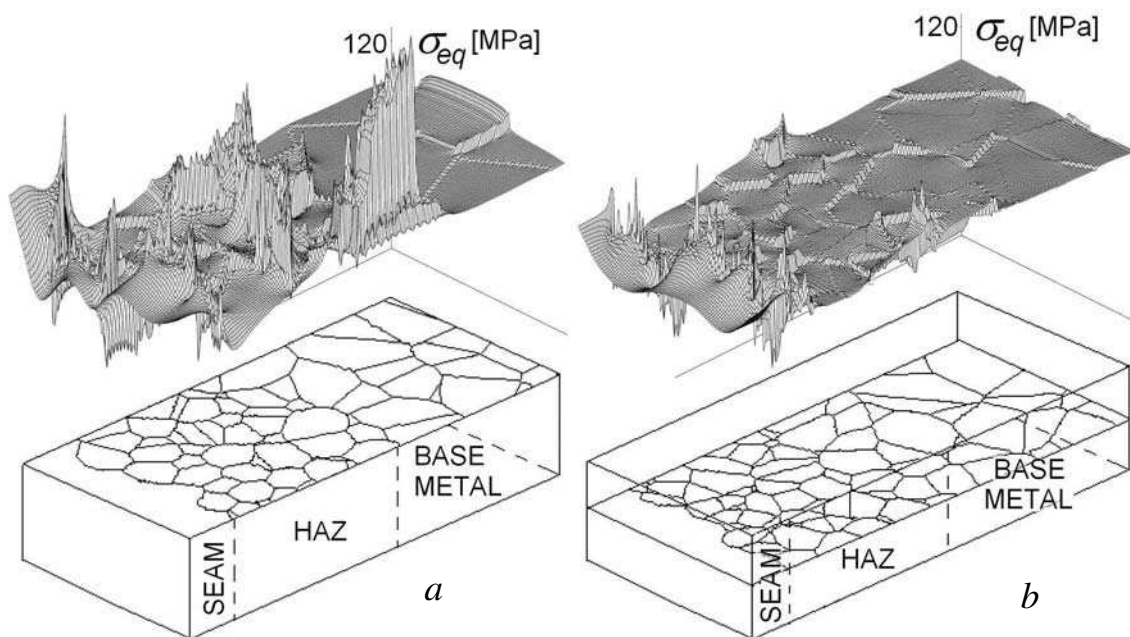


Fig. 4. Equivalent stress patterns on the free surface (a) and in the bulk (b) of the weld-affected microstructure under elastic deformation.

Acknowledgements

Financial support of Deutsche Forschungsgemeinschaft (DFG-project SCHM 746/102-1) and Russian Foundation for Basic Research (grant №10-01-90403-Ukr-a) is gratefully acknowledged.

References

1. Wilkins M., Computer Simulation of Dynamic Phenomena, Springer, New York, 1999.
2. Zhang J., Jiang Y., Lüders bands propagation of 1045 steel under multiaxial stress state. *Int. J. Plasticity*. V.21. 2005. P.651-670.
3. Panin V.E., Egorushkin V.E., Nonequilibrium thermodynamics of a deformed solid as a multiscale system. Corpuscular-wave dualism of plastic shear. *Physical Mesomechanics*. V. 11, I. 3-4. 2008. P. 105-123.

**Multi phase cellular automaton simulation
of the heat treatment of dual phase steel
F. Roters, Y. Li, N. Peranio, U. Witt, and D. Raabe**

Max-Planck-Institut für Eisenforschung
Max-Planck-Str. 1, 40237 Düsseldorf, Germany
f.roters@mpie.de

In the production of dual phase steels the final heat treatment, often combined with hot dip galvanizing, is decisive for the mechanical properties of the sheet. This is due to the fact, that the heat treatment determines the volume fractions of the phases in the material. In this presentation we introduce a multi phase cellular automaton (CA), which is capable of treating the processes of recrystallization and phase transformation. Depending on temperature both processes take place in parallel and therefore have to be considered competitively by the CA rules.

As the heat treatment is part of the overall production process the CA uses starting configurations for the microstructure, which are the result of crystal plasticity FEM rolling simulations. In turn the FEM simulations use microstructures fitted to experimental findings as starting configuration. The microstructure resulting from the CA simulation can be used for subsequent FEM simulations.

We present results for isothermal heat treatments as well as for non-isothermal treatments. The evolution of phase volume fractions has been experimentally determined for isothermal heat treatments at different temperatures. These data are used for parameter fitting. The parameters determined by this procedure are then used for the simulation of non-isothermal (industrial) heat treatments. In all cases the evolution of the volume fractions of the different phases is compared with experimentally determined volume fractions. Regarding industrial application the CA can be used for the optimization of the heat treatment process.

Hybrid Simulation between Microscopic and Macroscopic Particle Methods:

Application to Deformation and Fracture of Solid Material

Ken-ichi Saitoh¹, Takeshi Okada² and Noboru Shinke¹

¹Department of Mechanical Engineering, Kansai University
3-3-35 Yamatecho, Suita, Osaka, 564-8680 Japan
E-mail: saitou@kansai-u.ac.jp

²Materials and Mechanics Laboratory, Kansai University

1. Introduction

This study aims at hybridization between molecular/atomic dynamics (MD) and macroscopic particle method with continuum framework (e.g. smoothed particle hydrodynamics: SPH). We propose combination at the level of basic equations, i.e., equations of motions.

2. Method, Results and Conclusion

The combined equations of motion should be constructed by using the force bridging method. Formulation from Lagrangian of all the system is possible, too. Interatomic potential for MD region is pairwise type (LJ). The computational model is shown in fig.1. A crack of oval shape is put at the center of the MD domain and the specimen is subjected to tensile loading in mode 1 configuration of fracture mechanics. The SPH part is calculated assuming an isotropic elastic medium (E and ν). However, In order to avoid serious mismatch between material's constant, bi-linear elasticity with strong work hardening is applied, where E is switched to $10E$ when any stress component is more than a certain yield stress. As shown in fig.1, tensile instability does not occur in SPH region and full deformation just as pure MD simulation (right) can be observed in MD region (left). It is concluded that successful analysis of this kind would be relied on to match materials in parameters throughout the deformation and fracture responses. Besides, SPH analysis should include a natural damage variable or fracture criterion even though it is sure to be numerically broken with the original formulation.

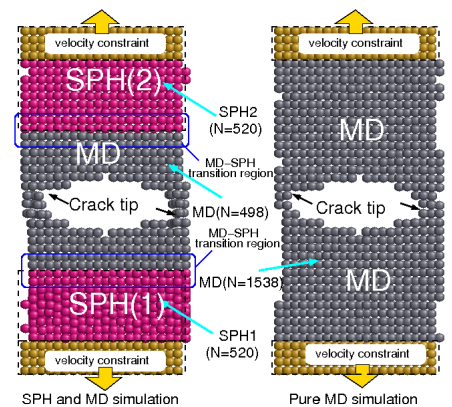


Fig.1 Computational model and result of MD-SPH hybrid (and pure MD) simulation

Acknowledgements: This study was supported by JSPS KAKENHI (21560103) (2010) and HRC Kansai university.

References:[1] G.R.Liu and M.B.Liu, *Smoothed Particle Hydrodynamics*, 341, (2003),World Scientific. [2] K.Saitoh, *et al.*, *Proceedings of 2nd International Conference on MMM*, 132-134, (2004). [3] K.Saitoh, *et al.*, *Proceedings of 3rd International Conference on MMM*, 518-521, (2006).

Molecular Dynamic Simulation of Crack Tip Propagation in Single Crystal FCC Metals Under Uniaxial Tension

H. Salahshoor¹, A. Mirfattahi², S. Mohammadi³

¹⁾ High Performance Computing Lab, Faculty of Civil Engineering, University of Tehran, Tehran, Iran

²⁾ Faculty of Civil Engineering, Sharif University of Technology, Tehran, Iran

³⁾ Associate Professor, High Performance Computing Lab, Faculty of Civil Engineering, University of Tehran, Tehran, Iran

Introduction

Studying mechanical properties of nano materials has stemmed from the technological importance of nano-scale devices and systems such as nano-electro-mechanical-systems (NEMS). Fracture strength of materials strongly depend on the existence and propagation of cracks and defects . The subject of crack propagation is an important area of research in computational material science.

Methods

The crack propagation phenomenon is an unstable process, in which the atoms near the crack tip are under tremendous amount of stress. In this study, three kinds of useful ductile metals, *Ni*, *Al* and *Cu*, with FCC crystal structure have been studied. These metals have FCC crystal structure including Ni, Al and Cu. The *molecular dynamics* (MD) has been employed for simulations. The interatomic potential used for MD modeling of FCC metals is assumed to be the *embedded-atom method* (EAM). Since occurrence of fracture in materials essentially involves bond breaking, an initial crack is introduced between the two layers by specifying a non-interaction potential between the atoms along the crack, and the crack propagation is studied. A uniaxial tensile loading is applied by first fixing the first set of atoms and then dragging them to a certain level of strain with a constant rate.

Results

The obtained results illustrate the way cracks are propagated and the deformation zones are formed in Ni, Al and Cu metals. Emission of the dislocations from the crack tip is also observed in different stages of the crack growth.

Conclusion

The proposed MD modeling of crack propagation in FCC metals has provided a reliable computational tool for simulation of this complex behavior, with results that well comparable to available reference data.

Atomistic Simulation of Solid-Solid Phase Transformations in Fe Nanowires Using Molecular Dynamics

H. Salahshoor¹, A. Mirfattahi², S. Mohammadi³

¹⁾ High Performance Computing Lab, Faculty of Civil Engineering, University of Tehran, Tehran, Iran, Email: h.salahshoor@ut.ac.ir

²⁾ Faculty of Civil Engineering, Sharif University of Technology, Tehran, Iran

³⁾ Associate Professor, High Performance Computing Lab, Faculty of Civil Engineering, University of Tehran, Tehran, Iran

Introduction

Desirable mechanical properties of nanowires have recently motivated researchers to study their structure and phase characteristics in more details. These materials may exist in several equilibrium phases with potential phase transformations which can be either stress induced or temperature induced. In this research, Fe, which is frequently used in nanoscale devices like actuators or sensors, has been the point of consideration.

Methods

The computational method employed in this research is the *molecular dynamics* (MD). A tensile loading is applied by first fixing the first set of atoms and then dragging them to a certain level of strain with a constant rate. As a result, the transformations induced in Fe is produced by axial strains which leads to phase change from BCC to close packed (CP) structure. The interatomic potential used for simulating Fe nanowires is the *embedded-atom method* (EAM). The studied prismatic nanowire possesses a square section with a constant edge, E_0 . This nanowire has been modeled with $\langle 111 \rangle$ axial orientation and an initial length L_0 . Periodic boundary condition (PBC) has been used along the nanowire axis to satisfy the fact that the nanowires have a bigger longitudinal length in comparison with their diameter.

Results

A series of simulations with different aspect ratios have been performed. Also different temperatures have been considered in the simulations and the temperature effect on the stress-strain relationship of Fe has been studied. The presented results include the stress-strain variations of Fe in different temperatures which demonstrate the influence of the temperature in shortening the height of the stress-strain curve. Also the results illustrate that from a certain aspect ratio the results become independent from the L_0 .

Conclusion

In this research effects of temperature and aspect ratio of cylindrical nanowires on solid-solid phase transformations have been discussed using MD simulation. The obtained results are well comparable to available reference data, showing that increasing temperature leads to lower stress-strain strength and also beyond a specific length the results become independent from aspect ratio.

Transformation Induced Plasticity Modelling Based on Micromechanical Approaches

Authors: B. Schmaling¹, A. Ma¹, A. Hartmaier¹

Affiliations: ¹ Micromechanical Modeling of Macroscopic Material Behavior
Interdisciplinary Centre for Advanced Materials Simulation (ICAMS)
Ruhr-Universität Bochum, Germany
benjamin.schmaling@rub.de

ABSTRACT

A micromechanical approach is presented to describe the transformation from austenite into martensite in multiphase steels. The strain-induced transformation model is based on evolving shear band intersections in austenite grains, which are estimated by a crystal plasticity model for the austenite deformation. The transformation model is applied to a representative volume element, in which the resulting internal stresses due to the transformation are calculated. The transformation model paves the way for a multiscale approach to accurately describe the deformation of multiphase steels including the microstructural level.

1. Introduction

Transformation Induced Plasticity (TRIP) steels belong to a generation of low-alloy steels that exhibit a good combination of enhanced strength and ductility. The application of these multiphase steels, containing phase fractions of ferrite, austenite and martensite, depends strongly on reliable constitutive models that accurately describe the material's deformation behaviour. Major challenges for such kind of model developments are posed by the formulation of physical laws for martensite nucleation and transformation kinetics.

The martensite transformation model introduced in this work is based on experimental observations of Venables [1] and the well-known work of Olson and Cohen [2] modified in the following aspect: A dislocation mechanism based crystal plasticity approach calculates local stress and plastic shear amounts for each slip system of face centered cubic (FCC) austenite. The plastic strain quantities, in particular shear band intersections, define the criterion for the start of the martensitic transformation and, hence, the model postulates strain-induced martensitic transformation. In our numerical model, we estimate the shear band intersections and calculate the resulting martensite nucleation probability. To calculate the macroscopic material properties we make use of a micromechanical approach, by setting up a representative volume element (RVE). Consequently, the properties of the RVE are homogenized to yield the macroscopic mechanical properties that result from the given microstructure.

2. Model

In the framework of continuum mechanics the deformation gradient is decomposed into

$$\mathbf{F} = \mathbf{F}_e \mathbf{F}_{tr} \mathbf{F}_p, \quad (1)$$

where F_e is the elastic and F_p the plastic part of the deformation gradient. The deformation resulting from martensite transformation is introduced as an intermediate stress-free configuration and denoted as F_{tr} . It is known from the theory of martensitic transformation that body centered tetragonal (BCT) martensite forms a coherent interface, the habit plane, to FCC austenite through special pairwise arrangement of twin-like structures [3-6]. Assuming a stress-free state in the austenite and averaging the deformation gradient about the twin-like structure consisting of two martensitic variants it follows [7]

$$F_{tr} = I + \sum_{\delta=1}^{24} f_{\delta} M_{\delta} \quad (1)$$

The solution for F_p inside the remaining austenite volume fraction $1 - \sum_{\delta=1}^{24} f_{\delta}$ is calculated by

$$F_p = (L_p \Delta t (1 - \sum_{\delta=1}^{24} f_{\delta}) + I) F_{p0}, \quad (1)$$

where L_p is the plastic velocity gradient. Each transformation system is treated as an individual phase with the volume fraction f_{δ} . F_{tr} describes the total deformation and is the sum of all deformations from the 24 martensitic transformations systems f_m . M_{δ} is defined in a similar way to be found in [7] as

$$M_{\delta} = \varepsilon_d \mathbf{d}^{\delta} \otimes \varepsilon_n \mathbf{n}^{\delta} \quad (2)$$

The parameters for all 24 transformation systems, namely the strain ε_d in shear direction \mathbf{d}^{δ} and the same quantity ε_n in normal direction \mathbf{n}^{δ} of the habit plane, are calculated from the theory of martensitic transformation and depend strongly on the carbon concentration in austenite. We make use of parameters for a carbon concentration of 1.4%, taken from [8].

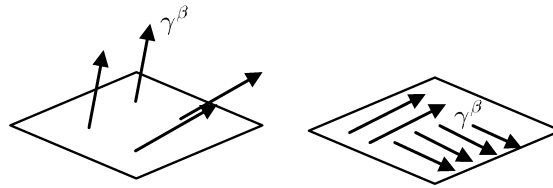


Figure 1: Schematic drawing of shear bands across (left) and parallel (right) to a glide plane α

The model assumes the martensite nucleation to happen at shear band intersections:

$$\dot{f}_{\delta} = \dot{f}_{ref} (1 - \sum_{\varepsilon=1}^{24} f_{\varepsilon}) \left(\frac{\tau_{\delta}}{\tau_c} \right)^m \sqrt{N_p^{\delta} \cdot N_F^{\delta}} \quad (3)$$

accounts for the number of shear band intersections. \dot{f}_{ref} is the reference shear rate. The shear stress which acts on a habit plane is denoted by τ_{δ} . N_F^{α} is defined as the forest shear band density for a glide plane α , according to

$$N_P^\alpha = \sum_{\beta=1}^{12} \frac{\sqrt{\gamma^\alpha \gamma^\beta}}{\gamma_{sb}} \cdot \left[\overset{\text{Edge dislocation part}}{(\mathbf{d}^\beta \times \mathbf{n}^\beta) \cdot \mathbf{n}^\alpha} + \overset{\text{Screw dislocation part}}{(\mathbf{d}^\beta \cdot \mathbf{n}^\alpha)} \right] / 2 \quad (4)$$

The amount of shear crossing a habit plane as depicted in Fig. 1 are projected into the normal direction of the considered plane. N_P^α is defined as the parallel shear band density for a glide plane as follows:

$$N_P^\alpha = \sum_{\beta=1}^{12} \left(\frac{\sqrt{\gamma^\alpha \gamma^\beta}}{\gamma_{sb}} \right) \cdot \left(\sqrt{1 - [(\mathbf{d}^\beta \times \mathbf{n}^\beta) \cdot \mathbf{n}^\alpha]^2} + \sqrt{1 - (\mathbf{d}^\beta \cdot \mathbf{n}^\alpha)^2} \right) / 2 \quad (5)$$

As opposed to implicitly solving for F_p (2) all quantities (4-7) are calculated explicitly using four fitting parameters \dot{f}_{ref} , τ_c , m and γ_{sb} . The material parameters for the FCC crystal plasticity model are shown in Tab. 1. Due to the explicit calculation the time step has to be sufficiently small.

Table 1: Material parameters used for the crystal plasticity model in FCC

$\dot{\gamma}_0$	m	τ_{c_0}	a	h_0	τ_c^s	c_{11}	c_{12}	c_{44}
0.001	0.05	150 MPa	2.25	345 MPa	480 MPa	242 GPa	146 GPa	112 GPa

The elastic constants for ferrite are taken from pure iron and increased by 10% for austenite due to the lack of material data.

3. Results

In Fig. 2 results are shown exemplarily for a circular austenite grain embedded in a pure ferrite matrix, occupying an area fraction of 8%. Loading occurs along the [110]-direction of the austenite grain. The transformation kinetics are shown as well as the internal stresses at the times when the martensitic volume fractions are $f_m = 0.5$ and $f_m = 1$.

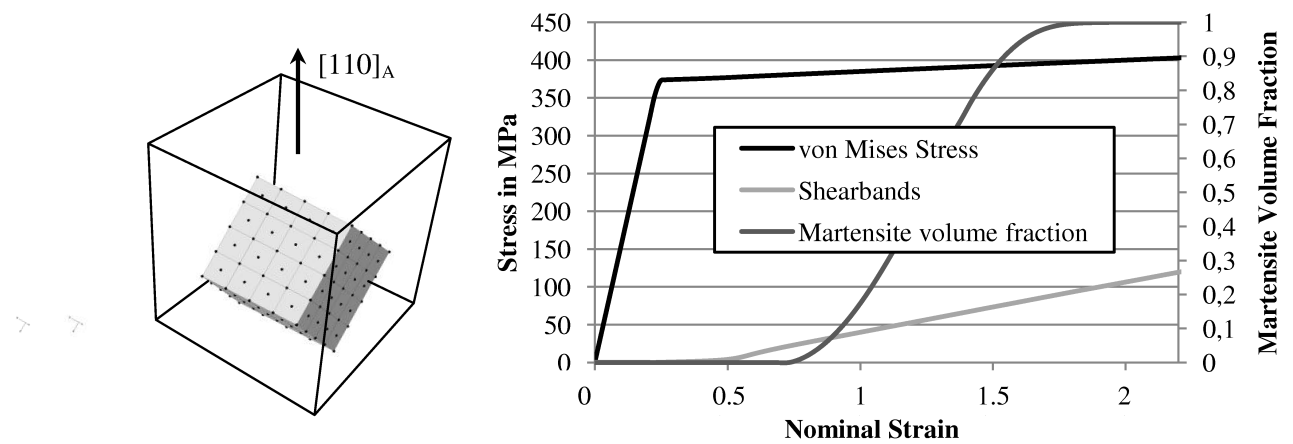


Figure 2: left: crystal orientation of the inclusion material, the loading axis is along the [110] direction; right: stress and equivalent shear band quantities

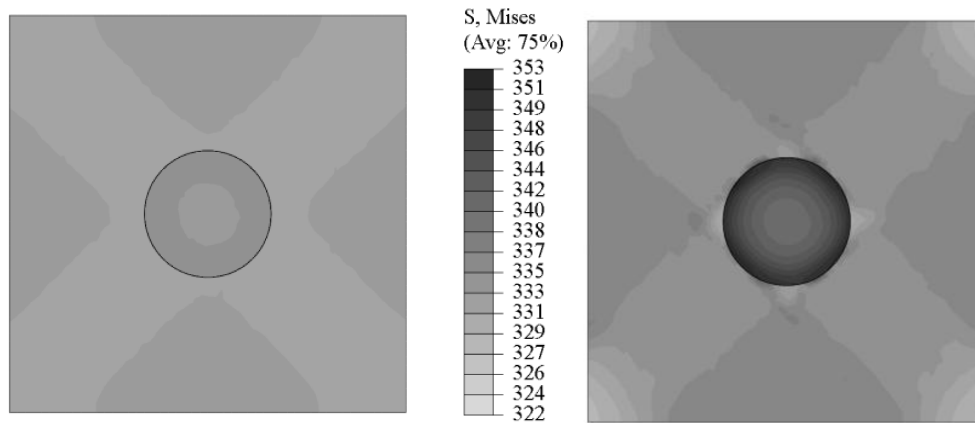


Figure 3: left: von Mises stress in MPa at $f_m = 0.5$; right: von Mises stress at $f_m = 1$

4. Discussion

In an early stage of the model development the transformation parameters are not yet identified. Therefore the model cannot reproduce transformation kinetics observed in experiments, i.e. the model reacts very sensitive to the orientation of the FCC material. Additionally the influence through transformation on the stress-strain curve is observed to be small for most of the cases.

Using the proposed micromechanical approach the stresses due to the transformation are accessible and can be used to study the failure behavior of these steels in the future. Ductile failure for ferrite and brittle fracture for martensite as two concurring failure typically observed in TRIP steels are to be studied and compared with experiments to verify the model.

References

- [1] Venables, J.A., The martensite transformation in stainless steel, *Phil. Mag.*, 7 (1962) 35
- [2] Olson, G.B., Cohen, M., A mechanism for the strain-induced nucleation of martensitic transformations, *J. Less-Common Metals*, 28 (1972)
- [3] Wechsler, M.S., Lieberman, D.S., Read, T.A., 1953. On the theory of the formation of martensite. *Trans.Am. Inst. Min. Metall. Eng.* 197 (11), 1503–1515.
- [4] Ball, J.M., James, R.D., 1987. Fine phase mixtures as minimizers of energy. *Arch. Ration. Mech. Anal.* 100 (1), 13–52.
- [5] Bhattacharya, K., 1993. Comparison of the geometrically nonlinear and linear theories of martensitic transformation. *Continuum Mech. Thermodyn.* 5 (3), 205–242.
- [6] Hane, K.F., Shield, T.W., 1998. Symmetry and microstructure in martensites. *Phil. Mag. A* 78 (6), 1215–1252.
- [7] James, R.D., Hane, K.F., 2000. Martensitic transformations and shape-memory materials. *Acta Mater.* 48 (1), 197–222.
- [8] Turteltaub, Suiker, Transformation-induced plasticity in ferrous alloys *J. Mech. Phys. Solids* 53 1747–88, 2005

Atomistic study of xenon crystal growth via low-temperature atom beam deposition (LT-ABD)

Nicola Totò¹, J. Christian Schön², and Martin Jansen³

Max Planck Institute for Solid State Research, Heisenbergstrasse 1, 70569 Stuttgart, Germany; email: ¹nico@fkf.mpg.de, ²C.Schoen@fkf.mpg.de, ³M.Jansen@fkf.mpg.de

ABSTRACT

We have used a multi-step approach to study the deposition of Xe-atoms on a sapphire substrate and the subsequent growth of ordered Xe-phases via the LT-ABD method, which is a new way to synthesize metastable solids. We employed molecular dynamics with empirical potentials to model the interatomic interactions. We simulated the Xe-deposition process and studied the growth mode depending on various synthesis parameters (deposition rate, substrate temperature). Simulated deposition at high rates resulted in hot, amorphous samples, whereas deposition at a lower rate produced samples displaying crystalline regions of fcc- or hcp-type. The substrate temperature determined the growth mode, with lower temperature favouring 3D growth, and higher temperatures layer-by-layer growth. Finally, upon simulation of tempering the deposited samples at several temperatures less than 100 K, we found that crystalline order was always established. In all simulations the deposited Xe displayed a slight preference for fcc- over hcp-packing, although extended defects were likely to form. The occurrence of different growth modes and the formation of defects were explained by studying relevant atomistic processes as well as the system energetics.

1. Introduction

Growth processes of solid materials are of great interest from both the fundamental and the technological point of view. Of particular relevance is the relationship between the synthesis route followed and the resulting modification of the material and its morphology. Recently, a new solid state synthesis technique, called the low-temperature atom beam deposition method, has been developed and used to produce stable and metastable phases of ceramic and oxide compounds.¹ The goal of this study is to model such a synthesis method.

As an example system, growth of xenon on a sapphire (Al_2O_3) substrate was studied throughout all its stages: the dynamics of the Xe atoms in the gas phase prior to adsorption, the impact of the gas-phase atoms on the substrate surface as well as their adsorption and diffusion, and, finally, the effect of tempering and annealing the system obtained as a result of the deposition.

2. Calculation method and preliminary studies

All calculations were performed by using classical MD. Simulations of deposition and tempering were carried out within a rectangular prismatic simulation unit cell periodically repeated in the horizontal xy-plane (sidelength about 50 Å). The system was comprised of the Al_2O_3 substrate and the depositing Xe species.

We used the Matsui potential² and the Lennard-Jones 12-6 potential³ for describing atomic interactions in Al_2O_3 and in Xe, respectively. The interactions between Xe atoms and the Al

and O atoms were described by a modified Lennard-Jones potential of the form:

$$V_{Y-Xe}(r_{ij}) = 4\varepsilon_{Y-Xe} \left[\left(\frac{\sigma_{Y-Xe}}{r_{ij}} \right)^{10} - \left(\frac{\sigma_{Y-Xe}}{r_{ij}} \right)^5 \right]; \quad (1)$$

where Y stands for either Al or O. The long-range attractive term varies as the inverse fifth power of the distance, thus mimicking the averaged effect of the interaction between several point charges and the induced dipole in Xe. The parameters chosen are: $\varepsilon_{Al-Xe} = \varepsilon_{O-Xe} = \varepsilon_{Al_2O_3-Xe} = 0.015$ eV, $\sigma_{Al-Xe} = 2.468$ Å, $\sigma_{O-Xe} = 2.977$ Å.

The substrate was an Al_2O_3 slab, in the corundum crystal structure, with the O-terminated (0001) surface exposed. Before the actual deposition, the slab was equilibrated by performing MD for 1 ps at the deposition temperature. The bottom part of the substrate was kept fixed and a simple thermostat based on velocity rescaling was applied to the lowest third of the slab.

The dynamics of Xe in the gas phase was modelled over a wide range of pressures (10^{-7} - 10^3 bar) by performing classical MD in the (NVT) ensemble. For temperatures ranging from 50 to 500 K, no stable cluster could form for all pressures less than about 10 bar. Since in the experiment the pressure during deposition was about 10^{-5} mbar, we could model the growth process as the sequential deposition of single Xe particles at a given frequency with a predefined initial kinetic energy in the range of 0.01 to 0.03 eV, corresponding to thermal deposition. The initial distance of the particle from the growing surface was 10 Å, with the lateral position randomly chosen and the initial velocity directed toward the substrate surface.

3. Results

We first simulated deposition at a rate of 2×10^{11} atoms s^{-1} , corresponding to a growth rate of about 10^9 monolayers/s. The structures deposited at this rate were all completely amorphous and did not display any degree of order. After tempering we observed that at all temperatures in the range of 10 to 100 K the structures underwent a phase transition towards a more ordered configuration.

In order to identify regions with crystalline structure, we studied the distribution of bond angles of all 12-fold coordinated Xe atoms. By comparing their bond angle distributions with those of an atom in an ideal fcc and hcp crystal, each atom could be labelled as fcc-like, hcp-like, or of undefined type. This analysis was employed to follow the crystallization process (see Fig. 1). Typically, after the temperature of the deposit had decreased down to approximately 130 K, the atoms started arranging themselves such that they gained 12-fold coordination. These 12-fold coordinated nuclei formed initially in proximity to the substrate surface. Upon further cooling, the 12-fold coordination spread over the whole Xe sample and the atoms slowly arranged into a close-packed crystal structure displaying large regions with fcc- or hcp-packing.

For all tempering temperatures the Xe deposit reached a close-packed crystalline configuration (see Fig. 2, top panels). An alternation of fcc and hcp stacking sequence was often observed and, consequently, a large presence of stacking faults. These results are consistent with the findings of a recent MD study where nucleation in a homogeneous Lennard-Jones liquid was investigated during moderate and deep undercooling⁴.

In order to speed up the equilibration process, we increased by a factor of 10 the strength $\varepsilon_{Al_2O_3-Xe}$ of the interaction between the deposited Xe and the substrate. Although increasing $\varepsilon_{Al_2O_3-Xe}$ did not affect the final crystalline structure of the deposited Xe, the direction of

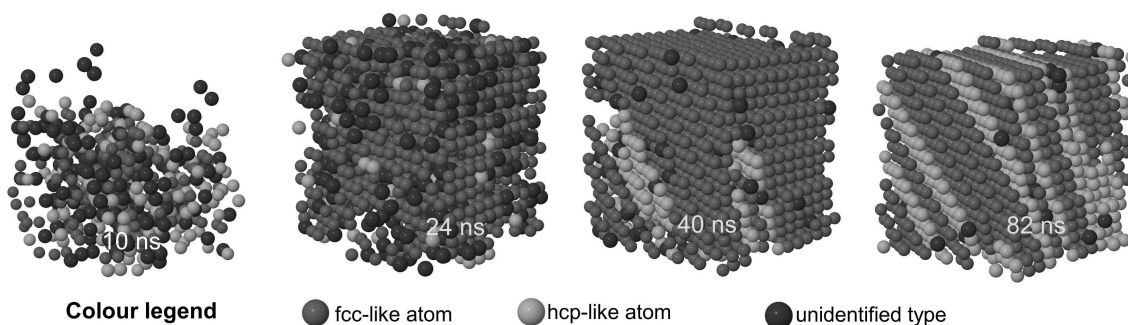


Figure 1: Result of single atom bond angle analysis performed on four consecutive instants during tempering at 25 K of a hot Xe deposit deposited at a rate of 2×10^{11} atoms s^{-1} . Only 12-fold coordinated Xe atoms are shown.

the stacking faults was always found parallel to the substrate surface, unlike the case with the weaker interaction, where the stacking faults preferentially ran along close-packed directions diagonal to the plane of the interface with the substrate.

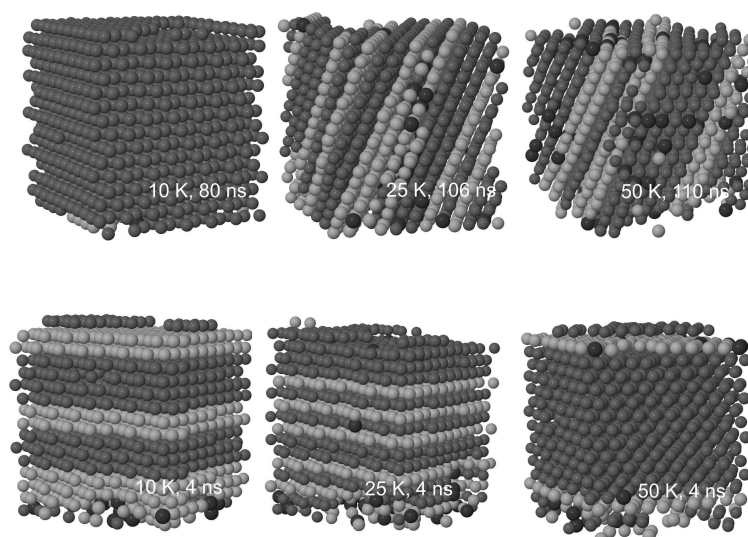


Figure 2: (Top panels) Snapshots during tempering of Xe deposited at high rate at three different temperatures. (Lower panels) Tempering with the strength $\epsilon_{Al_2O_3-Xe}$ of the interaction between the Xe and the substrate increased by a factor of 10. Only 12-fold coordinated Xe atoms are shown. The colour legend is as in Fig. 1.

Simulations were also performed where the deposition rate was decreased to 10^{10} atoms s^{-1} . Throughout the range of 10 to 100 K of investigated temperatures, the grown Xe assumed a close-packed crystal structure from the early stage of the deposition process. As the deposition continued, some surface roughness developed thus giving rise to three-dimensional islands, with decreasing roughness for increasing substrate temperature. Again fcc- and hcp-ordered regions coexisted, separated by stacking faults (see Fig. 3).

4. Discussion and conclusions

The roughness of the surface of the deposited species could be tuned by selecting an appropriate substrate temperature: the lower the deposition temperature, the rougher the surface. In general, a nearly perfect layer-by-layer growth was obtained in the approximate temperature range 60 to 70 K. These observations are consistent with previous MD studies of homogeneous growth

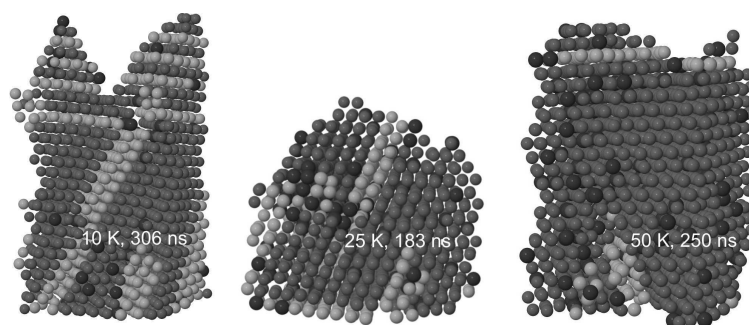


Figure 3: Bond angle analysis of structures grown at the lower rate of 10^{10} atoms s^{-1} and at different substrate temperatures. Only 12-fold coordinated Xe atoms are shown. The color legend is as in Fig. 1.

of a model Lennard-Jones system⁵, where it was found that the best substrate temperature for layer-by-layer growth corresponded to roughly half the system melting temperature.

In order to investigate the reason for different growth modes, calculations of activation barriers to diffusion for a single Xe adatom on a Xe(111) surface were undertaken. In particular, we focused on diffusion processes which resulted in the adatom hopping down a step edge on the Xe(111) surface. We found that step descent was seriously frustrated at temperatures below about 50 K. This caused the three-dimensional growth for temperatures below 50 K.

Regarding the presence of the stacking faults, we studied the energetics of an atom in bulk Xe in both the fcc- and hcp-crystal structure. The fcc-packing was found to lie lower in energy than the hcp-packing, although the difference was of only about 1.5 meV/atom. Furthermore, the adsorption energy in a three-fold hollow site of fcc- and hcp-type was calculated to be of around 1.6 meV in favour of the former adsorption site. Whereas for the investigated system fcc-packing is slightly favoured with respect to hcp-packing, the difference in stability is extremely tiny. Therefore, competition between fcc-like and hcp-like stacking is to be expected. Concerning the different growth directions of the stacking faults depending on $\varepsilon_{Al_2O_3-Xe}$ (compare upper and lower panels of Fig. 2) we suggest that, for small $\varepsilon_{Al_2O_3-Xe}$, inhomogeneities in the stress field experienced by the first Xe layer adsorbed onto the substrate surface could serve as seeds from which the stacking faults formed and grew. By contrast, for large $\varepsilon_{Al_2O_3-Xe}$, the adsorbed Xe layer closest to the substrate was subject to a more intense and more homogeneous stress field, without any obvious seed of the stacking faults. Therefore, in this case, the stacking faults arose naturally in the growth direction as a consequence of the strong competition between fcc- and hcp-packing.

References

- [1] D. Fischer and M.Jansen, *J. Am. Chem. Soc.* **124**, 3488, 2002.
- [2] M. Matsui, *Phys. Chem. Miner.* **23**, 345, 1999.
- [3] W. Hogervorst, *Physica* **51**, 77, 1971; A. A. Clifford, P. Gray, and N. Platts, *J. Chem. Soc. Faraday Trans. 1* **73**, 381, 1977.
- [4] L. J. Peng, J. R. Morris, and Y. C. Lo, *Phys. Rev. B* **78**, 012201, 2008.
- [5] M. Schneider, A.Rahman, and I. K. Schuller, *Phys. Rev. Lett.* **55**, 604, 1985; S. M. Paik and S. Das Sarma, *Phys. Rev. B* **39**, 1224, 1989; C. M. Gilmore and J. A. Sprague, *Phys. Rev. B* **44**, 8950, 1991.

Modeling Microstructure and Texture Evolution during Recrystallization considering Precipitation Effects

Carmen Schäfer¹, Volker Mohles¹, Günter Gottstein¹

¹Institut für Metallkunde und Metallphysik, RWTH Aachen, Kopernikusstr.14, 52075 Aachen

ABSTRACT

The presented work focuses on the modeling of microstructure and texture evolution during recrystallization in an Al-1wt% Mn alloy. The starting materials, containing a different initial microstructure and different levels of manganese in solid solution were subjected to cold rolling and final annealing. Dependent on the initial solute content, these two alloy variants show a different recrystallization behavior which originates from changes in microchemistry during the heat treatment and different pre-deformation microstructures. To model the experimentally observed recrystallization behavior a 3D cellular automaton was applied in combination with a precipitation and deformation texture model.

1. Introduction

It is known from literature [1, 2] that the recrystallization behavior is strongly influenced by the thermo-mechanical pre-treatment of the material, e.g. the dislocation density introduced during deformation, the initial pre-deformation texture, etc. Furthermore, during recrystallization, precipitation of second-phases accompanying the change in manganese solute content can influence the recrystallization behavior. The presence of small particles causes a Zener drag, which can hinder or in extreme cases even suppress recrystallization [1, 2]. The aim of this work was the modeling of recrystallization microstructure and texture after cold rolling considering effects such as different pre-deformation texture, microstructure and solute contents.

2. Experiments

The material used for this study was an Al-1 wt% Mn alloy, which was received as hot rolled material from industrial sheet metal fabrication. To produce two different sample series, the material was immediately cold rolled or underwent a homogenization treatment before cold rolling. The starting material, which was directly cold rolled to reductions of 50 % and 70 %, is in the following referred to as series R, respectively R50 and R70 to indicate the different rolling reductions (R = Rolling). For the other sample series RZ (RZ = Rolling + Zener drag), the hot rolled material was subjected to an additional homogenization treatment at $T = 610\text{ °C}$ for 14 hours to alter the manganese solute content. Like the previous material, this one also underwent thickness reductions of 50 % or 70 % during cold rolling. During the homogenization treatment smaller particles dissolved, so that the manganese solute content increased. To preserve this solute content the material was quenched afterwards. Accordingly, the material of series R had a solute content of 0.281 wt% Mn while the series RZ material displays a solute content of 0.4427 wt% Mn. Due to the additional homogenization treatment in the series RZ material both pre-deformed conditions differed in their initial microstructure as displayed in Fig. 1. The initial microstructure and texture are of relevance for the deformation texture simulations and for the later recrystallization process in terms of nucleus orientations and density. After initial cold rolling the material of series R and RZ were subjected to annealing at temperatures of $T = 350\text{ °C}$ and $T = 400\text{ °C}$. The recrystallization time required to reach a recrystallized volume fraction of 95 % amounted to 50 seconds for

series R50 and to 11 hours for series RZ50 in case of annealing the 50 % cold rolled material at $T = 350^{\circ}\text{C}$.

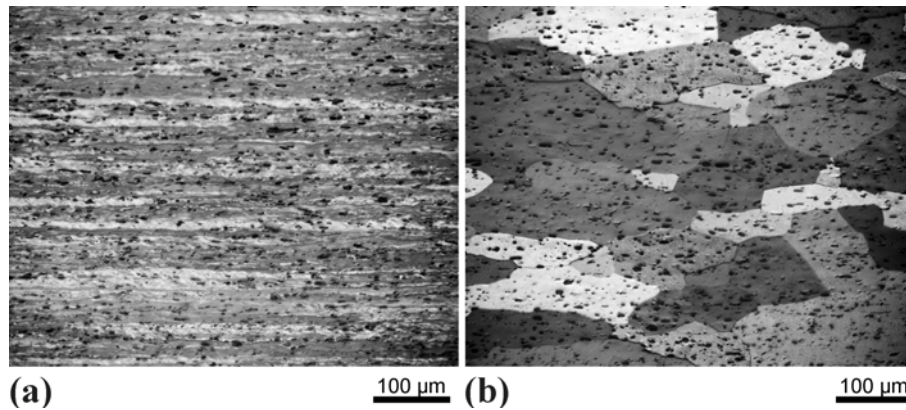


Fig. 1 Initial microstructure before final cold rolling and annealing: (a) for series R: hot rolled material from the industrial production line, (b) for series RZ: industrial hot rolled material subjected to an additional solution treatment at $T=610^{\circ}\text{C}$ for 14h, recrystallized microstructure. The small black dots represent second-phase particles (constituents).

3. Simulations

3.1. Recrystallization Simulations

The recrystallization simulations were carried out with the 3D cellular automaton CORE as indicated in Fig. 2b [3]. Cellular automata are pure growth models; hence the nucleation needs to be treated separately. For the prediction of nucleation efficiencies in a respective grain the ReNuc+ model was applied (ReNuc [4], extended by a model for particle stimulated nucleation [5]). To conduct the recrystallization simulations various inputs from different models were required. Beside deformation and precipitation inputs other important parameters are summarized in Tab.1.

Table 1: Parameters of the Recrystallization Simulations (HAGB = high angle grain boundaries, LAGB = low angle grain boundaries)

<i>parameter</i>	<i>value</i>
<i>Growth parameters:</i>	
activation energy for $40^{\circ}\langle 111 \rangle$	1.0 eV
pre-exponential factor for $40^{\circ}\langle 111 \rangle$	$3.0 \text{ m}^3/\text{N}\cdot\text{s}$
activation energy for HAGB	1.1eV
pre-exponential factor for HAGB	$3.0 \text{ m}^3/\text{N}\cdot\text{s}$
activation energy for LAGB	1.6 eV
pre-exponential factor for LAGB	$1000 \text{ m}^3/\text{N}\cdot\text{s}$
<i>Recovery parameters:</i>	
activation energy climb	1.54 eV 3IVM+ Fit [Mohles 2008]
activation energy cross slip	$\rightarrow \infty$ (unused since no stress is applied)

3.2 Deformation Simulations

To provide the initial microstructure for the recrystallization simulation, a deformation texture simulation with GIA-3IVM+ [3, 6] was carried out. The most important quantities from the GIA-3IVM+ output were the orientation-dependent dislocation densities and the individual grain orientations after deformation. The average total dislocation densities, which provide the driving force for recrystallization, obtained for the different material states were:

$$\rho_{R50} = 1.98 \cdot 10^{14} \text{ m}^{-2}, \quad \rho_{R70} = 2.99 \cdot 10^{14} \text{ m}^{-2}, \quad \rho_{RZ50} = 5.55 \cdot 10^{13} \text{ m}^{-2}, \quad \rho_{RZ70} = 6.7 \cdot 10^{13} \text{ m}^{-2}.$$

The modelled deformation textures comprised mainly orientations along the β -fiber. While for the rolled material of series RZ still some volume fraction of Cube component could be found, no remaining Cube texture components were obtained for series R.

In a subsequent step the deformation data was further analyzed with respect to substructural quantities (ReNuc [4]) and substructural inhomogeneities around constituent particles were calculated with the sub-model GIA-DZ [5]. From this data the effective nucleation mechanisms for the individual grain orientations could be identified. The quantitative nucleus density for the respective nucleation mechanism was later on calculated within the CORE model [3].

3.3 Precipitation Simulations

In the case of the series RZ material the recrystallization behavior was strongly influenced by precipitation. Therefore, prior to the actual recrystallization simulation, precipitation simulations were carried out with the classical nucleation and growth model for precipitation ClaNG [7] for the different material states (rolling reduction, temperature). To adjust modeling parameters in the ClaNG model, the predicted Mn solute content was at first validated using experimental data from thermo-electrical power measurements.

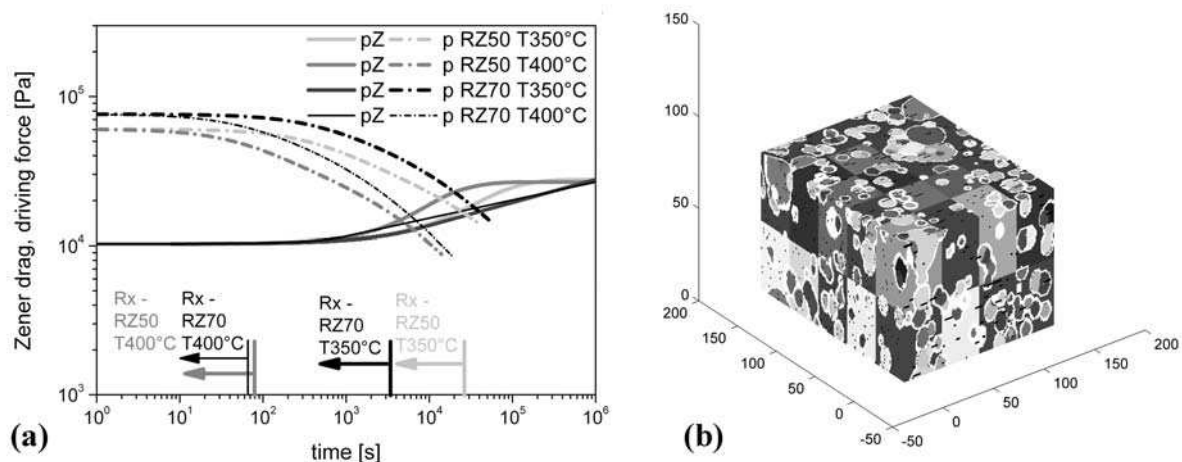


Fig. 2: (a) Zener drag p_Z as calculated from the modeled dispersoid radius and volume fraction for series RZ. The driving force p is shown for comparison. The arrows denote that recrystallization proceeds prior to the time indicated by the bar, and thus whether an interaction of recrystallization and precipitation is anticipated. (b) Cellular automata CORE displaying a partially recrystallized structure.

The ClaNG simulations provide the evolution of dispersoid radii, volume fractions and manganese solute content as a function of time. The above mentioned quantities were then used for the calculation of Zener drag and solute drag, which in turn influence the recrystallization behavior. The Zener drag as calculated from the precipitation simulation outputs, indicated a negligible influence of Zener drag for the series R material during the

recrystallization process. By contrast, for series RZ material significant back-driving forces were already present during recrystallization (Fig. 2a), as apparent from the overlap of recrystallization regime and concurrently increasing values of Zener drag.

4. Results and Discussion

For the recrystallization simulations, the input data from prior calculations as described in Secs. 3.1-3.3 was utilized. As stressed previously the used model was a pure growth model and hence required separate input of a nucleation model. However, the actual nucleus density was calculated within CORE for the respective grain and nucleation site: at particles, grain boundaries, shear bands, transition bands. The calculation of the critical nucleus size, which was crucial for the calculation of nucleus density, was based on the dislocation density at the onset of recrystallization. Hence, the reduction of the dislocation density due to recovery prior to recrystallization was taken into account. In the present case the incubation time was predicted using $\tau = \tau_0 \cdot \exp(Q/kT)$, where τ_0 is the incubation time at reference temperature and Q the activation energy for recrystallization, which depends on the solute content. The parameters τ_0 and Q were taken from experiments for the present materials. After completion of the incubation time for a certain heat treatment the nuclei were activated at the same time (site-saturation). The modelled recrystallization textures and microstructures considering the modelled Zener and solute drag are given in Figs. 3, 4.

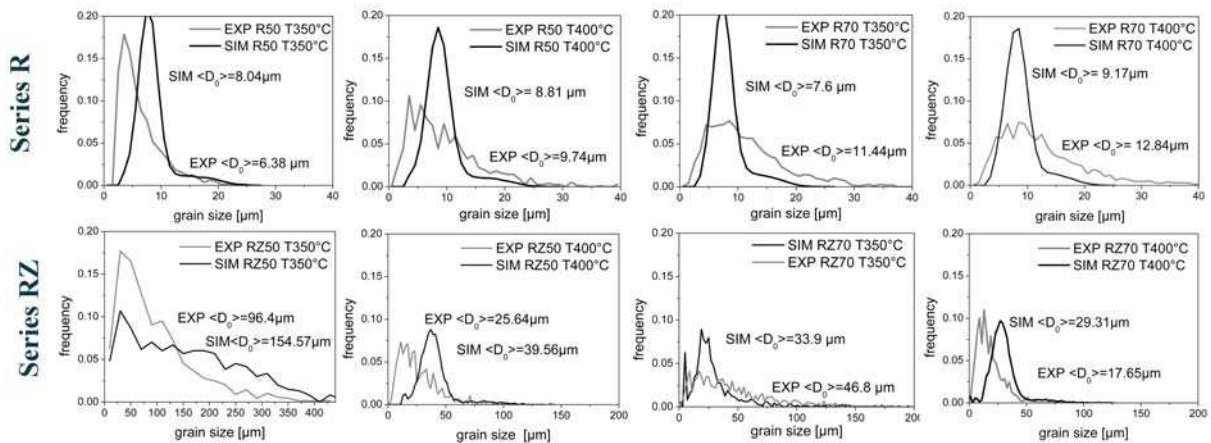


Fig. 3: Grain Size Distributions as modelled with the recrystallization model CORE for the series R and RZ. Note the vastly different grain size scale. (Experimental data - gray, Simulation data - black).

The simulated microstructures in Fig. 4 show good agreement with the experimental ones. The grain size distributions in Fig. 3 give a better measure of the quality of the simulation. The average grain size is predicted very well, whereas the distribution width shows deviations. An improvement in the prediction of the average grain size was obtained by the consideration of recovery in the calculation of the nucleus density, since recovery reduces the available nucleation sites. Without the consideration of recovery these huge differences in average grain size would not be feasible. Deviations in the grain size distributions can, of course, also result from experimental errors during the measurement. Further, deviations in the simulated grain size distribution can at least in part be attributed to variations in the grain boundary mobilities which are wider in reality than in the model. Moreover, in general the assumption of site-saturated nucleation leads to lower size distribution width.

Acknowledgement

This research was carried out under the financial support of the German Research School for Simulation Sciences (www.grs-sim.de) and under Project No. MC 4.03176 in the framework of the Strategic Research programme of the Netherlands Institute of Metals Research, respectively Materials to Industry M2i in The Netherlands (<http://www.nimr.nl>). The authors gratefully acknowledge the support of Hydro Aluminium Bonn for providing the thermo-electric power measurements.

References

- [1] G. Gottstein, *Physical Foundations of Material Science*, Springer, Heidelberg (1998).
- [2] F.J. Humphreys, M. Hatherly, *Recrystallization and related annealing phenomena*, Elsevier (2004).
- [3] C. Schäfer, G. Pomana, V. Mohles, G. Gottstein, O. Engler, J. Hirsch, *Adv. Eng. Materials* 12 (2010) 131.
- [4] M. Crumbach, M. Goerdeler, G. Gottstein, *Acta Mater.* 54 (2006) 3275.
- [5] C. Schäfer, J. Song, G. Gottstein, *Acta Mater.* 57 (2009) 1026.
- [6] V. Mohles, X. Li, C. Heering, G. Hirt, S. Bhaumik, G. Gottstein, in *Proc. of the 11th Inter. Esaform Conf. of Material Forming*, INSA de Lyon, Springer (2008).
- [7] M. Schneider, *Modellierung und Validierung zeitabhängiger mikrochemischer Prozesse in Aluminium Knetlegierungen*, Doctoral Thesis, IMM, RWTH Aachen (2006).

Homogenized Elasticity of Martensitic Microstructures

Authors: Hanuš Seiner^{1,2}, Ondřej Glatz^{1,2}, Michal Landa²

Affiliations: ¹Institute of Thermomechanics, Academy of Sciences of the Czech Republic, Dolejškova 5, 18 200 Prague 8, Czech Republic; ²Faculty of Nuclear Sciences and Physical Engineering, CTU in Prague, Trojanova 13, 120 00 Prague 2, Czech Republic.

ABSTRACT

In this paper, a procedure for determination of homogenized elastic properties of martensitic laminates is described and applied to analyze the elasticity of the 1st order laminates of the Cu-Al-Ni shape memory alloy. In particular, the evolution of the Young's modulus and the shear modulus of a laminating wire in tension is calculated and the contribution of the elastic energy to the reorientation process in a bulk laminate subjected to triaxial tension is discussed.

1. Introduction

Thermoelastic martensites (low temperature phases of the shape memory alloys) can be often found in a form of fine laminates or other geometrically ordered mixtures of different variants, called martensitic microstructures [1]. As seen in Fig.1, when such a laminate is subjected to external mechanical loadings, the process of the pseudoplastic deformation is provided by reorientation of one component of the laminate into another one, i.e. by a continuous change of the respective volume fractions within the laminate.

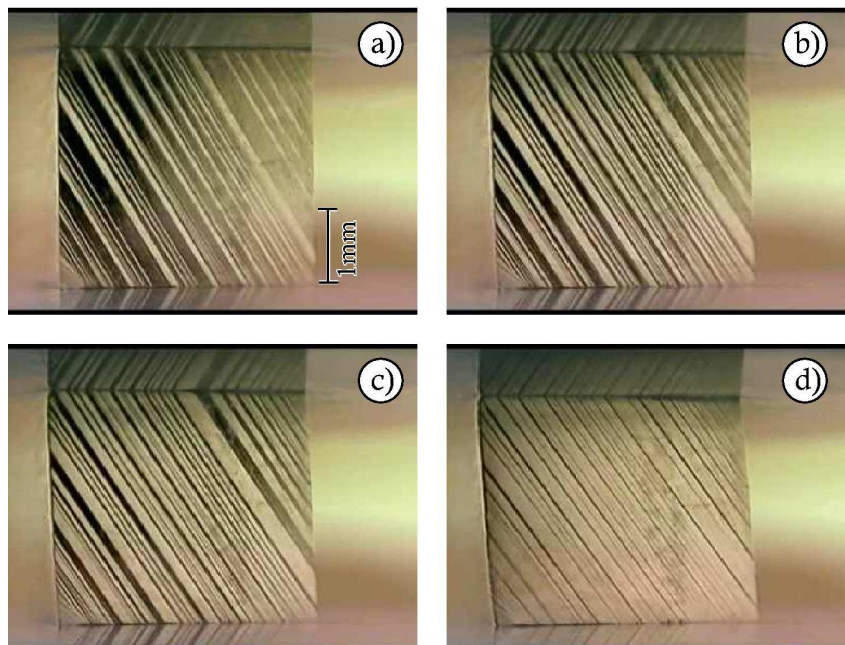


Figure 1: A sequence of snapshots taken during stress-induced reorientation of a Type-II laminate in a single crystal of the Cu-Al-Ni shape memory alloy: a)÷d) correspond approximately to 40%, 50%, 60% and 90% of the target variant of martensite. (Courtesy of V. Novák, IP ASCR.)

During such a change, the elasticity of the material is changing as well. As shown in this paper

by two examples, this change can be dramatic and contributes non-negligibly to the reorientation process. To investigate this phenomenon, it is necessary to construct a proper homogenizing procedure which takes the crystallographic relations between individual components of the laminate into account.

2. The homogenizing procedure

The procedure used for such analysis in this paper is a slight modification of the procedure described by the current authors in [2]: consider a fine (homogeneous) laminate consisting of variants of martensite, i.e. of two martensites with the atomic lattice differently rotated with respect to the parent austenitic lattice. Since these two components differ by a mutual rotation only (say a rotation \mathbf{R}^{IJ} between the variants denoted I and J), their elastic coefficients are related as follows

$$C_{abcd}^I = C_{ijkl}^J R_{ai}^{IJ} R_{bj}^{IJ} R_{ck}^{IJ} R_{dl}^{IJ}. \quad (1)$$

This rotation can be determined from the crystallographic theory and is specific for each pair of variants and for each twinning system (see [1] for more details). Consider further that each component gains a homogeneous deformation gradient (\mathbf{F}^I and \mathbf{F}^J) such that the entire deformation gradient of the laminate is

$$\mathbf{F} = \lambda \mathbf{F}^I + (1 - \lambda) \mathbf{F}^J, \quad (2)$$

where λ is the volume fraction of the variant I in the laminate. The natural conditions put on the gradients \mathbf{F}^I and \mathbf{F}^J are the geometric compatibility at the interfaces $((\mathbf{F}^I - \mathbf{F}^J)\mathbf{v}) = 0$ for each \mathbf{v} lying in the plane of the interface) and the stress equilibrium at the interfaces

$$[C_{ijkl}^I (F_{ij}^I + F_{ji}^I - 2\delta_{ij}) - C_{ijkl}^J (F_{ij}^J + F_{ji}^J - 2\delta_{ij})] n_k = 0 \quad (3)$$

for each l , where \mathbf{n} is a unit vector perpendicular to the interface. Under such conditions, and for the macroscopic gradient \mathbf{F} given, the stored elastic energy density of the laminate can be evaluated as

$$w = \frac{\lambda}{8} (F_{kl}^I + F_{lk}^I - 2\delta_{kl}) C_{ijkl}^I (F_{ij}^I + F_{ji}^I - 2\delta_{ij}) - \frac{1-\lambda}{8} (F_{kl}^J + F_{lk}^J - 2\delta_{kl}) C_{ijkl}^J (F_{ij}^J + F_{ji}^J - 2\delta_{ij}). \quad (4)$$

By evaluating this density for a sufficiently large and general set of macroscopic gradients \mathbf{F} , the resulting tensor of elastic coefficients of the laminate is obtained.

3. Examples of application on the Cu-Al-Ni shape memory alloy

In the following section, the homogenized elasticity of the 1st order laminates will be discussed for two special cases. In both of them, the considered material will be the Cu-Al-Ni shape memory alloy [1,3]. In this material, the martensite is orthorhombic with nine independent elastic coefficients known from ultrasonic measurements [2]. Three different systems are possible [1,3]: Compound twins, Type-I twins and Type-II. The Compound twins are highly symmetric (the twinning plane is the plane of mirror symmetry between the individual components of the laminate), and their elasticity is, thus, rather trivial [2] and will be not discussed in this paper. A more general behavior of elasticity due to reorientation of the laminate can be observed for Type-I and Type-II twins, which are both less symmetric.

3.1 Example 1: unidirectional tension of a single crystal wire

The first example will be the elastic response of a single crystal wire subjected to tension. Consider that, in the initial configuration, the wire is oriented such that its axial direction is parallel to the shortest dimension of the martensitic unit cell, and thus, the reorientation of the wire via fine lamination induces an axial elongation of the wire (the target variant is the one with the initial unit cell most elongated along the axial direction of the wire). Providing that the lamination of the wire is homogeneous, the axial elongation of the wire directly determines the volume fraction of the target variant. In Fig.2 the evolution of the Young's modulus in the axial direction of the wire and the shear modulus in the plane perpendicular to the wire is shown. In general, it is seen that the material of the wire gets elastically stiffer with the reorientation.

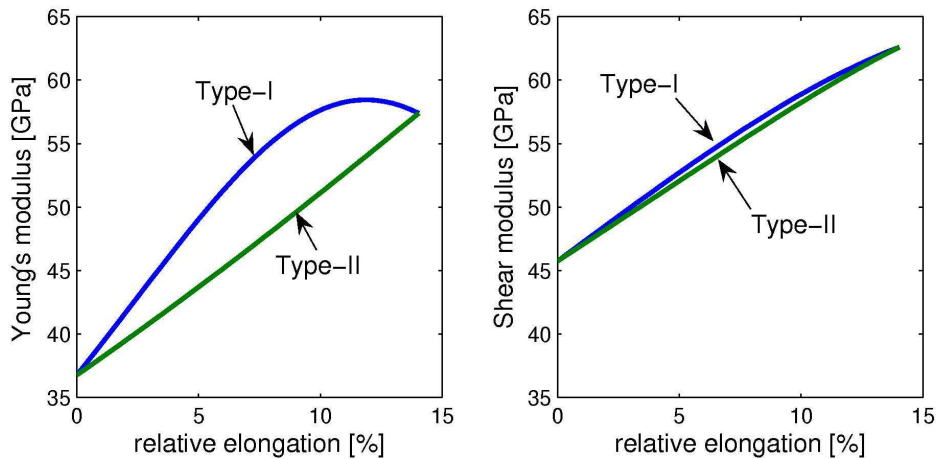


Figure 2: Evolution of elastic properties of a single crystal wire of Cu-Al-Ni shape memory alloy subjected to tension.

The Young's modulus increases from 37GPa up to approximately 59GPa, depending on which twinning system is active. The shear modulus behaves similarly.

3.2 Example 2: stability of a laminate under triaxial tension

As the second example, consider a bulk laminate reorienting due to external (i.e. macroscopic) tensional stress

$$\boldsymbol{\sigma} = [\sigma_1 \geq 0, \sigma_2 \geq 0, \sigma_3 \geq 0, 0, 0, 0], \quad (5)$$

such that $\sigma_1^2 + \sigma_2^2 + \sigma_3^2$ equals to some positive constant. The question is whether the changes of the elasticity contribute anyhow to the driving force governing the reorientation process. At some given level of the external stress $\boldsymbol{\sigma}$, this contribution can be expressed by the gradient $dw/d\lambda$ for the actual λ (the volume fraction of the target variant). If this gradient is positive (the elastic energy density increases with the reorientation), the elasticity lowers the driving force and the external stress must be increased to enforce the reorientation. On the contrary, negative gradients $dw/d\lambda$ lower the critical level of the reorientation stress. In Fig.3, the contour plots of the gradient $dw/d\lambda$ are shown for $\lambda = 0.5$. The two variants for this calculation were chosen such that the initial variant has the shortest dimension of the unit cell along the x_2 axis and the target variant along the x_3 axis, whereas the transformation strain along the x_1 axis is the same for both variants. It can be clearly seen that the uniaxial tension along the x_1 axis, which prefers none of the variants involved, corresponds to a zero gradient of the elastic energy density. On the other hand, the tension along the x_2 (which prefers the target variant) corresponds to a negative

gradient and the tension along the x_3 axis (which prefers the initial variant) corresponds to a positive gradient of the elastic energy.

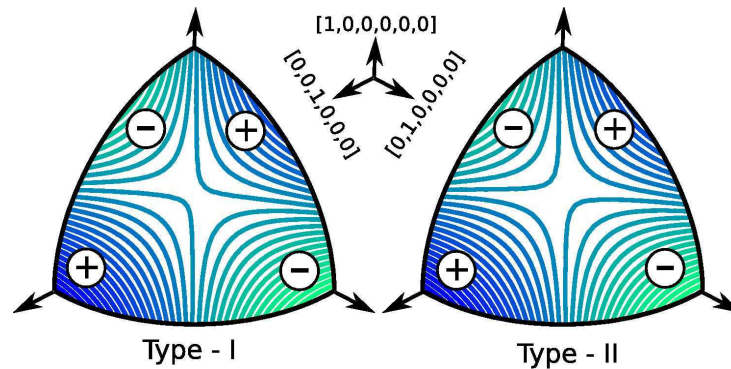


Figure 3: Contour plots of gradients $dw/d\lambda$ for Type-I and Type-II laminates of Cu-Al-Ni under triaxial tension. The '+' and '-' signs denote the positive and negative values, respectively.

Note that for hydrostatic tension ($\sigma_1 = \sigma_2 = \sigma_3$), the gradient is zero (i.e. the elasticity does not anyhow alter the fact that the reorientation cannot be induced by hydrostatic loadings).

4. Conclusions

The both discussed examples show that the elastic energy tends to contribute *cooperatively* to the reorientation, i.e. to lower the critical stress level for the reorientation, at least as far as tensional loadings are concerned (in compression, the effect must be inverse). On the other hand, there exist some singular modes of macroscopic loading of the laminate (tension which does not prefer any of the variants involved in the laminate, hydrostatic loads) under which the elasticity does not anyhow contribute to the driving force.

Acknowledgements

Supports from Czech Science Foundation (project No. 202/09/P164) and the research program of IT ASCR (CEZ:AV0Z20760514).

References

- [1] Kaushik Bhattacharya, *Microstructure of Martensite*, Oxford University Press, New York, 2003.
- [2] Michal Landa, Petr Sedlák, Hanuš Seiner, Luděk Heller, Lucie Bicanová, Petr Šittner, and Václav Novák. Modal resonant ultrasound spectroscopy for ferroelastics. *Appl. Phys. A.* **96**(3), 557–567, 2009.
- [3] Kevin F. Hane. *Microstructures in thermoelastic martensites*. Ph.D. thesis, University of Minnesota, 1998.

Grain growth modelling: a direct comparison of vertex model with phase-field model results

Michael Selzer¹, Daniel Weygand² and Britta Nestler¹

¹Institute for Materials and Processes, Karlsruhe University of Applied Science,
Moltkestrasse 30, 76133 Karlsruhe, Germany

²Institute for Reliability of Components and Systems, Karlsruhe Institute of Technology
(KIT), Kaiserstr 12, 76131 Karlsruhe, Germany
email: michael.selzer@hs-karlsruhe.de

Grain growth modeling is performed on identical initial microstructures to critically assess possible differences occurring in grain structures grown by a sharp interface or phase field approach. Grain growth models based on a sharp interface description are often called vertex dynamics model or front tracking models. In this approach the grain boundary structure is explicitly described geometrically, e.g. by a network of connected lines in two dimensions or triangles in three dimensions. The vertex model is in general used to explore the statistical properties and dynamics of grain structures, based on the knowledge of the properties of individual grain boundaries.

The formulation of the phase-field model for multiple order parameters is based on a Ginzburg-Landau energy density functional. To model grain systems, we introduce a vector-valued continuous order parameter where each component of the vector describes a physical state that depends on a three-dimensional spatial coordinate and on the time.

A direct comparison of the two models is done for different grain structures in 2D and in 3D. All grains have a different orientation such that no artificial grain coalescence events occur. In the phase field model, each orientation has its own field, therefore we used an optimized model which is able to calculate an unlimited number of grains. In the vertex model, each grain has its own orientation, and no limits in possible orientations exist.

A number of different simulations are used to compare the two methods, starting from well defined configurations, for which either analytical or previous numerical solutions are available. This allows to validate the chosen discretization parameters for the respective models. The time evolution of polycrystalline structures allow to check if the averaged behavior of both models are similar, e.g. the time evolution of a grain structure under normal grain growth is determined up to a geometrical constant.

Designing Lighter Ti Alloys using First-principles Computational Approach

G. Trimarchi¹, D. S. Shih², D. Shin³, C. Wolverton¹, and A. J. Freeman¹

¹Dept. of Physics and Dept. of Materials Science & Engineering, Northwestern University, Evanston, IL 60208, USA

²The Boeing Company, Boeing Research & Technology, MC S245-1003, PO Box 516, St. Louis, MO 63166-0516, USA

³Oak Ridge National Laboratory, Oak Ridge, TN, USA

Chris Wolverton, Dept. Of Materials Science and Engineering, Northwestern University, 2220 Campus Dr, #3013, Evanston, IL 60208 USA; c-wolverton@northwestern.edu

The merits of high specific strength, specific modulus, and excellent resistance to corrosion and oxidation make titanium alloys attractive and critical in aerospace structures. These benefits can be further enhanced by designing and developing lighter Ti alloys, while maintaining acceptable mechanical performance. As a key part of multiscale modeling and simulation in this lighter Ti alloy design effort, density functional theory based first-principles calculations and phase diagram calculations have been used. Among the elements to consider in the design of new light Ti alloys, Mg represents an appealing choice being isostructural to the hexagonal close-packed α -Ti phase. However, Mg has a limited solubility in α -Ti, *e.g.*, ~ 1.5 at % at 600°C, and nearly zero at room temperature. A detailed first-principles study combined with thermodynamical modeling schemes has been conducted to characterize the solubility of Mg in α -Ti. In addition, as a way to further increase the solubility of Mg in α -Ti, and to also achieve a larger weight reduction, first principles calculations on selected ternary Ti-Mg-X systems, where X=Al and Si, were performed. The microstructure of Ti alloys used in aerospace is usually consisted of α -Ti and body-centered cubic β -Ti phases in various morphologies and volume fractions, thus making weight reduction in both such phases necessary. Therefore, in order to devise comprehensive design rules for lighter Ti alloys, first-principles modeling of the solubility of light elements in β -Ti phase and phase diagram calculations will also be studied.

Comparison of Cellular Automata and Phase Field Methods for Modelling of Annealing

Brijesh Singh¹, Mirza Candic², Christof Sommitsch² and B. Tian³

¹Alloy Development Group/AMAT, Austrian Institute of Technology, Seibersdorf, Austria, brijesh.singh@ait.ac.at

²Institute for Materials Science and Welding, Christian Doppler Laboratory for Materials Modelling and Simulation, Graz University of Technology, Graz, Austria

³Böhler Edelstahl GmbH & Co KG, Kapfenberg, Austria

ABSTRACT

The growth kinetics during annealing is strongly influenced by various microstructure features, such as grain boundary curvature, stored deformation energy or dissolving of second phase particles. There are different methods for the modeling of grain growth that can be helpful for an optimization of the annealing process of complex industrial parts, i.e. the time-temperature history in order to get a homogeneous grain structure within specifications. Grain growth in austenitic steel 304L is modeled using 2D cellular automata and phase field methods. Both methods consider the influence of grain boundary curvature, annealing temperature and initial grain structure. The results of average normal grain sizes for different annealing temperatures and times were verified using experimental results.

1. Introduction

Grain growth is a thermally activated microstructural change. The driving force for the grain growth is the reduction of the grain boundary energy. Grain boundary energy is a function of curvature and mobility. At higher temperatures, the boundary atoms exhibit an increased mobility and are capable of crossing the grain boundary energy barrier. Grain growth is also influenced by the presence of irregularities like other phases or defects. Various modeling methods are available for studying grain growth for example phase field (PF), Monte Carlo, Vertex and cellular automaton (CA) model. In the current work the grain growth process during the solution annealing of austenitic steel 304L is analyzed using the CA and the PF methods. The simulation results obtained from the CA and PF calculations are compared to the experimental observations.

2. Cellular Automata Model

Cellular automaton presents a dynamic system in which space and time are discrete and has been widely developed in both physical and natural sciences with the development of computer technology [1-4]. In general, the lattice is divided into a regular network of square cells with a periodic boundary condition. Cells are assigned grain identity numbers. Every lattice cell represents either the grain interior or the grain boundary. Lattice cells which are adjacent to neighbouring cells with different grain identities are regarded as being part of the grain boundary. The cells surrounded by cells with the same identity are considered to be in the grain interior. In order to make the boundary move in any direction, Moore's neighbourhood configuration is considered where both the nearest and next-nearest

neighbours are used. One cellular automaton step (CAS) corresponds to one loop of re-identification attempt at a defined transition probability P_{temp} where the cell state of each step is updated simultaneously.

The temperature dependence of grain growth at a defined grain resolution of the CA model is described by the activation energy for grain boundary diffusion, Q_a , at a given grain structure resolution and by the constant A_{temp} , resulting in $P_{temp} = A_{temp} \exp(-125300/RT)$, where R is the universal gas constant.

The cellular automaton modelling strictly depends on the resolution of the microstructure where a high resolution of the microstructure leads to very long simulation times. Thus, the values of grid size and time step were chosen accurately for the desired resolution of the microstructure after a testing of grid size and time step sensitivity. The size of the calculation domain is $6.5 \cdot 10^5 \mu\text{m}^2$ with a grid size of $0.433 \mu\text{m}$, a microstructure resolution of 40000 (200x200) cells and a CA step of 1 s. The influence of temperature on grain growth is defined as the transition probability $P_{temp} = 17490 \exp(-125300/RT)$. The hindrance caused by the presence of precipitates during solution annealing or acceleration of grain growth resulting from stored deformation energy in the material is not taken into account, publicized in another work [5].

3. Phase Field Model

The speciality of the phase field model lies in the way of modelling the grain boundary. In contrary to the conventional way of modelling the grain boundary as a sharp interface, it is modelled as a diffuse region of a defined thickness.

The shape and the distribution of the grains in space and time are defined in terms of some functions known as the field variables. These field variables are continuous in both space and time. These variables have a nearly constant value within a grain and gradually take the value of the neighbouring grain on passing through the diffuse grain boundary. In other words, the field variables (which are related to chemical composition, orientation, shape etc.) do not change abruptly from one grain to other but there is a smooth and continuous transition in properties from one grain to the neighbouring grains.

The evolution of the relevant phase field variables, which is basically the evolution of the microstructure, is defined through a system of partial differential equations. The individual partial differential equations are based on the basic laws of thermodynamics, kinetics and energy balance..

The original microstructure delivered from the microscopic analysis of the 304L steel sample before annealing is imported in MICRESS [6] and used as the initial microstructure for simulation. The imported microstructure is discretized into a rectangular grid of an element size $0.433 \mu\text{m}$. The size of the simulation domain is 500X500 elements. The relevant thermodynamic data is obtained from THERMOCALC [7] database.

4. Results and Discussion

3.1 Experimental

Annealing of homogenised, un-deformed, specimens of 304L (Fe-18Cr-8Ni) alloy is performed for temperatures between 1000°C and 1200°C for 18000 seconds (5 h). Evolution of microstructure is recorded through microscopic analysis. Average grain size values are determined.

3.4 Discussion

It is observed that in comparison to the phase field method the cellular automata method is extremely efficient in terms of computation time (Tab.1).

Table 1: Comparison of the calculation times for the CA and PF method for simulating 5 hours of annealing.

Temperature [°C]	Calculation time CA [min.]	Calculation time PF [min.]
1000	23	1080
1100	22	2880
1200	32	7200

For the CA calculations the area of each grain at a given time step is directly calculated from the microstructure by counting the number of cells within a grain. The grain size is obtained from the area by assuming a circular shape for all grains, considering the defined grid size. The average grain diameter at a given time step is then obtained by averaging over all the grains in system. In the PF calculations, the average grain size is a standard output obtained from MICRESS simulation. Fig. 1 shows that the results from both the approaches of simulation are very similar. The authenticity of the simulation results is justified by comparing the simulation results with the experimental observations.

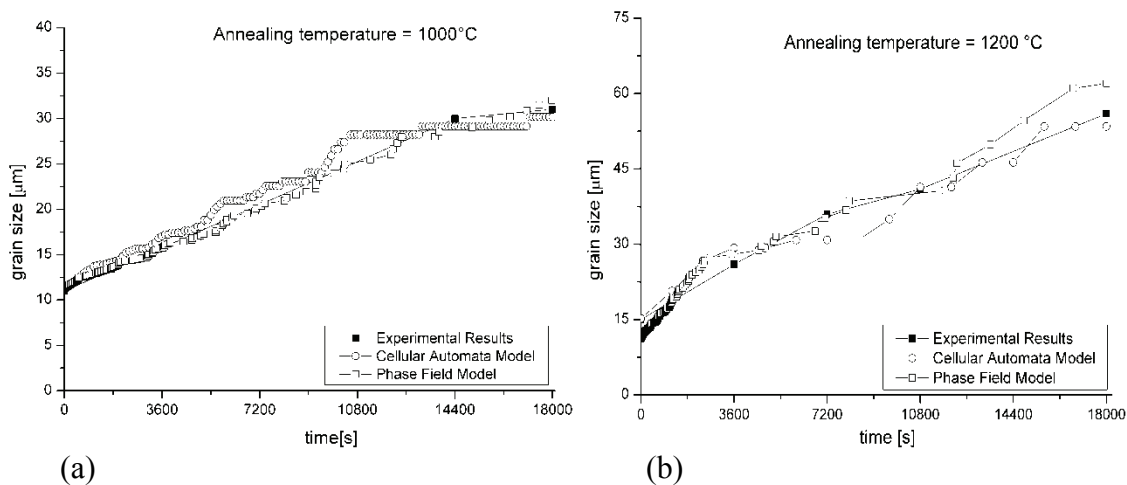


Figure 1. Experimental and simulation results for annealing at (a) 1000°C and (b) 1200°C.

It is observed from the simulated microstructures that curved boundaries tend to form straight lines with increasing computation time reflecting the curvature as driving force for migration, see Fig. 2. Microstructure evolution is driven by the excess free energies associated with the grain boundaries and resulting in an increase of the overall grain size. The growth of larger grains at the cost of smaller ones and the evolution of grains towards stable six-sided configurations are observed.

The accuracy of the evaluated grain growth constants, as activation energy for grain growth, do not depend on the grain structure resolution for PF, which is in contrast to the results of the CA, which strongly depend on the grain structure resolution. Nevertheless, the average grain size corresponds well of both models for all annealing temperatures and times.

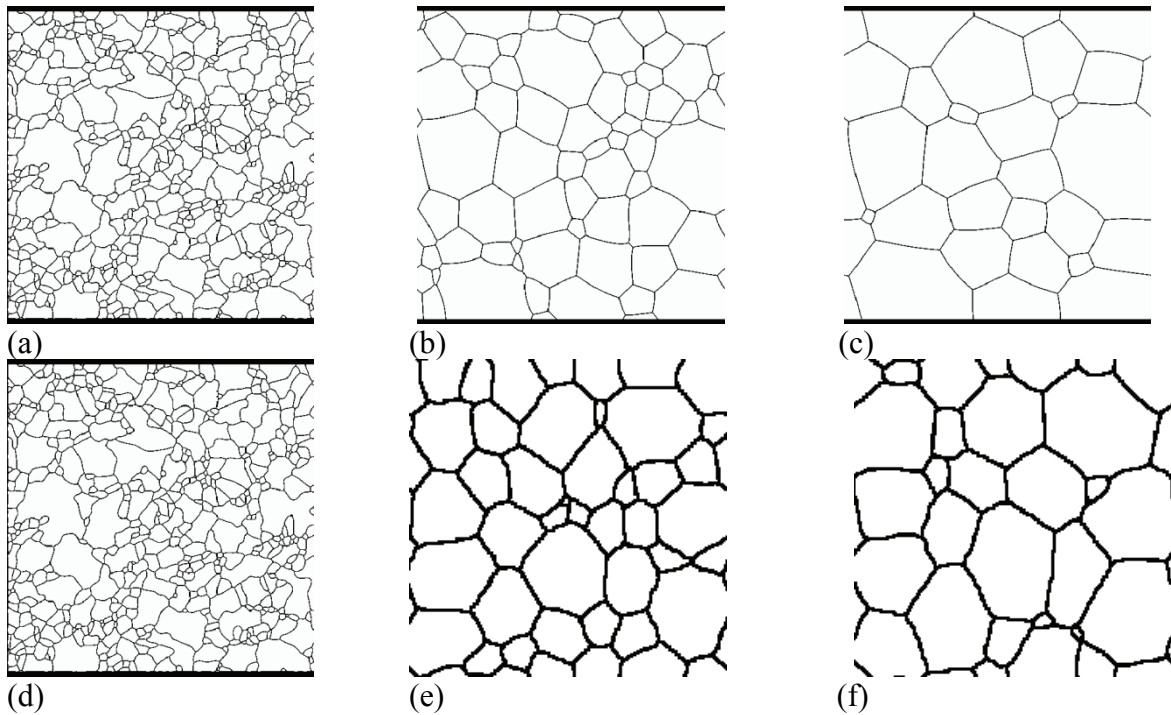


Figure 1. Evolution of grain structure during annealing at 1000°C. (a, d) Initial microstructure, (b, e) after 2 hours of annealing (c, f) After 5 hours of annealing for the PF (a, b, c) and for the CA Method (d, e, f).

5. Conclusion

The presented CA and PF model are flexible and can fully represent normal grain growth with virtue of linking topological and energy changes together and give comparable grain growth kinetics as those observed in experiments.

6. Acknowledgements

This publication is a part of the research project TPM funded by the Austrian Research Promotion Agency, FFG

7. References

- [1] D. Weygand, Y. Brechet, J. Lepinoux, *Acta. Mater.* 47 (1999) 961
- [2] W. Yu, S.P. Banks, E.J. Palmiere, *Thermomech. Process. Of Steels* 186
- [3] Y. Liu, T. Baudin and R. Penelle, *Script. Mater.* 34 (1996) 1679
- [4] H.W. Hasselbarth and I.P. Göbel, *Acta Metall. Mater.* 39 (1991) 2135
- [5] M. Candic, B. Tian, M. Kamaya, G. Winter and C. Sommitsch in: 2nd Intern. Confer. On Hot Forming of Steels and Product Properties, Grado, Italy (2009)
- [6] www.micress.de
- [7] www.thermocalc.com

Modeling and experimental investigation of microstructure, residual stresses and monotonic deformation behavior of aluminum matrix composites

**Marek Smaga¹, Dietmar Eifler¹, Tobias Zangmeister²
(tobias.zangmeister@itwm.fraunhofer.de) and Heiko Andrä²**

¹Institute of Materials Science and Engineering, University of Kaiserslautern, Gottlieb-Daimler-Straße in 67653 Kaiserslautern, Germany

²Fraunhofer ITWM, Fraunhofer-Platz 1 in 67663 Kaiserslautern, Germany

The significant improvements in mechanical performance of metal matrix composites over unreinforced metals are well known. In this paper the aluminum matrix composite AMC225xe, i.e. the aerospace grade aluminum alloy AA 2124 reinforced with 25 vol.-% ultrafine SiC particles was investigated in detail. In order to be able to simulate the thermo-mechanical material behavior, a complex coupled procedure of computer modeling and experimental validation has been created.

In a first step the microstructural details of the aluminum matrix composite AMC225xe were investigated by scanning electron microscopy and quantitatively evaluated by digital image software. The computer model of the material has been adopted to the statistic geometric parameters of individual grains as well as the overall structure.

The monotonic deformation behavior for tensile and compressive loading was characterized in detailed experiments. A pronounced difference in plastic strain response between tension and compression was observed under monotonic loading. It can be caused by several influence factors, e.g. the residual stress distribution in the composite due to the heat treatment. The residual stresses were measured in the aluminum matrix of the MMC by X-ray stress analyses.

The numerical simulation of the production process including a cooling process from 500 °C to room temperature led to thermal residual stresses in good accordance with the experimental data.

Analogously the simulation results under monotonic loading coincide with the experimental data.

In the future the cycle deformation behavior of AMC225xe will be modeled and experimentally validated.

Influence of plastic effects on the kinetics of phase transitions

R. Spatschek¹, B. Eidel¹, I. Steinbach¹, M. Fleck², and E.A. Brener²

¹Interdisciplinary Center for Advanced Materials Simulation, Ruhr University 44801 Bochum, Stiepeler Strasse 129, Germany (robert.spatschek@rub.de)

²Institute for Solid State Physics, Research Center Juelich, Germany

During many solid-state transformations mechanical effects can play a major role and largely influence the kinetics of these processes. Phase field simulations are a common tool to simulate the dynamics of these nonequilibrium moving boundary problems. The inclusion of elastic effects is nowadays well established, as their description naturally fits into the variational framework of typical phase field models. Plastic effects, however, introduce a new complexity, as they can lead not only to large deformations, but also introduce new dissipative mechanisms, and the coupling to the local interface velocity becomes much less straightforward.

In order to shed light on the issue of the proper coupling we investigate model systems, in particular in one dimension using von Mises plasticity, and sharp interface and analytical descriptions, to develop thermodynamically consistent descriptions. As an application, we discuss the influence of plastic effects on martensitic phase transformations under different phase transition conditions.

Atomistic Simulation of Laser Ablation of Gold

Authors: Sergey V. Starikov

Joint Institute for High Temperatures, Russian Academy of Sciences,
125412, Moscow, Russia

ABSTRACT

In this work presents the result of development of interatomic electronic-temperature-depended potential (ET-potential) for atomistic simulation of gold laser ablation. Using a force-matching method the ET-potential was created. The atomistic simulation of laser ablation has been performed for ET-potential testing. Simulation has shown that ET-potential imposition in two-temperature model can considerably expand this model. In particle ablation on short time can be investigated by direct atomistic simulation in the expanded two-temperature model.

1. Introduction

Laser ablation has many technological applications in material microprocessing and fabrication nanostructures [1, 2]. At the same time the mechanism of this process is not completely investigated. The characteristics of ablation are established not precisely. The various researches give strongly differing description of ablation (energy threshold, depth of crater etc.). In work [1] the threshold fluency of gold ablation I_a was found to be approximately 200 J/m^2 for absorbcency energy (central wavelength at 800 nm). Also in work [1] the single laser pulse produces a nanoscale modification in depth equal about 10 nm at I_a . Contrariwise in work [2] the value of I_a for gold was found to be approximately 1300 J/m^2 (at central wavelength of pulse equal 1200 nm). The depth of crater at ablation in work [2] was about 100 nm.

At laser ablation the heated electronic subsystem exchanges an energy with lattice (ionic) subsystem through electron-ion interaction. This process leads to a strong local overheating of substance and forms the shock wave near surface. One of the basic difficulties is that all processes at ablation (electronic and ionic thermal conduction, an electron-ion relaxation, melting, shock wave etc.) have comparable characteristic times. In addition the increasing of electron temperature changes the interatomic (i.e. interionic) interaction in system. The simple atomistic model of two-temperature system (TT-model) offered in [3]. In this model the electronic subsystem was modelled by the continuous environment and cooperated with an lattice subsystem as thermostat. Evolution of a lattice subsystem was studied by molecular dynamics method. Such approach allows to explain many features of laser ablation, but has some the serious restrictions. One of restrictions is impossibility to consider an influence of electronic excitation on the interatomic forces.

In the given work the improvement of TT-model by imposition of ET-potential was offered. In this case the model allows to include in atomistic simulation the possibility of correct description of the laser ablation on short times (initial stage at high electron temperature). In atomistic simulations without ET-potential only two ablation mechanisms for gold have been investigated: boiling [3] and spall on long times with crater depth equal about 100 nm [2]. At using of ET-potential these mechanisms remain but also there is a possibility of the new mechanism of *short* spall on short times and with small depth of a crater (about 10 nm). The *short* type of spall is not connected with shock wave propagation. This mechanism is caused mainly

by change of interatomic potential at change of electron temperature. The main object of this article is qualitative consideration of new possibilities which gives simulation with ET-potential and investigation of new type of ablation. Research was carry out on a gold example.

2. Numerical method

The ET-potential for gold has been developed at using of *force matching* method [4]. The *force matching* method provides a way to construct physically justified interatomic potentials even under such circumstances as absence of experimental data. The idea is to compute force and energies from first principles for a suitable selection of small reference systems and to adjust the parameters of the potential to optimally reproduce them. First of all the reference data was calculated by VASP package [5], a plane-wave based code using projected augmented wave potentials.

Second part of development was the force matching procedure. Potential was developed with use of Embedding Atom Method (EAM-form). The algorithm of search of potential functions was realized in the PotFit-code [4]. In final the EAM-potential having parametric dependence on T_e (ET-potential) has been created for gold.

At heating of an electronic subsystem there is a change of thermodynamic properties of lattice subsystem . Figure 1 shows the gold isotherms at various T_e (lattice temperature T_l is equal 300 K). These dependences obtained in molecular dynamic simulation with use of ET-potential at constant T_e . All the calculations were carried out using the LAMMPS code [6]. Note the pressure P strong increase at increasing of T_e and constant density. Though in real experiment a high T_e (1 - 6 eV) exists time about 10 ps but the high pressures can deform a material considerably.

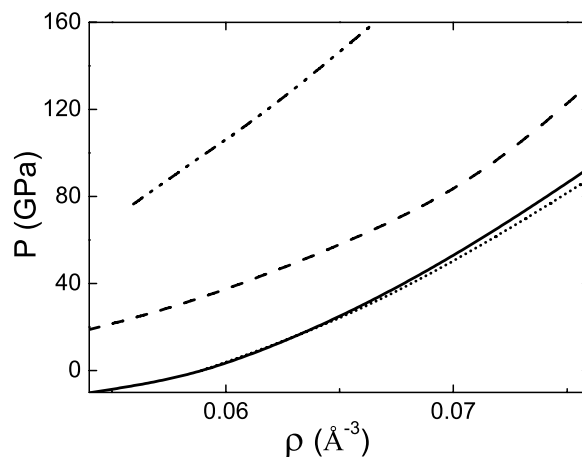


Figure 1: Dependence of pressure P on ion density ρ at various T_e : dots — experimental *cold curve*. This work: solid line — $T_e = 0.1$ eV; dashed line — $T_e = 3$ eV; dots-dash line — $T_e = 6$ eV. Lattice temperature T_l at calculation is equal 300 K.

The simulations of gold laser ablation had been performed with use of hybrid TT-model and ET-potential. In TT-model the electronic subsystem is described as continuous environment with temperature T_e [3]. Evolution of T_e is determined by formula:

$$C_e \frac{\partial T_e}{\partial t} = k_e \Delta T_e - g_p (T_e - T_l), \quad (1)$$

where $C_e = 2.75 \times 10^6 \text{ J m}^{-3}\text{K}^{-1}$ is the electron heat capacity, $k_e = 240 \text{ W m}^{-1}\text{K}^{-1}$ is the electron thermal conductivity, $g_p = 2.1 \times 10^{16} \text{ W m}^{-3}\text{K}^{-1}$ is the coupling constant for the electron-ion interaction, T is temperature, the e and l subscripts represent electronic and lattice (ion) subsystems respectively. In more difficult model it is necessary to consider dependence of this characteristics on T_e but our purpose was to consider influence of T-potential on simulation results. Lattice subsystem was studied as molecular dynamic model with ET-potential. Thus electronic subsystem cooperated with an lattice subsystem as warming Langevin thermostat (TT-model) and ET-potential.

The simulation box has the dimensions 300 nm in the x direction, 4.1 nm in the y and z directions. Three dimensional periodic boundary conditions are used. Gold atoms formed f.c.c. crystal in one half of the simulation box (at $150 < x < 300 \text{ nm}$).

After the preparation of the system in equilibrium state ($P = 0 \text{ GPa}$, $T_l = 300 \text{ K}$, $T_e = 300 \text{ K}$) the initial Gauss distribution of T_e with maximum on front surface was created. The distribution correspond to absorbed energy fluency and central wavelength of laser pulse λ . Simulation was carry out for $\lambda = 400 \text{ nm}$.

3. Results

Three mechanisms of ablation was observed in simulation: boiling, *long* ablation associated with shock wave propagation and *short* ablation. The energy threshold fluency of boiling I_b is equal 2200 J/m^2 . This value is more than in work [3]. Reason of this fact is great number of particles and large size of system unlike work [3] where homogeneous melting in thin film was considered. The energy threshold fluencies of spall (*long* ablation) $I_{a,l}$ is equal 1100 J/m^2 . Depth of the formed crater is equal approximately 60 nm and well corresponds with results from works [2]. Stages of the *long* ablation: formations of the big pressure upon surfaces (because of lattice heating); shock wave propagation in depth of crystal; reflection from a rear surface (if a film is not very thick); spall. This type of ablation is in details described in work [2]. In our simulation the *long* spall occurred after $t = 150$ of evolution.

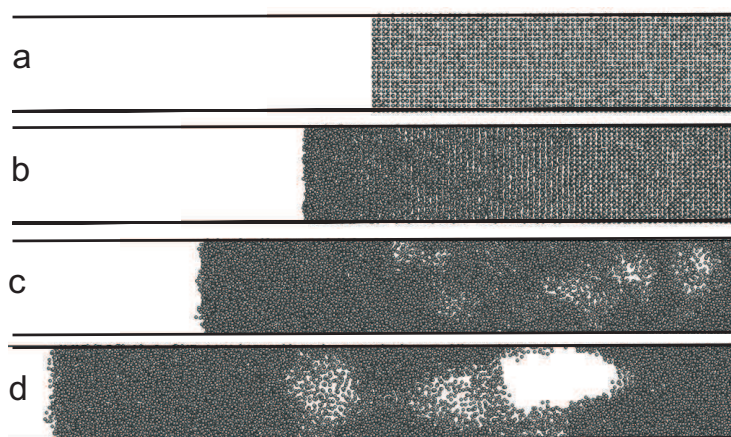


Figure 2: The stages of gold *short* ablation at atomistic simulation with use of ET-potential: a — $t = 0 \text{ ps}$ (initial arrangement of atoms); b — $t = 3 \text{ ps}$; c — $t = 8 \text{ ps}$; d — $t = 16 \text{ ps}$.

At an initial stage the very big pressure near to a surface was created because of instantaneous increasing of T_e (at creation initial T_e distribution). This fact has led to occurrence of the new *short* mechanism of ablation. Stages of the *short* ablation: formations of the very big pressure upon surfaces (because of high T_e); relaxation of pressure (expansion of crystal) and

independently the decreasing of T_e ; formation of region near surface with low density (relative to initial equilibrium state) and low T_e ; spall. At decreasing of T_e the relaxation of ET-potential to equilibrium form occurs (time of this process is equal about 10 - 30 ps). In result the region of negative pressure was formed where the spall take place. Figure 2 shows this process. The energy threshold fluencies of *short* ablation $I_{a,s}$ is equal 400 J/m². Depth of the formed crater is equal 10-15 nm and spall occurred after about 20 ps of evolution. Generally three type of ablation can exist simultaneously in hybrid model.

4. Conclusion

The ET-potential using has appreciably changed behaviour of system at simulation of ablation. *Short* ablation is a consequence of change of ET-potential at changing of T_e . Though the model considered in work is simple, but it gives the chance to estimate possibilities of use of ET-potential in atomistic simulation. In addition *short* ablation presence allows to explain existing contradictions in experimental data on gold [1, 2] as ablation can occur on various mechanisms.

Acknowledgements

We are thankful to N.A. Inogamov and Yu.V. Petrov for the useful discussion. Simulations were carried out on computing cluster MIPT-60 (Moscow Institute of Physics and Technology). The study was performed within the frameworks of the Program for Basic Research of the Presidium of the Russian Academy of Sciences No. 12 and the RFBR09-08-01116-a and PFBR09-08-12161-ofi-m grants .

References

- [1] A.Y. Vorobyev and Chunlei Guo. Enhanced absorptance of gold following multipulse femtosecond laser ablation. *Phys. Rev. B*, **72**, 195422(5), 2005.
- [2] N.A. Inogamov et al. Nanospallation induced by an ultrashort laser pulse. *JETP*, **107**(1), 1-19, 2008.
- [3] D.S. Ivanov and L.V. Zhigilei. Combined atomistic-continuum modeling of short pulse laser melting and disintegration of metal films. *Phys. Rev. B*, **68**, 064114(16), 2003.
- [4] P. Brommer and F. Gahler. Potfit: effective potentials from ab-initio data. *Modelling Simul. Mater. Sci. Eng.*, **15**(3), 295304, 2007.
- [5] G. Kresse and J. Furthmuller. Efficient iterative schemes for ab initio total-energy calculations using a plane-wave basis set. *Phys. Rev. B*, **54**, 11169-11186, 1996.
- [6] S. J. Plimpton. Fast Parallel Algorithms for Short-Range Molecular Dynamics. *J. Comp. Phys.*, **117**, 119, 1995.

Influence of mechanical stresses on grain growth mechanisms in nanocrystalline materials

Ingo Steinbach¹, Reza Darvishi Kamachali¹, Jun Hua¹, Alexander Hartmaier¹

¹ ICAMS, Ruhr-University Bochum, Germany

In this study, multi-phase field and molecular dynamics simulations have been applied to study grain growth mechanisms on the nanoscale.

In molecular dynamics simulations we study directly the shrinkage of a small spherical grain, embedded in a single crystal, thus eliminating effects of triple lines and focusing on the pure grain boundary mobility. For nanometer size grains we observe a constant grain boundary velocity, independent of the radius of curvature of the grain boundary. The activation energy of grain boundary motion in this regime is determined to be on the order of one tenth of the self-diffusion activation energy, which is consistent with experimental data. Furthermore, we calculated the evolution of mechanical stresses (Laplace pressure) during the shrinkage and the concentration of vacancies that result from the release of grain boundary free volume into the bulk caused by the reduction of grain boundary area.

Based on these observation a model for grain growth on the mesoscopic scale is developed considering reduction of interface area, vacancy diffusion and stress due to the rearrangement of the defect distribution into account.

The combination of both approaches leads to a consistent picture of the interplay of short range diffusion and long range stress effects which explains the linear grain growth in the nano regime and the transition to normal grain growth at elevated temperatures.

Comparing grain growth experiments and simulations of SrTiO₃ specimen in three dimensions

Bäurer, M.¹, Lauridsen, E.³, Ludwig, W.⁴, Syha, M.² and Weygand, D.²

Karlsruhe Institute of Technology (KIT), Kaiserstr. 12, 76131 Karlsruhe, Germany

¹Institut für Keramik im Maschinenbau

²Institut für Zuverlässigkeit von Bauteilen und Systemen, melanie.syha@kit.edu

³Risø National Laboratory, Frederiksborgvej 399, 4000 Roskilde, Denmark

⁴European Synchrotron Radiation Facility, BP220, 38043 Grenoble, France

SrTiO₃ crystals show a temperature dependent anisotropy in grain boundary energy [1,2], which is suspected to be a possible explanation for the recently observed phenomenon of grain growth retardation with increasing temperature [3]. Since 3D grain growth simulations [4] allow for a proper characterization of the influence of anisotropic grain boundary properties on the microstructural evolution it is of outstanding interest to compare simulation data to structural data gained from experiments. Up to now however, the possibility of a comparison between experimental and simulation data is limited, due to the 2D character of conventional metallographic techniques.

Synchrotron based x-ray experiments, using the diffraction contrast tomography (DCT) technique presented in [5], provide the possibility to map structure and crystallography of single 3D grains, see figure 1.

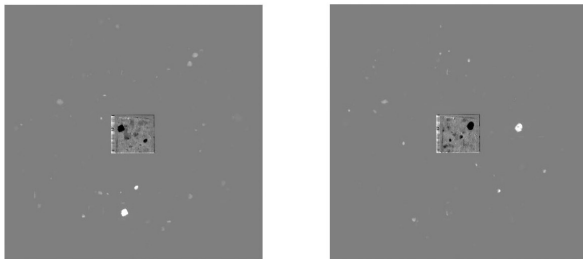


Figure 1: Two background corrected diffraction contrast tomography images of a SrTiO₃ specimen.

Fully reconstructed grain structures captured at different stages of microstructural evolution will be presented and compared to structures obtained by 3D grain growth simulations.

References:

- [1] T. Sano, C.-S. Kim, G. S. Rohrer, Shape evolution of SrTiO₃ crystals during coarsening in a titania-rich liquid, *J. Am. Ceram. Soc.* 88 (2005) 993–996.
- [2] S. B. Lee, W. Sigle, W. Kurtz, M. Rühle, Temperature dependence of faceting in sigma5(310)[001] grain boundary of srTiO₃, *Acta Mater.* 51 (2003) 975–981.
- [3] M. Bäurer, D. Weygand, P. Gumbsch, M. Hoffmann, Grain growth anomaly in strontium titanate, *Scr. Mater.* 61 (2009) 584–587.
- [4] M. Syha, D. Weygand, A generalized vertex dynamics model for grain growth in three dimensions, *Modeling and Simul. Mater. Sci. & Eng.* 18 (2010)
- [5] W. Ludwig, S. Schmidt, E.M. Lauridsen, H.F. Poulsen, *J. Appl. Cryst.* 41 (2008) 302-309

Three dimensional Reconstruction of PEFC Catalyst Layers

S. Thiele, R. Zengerle, C. Ziegler

Laboratory for MEMS Applications,
Department of Microsystems Engineering – IMTEK, University of Freiburg,
Georges-Köhler-Allee 106, 79110 Freiburg, Germany
christoph.ziegler@imtek.de

ABSTRACT

The introduction of hybrid electric vehicles has prepared the complete replacement of gasoline systems by systems based on batteries or polymer-electrolyte fuel cells. One of the main sources for performance losses, degradation problems and cost are the catalyst layers. Therefore there is a great need for detailed insight into catalyst layer materials to exploit their potential. In order to solve this problem we define a threefold aim: The first step is to develop a new method for morphology analysis in order to get a 3D image of the catalyst layer. The second step is finding a means to quantitatively describe the morphology of such a geometry. Finally we intend to calculate an optimum morphology eliminating or at least reducing some of the sources of performance loss. In this paper we present an analytical method for morphology analysis suited for the catalyst layer and the first 3D reconstruction of such a layer of a polymer electrolyte fuel cell. We further present first results on our way to quantitatively describe the morphology.

1. Introduction

The three dimensional reconstruction of polymer electrolyte fuel cell (PEFC) catalyst layers requires a spatial resolution of 10-1000 nm to capture the characteristic length scales of the pore space. Neutron tomography, magnetic resonance imaging (MRI) and x-ray-tomography are inappropriate methods for this task due to their relatively low spatial resolution [1]. Atomic force tomography does not provide element information which is important for investigation of catalyst layers. Compared to scanning electron microscope (SEM) imaging the transmission electron microscope (TEM) has better spatial resolution; the image dimension is small which makes this method suitable for small scale features such as individual catalyst agglomerates. A promising method for direct reconstruction available in materials science is focused ion beam - scanning electron microscope (FIB-SEM)-tomography. The apparatus for this method consists of two cross beams: An electron beam for the SEM and an ion beam for etching having a precision of 20 nm and below [2]. By successively etching slices from the sample and taking images of the surface a 3D dataset can be produced. Reconstruction yields a three-dimensional picture of the nano material. Recently, this method has been shown useful for ceramic fuel cell electrodes [3]. Here we present the direct reconstruction of a PEFC catalyst layer in section two.

Stochastic methods can be used to describe porous, heterogeneous materials [4,5]. Different stochastic descriptors (morphologic functions) correlate with different material properties [6]. These functions can be used to derive a stochastic reconstruction of a material which is called 'stochastic reconstruction'. For stochastic reconstruction the most established reconstruction method is Simulated Annealing (SA) [7]. The question which group from the set of all stochastic descriptors is sufficient for a reliable material description is still a matter of research [8]. In this paper we present the evaluation of two promising candidates on the quest

to find the right set of stochastic descriptors: The Pore-Size Density Function (PSDF) and the cumulative Pore-Size Distribution Function (cPSDF) which are directly calculated from the reconstruction of the PEFC catalyst layer which is presented in section three.

2. Direct reconstruction of a PEFC catalyst layer

The reconstruction procedure can be subdivided into image acquisition, segmentation and visualization of the material (Fig. 1).

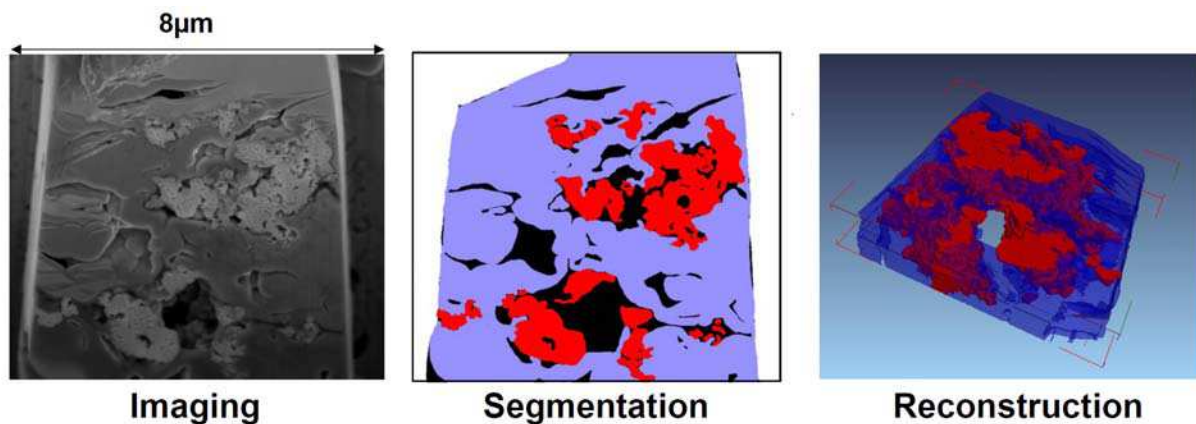


Figure 1: The three basic steps in 3D reconstruction: Image acquisition means actually taking the images. Segmentation is the division of the image into different material types. 3D Reconstruction means producing a 3D geometry from the segmented images.

A Fumapem F-950 membrane, which is a per-fluorinated sulphonic acid/PTFE copolymer, is investigated as example material. The sample was investigated with a dual-beam FIB/SEM instrument. A representative area was chosen to perform the reconstruction. A series of 113 images with a distance of 30 nm was taken where the thickness of the layer was about 2 μm.

Due to the time consumption segmentation being the subdivision of the acquired image is one of the most important steps in tomography. In the present case the image is divided into pore space and solid space. Due to the complexity of the structure a simple segmentation approach like threshold segmentation fails. One way of approaching this challenge is via a manual segmentation which can take between 2-3 hours per image. Therefore we developed a semi-automatic approach. It is based on preselecting with an optimized threshold value in the first step and manually improving the results in the second step. With this approach the manual segmentation time was reduced to about 45 min.

For three-dimensional visualization of porous media it has become a state-of-the-art to use Amira® [9]. The images were cut to 1650x700 pixels. In the z-direction 113 images are taken with a distance of 30 nm. The resolution of the images is 2.5 nm/pixel. Hence the final geometry was 4150x1750x3390 nm³ in x-,y- and z-direction respectively. The final voxel size is 1x1x12 pixels that is 2.5x2.5x30 nm³. A cube of the geometry is shown in Fig. 2.

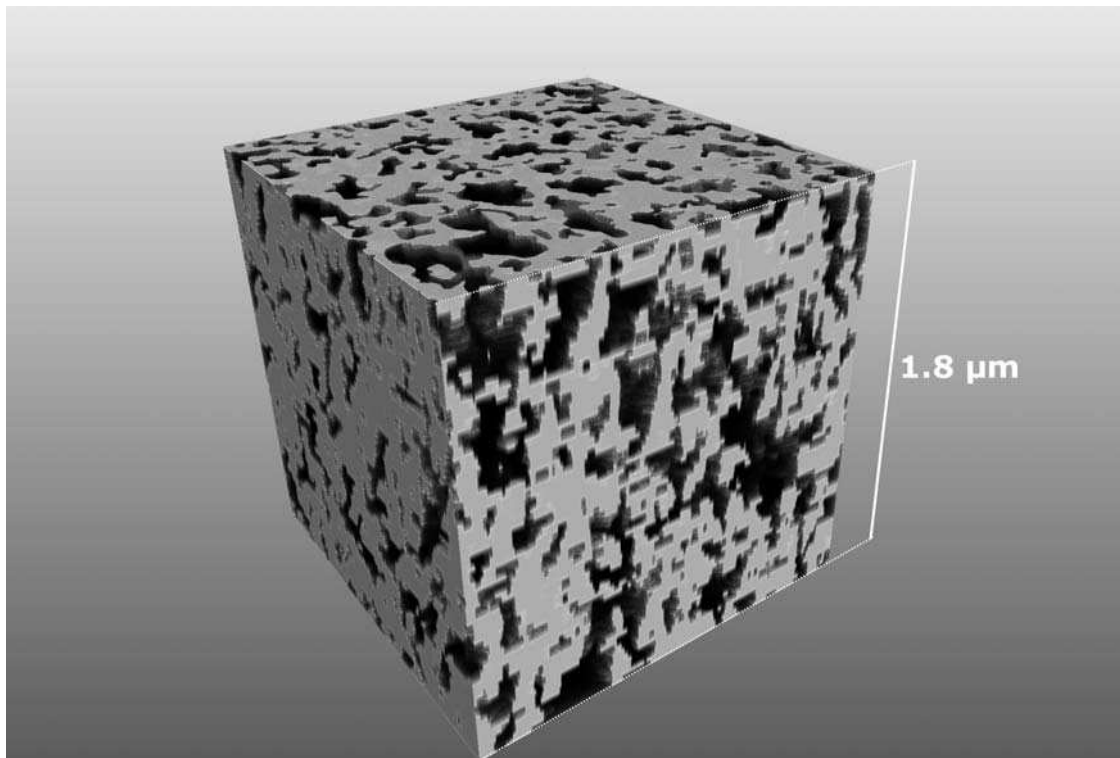


Figure 2: A cube from the 3D reconstruction of a porous polymer-electrolyte fuel cell cathode catalyst layer. The reconstruction is based on 113 SEM images obtained with a separation of 30 nm. The layer is a highly porous carbon network with well-connected pores that form continuous pathways within the layer. The side-length of the cube geometry is 1.8 μm.

3. Description of the morphology

The PSDF $P(r)$ of the pore space is defined as the probability that a randomly chosen point of this phase lies at a distance r from the nearest point on the solid-pore interface. It normalizes to unity. The associated cPSDF $F(r)$ is defined as:

$$F(r) = \int_r^{\infty} P(r') dr' \quad (1)$$

Thus $F(r)$ is the fraction of the pore space with a pore radius bigger than r . The $F(r)$ can be imagined as the probability that a randomly inserted sphere of radius r completely lies within the specified phase (e.g. pore space). It therefore contains information about three-dimensional connectivity [5]. The functions were evaluated by creating a distance transform of the geometry (Fig.3). The PSDF was then evaluated by summing up the amount of pixels at a radius value r and dividing it by the overall number of pixels. The cPSDF was calculated from this data.

4. Conclusion and Outlook

On our way to fulfil the threefold aim presented in the introduction we can state that we have reached the first aim: Developing an analytical method for PEFC catalyst layer 3D reconstruction. A full 3D reconstruction by FIB-SEM has been presented. The availability of a real 3D pore-structure model will make it possible to solve the next step in our approach: To quantitatively describe the morphology of this structure. Algorithms for calculating other stochastic descriptors like n -point correlation functions will be implemented in the near future. At the same time an optimized Simulated Annealing algorithm will be implemented.

This will give rise to new model approaches for PEFC catalyst layers which we finally wish to find approaching our final step: Finding better nano geometries for catalyst layers with improved transport properties and catalyst utilization.

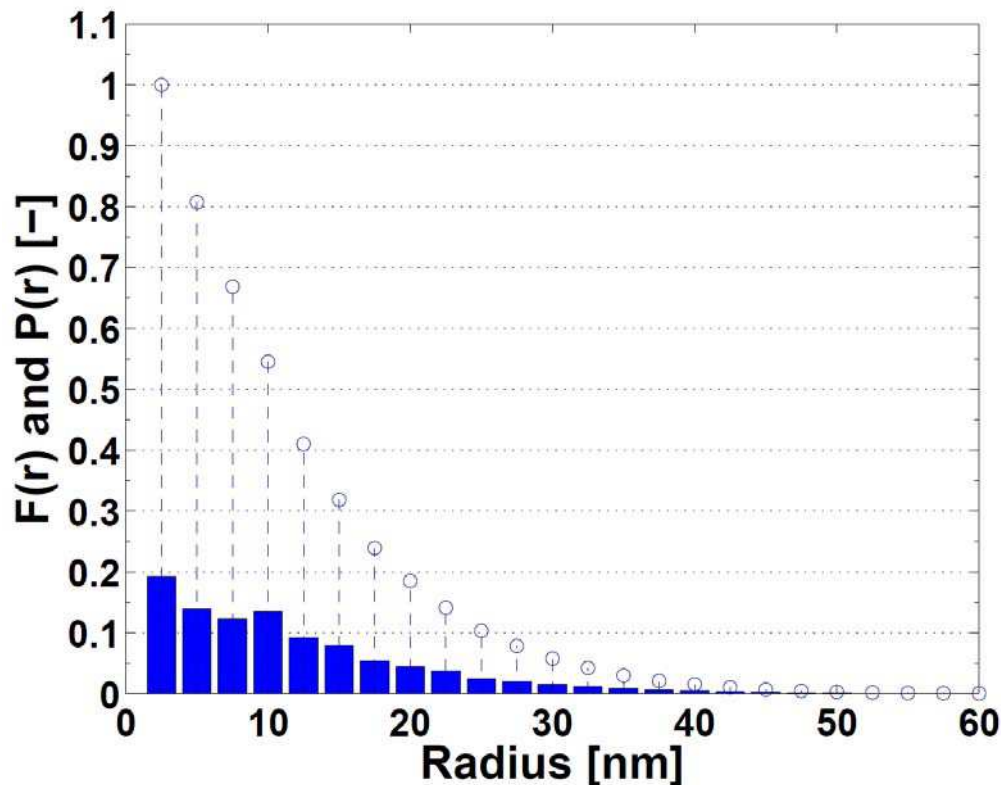


Figure 3: Pore-Size Density Function (PSDF) as a histogram and the cumulative Pore-Size Distribution Function (cPSDF) as points are shown as a function of the radius. These functions can be used to reconstruct a 3D geometry by using the Simulated Annealing method.

5. Acknowledgements

This work was supported by the German Research Foundation (DFG) under grant no. ZI 1201/1. The authors acknowledge the fruitful collaboration on electron microscopy with H. Blumtritt (Max Planck Institute for Microstructure Physics) who acquired the REM images.

6. References

- [1] G. Moebus et al., *Materials Today*, 10(12), 18-25, 2007
- [2] L. Holzer et al., *J. of Microscopy*, 216(1), 84, 2007
- [3] J.R. Wilson, *Nature Materials*, 5(7), 541-544, 2006
- [4] J. Ohser, F. Muecklich, John Wiley, New York, 2000
- [5] S. Torquato, Springer, New York, 2001
- [6] S. Torquato, *Annual Review of Materials Research*, 32(1), 77-111, 2002
- [7] C. L. Y. Yeong et al., *Physical Review E*, 57(1), 1998
- [8] M. S. Talukdar et al., *J. of Colloid and Interface Science*, 248(2), 419-428, 2002
- [9] A. E. Efimov et al., *J. of Microscopy* 2007, 226(3), 207-216

Relaxed grain cluster (RGC) scheme polycrystalline homogenization

D.D. Tjahjanto, P. Eisenlohr, F. Roters

*Max-Planck-Institut für Eisenforschung,
Max-Planck-Straße 1, 40237 Düsseldorf, Germany*

A grain cluster-based homogenization (or coarse-graining) method, called the relaxed grain cluster(RGC) scheme [1] is presented. The scheme is a generalization of the grain interaction (GIA) model [2], which is based on the relaxed constraints (RC) Taylor framework. The kinematics of the present scheme is formulated using a finite deformation framework. A so-called *relaxation vector* is applied to each interface of the grain as an additional degree of freedom to the classical full constraint (FC) Taylor assumption. Interactions between neighboring grains in the cluster are derived from the minimization of total energy, which includes the constitutive energy or mechanical work of individual grains, and a penalty term representing deformation mismatch due to the interface relaxations.

In order to demonstrate the predicting power of the model, the overall response of a grain-cluster undergoing elementary boundary conditions is simulated. The predictions of the RGC scheme are compared with results from other coarse-graining schemes. Furthermore, for simulating the response of polycrystalline samples undergoing forming process [3], the RGC scheme is implemented into a standard finite element (FE) program as a user material subroutine. In this case, the FE method is used to solve the macroscale boundary value problem associated with forming process, whereas the RGC scheme provides the polycrystalline material response at mesoscale. The predictions of the model are analyzed and compared to experimental results.

References

- [1] D.D. Tjahjanto, P. Eisenlohr, F. Roters. A novel grain cluster-based homogenization scheme, *Modelling and Simulations on Materials Science and Engineering*, 2009. To appear.
- [2] M. Crumbach, M. Goerdeler, G. Gottstein, L. Neumann, H. Aretz, R. Kopp. Through-process texture modelling of aluminium alloys, *Modelling and Simulations on Materials Science and Engineering* **12** S1–S18, 2004.
- [3] D. Raabe, Y. Wang, F. Roters. Crystal plasticity simulation study on the influence of texture on earing in steel, *Computational Materials Science* **34** 221–234, 2005.

Ab initio modeling to improve oxygen tolerance of Ti alloys

D. R. Trinkle^{1*}, H. M. Lawler¹ and D. S. Shih²

¹Materials Science & Engineering, University of Illinois, Urbana-Champaign, IL, USA

²The Boeing Company, Boeing Research & Technology, St. Louis, MO, USA

* dtrinkle@illinois.edu

Titanium alloys and their structures are very important in aerospace applications. While Ti property and its tradeoff are sensitive to microstructural variations, the microstructures are strongly dependent on alloy additions and processing route. Oxygen's high affinity and solubility in Ti alloys pose a processing challenge, as higher oxygen concentration reduces ductility and fracture energy of Ti alloys. One possible strategy to improving the tolerance of Ti alloys to oxygen is the introduction of solutes that can reduce the driving force for diffusion or oxygen diffusivity. We use ab initio calculations of oxygen-solute interactions in Ti together with thermodynamic and kinetic modeling to quantify the effect of different solutes, concentrations, and temperatures on oxygen diffusivity and free energy. This modeling framework allows us to move beyond dilute solute concentrations, and also consider the effects of different solutes simultaneously in an alloy, and make predictions for alloy design.

First-principles calculation of dislocation/solute interactions and modeling of strength in Mg

Joseph A. Yasi¹, Louis G. Hector, Jr.² and Dallas R. Trinkle^{3*}

¹Physics, Univ. Illinois, Urbana-Champaign, Urbana, IL, USA

²General Motors Technical Center, Warren, MI, USA

³Materials Science and Engineering, Univ. Illinois, Urbana-Champaign, Urbana, IL, USA

New lightweight, strong, formable Mg alloys are of considerable interest to the transportation industries for improved fuel economy. Efficient, accurate computational modeling of dislocations and solute interactions with dislocations is essential for the development of meaningful constitutive models of strength. In magnesium, the basal slip system is the most active. Prismatic dislocations are two orders of magnitude stronger than basal dislocations, but mobility is necessary to achieve the five independent slip systems required for forming. The first-principles flexible boundary condition method is used to compute a-type basal screw and edge, a-type prismatic edge, and c-type prismatic screw and edge atomic-scale Mg dislocation geometries. For these dislocations, we calculate solute binding energies for many industrially important solutes by direct substitution in the optimized dislocation cores. We also model the solute/dislocation interaction with a small set of solute interaction parameters for size and slip changes; this computationally efficient model is validated against our direct first-principles calculations. The solute/dislocation interaction data is input into strengthening models that account for the distribution of solutes and in affecting dislocation motion; the comparison of the basal strengthening with available experimental data validates our general first-principles calculation and modeling approach.

Fe-Cr alloys by first-principle calculations and synchrotron x-ray measurements.

A. Uldry¹, C. Borca¹, A. Idhil¹, M. Victoria¹, W. Hoffelner¹ and M. Samaras¹

¹Paul Scherrer Institute, 5232 Villigen PSI, Switzerland.
E-mail: anne-christine.uldry@psi.ch

Fe-Cr alloys have long been a subject of interest for their suitability as corrosion-resistant industrial material. The need of understanding at a fundamental level the mechanisms at work in the Fe-Cr alloys and their relations to structure has been rekindled by these materials being considered for the next generation of nuclear power plants. Defects, clustering and segregation are crucial issues to resolve in this context for their role in altering the structural and mechanical properties of the material. We propose to address the phenomenon of Cr clustering in ferritic Fe-Cr alloys in the range 2-16at%Cr by means of Density Functional Theory (DFT), from first-principles calculations and synchrotron Extended X-ray Absorption Fine Structure (EXAFS) measurements.

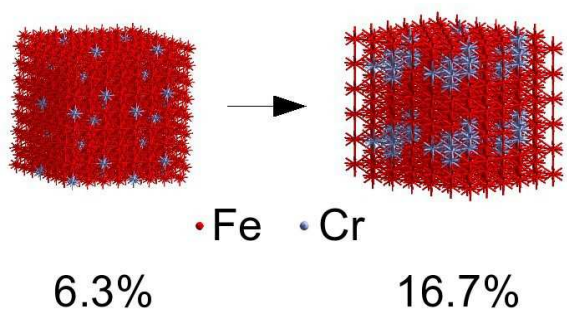


Figure 1: DFT lowest energy structures.

The propensity of the Cr atoms in Fe-Cr to exhibit short-range order below ~10at %Cr and short-range clustering tendency beyond this concentration was shown in 1984 by diffuse neutron scattering experiment [1]. The preferred configurations of substitutional Cr in Fe can be investigated by DFT calculations, where supercells of Fe and Cr for a given concentration of Cr are built and tested for lowest energy.

The structures of lowest energy for 6.3, 9.3, 12.5 and 16 at%Cr clearly show a transition to clustering at 12.5 at%Cr concentration [Figure 1]. Moreover, a series of EXAFS measurements on model Fe-Cr alloys with up to 16% Cr content were taken at the microXas beamline of the PSI Swiss Light Source. EXAFS is an experimental technique particularly suited to probe the structural local environment of an atomic species. The selected DFT structures are used as the basis for fitting the EXAFS measurements, thereby validating the model and fully quantifying short-range ordering and clustering in this concentration range.

[1] I. Mirabeau, M. Hennion and G. Parette, Phys. Rev. Letters 53 687 (1984).

Kinetics of Al-Au Wirebonds: Phenomenological Model and First-Principles Investigation

Christian M. Ulrich^{1*}, Adham Hashibon¹, Jiří Svoboda³, Christian Elsässer^{1,2} and Hermann Riedel¹

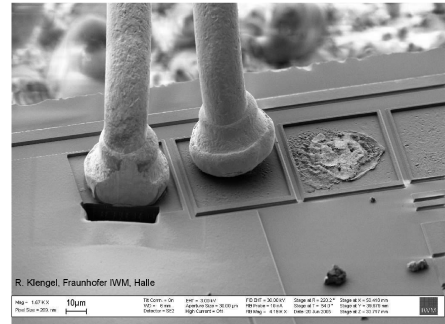
¹Fraunhofer Institute for Mechanics of Materials IWM,
Wöhlerstr. 11, 79108 Freiburg, Germany

²IZBS, Karlsruhe Institute of Technology, Kaiserstr. 12, 76131 Karlsruhe, Germany

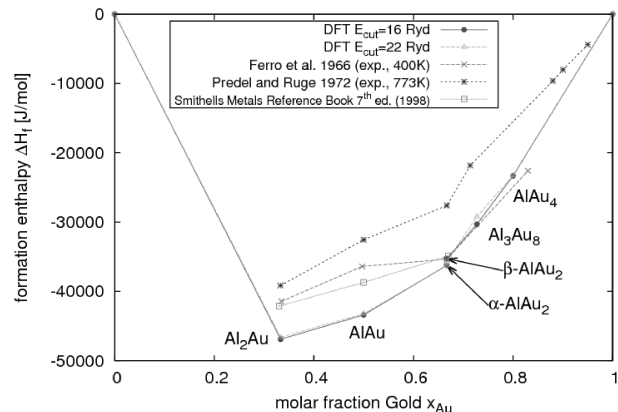
³Institute of Physics of Materials, Academy of Sciences of the Czech Republic,
Žitkova 22, Cz-616 62 Brno, Czech Republic

*Email: christian.ulrich@iwm.fraunhofer.de

The ongoing progress of miniaturization in microchip design and packaging technology has created steadily increasing demands to the integration density of thermosonic wire bonds, which are a common way to provide electrical contact to integrated circuits. Contacts of Gold wires on aluminium bond pads are of particular interest due to their complexity of interfacial intermetallic phases and due their ubiquity in real-life applications. Microscopic defects in these contacts have been identified as one of the key causes for the failure of electronic components due to aging at elevated temperatures. Cracks and void layers are frequently observed in micrographs. Their incidence is correlated with diffusion mediated phase transformation processes, which involve the formation and growth of stoichiometric compounds. Weak bonds commonly break at phase boundaries.



We present a phenomenological model based on a *Thermodynamic Extremal Principle* that allows calculating the phase kinetics and unbalanced diffusion (Kirkendall effect) in a layered system of intermetallic phases. Determination of the model parameters still represents a challenge. Hence *Density Functional Theory* (DFT) in the *Local Density Approximation*, implemented in a mixed-basis pseudopotential code, is employed to obtain useful thermodynamic and kinetic quantities for six ordered low-temperature phases in the Al-Au system. In particular, activation energies and minimum energy trajectories for elementary jump processes have been calculated for the compound AlAu_4 . From these results, we conclude that gold is the dominantly diffusing element in AlAu_4 as compared to aluminium. Hence, unbalanced diffusion of the two species is likely to contribute to delamination at the boundaries of the AlAu_4 phase in bond samples that have degraded to zero pull strength.



Atomistic Models for Variable Oxidation States

Steven M. Valone¹

¹Materials Science and Technology Division, Los Alamos National Laboratory,
Los Alamos, NM USA, 87545
smv@lanl.gov

Oxygen concentration in metal oxides can vary because of contact with the environment, contact with another material, or the presence or formation of defects. For the present purposes, the variation in oxygen concentration between metal sesqui- and di-oxides illustrates the point. If one desires to investigate such materials via atomistic methods, the corresponding atomistic models should allow the oxidation states of the cations to adjust accordingly. Typically this is not the case [1], although there are notable exceptions [2]. There are seemingly less demanding, yet subtle, applications such as the solid phases of ZrO₂ where rebalancing of covalent and ionic contributions in the anions is necessary [3].

Certainly *ab initio* [4] and semi-empirical methods [5] are able to make such adjustments, with the more advanced methods giving the better descriptions [6]. It is natural to look to electronic structure methods to guide the development of atomistic potentials. Unfortunately, this guidance, in terms of orbital-based quantities, tends not to be a form that directly informs an atomistic potential. Consequently, the choice often is to fit different atomistic potentials to the different stoichiometries of interest, with no way to link from one to the other.

Here we present a type of potential that is atomistic from its inception. It is founded on the decomposition of the many-electron Hamiltonian into site and interaction contributions. It preserves a sense covalent-ionic balance, and important theoretical limits. Most significantly, oxidation states of the ions appear naturally and directly in the formulation.

[1] G. V. Lewis and C. R. A. Catlow, J. Phys. C: Solid State Phys. **18**, 1149 (1985).

[2] Q. Zhang, T. Çagin, A. C. T. van Duin, and W. A. Goddard, Phys. Rev. B **69**, 45423 (2004);

S. R. Phillpot, S. B. Sinnott, and A. Ashtagiri, Annu. Rev. Mater. Res. **37**, 239 (2007).

[3] S. Fabris, A. T. Paxton, and M. W. Finnis, Phys. Rev. B **61**, 6617 (2000).

[4] W. Metzner and D. Vollhardt, Phys. Rev. Lett. **62**, 324 (1989); G. Kotliar and D. Vollhardt, Phys. Today **57**, No. 3, 53 (2004).

[5] See for instance, among many others, O. F. Sankey and D. J. Niklewski, Phys. Rev. B **40**, 3979 (1989), and references therein.

[6] J. Kunes, V. I. Anisimov, S. L. Skornyakov, A.V. Lukoyanov, and D. Vollhardt, Phys. Rev. Lett. **99**, 156404 (2007).

Multiscale Description of the Domain Wall Motion

P. Weinberger¹, E. Y. Vedmedenko², R. Wieser² and R. Wiesendanger²

¹ Center for Computational Nanoscience, Seilerstätte 10/22, A1010 Vienna, Austria

²Jungiusstr. 11, IAP, University of Hamburg, 20355 Hamburg Germany
vedmeden@physnet.uni-hamburg.de

The more exciting developments towards new all-solid-state storage and logic devices without moving parts are based on current- and field-driven motions of domain walls in soft magnetic materials. Often domain walls have to be regarded as excited states and their dynamics is treated therefore theoretically in the framework of phenomenological theories or by means of micromagnetic simulations [1]. For the same reason first-principles ab-initio calculations are often limited to static descriptions of single domain magnetic ground states. Here, we bridge different theoretical approaches and make a first step towards a fully relativistic description of domain wall motions without mean-field approximations.

We demonstrate that viewed over the whole concentration regime of magnetic substitutional binary alloys the velocity of domain walls can show quite a complicated dependence on the domain wall thickness, in some cases distinctly other than expected from the classical Landau-Lifshitz relation. In view of a generalized Landau-Lifshitz-Gilbert equation, it appears that deviations from a Landau-Lifshitz-type behavior are perhaps due to a non-trivial width dependence of the Gilbert damping parameter, the nonadiabaticity parameter, and the profile of a magnetic domain wall.

[1] R. Wieser, E. Y. Vedmedenko, and R. Wiesendanger, Phys. Rev. B 81, 024405 (2010)

Multipolar Approach for Large-Scale Simulations of Magnetic Arrays

E. Y. Vedmedenko¹

¹Jungiusstr. 11, IAP, University of Hamburg, 20355 Hamburg Germany
vedmeden@physnet.uni-hamburg.de

New phenomena at the nanoscale can be expected not only in the individual magnetic structures but also in magnetic arrays obtained experimentally by structuring of a continuous film or by self-organization. Because of the vanishing interparticle exchange coupling magnetic properties of the arrays are governed by the magnetostatic interaction and the magnetocrystalline anisotropy. Magnetic memory applications require increase in the density of dots per unit area, which is correlated with a decrease of dot sizes and interdot distances. With increasing density of packing the magnetostatic interactions become increasingly important for the ground state properties as well as for magnetic switching of individual elements.

The large-scale micromagnetic simulations of such arrays are difficult because of the long-range interactions and a huge number of elementary cells. Therefore, we have developed a multiscale approach based on approximation of nanoparticles by their multipole moments depending on geometry, time-scale and magnetization orientation [1,2]. Elaborated procedure permits to decrease drastically the computational efforts for calculation of magnetostatic interactions in magnetic arrays. By means of the new techniques it has been demonstrated that depending on the geometry of the particles, the higher order interactions might significantly change the hysteretic properties and the dynamics of nanoarrays and might be used for future logics or memory applications [3,4].

[1] E. Y. Vedmedenko, N. Mikuszeit, H. P. Oepen, and R. Wiesendanger, Phys. Rev. Lett. 95, 207202 (2005)

[2] E. Y. Vedmedenko and N. Mikuszeit, ChemPhysChem. 9, 1222 (2008)

[3] S. Hankemeier, R. Frömter, N. Mikuszeit, D. Stickler, H. Stillrich, S. Pütter, E. Y. Vedmedenko, and H. P. Oepen, Phys. Rev. Lett. 103, 147204 (2009)

[4] A. Remhof, A. Schumann, A. Westphalen, H. Zabel, N. Mikuszeit, E. Y. Vedmedenko, T. Last, and U. Kunze, Phys. Rev. B 77, 134409 (2008)

Phase-field modeling of the columnar-to-equiaxed transition in AlSi7 alloy solidification

A. Viardin¹, L. Sturz¹ and M. Apel¹

¹ACCESS e.V., Materials and Processes, Intzestr. 5, D-52072 Aachen, Germany
a.viardin@access-technology.de

Multiscale and multiphase modeling of solidification is a subject of active research since more than 30 years. Understanding the effects of macroscopic process conditions on the microstructure evolution is important to assure e.g. the mechanical properties of the casting.

The columnar-to-equiaxed transition (CET) in dendritic solidification describes a discontinuous change in microstructure and is a common morphological transition in technical castings. The microstructure is called columnar if the dendritic orientation growth tends to one direction, whereas equiaxed grains are oriented in all directions. The CET depends on the thermal conditions defined on a macroscopic scale, the local undercooling near the solid-liquid interface which is determined by their morphology on a microscale and the thermophysical properties of the alloy.

In our study, we have performed phase field simulations in order to explore the effect of equiaxed grain nucleation undercooling on the CET in the AlSi7 alloy system. Our phase field model is based on the multiphase-field method and is coupled to a thermodynamic database [1]. The simulation results are compared to experimental microgravity results under purely diffusive growth conditions. The experimental investigation [2,3] is made within the framework of the ESA-map programme CETSOL (Columnar Equiaxed Transition in Solidification Processing) during the sounding rocket campaign MAXUS-7.

[1] J. Eiken, B. Böttger, I. Steinbach, Phys. Rev. E 73 (2006), 115701-115705

[2] L. Sturz, A. Drevermann, C. Pickmann, G. Zimmermann, Mat. Sci. Eng. A 413-414 (2005), 379-383

[3] H. Jung, N. Mangelinck-Noel, C. Bergman, B. Billia, Journal of Alloys and compounds (2009), 622-627

3D atomistic modeling of quasi-brittle microcrack propagation in alpha-iron

V.A.Borodin^{1,2}, P.V. Vladimirov¹

¹ Karlsruhe Institute of Technology, Hermann-von-Helmholtz-Platz 1, 76344 Eggenstein-Leopoldshafen, Germany: e-mail: pavel.vladimirov@kit.edu

² RRC Kurchatov Institute, Kurchatov Sq. 1, 123182 Moscow, Russia

We present the results of molecular dynamics (MD) simulations of three-dimensional kinetics of micro-crack propagation in alpha-iron and the accompanying lattice transformations at the crack tips. We show that crack initiation on {001} planes in iron is preceded with the emission of compact slip bands from the pre-crack tips, in agreement with the predictions of the earlier quasi-two-dimensional simulations. The application of Voronoi decomposition technique for atomic short-range order processing has allowed us to clarify the kinetics of structural transformations at the tips of nucleating and propagating cracks for three most common systems of crack propagation in iron. It is demonstrated that the compact slip bands emanating from the crack tips not only accompany crack nucleation, but remain an essential feature of the crack propagation on {001} planes. On the contrary, crack propagation on {110} planes involve complicated structural transformations at the crack tip, including phase transitions and full dislocation emission. In neither case amorphization at the crack tip is observed.

Sub Grain Formation in Plastically Deformed Microstructures in the Combined Simulation of Rolling and Annealing for Static Recrystallization with the Phase-Field Method

Alexander Vondrous¹, Michael Selzer¹ and Britta Nestler²

¹Institute of Materials and Processes Moltkestr. 30 76133 Karlsruhe Germany, alexander.vondrous@hs-karlsruhe.de, michael.selzer@hs-karlsruhe.de, ²Institute of Reliability of Components and Systems, Karlsruhe Institute of Technology, Germany, britta.nestler@kit.edu

ABSTRACT

The microstructure and the mechanical properties of cold rolled metal sheets after annealing strongly depend on the prior deformation step and the recrystallization process. To obtain a recrystallized microstructure after annealing, we simulate the recrystallization and sub grain formation process for plastically deformed microstructures, considering crystallographic orientations and deformation with the phase-field method. The first step is the conversion of the simulation data for a rolling process which is calculated with the finite element method (FEM) on an irregular grid. These data are subsequently projected on a regular grid to simulate the static recrystallization with the phase-field method. Before the misorientation between discretisation points can be used to generate sub grains, the data of the FE simulation must be transferred in an appropriate manner on the regular grid. Voronoi tessellation is a common technique, which is used to map irregular grid points on a regular grid, e.g. in simulation of recrystallization processes with cellular automata [1]. The accumulated plastic slip of the crystal plasticity FE simulation is considered as a measure of the plastic deformation for the recrystallization and is included in the mapping process. Nucleation of sub grains is modeled depending on the deformation of the grain structure and the misorientation of the grain boundary. An additional driving force for the growth of the nuclei during recrystallization is incorporated in the phase-field model [2] by using the accumulated plastic slip (stored energy) as an additional system variable.

1. Introduction

Recrystallization plays a big role in metal processing industry and occurs under certain conditions. It is not easy to control the recrystallization process which determines material properties. Simulations can help to understand the recrystallization process and to predict material properties more accurately.

Many processes are assigned to recrystallization, such that we constrain recrystallization to primary recrystallization, which is also called discontinuous recrystallization [3,4]. Early attempts as the analytical Johnson-Mehl-Avrami-Kolmogorov (JMAK) model [5] have taken nucleation rates and volume fractions into account without incorporating the microstructure of the deformed material. Monte Carlo models [6] which can describe grain growth in 2 or 3 dimensions very well, are used to study recrystallization. Cellular automata [1] are used to simulate microstructure evolution during annealing too. The newest approach is a combination of the finite element method and the phase-field method to simulate deformation and recrystallization [7]. Our approach follows the current development by using a finite element crystal plasticity model to simulate cold rolling and a phase-field model to simulate nucleation and nuclei growth. Nu-

cleation is controlled by the stored energy (accumulated plastic slip) after deformation by setting a level, at which grains will be defined as nuclei. Nuclei growth is driven by the stored energy around the nucleus. The higher the stored energy, the faster the nucleus is growing. Boundary energy is misorientation dependent and set by the Read and Shockley function [8]. First results in 2D show a different development of the recrystallizing and not recrystallizing microstructure. The next step is to simulate a 3D microstructure and compare the results with experiments to find model parameters and to validate the model.

2. Data conversion

The finite element grain structure is based on EBSD measurements¹ of DC04 steel. Volume fractions of measured crystal orientations are maintained in the representative FE grain structure. Cubic elements are used to produce the FE grain structure with the voronoi construction. A grid of $60 \times 60 \times 60$ cubic elements is used with periodic boundary condition in each dimension. To obtain a good representation of the material, as many EBSD crystal orientation information as possible is used. This leads to a coarse grain structure, in which a lot of grains consist of just one to three cube elements. The simulation domain is rolled² until 63% of the original height is reached. To transfer crystal orientation and stored energy to a regular grid with a higher resolution (e.g. $800 \times 400 \times 200$ discretization points), we construct a voronoi diagram. Each FE integration point is used as a voronoi point. All discretization points of the regular grid inside a voronoi cell obtain information (crystal orientation and stored energy) of the corresponding FE integration point. To obtain a grain structure, we apply the algorithm described in [9] with a 3° misorientation treshold, which groups discretization points with similar crystal orientations to a grain. The similarity is contained in the treshold, which is small for a fine and big for a coarse grain structure.

3. Phase-Field model extension

The phase-field functional in Eqn. 1 is derived in [2] and is extended by an additional energy term given in Eqn. 2, which increases the growth speed of recrystallizing grains (α_i). The non-recrystallizing grains are not effected by the additional driving force. The equations read

$$\mathcal{F}(\phi) = \int_{\Omega} \varepsilon a(\phi, \nabla \phi) + \frac{1}{\varepsilon} w(\phi) + f(\phi, E_{store}) dx \quad (1)$$

$$f(\phi, E_{store}) = E_{store} \cdot \sum_{\alpha_i} h(\phi) \quad (2)$$

A misorientation dependent grain boundary energy and grain boundary mobility between grains is set with the description of Read and Shockley [8] defined, e.g. for the mobility $\tau(\theta)$ by

$$\tau(\theta) = 0.9 \frac{1}{1 + e^{-2\theta - 15}} + 1, \quad (3)$$

where θ is the misorientation of the grain boundary. We define nuclei depending on the stored energy of each grain at the simulation start. A grain is set to be a nucleus, if the stored energy per grain volume is above a predefined value.

¹Measurements are carried out by Simone Schendel at the Karlsruhe Institute of Technology

²Simulation is carried out by Pierre Bienger at the Fraunhofer Institute for Mechanics of Materials in Freiburg

4. Results and Outlook

Two simulations, with and without recrystallization show a different development of the grain structure (see Figure 1). The recrystallizing grains overgrow the original grains and change the final grain structure significantly. The starting grain structure looks very artificial because of the low finite element resolution. A more detailed finite element mesh will be used for simulations in a forthcoming paper. Nucleation has been assumed to be independent on time and occurs only at the beginning of the simulation. An extension of this assumption is the formulation of a time dependent nucleation model.

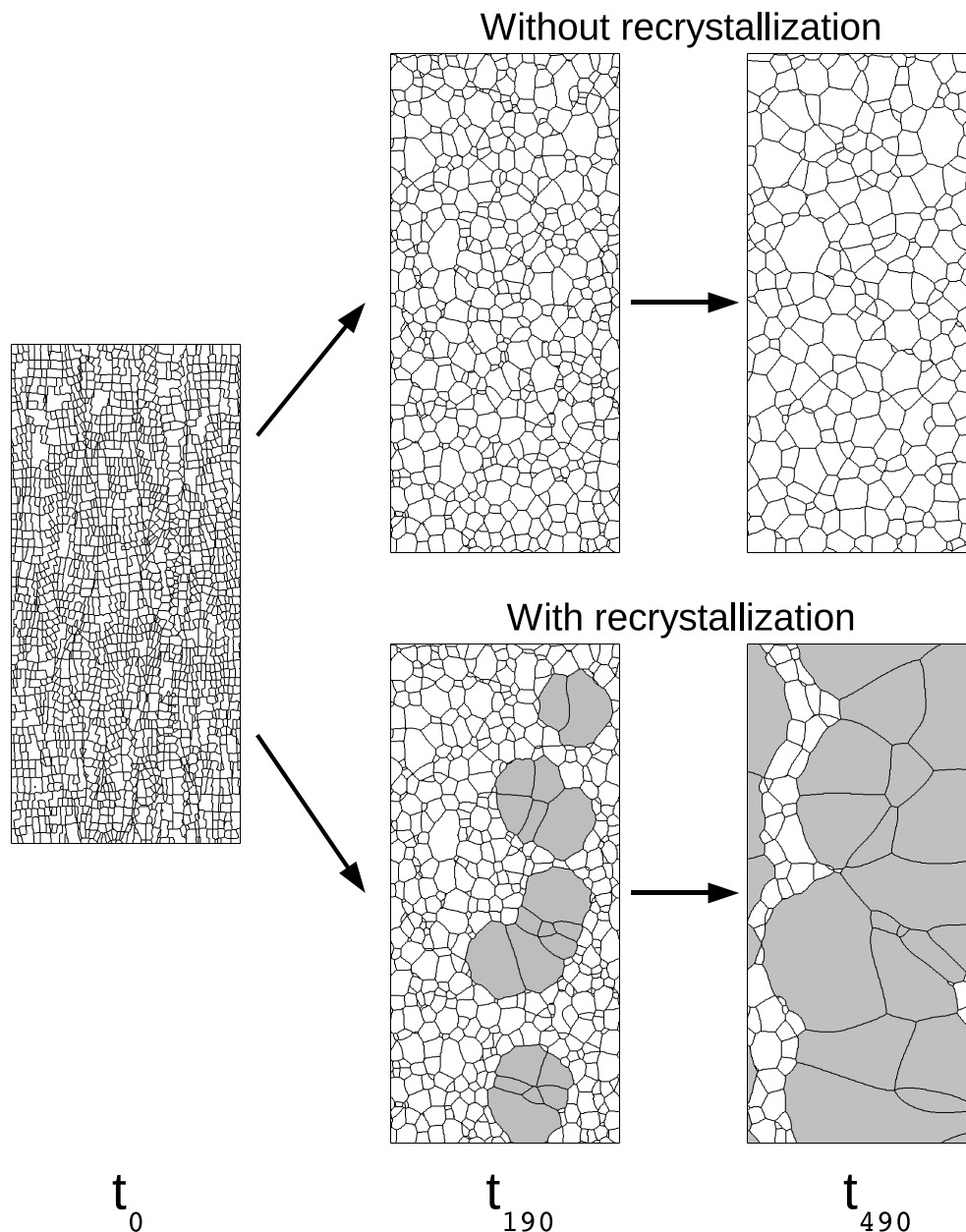


Figure 1: Starting condition (left) after data conversion and simulation snapshots with (bottom) and without (top) recrystallization at two different time steps. Grey colored grains are recrystallizing grains under the influence of the stored energy driving force.

Future work incorporates 3D simulations and comparison with EBSD measurements of rolled DC04 sheet metal to identify processing parameters and to validate the model.

References

- [1] Raabe, D., Becker, R., 2000, Coupling of a crystal plasticity finite-element model with a probabilistic cellular automaton for simulating primary static recrystallization in aluminium, *Modelling Simul. Mater. Sci. Eng.*, **8** (2000): 445462
- [2] Nestler, B., Garcke, H., Stinner, B., 2005, Multicomponent alloy solidification: Phase-field modeling and simulations, *Phys. Rev. E*, **Vol. 71 No. 4** (2005), 041609-1-6
- [3] Humphreys, F.J., Hatherly, M., 1996, Recrystallization and Related Annealing Phenomena, *Elsevier Science*, ISBN 0-08-042685-9
- [4] Gottstein, G., 2007, Physikalische Grundlagen der Materialkunde, 3rd Edition, *Springer*, ISBN 978-3-540-71104-9
- [5] Avrami, M. 1939, Kinetics of Phase Change. I General Theory, 3rd Edition, *J. Chem. Phys.*, **Volume 7**, 1103
- [6] Walasek, T.A., 2004, Experimental verification of Monte Carlo recrystallization model, *Journal of Materials Processing Technology*, **Volumes 157-158**, Pages 262-267
- [7] Takaki, T., Tomita, Y., 2009, Static recrystallization simulations starting from predicted deformation microstructure by coupling multi-phase-field method and finite element method based on crystal plasticity, *Int. Journal of Mechanical Sciences*, **Volume 52, Issue 2**, Pages 320-328
- [8] Read, W.T., Shockley, W., 1950, Dislocation Models of Crystal Grain Boundaries, *Phys. Rev.*, **78**, 275
- [9] Selzer, M., Nestler, B., Reichardt, M., Unser, A., Plötschke, M., Roth, S., 2010, Phase-Field simulations of grain structure dynamics based on EBSD data of austenitic NiMnGa samples, *Elsevier Acta. Mat.*, Submitted February 2010

Effect of impurities on structural, cohesive, and magnetic properties of grain boundaries in α -Fe

E. Wachowicz and A. Kiejna

Institute of Experimental Physics and Interdisciplinary Centre for Materials Modeling,
University of Wrocław, Plac M. Borna 9, PL-50-204 Wrocław
elwira@ifd.uni.wroc.pl

The effects of several metalloid (B), metalloid-like (C, P) and nonmetallic impurities (N, O and S) on structure, energetics and mechanical properties of $\Sigma 3(111)$ and $\Sigma 5(210)$ grain boundaries (GBs) in ferromagnetic α -Fe have been studied from first principles. For two different concentrations and positions of impurity atoms the variations in GB properties have been analyzed in terms of the structural, electronic, and magnetic properties of the system. Most of the impurities enhance the relaxation of the interplanar spacing of the pure grains. Interstitial impurities at both GBs are shown to increase separation of the grains while substitutional ones in general either do not alter or decrease the grains' separation. It is shown that at the $\Sigma 5$ GB for all impurity atoms considered the positions in the boundary layer are energetically favored independently of interstitial or substitutional site, whereas the enrichment of the $\Sigma 3$ GB is favoured for the impurities of the interstitial sites as well as for a substitutional P and C. We have found that, in most cases, impurity atoms both in interstitial and substitutional positions at GBs act as embrittlers. Interstitial B, P and C at $\Sigma 3$ strengthens the GB, while at the $\Sigma 5$ only a lower concentration of interstitial B and C enhances the GB bonding. A monolayer of S and O only weakens the GB. All substitutional impurities, except for B, weaken the GBs. Interstitial impurities modify magnetic moments on the GB atoms stronger than substitutional ones. The moments on the impurities are much smaller in comparison to those on iron and they do not exceed $0.15 \mu_B$. In most cases they are oriented antiparallel to the moments on the neighbouring Fe atoms.

Formation of Stacking-Fault Tetrahedra in Selected Metals and in TiAl by Annihilation of Edge Dislocations

Hao Wang^{1,*}, Dongsheng Xu¹, Patrick Veyssi re², David Rodney³ and Rui Yang¹

¹ IMR, CAS, 110016, Shenyang, China

² LEM, CNRS-ONERA, BP 72, 92322 Ch tillon, France

³ SIMAP-GPM2, GINP, BP 75, 38402 Grenoble, France

* haowang@imr.ac.cn, 72 Wenhua Road, 110016, Shenyang, China

ABSTRACT

Molecular dynamics simulations show that stacking-fault tetrahedra (SFTs) form upon annihilation of edge dislocation dipoles in fcc metals, Al and Cu, and in TiAl, whereas not in Ni within simulation times of the order of a few ns. SFT nucleation is promoted by relatively small vacancy migration barriers along defected channels, forming small vacancy clusters and elemental SFTs. The formation of small-sized SFTs does not pre-require a triangular Frank loop. Instead, SFTs grow by agglomeration of vacancies and their clusters. The growth stage of a double-SFT into a perfect SFT is specifically analyzed. It is concluded that strain-induced SFTs originate from a local mechanism of forced vacancy injection by dislocation reactions.

1. Introduction

The presence of SFTs [1-10] may significantly influence the mechanical properties of fcc metals and alloys [11-19]. In addition to quenching and irradiation, SFTs were found by transmission electron microscopy (TEM) in a number of straining experiments [6, 9, 10, 20], including Al [20] which because of its relatively large stacking fault energy had been believed SFT-free. In these experiments, a large amount of vacancy clusters always accompany the SFTs in the most severely deformed regions which are exempt of dislocations. None of the accepted mechanisms of SFT formation [21, 22] provides a satisfactory rationale for the outcome of straining experiments, which led Kiritani to propose the “glide element” concept [23]. On the other hand, a series of MD investigations carried out in fcc metals and TiAl indeed indicate that dipolar dislocations do not simply “disappear” by annihilation, but instead transform into height- and temperature-dependent complex structures [24, 25]. SFT formation processes in Al and Cu have been studied at the atomic level in [26-28]. The present study is aimed at providing a deeper insight onto SFT formation by annihilation of edge dislocation dipoles in Al, Cu, Ni and TiAl.

2. Method

Mutually approaching edge dislocations in dissociated states were simulated using the method designed in [25]. Dipoles with heights $1d$ to $4d$ (d is the $\{111\}$ interplanar distance) were constructed in simulation boxes of sizes $[6, 40, 30]$ in Al and TiAl, $[6, 60, 30]$ in Ni and $[6, 80, 30]$ in Cu, counted in units of lattice vectors $[\bar{1}\bar{1}2]$, $[1\bar{1}0]$ and $[112]$. These dipoles were then MD-annealed at temperatures of 900 K for Al, 1300 K for Cu and TiAl, 1700 K for Ni, during at most 5 ns in time steps of 1 fs until no perceivable changes were noticed. Embedded-atom-method interatomic potentials were employed [29-31]. Periodic boundary conditions were imposed in three dimensions. The activation barriers of individual atomic jumps and the configurational energies afterwards were calculated using the Activation-Relaxation Technique (ART) [32-34] with the same potentials used in the MD calculations.

3. Results and Discussion

3.1. Annihilation product after high temperature annealing

Here SFT formation is analyzed for dipoles $1d$ high. An extensive set of dipole transformations under various conditions, e.g. height, temperature, potential, etc. is available in [24, 25]. Quenched configurations after annealing during 1 ns in Cu and TiAl, 2 ns in Al and 5 ns in Ni are shown in Fig. 1. Little noticeable change, if any, resulted from longer annealing and in particular no change occurred beyond 1 ns in both Cu and Al. The Cu dipole transforms into an SFT and a vacancy cluster (labeled “1” and “2” in Fig. 1a with 21 and 3 vacancies, respectively) and TiAl forms a vacancy cluster (labeled “2” in Fig. 1b), and incomplete and connected SFTs (labeled “1” and “3” in Fig. 1b, respectively). By contrast, the Al dipole yields vacancy clusters (labeled “1” to “6” in Fig. 1c) and an elemental SFT (labeled “7” in Fig. 1c). Even though annealed up to 5 ns, the Ni dipole changes slowly exhibiting the most featureless debris among all the materials tested (i.e. interconnected clusters with an SFT-like structure in places (Fig. 1d)).

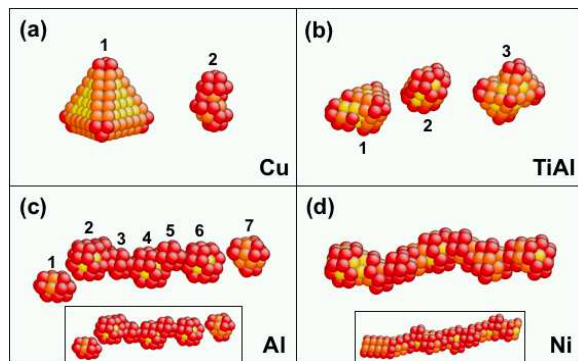


Fig. 1 Annealed $1d$ -dipoles for (a) Cu after 1 ns at 1300 K, (b) TiAl after 1 ns at 1300 K, (c) Al after 2 ns at 900 K, and (d) Ni after 5 ns at 1700 K. Only atoms with non-fcc-coordination are displayed. Cu forms a perfect SFT (1) and a cluster (2). In TiAl dipole annihilation yields an incomplete SFT (1), a cluster (2) and a double SFT (3). Al forms interconnected clusters (2-6) together with a single cluster (1) and an elemental SFT (7), while Ni is the least perturbed by atomic transport. Insets in (c) and (d) are instant configurations after 1 ns annealing in Al (almost unchanged with respect to 2 ns) and Ni, respectively. Atoms are visualized using AtomEye [35].

3.2. SFT nucleation

To elucidate the above transformation features, the initial atomic jumps during SFT nucleation were studied by ART in Al, Cu, Ni and TiAl on $1d$ to $4d$ dipoles. Calculations start from dipoles after 50 ps annealing (the instantaneous configurations can also be found in Fig. 3 in [24] and Fig. 1 to Fig. 3 in [25]). Fig. 2 shows relaxed configurations in Al after selected primary jumps were achieved and the corresponding activation barrier and energy gain. $(11\bar{1})$ cross-sections of the original dipoles are displayed in the insets. A full list for all the four systems is available in Tab. 1 for paths with activation barriers smaller than bulk vacancy migration barrier. Paths with negative energy gains are in bold.

For $1d$ dipoles, there exist possible primary jumps with activation barriers lower than bulk vacancy migration and negative energy gains in all the four systems, whereas for higher dipoles the situation is much more system-dependent. No easy path is found for $2d$ to $4d$ dipoles in Cu and $4d$ dipoles in Ni and TiAl. Concerning the implication on diffusion, the above results are in good agreement with e.g. Fig. 1. The

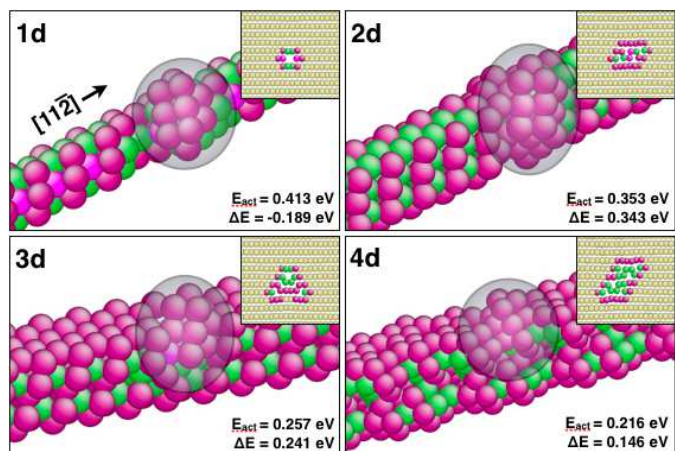


Fig. 2 Configurations after primary jumps for $1d$ to $4d$ dipoles in Al. Activation barriers and energy gains are indicated. Insets are $(11\bar{1})$ cross-sections of the original dipoles. Atoms are colored by the coordination number, with normal atoms visualized only in the insets.

relative high activation barriers in Ni prohibit fast dipole transformation and the fact that Cu has generally smaller barriers than TiAl is consistent with the complete and incomplete SFTs in Fig. 1a and 1b, respectively. The small barriers in Al accelerate the nucleation of clusters, whereas growth into SFTs is slowed down.

Such results indeed confirm that vacancy migration is very much facilitated by the existence of the hollow cores or ordered dipole cores [25] with integer or fractional vacancies resulting in the lower migration barriers.

Table 1. Primary jump paths for 1d to 4d dipoles in Al, Cu, Ni and TiAl. Only paths with an activation barrier (in eV) lower than the bulk vacancy migration energy are listed. Those with negative energy gains are in bold. For simplicity, at most three non-bold paths are listed for each case.

Height	Al		Cu		Ni		TiAl	
	E_{act}	ΔE						
1d	0.509	0.0843	0.650	0.350	1.238	0.408	0.616	0.171
	0.412	-0.189	0.376	-0.011	0.978	0.211	0.580	0.306
	0.407	0.0027	0.375	0.123	0.939	0.201	0.574	-0.053
	0.329	0.0331	0.367	0.020	0.853	-0.045		
2d	0.353	0.343			0.265	0.259	0.119	-0.045
					0.234	0.217	0.105	0.099
					0.233	0.204	0.098	0.068
3d	0.257	0.241			0.165	0.079	0.394	0.311
4d							0.156	0.063
	0.217	0.146						
	0.089	-0.053						

3.3. SFT growth

Once nucleated, SFTs and vacancy clusters further aggregate into large complex clusters and SFTs. Among these the double-SFT is frequently found at high temperature MD simulations. Fig. 3 shows a typical growth process of a double-SFT. Originally, the two interconnected SFTs are of about equal size (a), and through (b)-(c) the upper SFT shrinks losing the left-most stacking fault plane, while the lower SFT grows (note the areas enclosed by the dashed triangles in (a) and (d)). The double-SFT will eventually evolve to the perfect SFT in Fig. 1a.

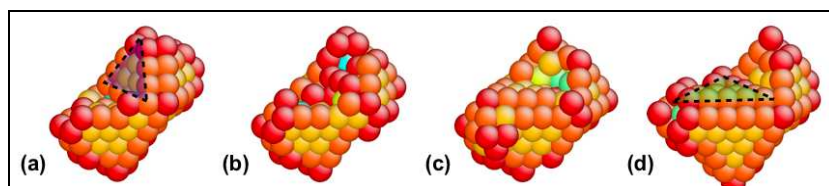


Fig. 3 Growth of a double-SFT configuration. The upper SFT grows in the expense of the lower one, as indicated by the dashed triangles in (a) and (d). Only atoms with non-fcc-coordination are displayed.

4. Conclusions

SFTs are formed upon the annihilation of edge dislocation dipoles in Al, Cu and TiAl. Transformed dipole cores significantly reduce the vacancy migration barriers, resulting in fast SFT nucleation. SFTs further grow by absorbing vacancies and their clusters and does not pre-require a triangular Frank loop. The unique presence of deformation-induced SFTs in Al originates from a local mechanism of forced vacancy injection by dislocation reactions.

The present simulation confirms a deformation-induced debris formation mechanism, proposed by early simulations in Cu [36] and TiAl [37], where vacancy clusters are created upon dislocation mutual annihilation. MD simulations of shear deformation in Al, Cu and Ni at high strain rates and various temperatures are in progress in order to complete the present analysis. Here the key point lies in the necessity of a strain rate high enough to produce a

local vacancy supersaturation as realized in a series of experiments by Kiritani *et al.* in Au, Cu, Ni and Al [6, 20, 38].

Acknowledgements

The support of the Ministry of Science and Technology of China under Grant No. 2006CB605104 and of the National Natural Science Foundation of China under Grant No. 50911130367 and No. 50631030 is gratefully acknowledged.

References

- [1] Silcox J, Hirsch PB. *Philos Mag* 1959;4:72.
- [2] Shimomura Y, Fukushima H, Kami M, Yoshiie T, Yoshida H, Kiritani M. *J Nucl Mater* 1986;141:846.
- [3] Zinkle SJ, Seitzman LE, Wolfer WG. *Philos Mag A* 1987;55:111.
- [4] Kojima S, Satoh Y, Taoka H, Ishida I, Yoshiie T, Kiritani M. *Philos Mag A* 1989;59:519.
- [5] Kiritani M. *Mater Chem Phys* 1997;50:133.
- [6] Kiritani M, Yasunaga K, Matsukawa Y, Komatsu M. *Radiat Eff Defects Solids* 2002;157:3
- [7] Matsukawa Y, Yasunaga K, Komatsu M, Kiritani M. *Mater Sci Eng A* 2003;350:17.
- [8] Schäublin R, Yao Z, Baluc N, Victoria M. *Philos Mag* 2005;85:769.
- [9] Loretto MH, Clarebrough LM, Segall RL. *Philos Mag* 1965;11:459.
- [10] Loretto MH, Pavey A. *Philos Mag* 1968;17:553.
- [11] Sharp JV. *Philos Mag* 1967;16:77
- [12] Singh BN, Trinkaus H, Golubov SI, Buschow KHJ, Cahn RW, Flemings MC, Ilschner B, Kramer EJ, Mahajan S, Veysière P. *Encyclopedia of Materials: Science and Technology*. Oxford, Elsevier, 2001, p.7957-7972.
- [13] Yao Z, Schäublin R, Victoria M. *J Nucl Mater* 2002;307:374.
- [14] Yao Z, Schäublin R, Victoria M. *J Nucl Mater* 2004;329-33:1127.
- [15] Singh BN, Golubov SI, Trinkaus H, Edwards DJ, Eldrup M. *J Nucl Mater* 2004;328:77.
- [16] Yao Z, Schäublin R, Spätig P, Victoria M. *Philos Mag* 2005;85:745.
- [17] Wirth BD, Bulatov VV, de la Rubia TD. *J Eng Mater Technol* 2002;124:329.
- [18] Osetsky YN, Stoller RE, Matsukawa Y. *J Nucl Mater* 2004;329-33:1228.
- [19] Osetsky YN, Rodney D, Bacon DJ. *Philos Mag* 2006;86:2295.
- [20] Kiritani M, Satoh Y, Kizuka Y, Arakawa K, Ogasawara Y, Arai S, Shimomura Y. *Philos Mag Lett* 1999;79:797.
- [21] Jossang T, Hirth JP. *Philos Mag* 1966;13:657.
- [22] Hirth JP, Lothe J. *Theory of dislocations*. New York: Wiley, 1982, 800 p.
- [23] Kiritani M, Sota T, Tawara T, Arimura H, Yasunaga K, Matsukawa Y, Komatsu M. *Radiat Eff Defects Solids* 2002;157:53.
- [24] Wang H, Xu DS, Yang R, Veysière P. *Acta Mater* 2008;56:4608.
- [25] Wang H, Xu DS, Yang R, Veysière P. *Acta Mater* 2009;57:3725.
- [26] Wang H, Xu DS, Yang R, Veysière P. submitted to *Acta Materialia* 2010.
- [27] Wang H, Xu DS, Yang R, Veysière P. submitted to *Acta Materialia* 2010.
- [28] Wang H, Xu DS, Yang R, Veysière P. submitted to *Acta Materialia* 2010.
- [29] Mishin Y, Farkas D, Mehl MJ, Papaconstantopoulos DA. *Phys Rev B* 1999;59:3393.
- [30] Mishin Y, Mehl MJ, Papaconstantopoulos DA, Voter AF, Kress JD. *Phys Rev B* 2001;63:224106.
- [31] Zope RR, Mishin Y. *Phys Rev B* 2003;68:024102.
- [32] Barkema GT, Mousseau N. *Phys Rev Lett* 1996;77:4358.
- [33] Mousseau N, Barkema GT. *Phys Rev E* 1998;57:2419.
- [34] Mousseau N, Barkema GT. *Phys Rev B* 2000;61:1898.
- [35] Li J. *Model Simul Mater Sci Eng* 2003;11:173.
- [36] Schiotz J, Leffers T, Singh BN. *Philos Mag Lett* 2001;81:301.
- [37] Xu DS, Wang H, Yang R, Veysière P. *IOP Conf Series: Mater Sci Eng* 3 2009:012024.
- [38] Kiritani M. *Mater Sci Eng A* 2003;350:1.

Multiscale simulations of thermal stability of nanocrystalline iron

Tomasz Wejrzanowski, Krzysztof Jan Kurzydłowski

Warsaw University of Technology, Faculty of Materials Science and Engineering,
Woloska 141 str., 02-507 Warsaw, Poland
e-mails: twejrzanowski@inmat.pw.edu.pl, kjk@inmat.pw.edu.pl

In the present paper, in order to fully account for the microstructural features of the grain growth in nanometals, the simulations in two different length scales (atomic and meso-sopic) have been performed. The motion of individual grain boundaries (GBs) was modeled at atomic scale by molecular dynamics. The results of these calculations were transferred to the MonteCarlo model of nano-sized aggregate of grains with varying populations of grain boundaries (GB). The special focus was on the effect of the grain size distribution function and the fraction of low-angle grain boundaries on the grain growth kinetics. The results show that grain size distribution and the distribution function of the grain boundary orientations have an important impact on the stability of nanometals. These results are verified and discussed using the data for nanometals obtained by Severe Plastic Deformation methods.

An integrated approach for cellular materials: Phase-field modelling of foam evolution and processing

Frank Wendler^{1,2} and Britta Nestler¹

¹Institute of Materials and Processes, Karlsruhe University of Applied Sciences,
Moltkestr. 30, 76133 Karlsruhe, Germany

²frank.wendler@hs-karlsruhe.de

Open and closed cell foams represent a wide class of materials, having gained major interest in the last years due to the advantageous properties in many structural mechanic, thermal isolating or filtering applications. Contrary to the final use, foam is always generated in the fluid state, subject to a limited set of process variables (e.g. pressure, shear). Recent results point to the strong influence of the actual microstructure (cell topology, ligament geometry) on quantitative macroscopic properties like Young moduli, yield stress and thermal conductivity of the solid product, which have to be taken into account in simulations of mechanical and thermal properties.

We present an integrated approach to model and simulate microstructure evolution and processing of a foam combining methods from thermodynamics, continuum mechanics and algorithmics. For the evolution of the liquid-gas boundaries, we base on a free energy formulation using a multi-phase-field model of Allen-Cahn type [1]. The diffuse interface picture, based on a free energy formulation of the two-phase problem, brings major benefits in regard to numerics and modeling and is extended to include compressibility of the gas phase [2] and fluid flow. This enables to study mechanical loading of the fluid foam, studied in detail at the bubble scale ($< 1\text{mm}$). As this work is directed towards the prediction of process modifications effecting on macro scale properties, simulation domains in the size of representative volume elements with coarser resolution are necessary. A large scale (foam scale, \sim several cm) phase-field model is built up, where individual order parameters $\phi_\alpha, \alpha \in \{1\dots N\}$ are introduced for all $N \approx 1000$ bubbles and ϕ_l for the liquid phase. The bubble scale studies validate the coarse grained approach concerning energetics and dynamics, and enable to find threshold values for the stability of the liquid walls, necessary for triggering events of wall rupturing.

Open and closed cell foam structures of different liquid fraction from simulations in 3D are characterized in terms of bubble topology and ligament geometry, and compared to real foam samples. Geometries showing pronounced anisotropic features result from abrupt pressure changes. First results from an evaluation of the elastic moduli of the virtual foams within the phase-field framework are given.

[1] H. Garcke, B. Nestler, B. Stinner and F. Wendler, *Math. Mod. Meth. Appl. Sci.* 18 (8) 2008, 1347 - 1381

[3] F. Wendler and B. Nestler, in preparation

Simulation of abnormal grain growth in two and three dimensional grain structures

Melanie Syha¹, Daniel Weygand¹

¹Karlsruhe Institute of Technology, izbs, Kaiserstr.12, 76131 Karlsruhe, Germany

e-mail: Daniel.Weygand@kit.edu

The condition for abnormal grain growth in thin films with columnar grain structure, treated as model example for two dimensional grain structures, and three dimensional bulk materials are studied by means of a two and three dimensional vertex model.

The simulations were performed using an enhanced vertex dynamics model [1,2], which allows for a fine discretization of the interfaces and which has been validated against analytical descriptions for the growth rate in two – the Neumann Mullins law – and three dimensions – the McPherson Srolovitz relation [3]. The role of grain boundary energy and mobility on the nucleation of abnormally growing grains is studied. Taking into account the grain boundary energy and averaged properties from the embedding matrix only, the simulation results indicate a deviation from mean field criteria [4] for the occurrence of discontinuous growth. The simulations clearly show that a small grain boundary energy advantage has a strong effect in promoting abnormal grains starting from a population of grains, described by a grain size distribution typically for ideal normal grain growth. The influence of the grain boundary mobility on the nucleation of abnormally growing grains is less pronounced in the three-dimensional model than predicted by mean field approaches.

References:

- [1] D. Weygand, Y. Bréchet and J. Lépinoux, *A vertex dynamics simulation of Grain Growth in two dimensions*, Phil. Mag. B 78 (1998) 329-352
- [2] M. Syha and D. Weygand, *A generalized vertex dynamics model for grain growth in three dimensions*, Modeling and Simul. Mater. Sci. & Eng. 18 (2010)
- [3] R.D. MacPherson and D.J. Srolovitz, *The von Neumann relation generalized to coarsening of three-dimensional microstructures*, Nature 446 (2007), 1053-1055
- [4] F.J. Humphreys, *A unified theory of recovery, recrystallization and grain growth, based on the stability and growth of cellular microstructures—I. The basic model*, Acta Mat. 45(1997) 4231-4240

Multiscale simulations of atomic ordering in nano-layered FePt

**Jan Wróbel¹, Tomasz Wejrzanowski¹, Mirosław Kozłowski², Rafał Kozubski²,
Krzysztof J. Kurzydłowski¹**

¹ Interdisciplinary Centre for Materials Modelling, Faculty of Materials Science and Engineering, Warsaw University of Technology, Wołoska 141, 02-507 Warszawa, Poland

² Interdisciplinary Centre for Materials Modelling, M. Smoluchowski Institute of Physics, Jagiellonian University, Reymonta 4, 30-059 Kraków, Poland
E-mail: jan.wrobel@inmat.pw.edu.pl

The study concerns FePt thin layers as a candidate material for ultra-high density magnetic storage media. The material in question reveals metastability of the L1₀ c-variant superstructure with mono-atomic planes parallel to the layer surface and off-plane easy magnetization.

Combined atomic and meso-scale simulations of ordering kinetics in nano-layered L1₀ AB binary intermetallic were performed. At the atomic scale, Monte Carlo (MC) technique implemented with vacancy mechanism of atomic migration was used under various models for the system energy. The evolution of meso-scale surface anti-phase domains was modeled by Kinetic Monte Carlo simulations of the re-orientation of the atoms arranged according to particular variant of the L1₀ superstructure. It has been assumed that the re-orientation process is controlled by temperature dependent anti-phase-boundary energies evaluated within the atomic (nano-) scale simulations.

Two “atomistic-scale” processes: (i) homogenous disordering and (ii) nucleation of the a- and b-L1₀-variants domains revealed characteristic time scales. The same was obtained for the meso-scale process: (i) heterogeneous L1₀-variant domain growth and (ii) domain microstructure relaxation. The results obtained by multi-scale Monte-Carlo simulations have recently been confirmed experimentally in the epitaxial thin films of FePt.

The Molecular dynamics simulation on the Evolution of Deformation-Induced Nano-Crystallization in Metallic Glasses

Wang Yu, Ni Xianggui

CAS Key Laboratory of Mechanical Behavior and Design of Materials , University of Science and Technology of China, Hefei, 230026, China

wyu@ustc.edu.cn, xianggui@ustc.edu.cn

With the development of techniques to produce bulk metallic glasses, the mechanical properties of amorphous alloys have become topics of scientific and technological interest in terms of structural and functional applications. Recently, nano-crystallization in amorphous metals induced by plastic deformation has received increased attention. The deformation-induced nano-crystallization behavior of amorphous pure Ni has been investigated by using a molecular dynamics simulation in this paper. It is shown that the small nano-crystalline grain will nucleate and grow during the compression deformation. The micro-evolution mechanism of the nano-crystallization was studied. It is believed that the deformation induced the growth of the ordered clusters in the amorphous metals and the nano-crystalline grain grows under the shearing combination and shearing deposition. The crystallization process in the multi-component amorphous Ni-Pd alloys is also studied. The temperature effect on the nano-crystallization behavior in amorphous metals is also been presented. The nano-crystalline grain will nucleate in a lower strain under a higher temperature. It indicated that combining severe plastic deformation with thermal annealing treatments presents a new opportunity for developing bulk nano-crystalline materials with controlled microstructures.

Keywords: Atomic Simulation, Nano-Crystallization, Amorphous Metals

Two-dimensional Real-valued Cellular Automata and Applications in Micro-structure Modelling

Xu Xu¹, Stephen P. Banks² and Mahdi Mahfouf³

^{1,2,3} Department of Automatic Control and Systems Engineering, University of Sheffield, Mappin Street, Sheffield, S1 3JD, UK.

¹Xu.Xu@sheffield.ac.uk

ABSTRACT

In this paper, a new form of cellular automata is introduced, which are generated by local transition rules, defined on real-valued rather than binary system states. We show that these systems have more complex and richer behaviours than the ones associated with binary states. The real-state automata should also give much more realistic approaches to micro-structure modelling of material systems and generate more accurate results.

1. Introduction

Ever since the original concept of cellular automaton being brought into attention in the late 1940's by von Neumann, much research has been carried out on the theory of cellular automata based on binary states [1,2]. They have recently been implemented as a simple and effective computational tool of modelling physical systems [3,4]. Such models have the advantage of simulating global systems governed by simple local rules. However, there exists a limitation associated with the universality of behaviours which can be modelled by binary systems. In this paper, we present a new type of cellular automata which are defined by local rules, on real-valued system states. We illustrate in Section 2 that two-dimensional real-valued automata generate more variety of dynamical behaviours by comparison to the binary case. In Section 3, we show that the real automaton can be used in modelling microstructure evolutions of austenite grains during reheating. This type of automata also has the potential of modelling other metal processing systems, ideas of which will be studied in a future paper.

2. Dynamical Behaviours of Two-dimensional Real Automata

A traditional binary two-dimensional cellular automaton is a discrete nonlinear dynamical system defined on a discrete space by a local rule. A typical example is Conway's game of life which is defined by a rule R_{Con} in Moore neighbourhoods:

$$\begin{pmatrix} m_{11} & m_{12} & m_{13} \\ m_{21} & m_{22} & m_{23} \\ m_{31} & m_{32} & m_{33} \end{pmatrix} \xrightarrow{R_{Con}} r ,$$

$$\text{where } r = \begin{cases} 1 & \text{if } (m_{22} = 1 \text{ and } \#m = 3 \text{ or } 4) \\ & \text{or } (m_{22} = 0 \text{ and } \#m = 3) \\ 0 & \text{otherwise} \end{cases} \quad \text{and} \quad \#m = \sum_{i=1}^3 \sum_{j=1}^3 m_{ij} .$$

This cellular system has surprisingly complex dynamical behavior which produces many interesting patterns evolved from certain initial conditions after some time-steps. Initial

configuration of the ‘Gosper glider gun’ automaton shown in Fig. 1 (a) generates glider states in the 15th, 45th, 75th and 105th iteration plotted in Fig. 1 [5]. White colour here represents dead cells having the values ‘0’ and black colour indicates alive cells with the ‘1’ values.

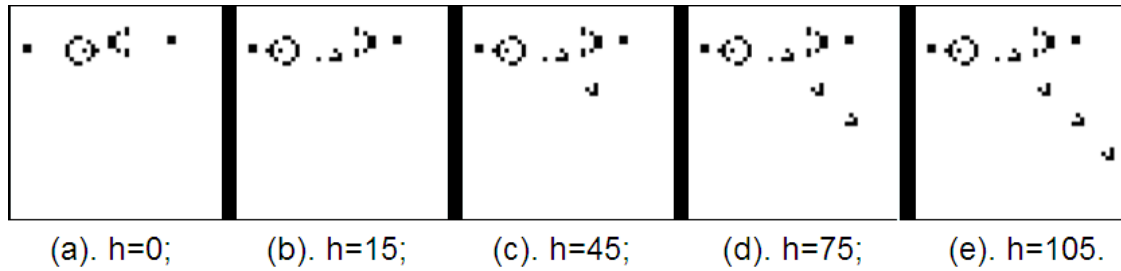


Figure 1. Glider gun of the game rule.

The states of two-dimensional real-valued cellular automata are given by matrices

$$X = \begin{pmatrix} x_{11} & \cdots & x_{1n} \\ \vdots & \ddots & \vdots \\ x_{n1} & \cdots & x_{nn} \end{pmatrix} \in \mathfrak{R}^{n^2},$$

and the dynamics are defined by

$$Y = F(X),$$

where

$$Y = \begin{pmatrix} y_{11} & \cdots & y_{1n} \\ \vdots & \ddots & \vdots \\ y_{n1} & \cdots & y_{nn} \end{pmatrix}$$

is given by

$$y_{ij} = f(x_{i-1,j-1}, x_{i-1,j}, x_{i-1,j+1}, x_{i,j-1}, x_{i,j}, x_{i,j+1}, x_{i+1,j-1}, x_{i+1,j}, x_{i+1,j+1}), \quad 1 \leq i \leq n \quad (1)$$

for some function $f: \mathfrak{R}^9 \rightarrow \mathfrak{R}$ [6]. For the convenience of computation, the real automata can be defined on some bounded interval, say $I=[0,1]$.

A real-state version of the game of life cellular automaton is defined by a local function in the form of (1) but $f: I^9 \rightarrow I$. The real-state automaton displays similar qualitative behaviour to the binary case. However, by nature of being a real-valued system, the behaviour is more complex and more interesting. In Fig. 2, we show the real-valued ‘glider gun’ starting from the same initial configuration as in the binary case. In this automaton, states with the values ‘0’ are plotted in black, states having the values ‘1’ are plotted in white, and the higher value a state is, the ‘lighter’ they appear in the system image.

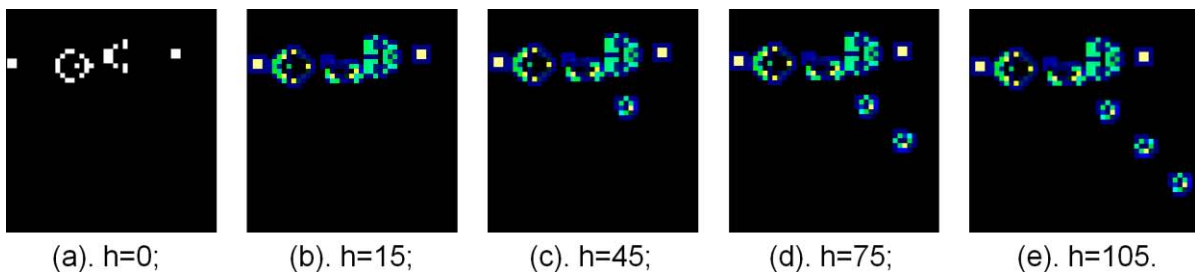


Figure 2. ‘Glider gun’ of the real-valued game of life automaton.

In order to demonstrate the rich behaviours produced by real-valued cellular automata, we show another example that a function

$$f = \frac{1}{1 + (x_{i-1,j} + x_{i,j-1} + 2x_{i,j} + x_{i,j+1} + x_{i+1,j} - 1)^4}$$

generates a cell-like evolutionary automaton with time steps t plotted in Fig. 3. We can see from Fig. 3 that this automaton has self-cleaning and self-organizing behaviour which could be used in simulating some system in life science.

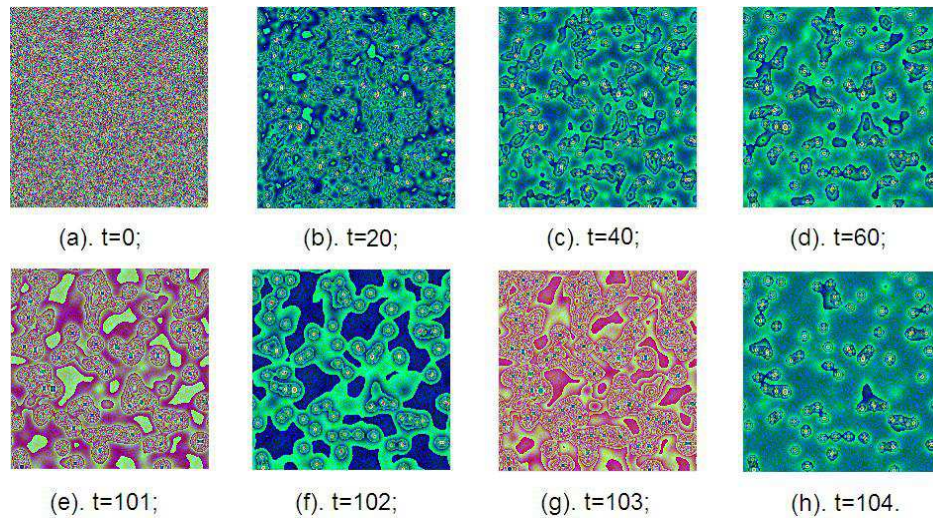


Figure 3. A 2-Dimensional Cellular Automaton.

3. Applications in Micro-structure Modelling

Crucial mechanical properties such as strength and toughness of a final product are closely related to the grain size; therefore, micro-structural evolution of austenite grains during the coarsening process through reheating is an important problem [7]. However, this problem is non-trivial and difficult to solve theoretically. In this section, we present a real-valued cellular automaton model to simulate the normal austenite grain coarsening process during reheating. Simulation results of the initial nucleation stage and then the grain coarsening stage are shown in Fig. 4; different colours in the figure represent different grains.

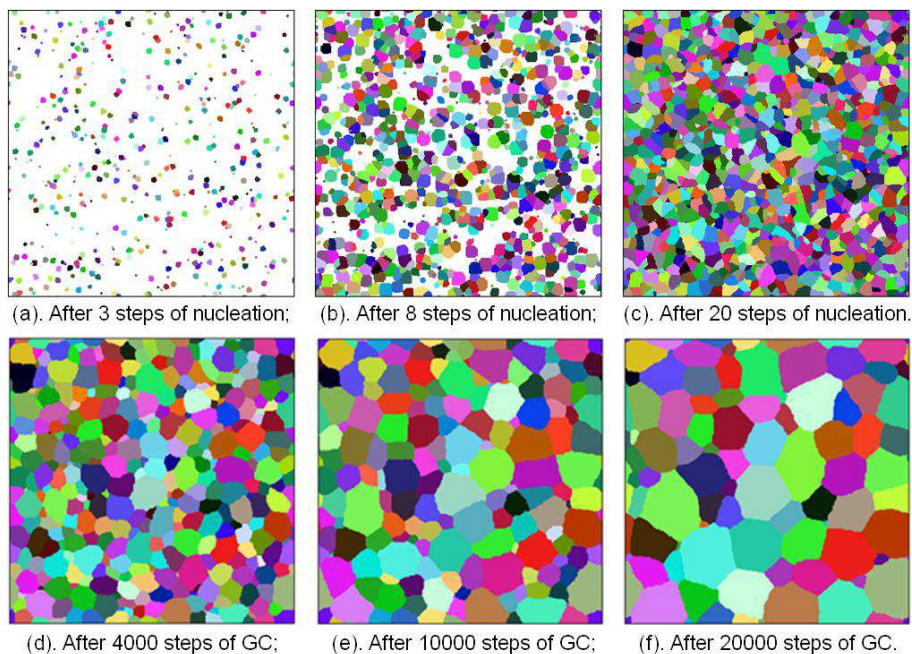


Figure 4. Simulated nucleation and grain coarsening evolution.

By comparing simulation results to experimental data, the model resembles the physical system from various aspects, including: grain evolution in that big grains expand at the expense of small ones; grain sides – grains with 5-6 sides are dominant; grain boundaries which tend to form straight lines rather than curves; and grain shapes in that 120° dihedral angles form between grains. Furthermore, this grain coarsening automaton model is governed by a function f defined as follows (for the convenience of denotation, we use $x_1, x_2, x_3, x_4, x_5,$

x_6, x_7, x_8 and x_9 instead of $x_{i-1,j-1}, x_{i-1,j}, x_{i-1,j+1}, x_{i,j-1}, x_{i,j}, x_{i,j+1}, x_{i+1,j-1}, x_{i+1,j}, x_{i+1,j+1}$ in the function):

$$f = \begin{cases} x_1, & \text{if } x_1 = x_3 = x_7 \text{ or } x_1 = x_7 = x_9 \text{ or } x_1 = x_3 = x_9; \\ x_2, & \text{if } x_2 = x_4 = x_6 \text{ or } x_2 = x_6 = x_8 \text{ or } x_2 = x_4 = x_8 \\ & \text{or } (x_2 = x_6 \text{ and } x_5 = x_4 = x_8 \text{ and } x_2 \neq x_5 \text{ and } P_1) \\ & \text{or } (x_2 = x_4 \text{ and } x_5 = x_6 = x_8 \text{ and } x_2 \neq x_5 \text{ and } P_1); \\ x_3, & \text{if } x_3 = x_7 = x_9; \\ x_4, & \text{if } x_4 = x_6 = x_8 \text{ or } (x_4 = x_8 \text{ and } x_5 = x_2 = x_6 \text{ and } x_4 \neq x_5 \text{ and } P_1); \\ x_6, & \text{if } x_6 = x_8 \text{ and } x_5 = x_2 = x_4 \text{ and } x_6 \neq x_5 \text{ and } P_1; \\ x_2, & \text{otherwise if } x_2 \neq 0 \text{ and } x_5 \neq 0 \text{ and } x_2 \neq x_5 \text{ and } P_2; \\ x_4, & \text{otherwise if } x_4 \neq 0 \text{ and } x_5 \neq 0 \text{ and } x_4 \neq x_5 \text{ and } P_2; \\ x_6, & \text{otherwise if } x_6 \neq 0 \text{ and } x_5 \neq 0 \text{ and } x_6 \neq x_5 \text{ and } P_2; \\ x_8, & \text{otherwise if } x_8 \neq 0 \text{ and } x_5 \neq 0 \text{ and } x_8 \neq x_5 \text{ and } P_2; \\ x_1, & \text{otherwise if } x_1 \neq 0 \text{ and } x_5 \neq 0 \text{ and } x_1 \neq x_5 \text{ and } P_3; \\ x_3, & \text{otherwise if } x_3 \neq 0 \text{ and } x_5 \neq 0 \text{ and } x_3 \neq x_5 \text{ and } P_3; \\ x_7, & \text{otherwise if } x_7 \neq 0 \text{ and } x_5 \neq 0 \text{ and } x_7 \neq x_5 \text{ and } P_3; \\ x_9, & \text{otherwise if } x_9 \neq 0 \text{ and } x_5 \neq 0 \text{ and } x_9 \neq x_5 \text{ and } P_3; \\ x_5, & \text{otherwise.} \end{cases}$$

$P_1, P_2,$ and P_3 in the function f are probabilistic terms which control the coarsening speed. The terms need to be linked with the reheating temperature and the material compositions in future work.

4. Conclusions

In this paper, we defined the real-functional cellular automata, and showed that such systems can generate more interesting dynamical behaviours than the traditional binary ones. We also presented a real automaton model of micro-structural evolutions of steel reheating process. Future work will be focused on improving the model when varying physical parameters.

Acknowledgements

The authors wish to acknowledge the UK- EPSRC for their financial support under Grant No. EP/F023464/1.

References

- [1]. S. Wolfram, *Physica D.*, 10(1984), p.1.
- [2]. X. Xu, Y. Song and S.P. Banks, *Int. J. Bifurcation and Chaos*, 19(2009), p.1147.
- [3]. B. Chopard and M. Droz, *Cellular Automata Modelling of Physical Systems*. Cambridge University Press, 1998.
- [4]. H.L. Ding, Y.Z. He, L.F. Liu and W.J. Ding, *J. Cryst. Growth*, 293(2006), p.489.
- [5]. X. Xu, *Nonlinear Systmes and Cellular Maps*, University of Sheffield Ph.D thesis, 2009.
- [6]. X. Xu, S.P. Banks and M. Mahfouf, submitted to *Int. J. Bifurcation and Chaos*, 2010.
- [7]. W. Yu, *Cellular Automata Modelling of Austenite Grain Coarsening During Reheating*, University of Sheffield Ph.D thesis, 2002.

Crystal plasticity modeling and experiments to improve the micromechanical understanding of single crystal γ -TiAl and γ -TiAl based microstructures

Claudio Zambaldi¹, F. Roters¹ and D. Raabe¹

¹Max-Planck-Institut für Eisenforschung, Max-Planck-Str. 1, 40237 Düsseldorf, Germany
c.zambaldi@mpie.de

The plastic anisotropy of γ -TiAl, as present in two-phase microstructures, was analyzed by axisymmetric indentation into known crystallographic orientations. The deformation of the free surface around the imprints, the pile-up profile, was characterized by AFM. It is characteristic for the activation of specific deformation mechanisms. Corresponding crystal plasticity finite element (CPFE) simulations based on an appropriate material model can explain the developed surface features if the constitutive parameters are chosen correctly. Through this novel approach the constitutive behavior of near-stoichiometric γ -TiAl could be quantified. Easy activation of ordinary dislocation glide was found and this result is in good agreement with the findings from TEM dislocation analysis. The main advantage of the method is that it is based only on values that can be measured with a high level of accuracy.

During the development of the described method, a new material property, the *inverse pole figure of indentation pile-up topographies*, was defined. It provides useful information about the mechanical behavior of ductile crystals. A pronounced plastic anisotropy of a given material will be reflected in orientation-dependent and highly characteristic pile-up topographies. The inverse pole figure of pile-up topographies of γ -TiAl will be presented and discussed.

For the micromechanics of two-phase γ -TiAl / α_2 -Ti₃Al lamellar microstructures, a homogenized CPFE material law was developed. Kinematic constraints from the crystallographic interfaces lead to a strong plastic anisotropy of this material which is, however, completely different from the plastic anisotropy of single phase γ -TiAl. The model was applied to the deformation of a multi-grain aggregate. Changing the constitutive parameters of the model, different two-phase microstructures could be studied. Thereby, the pre-yielding behavior of lamellar microstructures could be explained in terms of the strong flow strength anisotropy.

References

- [1] C. Zambaldi, S. Zaeferrer, S.I. Wright, Characterization of order domains in γ -TiAl by orientation microscopy based on electron backscatter diffraction, J Appl Crystallography 42 (2009), 1092-1101, <http://edoc.mpg.de/439331>
- [2] C. Zambaldi, D. Raabe, Plastic anisotropy of γ -TiAl revealed by axisymmetric indentation, Acta Mater (in press) doi: 10.1016/j.actamat.2010.02.025
- [3] F. Roters, P. Eisenlohr, L. Hantcherli, D.D. Tjahjanto, T.R. Bieler, D. Raabe, Overview of constitutive laws, kinematics, homogenization, and multiscale methods in crystal plasticity finite element modeling: theory, experiments, applications, Acta Mater, 2010, 58(4), 1152-1211

Study of Electronic Structure and Conductivity of Liquid Metallic Sodium Under High Pressure and Temperature

Peter Zhilyaev^{1,2} and Vladimir Stegailov¹

¹Joint Institute for High Temperatures, Russian Academy of Sciences, Izhorskaya ul. 13/19, Moscow, 127412, Russia

²Moscow Institute of Physics and Technology, Institutski per. 9, Dolgoprudny, Moscow region, 141700, Russia
e-mail: PeterZhilyaev@gmail.com

Dynamics methods (shock-waves experiments), in comparison with statistic methods (diamond anvil) provide us possibility to reach higher pressures and temperatures, but on the other hand less information could be obtained in such experiments. And mostly the information would be indirect. The goal of calculation is to provide more data than in experiments to understand the phenomenon more precisely. But there should be the confirmation with experimental data therefore *point of contact* should be exist.

Recently, there is a great interest about behavior of alkali metals under extreme conditions. Properties of liquid metallic sodium are studied by means of Quantum Molecular Dynamics (QMD) under pressures up to 250 GPa and temperatures up to 3000 K. In this range of pressures and temperatures EOS is obtained and electronic structure is analyzed. Also phase transitions and evolution of electronic structure are examined. The Electrical conductivity for some values of pressure and temperatures is calculated. That is the electrical conductivity is our *point of contact* with experimental data. The electrical conductivity not only compare with experimental data, but we also implement it in hydrodynamical code to compare with the experiment directly.

